

Experimental Evaluation and Modeling of an In-duct Ultraviolet Germicidal Irradiation  
(UVGI) System for Bioaerosol Disinfection

by

Hao Luo

A thesis submitted in partial fulfillment of the requirements for the degree of

Doctor of Philosophy

Department of Mechanical Engineering  
University of Alberta

© Hao Luo, 2024

## Abstract

Airborne pathogen transmissions have played critical roles in the previous COVID-19 pandemic and various respiratory epidemics, such as *influenza*, *severe acute respiratory syndrome (SARS)*, etc. Inhaling airborne pathogens can cause adverse health effects, resulting in respiratory infections, severe illnesses, and, in some cases, fatalities. One practical approach to combat airborne transmission is to use ultraviolet-C (UVC) lamps. When integrated with ventilation and filtration measures in heating, ventilation, and air conditioning (HVAC) ducts or room settings, these systems effectively inactivate airborne microorganisms and mitigate airborne pathogen transmission. However, its broader implementation in commercial, residential, and industrial buildings has been limited by the complexity of designing systems for optimal UV inactivation efficiency. Specifically, for the in-duct UV germicidal irradiation (UVGI) systems (this thesis's focus), the effects of system designs, operating conditions, and bioaerosol characteristics on the inactivation efficiency are insufficiently investigated or interpreted. Therefore, the main objectives of this study are twofold: first, to investigate the effects and underlying mechanisms of influencing factors, including the lamp arrangements, duct wall materials, relative humidity (RH), bioaerosol particle size, and microorganism species, on UV inactivation efficiency through comprehensive experimental and modeling works; and second, to integrate the insights into a practical flowchart, supplemented with a case study, to guide the design and implementation of UVGI technology in HVAC ducts.

For this purpose, a pilot-scale duct system with twin-tube low-pressure mercury UV lamps emitting 254 nm radiation was designed and constructed. This study experimentally

examined the impacts of the abovementioned influencing factors on UV inactivation of airborne microorganisms. Airborne *MS2* and *E. coli*, commonly used surrogates for pathogenic viruses and bacterium, were employed in the UV disinfection tests. Additionally, a comprehensive mathematical model was developed to characterize the in-duct UVGI system. This model integrated a new view factor-based model to predict irradiance distribution and an improved genomic model to predict UV rate constants of airborne single-strand RNA (ssRNA) viruses. The UV irradiance model considered multiple factors, such as direct emissive irradiance, specular reflection irradiance, diffusive reflection irradiance, and shadowing effects caused by the arrangement of multiple lamps. The UV rate constant model considered genomic damage, protein capsid damage, and the ratio of aerosol and liquid to represent the UV-induced inhibition of genome replication inside host cells, the prevention of the virus attachment, entry, and genome penetration into the host cell, and the bridge of the UV rate constant between the liquid-based matrix and the airborne state. Finally, computational fluid dynamics (CFD) simulation was utilized to calculate the average received UV dose and predict the disinfection efficiency of the in-duct UVGI system. The mathematical model and CFD simulations were validated using experimental data.

The results demonstrated effective inactivation of airborne microorganisms by UV irradiation, as measured by reduction in live virus/bacteria titers (using conventional culturing methods) and damage to viral genomes (using quantitative polymerase chain reaction (qPCR)). The design of the duct system played a crucial role in regulating irradiance distribution inside the duct. The combination of increasing the number of UV lamps, placing them perpendicular to airflow in the same row (2 lamps scenario), and using

more diffusively reflective duct materials resulted in a higher and more uniform irradiance distribution inside the duct, thus providing better disinfection performance. In addition, operating conditions significantly impacted UV inactivation performance, where increasing RH (25% to 60%) initially increased and then decreased inactivation efficiency due to the combined effects of the bioaerosol water sorption and viral structural damage. Moreover, bioaerosol characteristics critically determined the performance of the UVGI system. Larger bioaerosols posed a more significant challenge for inactivation than smaller bioaerosols due to potential virion aggregations, particle aggregations, and larger salt crystals. In addition, different microorganisms exhibit distinct UV rate constants, thus critically defining the UV inactivation efficiency.

In the end, this thesis proposed a comprehensive UVGI system design flowchart, integrating with the abovementioned insights. A case study was included to demonstrate the practical application of the flowchart. It summarized existing in-duct UVGI system designs from the literature and predicted their germicidal performance, specifically focusing on mitigating possible airborne transmissions of ssRNA viruses. Ten designs were identified as suitable for achieving 90% inactivation of all potential airborne ssRNA viruses.

## Preface

This thesis is an original work by Hao Luo under the supervision of Dr. Lexuan Zhong.

Work published as Hao Luo and Lexuan Zhong, “Ultraviolet germicidal irradiation (UVGI) for in-duct airborne bioaerosol disinfection: review and analysis of design factors”, *Building and Environment*. **2020**, 197, 107852. <https://doi.org/10.1016/j.buildenv.2021.107852> was split between Chapters 2 and 4. Hao was responsible for the concept formulation, literature review, data collection, data analysis, model development and validation, and manuscript composition. Dr. Lexuan Zhong was the supervisory author involved with supervision, concept formulation, evaluation, and manuscript review & editing.

Work published as Hao Luo and Lexuan Zhong, “Development and experimental validation of an improved mathematical irradiance model for in-duct ultraviolet germicidal irradiation (UVGI) applications”, *Building and Environment*. **2022**, 226, 109699, <https://doi.org/10.1016/j.buildenv.2022.109699> was split between Chapters 3, 4 and 6. Hao was responsible for visualization, model development and validation, data collection and analysis, and manuscript composition. Dr. Lexuan Zhong was the supervisory author involved with supervision, project administration, conceptualization, funding acquisition, methodology, and manuscript review & editing.

Work to be submitted to *a journal* as Hao Luo and Lexuan Zhong, “Improving an In-Duct System for Bioaerosol Hazard Mitigation: Evaluating the Role of Particle Size and Relative Humidity in Ultraviolet Germicidal Irradiation Efficiency” was split into Chapters 3, 4, 6, and 7. Hao was responsible for visualization, methodology, data collection and analysis,

and manuscript composition. Dr. Lexuan Zhong was the supervisory author involved with supervision, project administration, conceptualization, funding acquisition, methodology, and manuscript review & editing.

Work published as Hao Luo, Shuce Zhang, and Lexuan Zhong, “Ultraviolet Germicidal Irradiation: A Prediction Model to Estimate UV-C-induced Infectivity Loss in Single-strand RNA Viruses”, *Environmental Research*, **2024**, 241, 117704, <https://doi.org/10.1016/j.envres.2023.117704> was split into Chapters 3, 5, 6, 7. Hao was responsible for the concept formulation, methodology, data collection, data analysis, model development and validation, and manuscript composition. Dr. Shuce Zhang was responsible for the concept formulation and model development. Dr. Lexuan Zhong was the supervisory author involved with supervision and manuscript review & editing.

## Acknowledgments

I would like to take this moment to convey my heartfelt gratitude and deep appreciation to the individuals who have played an indispensable role in supporting and guiding me throughout my Ph.D. journey.

First and foremost, I extend my sincerest gratitude to my esteemed supervisor, Dr. Lexuan Zhong. Dr. Zhong's unwavering belief in my potential, coupled with her generous guidance, unending encouragement, and steadfast support, have been instrumental in shaping the success of my research endeavors. Under her expert mentorship, I have been able to navigate the intricate path of my Ph.D. studies and ultimately achieve the successful culmination of this thesis.

Additionally, I would like to express my profound gratitude to the Built Environment Technology Lab members. Specifically, I am immensely thankful to Jay Hasmukhbhai Patel, Shuce Zhang, Jing Wu, and Caitlyn Shum for their invaluable contributions to my academic pursuits and daily life. Their assistance, camaraderie, and shared academic endeavors have enriched my journey in ways beyond measure.

Lastly, I wish to extend my most profound appreciation to my parents. Their consistent and unwavering support has been a pillar of strength throughout this arduous journey. Their encouragement, sacrifices, and unwavering belief in my abilities have been a constant source of motivation and inspiration.

# Table of Contents

Abstract.....	ii
Preface.....	v
Acknowledgments.....	vii
Table of Contents.....	viii
List of Tables.....	xiii
List of Figures.....	xv
List of Acronyms.....	xix
List of Symbols.....	xxii
1 Introduction.....	1
1.1 Background.....	1
1.2 Research Objectives.....	3
1.3 Outline of the thesis.....	5
2 Literature Review.....	9
2.1 UV inactivation mechanisms.....	9
2.2 UVGI system modeling.....	12
2.2.1 Characterizing UV inactivation efficiency.....	12
2.2.2 UV rate constant models.....	14
2.2.3 UV dose models.....	15
2.3 Factors affecting the UV inactivation efficiency for airborne microorganisms.....	20
2.3.1 In-duct UVGI system designs.....	21
2.3.1.1 Germicidal sources.....	21
2.3.1.2 In-duct UVGI system designs.....	24
2.3.2 In-duct UVGI system operating conditions.....	27
2.3.3 Bioaerosol characteristics.....	28
2.3.3.1 Bioaerosol particle size.....	28
2.3.3.2 Airborne microorganism species.....	29
2.4 Critical research gaps.....	30
2.4.1 The UV irradiance model.....	31
2.4.2 The UV rate constant model.....	31
2.4.3 The effect of RH on UV inactivation efficiency.....	32

2.4.4	The effect of bioaerosol particle size on the UV inactivation efficiency.....	33
3	Experimental Evaluation of the In-duct UVGI System.....	34
3.1	Pilot HVAC system and in-duct UVGI reactor design .....	34
3.2	In-duct UVGI system prequalification tests .....	36
3.2.1	Leakage Test .....	36
3.2.2	Aerosol uniformity test .....	39
3.2.3	Isokinetic sampling test.....	40
3.2.4	Microorganisms' decay in the nebulizer .....	41
3.2.5	Aerosols particle size distribution stability .....	43
3.2.6	Bioaerosols light-off loss (correlation ratio test) .....	44
3.2.7	Other prequalification tests .....	47
3.3	Experimental evaluation of the in-duct UVGI system .....	50
3.3.1	UV irradiance measurement.....	50
3.3.2	UVGI disinfection tests.....	54
3.3.2.1	Microorganisms' preparation .....	55
3.3.2.2	Bioaerosols preparation.....	55
3.3.2.3	Bioaerosols sampling .....	56
3.3.2.4	UVGI test procedures.....	59
3.3.2.5	qPCR assay.....	62
3.3.2.6	Data analysis .....	64
3.4	Results and discussions .....	66
3.4.1	UV irradiance distribution inside the duct .....	66
3.4.1.1	UV lamp emitting wavelength distribution.....	66
3.4.1.2	Effects of lamp arrangements and duct wall materials.....	66
3.4.2	UV inactivation efficiencies.....	68
3.4.2.1	Effects of lamp arrangements and duct wall materials.....	68
3.4.2.2	Effect of RH .....	69
3.4.2.3	Effect of bioaerosol particle size.....	70
3.4.2.4	Effect of genome sequence .....	70
4	UVGI Modeling: Prediction of the UV Doses for the In-duct UVGI Systems..	73
4.1	UV irradiance model .....	73

4.1.1	Lamp output prediction: r method.....	74
4.1.2	Mathematical model of in-duct spatial irradiance.....	76
4.1.2.1	One lamp scenario.....	76
4.1.2.2	Two lamps' scenarios .....	84
4.2	UV dose and inactivation efficiency simulation .....	95
4.2.1	CFD models for UV dose estimation.....	95
4.2.2	UV rate constant calculation .....	97
4.2.3	Numerical methodology.....	98
4.3	Model validations .....	101
4.3.1	UV irradiance model .....	101
4.3.2	CFD simulation validation.....	113
4.4	Results and discussions .....	115
4.4.1	Effects of the in-duct UVGI system designs.....	116
4.4.1.1	Effects of lamp arrangements.....	116
4.4.1.2	Effects of duct wall materials.....	117
4.4.2	Effects of the in-duct UVGI system operating conditions (RH).....	117
4.4.3	Effects of the bioaerosol characteristics (particle size).....	119
5	UVGI Modeling: Prediction of the UV Rate Constants for ssRNA Viruses ...	122
5.1	UV rate constant model.....	122
5.1.1	Literature mining.....	123
5.1.2	The UV rate constant prediction model of the infectivity loss for liquid-based viruses .....	126
5.1.2.1	Genome damage prediction.....	126
5.1.2.2	Infectivity loss prediction.....	129
5.1.3	The UV rate constant prediction model of the infectivity loss for airborne viruses	130
5.1.4	Model validation .....	131
5.1.4.1	Quantitative validation of the infectivity loss UV rate constant model for liquid-based and airborne viruses .....	131
5.1.4.2	Qualitative validation of the genome damage UV rate constant model using liquid-based <i>MS2</i> .....	131

5.1.4.3	Qualitative validation of the genome damage UV rate constant model using airborne <i>MS2</i> .....	132
5.2	Determination of model parameters .....	132
5.2.1	Genome damage prediction model for liquid-based viruses.....	132
5.2.2	Protein damage prediction model for liquid-based viruses.....	134
5.2.3	Infectivity loss prediction model for liquid-based viruses.....	135
5.2.4	Infectivity loss prediction model for airborne viruses .....	139
5.3	Model validations .....	140
5.3.1	UV rate constant model for overall infectivity loss .....	140
5.3.2	Genome damage model.....	146
5.4	Results and discussions .....	152
5.4.1	Prediction of infectivity loss UV rate constants for ssRNA viruses in liquid and comparisons of different UV rate constant models in the literature .....	152
5.4.2	Prediction of infectivity loss UV rate constants for airborne ssRNA viruses	157
6	Analysis of influencing Factors affecting the In-duct UVGI System Inactivation Efficiency .....	159
6.1	Effects of the in-duct UVGI system designs .....	159
6.2	Effect of the in-duct UVGI system operating condition (RH) .....	162
6.2.1	Underlying mechanisms of the impact of RH on the UV rate constant in the current UVGI system .....	162
6.2.2	Discussion of the impact of RH on the UV rate constant in the literature.....	165
6.3	Effect of the bioaerosol characteristics.....	167
6.3.1	Impact of bioaerosol particle size on UV rate constant for airborne <i>MS2</i> .....	167
6.3.2	Impact of microorganism species on UV rate constant .....	171
7	Engineering Implications: A Case Study Aiming at Airborne ssRNA Viruses' Inactivation .....	173
7.1	UVGI system design flowchart .....	173
7.2	A case study aiming at airborne ssRNA viruses inactivation.....	176
7.2.1	Define the types and goals of the UV facility .....	176
7.2.2	Identify UV facility working conditions.....	176
7.2.3	Design the UVGI systems.....	178

7.2.4	Evaluate the UVGI system performance.....	178
8	Conclusions and Recommendations.....	182
8.1	Summary and conclusions.....	182
8.1.1	The effects of key influencing factors on UV inactivation.....	182
8.1.2	Engineering implications.....	184
8.2	Recommendations for future research.....	185
8.2.1	The mechanisms behind the effects of particle size and environmental RH on the airborne virus UV inactivation.....	185
8.2.2	The mechanisms behind the UV rate constant model.....	187
8.2.3	Engineering implication case study.....	188
	Reference.....	189
	Appendix A: View factor model equations.....	245
	Appendix B: UDF code for UV irradiance model (example for the “projection area” method calculation).....	255
	Appendix C: UDF codes for UV dose calculation.....	271
	Appendix D: Average accumulated UV dose at the UVGI reactor outlet.....	273
	Appendix E: ANOVA results and multiple comparisons.....	277
	Appendix F: Rstudio code for extracting genome composition information.....	284
	Appendix G: Statistical analysis of the UV rate constant model.....	286
	Appendix H: The pilot HVAC setup and in-duct UVGI system.....	289

## List of Tables

Table 1 In-duct UVGI system design suggestions from the CFD studies in the literature	19
Table 2 UV rate constants for the airborne microorganisms in UV-LED and low-pressure mercury UV lamp systems.....	23
Table 3 All available in-duct UVGI system designs in the literature .....	25
Table 4 UV rate constants for the infectivity loss of airborne ssRNA viruses .....	30
Table 5 Aerosol concentration differences between 45° and 90° sampling tubes in the duct system .....	40
Table 6 Pilot HVAC system pre-qualification test results.....	48
Table 7 The operating conditions and the sampling times for the <i>E. coli</i> and <i>MS2</i> UVGI experiment.....	61
Table 8 Seventeen primer sets used for airborne <i>MS2</i> UV inactivation tests.....	63
Table 9 Experimental data of the measured irradiance (direct emissive irradiance and overall total irradiance) under different lamp arrangements and duct wall materials .....	67
Table 10 Experimental data of inactivation efficiencies of seventeen primer sets used for airborne <i>MS2</i> UVGI tests.....	71
Table 11 Experimental data of inactivation efficiencies of UVGI tests under different UVGI system designs and operating conditions for airborne <i>E. coli</i> and <i>MS2</i> .....	72
Table 12 Schematic diagram and model equations of the viewpoint P receiving the radiation from the twin-tube UV lamp.....	88
Table 13 Mesh independence test.....	99
Table 14 Comparisons of the model predictions and experimental data of one-lamp with galvanized steel duct walls and multiple lamps with stainless steel duct walls.....	112
Table 15 Airborne <i>E. coli</i> inactivation efficiencies under various conditions.....	116

Table 16 Summary of the model parameter information and genome damage UV rate constants in the literature for various genome segments of ssRNA viruses in liquid.....	124
Table 17 UV rate constant ratio of aerosol and liquid for different ssRNA viruses.....	139
Table 18 Model predictions and experimental data (in the literature) of the infectivity loss UV rate constants for ssRNA viruses in liquid.....	141
Table 19 UV rate constants for the infectivity loss of airborne ssRNA viruses .....	146
Table 20 Twelve primer sets used for <i>MS2</i> UV inactivation tests in liquid and the experimental data of inactivation efficiencies[165].....	149
Table 21 Seventeen primer sets used for airborne <i>MS2</i> UV inactivation tests and the experimental data of the genome damage UV rate constant.....	150
Table 22 Comparisons of the model performance for the predicted infectivity loss UV rate constants of ssRNA viruses in liquid.....	155
Table 23 Predicted UV rate constants for potential airborne ssRNA viruses.....	157
Table 24 Effect of duct wall materials on the UVGI efficiency in different reactors.....	161
Table 25 In-duct UVGI system designs in the literature and the estimated airborne ssRNA viruses' inactivation efficiencies.....	180

## List of Figures

Figure 1 illustrative schematic of (a) virus infection steps and (b) photodimer formations on the RNA upon the UV illumination.....	10
Figure 2 The schematic of (a) the pilot HVAC system and (b) in-duct UVGI reactor.....	36
Figure 3 Schematic of the leakage test .....	37
Figure 4 Pentane decay curves during the leakage test.....	39
Figure 5 The (a) <i>E. coli</i> and (b) <i>MS2</i> concentration in the nebulizer during the nebulization .....	42
Figure 6 The normalized PBS aerosol particle size distributions for ten samples that are collected for a 3-hour experiment period.....	44
Figure 7 Particle size distributions for (a) <i>E. coli</i> and (b) <i>MS2</i> bioaerosols at the upstream and downstream of the UVGI reactor (0.5m/s and 25% RH), with #1 and #2 representing the testing times of 25 minutes and 1 hour and 45 minutes since the start of nebulization .....	46
Figure 8 Schematic illustration of the irradiance measurement locations inside the duct (a: measured four cross-sections under the one-lamp stainless steel scenario, b: measured four cross-sections under the one-lamp galvanized steel and multiple-lamps scenarios) .....	51
Figure 9 (a) The direct emissive irradiance measurement in an open-air environment setup; (b) the overall total irradiance measurement inside the duct; and (c) lamp surface emitting irradiance at the bottom point .....	53
Figure 10 Schematic of lamp arrangements inside a duct: (a) one lamp at the center, (b) two lamps per row (one row), and (c) one lamp per row (two rows) .....	54
Figure 11 The setup of sampling bioaerosols on the TEM grid .....	58
Figure 12 The emitting UV wavelength spectra of the low-pressure mercury UV lamp in this thesis.....	66

Figure 13 Experimental data of inactivation efficiencies for airborne <i>MS2</i> across different impactor stages at different RHs at a temperature of $24.8^{\circ}\text{C} \pm 0.4^{\circ}\text{C}$ (error bars represent the standard deviations from the triplicate experiments).....	70
Figure 14 UV lamp output as a function of lamp surface temperature.....	76
Figure 15 One UV lamp scenario layout in the duct and the schematic illustration of the view factor calculations .....	78
Figure 16 A specular reflector shows a virtual image of a lamp at an equivalent distance behind the reflector surface.....	80
Figure 17 Schematic of two-lamp arrangements inside a duct: (a) two lamps per row (one row) and (b) one lamp per row (two rows).....	84
Figure 18 Schematic illustration of the shadowing effects between Lamp1 and Lamp2 placed in two rows .....	87
Figure 19 (a) – (k) Schematic of the view factor calculations for different lamp arrangements and scenarios .....	88
Figure 20 Numerical grid of the in-duct UVGI system with a single lamp.....	99
Figure 21 Predicted lamp surface temperature and convective heat loss ratio $r_Q$ for (a) mixed convection ( $U = 0.31$ m/s) with lamp type 1; (b) forced convection ( $U = 2.5$ m/s) with lamp type 1; and (c) forced convection ( $U = 3$ m/s) with lamp type 2.....	103
Figure 22 Contours of the numerical results for the irradiance distribution within the stainless steel duct for one lamp .....	108
Figure 23 Contour of the numerical results for the total irradiance distribution within the galvanized steel duct for one lamp.....	109
Figure 24 Contours of the numerical results for the cross-sectional total irradiance distributions under different lamp arrangements .....	112
Figure 25 Comparison of the UV rate constant for airborne <i>E. coli</i> in this study and literature .....	115

Figure 26 (a) UV rate constants of airborne *MS2* exposed to UVGI across three RH levels, categorized by particle sizes and (b) – (g) UV rate constants and statistical analysis from the one-way ANOVA followed by Tukey’s multiple comparisons tests (Appendix E). 118

Figure 27 (a) Inactivation efficiencies and UV rate constants for airborne *MS2* across different impactor stages at different RHs and a temperature of  $24.8^{\circ}\text{C} \pm 0.4^{\circ}\text{C}$  and (b) – (d) UV rate constants and statistical analysis from the one-way ANOVA followed by Tukey’s multiple comparisons tests (Appendix E)..... 120

Figure 28 (a) – (h) Comparisons between the model predictions and experimental data of the infectivity loss UV rate constants for 36 viruses using eight genome damage equation forms (Eq. (9a) – (9h)) with ten genome segment division lengths (500, 1000, 2000, 3000, 4000, 5000, 6000, 7000, 8000, and no division), and (i) Mean relative errors of the predicted infectivity loss UV rate constants (36 ssRNA viruses) for eight genome damage equations with ten segment division lengths ..... 137

Figure 29 Comparisons between model predictions and experimental data for the infectivity loss UV rate constant of ssRNA viruses in (a) liquid-based and (b) airborne applications. .... 140

Figure 30 Comparisons of the model predictions of the genome damage (inactivation efficiency and UV rate constant) for liquid-based and airborne *MS2* inactivation..... 148

Figure 31 Comparisons between model predictions and experimental data from the literature for the UV rate constants of ssRNA viruses..... 153

Figure 32 The comparisons between the model predictions (models from the literature [31,33,38,41] and this study) and experimental data for the ssRNA viruses in liquid ... 156

Figure 33 Comparisons of UV rate constants for airborne viruses exposed to UVGI at different RH levels in the literature [106–109,114]..... 167

Figure 34 (a) TEM image of an *MS2* bioaerosol (sample comes from stage 4); and (b) EFTEM analysis of an *MS2* bioaerosol from stage 4. .... 170

Figure 35 A flowchart describing the process of planning UV facilities for inactivating airborne microorganisms (red highlights: potential causes of system failure during UVGI evaluation)..... 175

Figure 36 Predicted inactivation efficiencies of airborne ssRNA viruses (potentially harmful to humans) using various in-duct UVGI system designs in the literature (design details see in Table 3) ..... 179

## List of Acronyms

A	Adenine
ASHRAE	American society of heating, refrigerating and air conditioning engineers
C	Cytosine
CFD	Computational fluid dynamics
CFU	Colony-forming unit
CPD	Cyclobutene pyrimidine dimer
Ct	Threshold cycle
DNA	Deoxyribonucleic acid
DNase	Deoxyribonuclease
DO	Discrete ordinates
DPM	Discrete phase model
ds	Double-strand
<i>E. coli</i>	Escherichia coli
EFTEM	Energy-filtered transmission electron microscopy
EPA	Environmental protection agency
FTIR	Fourier transform infrared spectroscopy
G	Guanine
GCI	Grid convergence index
GFP	Green fluorescent protein
GUV	Germicidal ultraviolet
HEPA	High efficiency particular air
HVAC	Heating, ventilation, and air conditioning

LB	Lysogeny broth
LED	Light-emitting diode
MHV	Mouse hepatitis virus
NCBI	National center for biotechnology information
OD	Optical density
OPS	Optical particle sizer
PCA	Principal component analysis
PBS	Phosphate-buffered saline
PFU	Plaque-forming unit
PP	Pyrimidine-pyrimidine
PTFE	Polytetrafluoroethylene
qPCR	Quantitative polymerase chain reaction
RED	Reduction equivalent dose
RH	Relative humidity
RNA	Ribonucleic acid
RNase	Ribonuclease
RT	Reverse transcription
RTE	Radiative transfer equation
SARS-CoV	Severe acute respiratory syndrome coronavirus
SARS-CoV-2	Severe acute respiratory syndrome coronavirus-2
ss	Single-strand RNA
S2S	Surface-to-surface
T	Thymine
TEM	Transmission electron microscopy
U	Uracil

UDF	User-defined functions
UDG	Uracil DNA glycosylase
UVC	Ultraviolet C radiation
UVGI	Ultraviolet germicidal irradiation

## List of Symbols

a	Fractions
A	Aera, $m^2$
AF	Amplification factor
C	Concentration, ppm or particle/ $m^3$
$C_D$	Drag coefficient
d	Diameter, m
D	UV dose, $mJ/cm^2$ or $J/m^2$
$D_{P-c}$	Normal distance between the viewpoint P and the cylinder axis, m
$D_{P-a}$	Normal distance between the viewpoint and the cylinder's axis, m
$D_{P-e}$	Normal distance between the viewpoint and cylinder's circle, m
$f_{two-stage}$	Fractions of microbial population that is more resistant to UV illumination
F	Force, N
$F_p$	View factor, dimensionless
g	Acceleration due to gravity, $m/s^2$
Gk	Generation of turbulence kinetic energy due to the mean velocity gradients, $m^2/s^3$
Gb	Generation of turbulence kinetic energy due to buoyancy, $m^2/s^3$
Gr	Grashof number, dimensionless
h	Relative contribution of protein damage to the total viral infectivity loss, dimensionless
H	Height, m

I	UV irradiance, $\text{W}/\text{m}^2$
$I_{\text{unit}}$	Unit tensor for momentum equation
k	UV rate constant, $\text{cm}^2/\text{mJ}$ or $\text{m}^2/\text{J}$
K	Thermal conductivity coefficient, $\text{W}/\text{mK}$
$k_{\text{turbulent}}$	Turbulent kinetic energy, $\text{m}^2/\text{s}^2$
l	Length, m
L	Length, m
$n_{\text{multitarget}}$	Multitarget exponent, dimensionless
$n_t$	Number of time steps, dimensionless
N	Particle numbers, dimensionless
Nu	Nusselt number, dimensionless
p	Pressure, Pa
PL	Path length, m
Pr	Prandtl number, dimensionless
q	Flowrate, $\text{m}^3/\text{min}$
Q	Heat loss, W
r	Radius, m
$r_Q$	Ratio of convective heat dissipation to radiative heat dissipation, dimensionless
$r_{UV}$	UV rate constant correction ratio for converting from water-borne to airborne viruses, dimensionless
R	Reflectivity, dimensionless
Re	Reynolds number, dimensionless
S	Source term
t	Time, minute or second
T	Temperature, $^{\circ}\text{C}$

$u$	Velocity, m/s
$U$	Velocity, m/s
$V$	Volume, m <sup>3</sup>
$w$	Lamp power, W
$W$	Width, m
$Y_M$	Contribution of the fluctuating dilatation in compressible turbulence to the overall dissipation rate, m <sup>2</sup> /s <sup>3</sup>

### **Greek letters**

$\eta$	Inactivation efficiency, dimensionless
$\rho$	Density, kg/m <sup>3</sup>
$\varphi$	Independent variable
$\varepsilon$	Emissivity, dimensionless
$\varepsilon_t$	Turbulent energy dissipation rate, m <sup>2</sup> /s <sup>3</sup>
$\sigma$	Stefan-boltzmann constant, W/m <sup>2</sup> K <sup>4</sup>
$\sigma_s$	Standard deviation
$\alpha_\lambda$	UV extinction coefficient, cm <sup>-1</sup>
$\mu$	Viscosity, kg/m-s
$\mu_t$	Turbulent viscosity, kg/m-s
$\tau$	Stress tensor

### **Subscripts**

0	Initial
1, 2, ... n	Numbers
amb	Ambient environment
conv	Convective heat loss
cylinder	Lamp cylinder number

dw	Sidewall numbers
Downstream	Downstream sampling
exp	Experimental data
genome damage	Genome damage
i	Grid cell
iprimer	Primer sets
infectivity loss	Viral infectivity loss
max	Maximum
number	Number of pyrimidines
on	UV light on
off	UV light off
rad	Radiative heat loss
ratio	Ratio of pyrimidines
rd	Diffusive reflection
rs	Specular reflection
s	Stage numbers
sur	Surface
te	Total number of face grid cell
tube	Lamp tube number
unit	Unit tensor
Upstream	Upstream sampling
UV	Ultraviolet
we	Wall grid cell

# 1 Introduction

## 1.1 Background

The coronavirus disease (COVID-19) pandemic, caused by the *severe acute respiratory syndrome coronavirus-2 (SARS-CoV-2)*, has had a profound global impact, resulting in over 771 million cumulative cases and 6.9 million deaths as of October 2023. Analogous to other contagious respiratory pathogenic viruses, *SARS-CoV-2* is mainly transmitted through droplet, contact, and airborne modalities. The short-range droplet-based (large droplets deposited on a surface within 1–2 m) and contact transmission routes have been well recognized, and adequate precautions have been implemented, including maintaining a physical distance and washing hands frequently. However, the long-range transmission route in bioaerosols is gaining attention, and mitigating the spread via this route is the most challenging [1–6].

Engineering controls, such as ventilation with fresh outdoor air or filtered/purified air, are suggested to prevent long-range airborne contaminant transmission [7]. However, fully intaking fresh outdoor air or entirely shutting down air recirculation is not feasible in most building heating, ventilation, and air conditioning (HVAC) systems due to the extensive energy consumption required and limited heating/cooling capacities to provide a comfortable indoor environment. Thus, practical air purification technologies, such as filtering or using ultraviolet germicidal irradiation/germicidal ultraviolet (UVGI/GUV) to remove or inactivate potential viral contaminations, are proposed [8]. Among them, UV inactivation is recognized and recommended for efficient bioaerosol elimination in indoor environments [9]. It uses short-wave ultraviolet energy (UVC, 200–280 nm) to inactivate

viral, bacterial, and fungal organisms by disrupting the genetic materials and structural components, thus preventing their expressions and replications [10,11].

Germicidal ultraviolet systems can be applied in various ways for air disinfection. The oldest implementation of UVGI to disinfect air is the “upper room” system, in which wall-mounted or pendant fixtures create a disinfection zone above the occupied zone. Such systems were first used in the 1930s and demonstrated excellent effectiveness against measles and other childhood diseases in schools [12]. Germicidal UV is also effective for airstream disinfection in HVAC systems [13]. Airstream disinfection systems installed in air handling units can simultaneously prevent microbial growth on cooling coils, which in return reduces maintenance cost and energy use [14]. In addition, UVGI can also be incorporated into a stand-alone (portable) air cleaner in the indoor environment [15].

Despite the well-recognized effectiveness of UVGI systems, their broader implementation in commercial, residential, and industrial buildings has been hindered. This delay is attributed to the need for specialized expertise and comprehensive knowledge in designing systems that ensure adequate UV inactivation efficiency is achieved within complex built environments. The disinfection performance of UVGI systems is contingent on two critical parameters: the UV dose delivered to airborne microorganisms and the microorganisms' susceptibility to UV exposure (termed as the UV rate constant). Various engineering and biological factors substantially influence these parameters. For instance, in this thesis's focus, the in-duct UVGI system, various design elements, such as duct dimensions, materials, and lamp configurations, significantly affect UV radiation distribution [16]. Similarly, operational conditions, including air velocity, temperature, and relative humidity (RH), impact UV radiation distribution [16–19], UV exposure duration of airborne

microorganisms [16], and their survivability, infectivity, and UV rate constants [20–23]. Additionally, the characteristics of bioaerosols, such as composition, size, and the microorganism species, determine the UV rate constants [17,20,24–26]. Therefore, a detailed understanding of how these factors influence UVGI system performance is crucial. Additionally, how to utilize this knowledge to design an effective UVGI system is critical, especially considering the varying operating conditions and the diverse characteristics of bioaerosols in complex built environments.

This thesis aims to explore the effects and underlying mechanisms of various influencing factors on UV inactivation of airborne microorganisms. It specifically addresses those factors that have been insufficiently investigated or inadequately interpreted in existing literature, including the impacts of lamp arrangements, duct wall materials, environmental RH, bioaerosol particle size, and microorganism species. This thesis goes beyond theoretical analysis to integrate practical findings into a comprehensive flowchart. A case study is included to demonstrate the application of this flowchart, focusing on the inactivation of potential airborne ssRNA viruses within HVAC ducts. Ultimately, this thesis aims to provide valuable insights and tools to enhance the design and implementation of UVGI technology in HVAC ducts, thereby contributing to mitigating airborne disease transmissions.

## 1.2 Research Objectives

The principal objective of the thesis is to thoroughly investigate the effects and underlying mechanisms of diverse influencing factors on UV inactivation. It concludes with a detailed presentation of practical implications, accompanied by a flowchart. This flowchart serves

as a guide, illustrating the application of the research findings to optimize the design and implementation of UVGI technology in HVAC systems. To achieve these objectives, this thesis undertakes systematic experimental investigations and develops comprehensive mathematical models to characterize the performance of in-duct UVGI systems. The detailed objectives are summarized below:

- a) **Identifying understudied influencing factors in UV inactivation of airborne microorganisms through literature review:** The first objective is to pinpoint key factors that influence the inactivation performance of in-duct UVGI systems, yet insufficiently investigated or inadequately interpreted, from both engineering and biological perspectives.
- b) **Assessing inactivation efficiency variations in the in-duct UVGI system under varying influencing factors through experiments:** The following objective is to assess inactivation efficiency variations in the in-duct UVGI system under various previously identified influencing factors, including in-duct UVGI system designs, operating conditions, and bioaerosol characteristics, through systematic experimental investigations.
- c) **Developing mathematical models and using numerical simulations to characterize the in-duct UVGI system:** This objective is to predict the UV irradiance field inside the in-duct UVGI system and UV rate constant of airborne microorganisms through a novel view factor-based UV irradiance model and an enhanced genome damage-based model. Further, this object includes the use of computational fluid dynamics (CFD) simulations to obtain the average accumulative UV dose at the UVGI system outlet.

- d) **Analyzing the underlying mechanisms of the influencing factors on the UV inactivation in the in-duct UVGI system:** This objective is to provide a detailed analysis of the underlying mechanisms of how influencing factors, including in-duct UVGI system designs, operating conditions, and bioaerosol characteristics, affect the UV inactivation performance in the in-duct UVGI system.
  
- e) **Integrating the research outcomes on the influencing factors into the design of an effective in-duct UVGI system in the real world:** The final objective aims to integrate the practical findings from the thesis into a comprehensive flowchart. This flowchart will be a valuable tool for facilitating the effective design and implementation of UVGI technology in controlling bioaerosol hazards within built environments. To demonstrate its utility, a case study will be presented, illustrating its application in targeting the inactivation of potential airborne ssRNA viruses within HVAC ducts in North American cities.

### 1.3 Outline of the thesis

The thesis is structured into eight chapters, with the introductory chapter providing the foundational background and objectives of the research.

#### **Chapter Two: Literature Review**

Chapter Two offers a thorough literature review that provides a comprehensive exploration of UV inactivation of bioaerosols. It identifies critical engineering and biological parameters influencing in-duct UVGI system inactivation efficiency and delves into their effects. This chapter also critically analyzes current research gaps, laying the groundwork for the subsequent research presented in this thesis.

### **Chapter Three: Experimental Evaluations of the In-duct UVGI System**

Chapter Three presents the systematic experimental evaluations of a pilot in-duct UVGI system. It commences by detailing the system's design and prequalification tests. The chapter then explicates the experimental methodology and presents the results. Specifically, this chapter experimentally examines the impacts of duct system designs (UV lamp arrangements and duct wall materials), operating conditions (air RH), and bioaerosol characteristics (bioaerosol particle size and airborne microorganism genome sequences) on UV inactivation efficiency. The study employs airborne *MS2* and *E. coli* as surrogates for pathogenic viruses and bacteria in the UV disinfection tests.

### **Chapter Four: UVGI Modeling: Prediction of the UV Doses for the In-duct UVGI Systems**

Chapter Four introduces a comprehensive modeling approach to characterize and predict the UV dose of an in-duct UVGI system. This model incorporates a novel view factor-based model for predicting irradiance distribution and utilizes CFD simulations to calculate the average accumulative UV dose of the UVGI system. The mathematical model and CFD simulation are validated using experimental data in this study. This chapter reports and examines the impacts of duct system designs (UV lamp arrangements and duct wall materials), operating conditions (air velocity), and bioaerosol characteristics (bioaerosol particle size) on the average accumulative UV dose at the UVGI reactor outlet.

### **Chapter Five: UVGI Modeling: Prediction of the UV Rate Constants for the ssRNA Viruses**

Chapter Five develops an enhanced genomic model for predicting UV rate constants of ssRNA viruses in both liquid and airborne states. This model accounts for genomic damage, protein capsid damage, and the ratio of aerosol to liquid, which characterize the UV-induced inhibition of genome replication within host cells, the prevention of virus attachment and entry, and the bridge of UV rate constant between liquid-based and airborne matrices. The UV rate constant prediction model is rigorously validated using experimental data from the literature and this study.

### **Chapter Six: Analysis of Influencing Factors Affecting the In-duct UVGI System Inactivation Efficiency**

Chapter Six provides a detailed analysis of the essential factors that influence the performance of in-duct UVGI systems. It offers in-depth engineering and biological insights into the fundamental mechanisms at play. This chapter analyzes how various elements of duct system design, such as UV lamp arrangements and duct wall materials, impact the average accumulated UV dose. The chapter also explores how operating conditions (air RH) and bioaerosol characteristics (bioaerosol particle size and microorganism species) influence the UV rate constant for airborne microorganisms. These insights shed light on the factors affecting UV inactivation efficiency in in-duct UVGI systems.

### **Chapter Seven: Engineering Implications: A Case Study Aiming at Airborne ssRNA Viruses' Inactivation**

Chapter Seven goes beyond theoretical analysis to integrate practical findings from Chapter Six into a comprehensive flowchart. This flowchart is a practical tool for designing and implementing UVGI technology to mitigate bioaerosol hazards. Furthermore, the chapter

presents a case study to demonstrate the application of the flowchart, focusing on the inactivation of potential airborne ssRNA viruses within HVAC ducts.

### **Chapter Eight: Conclusion and Recommendations**

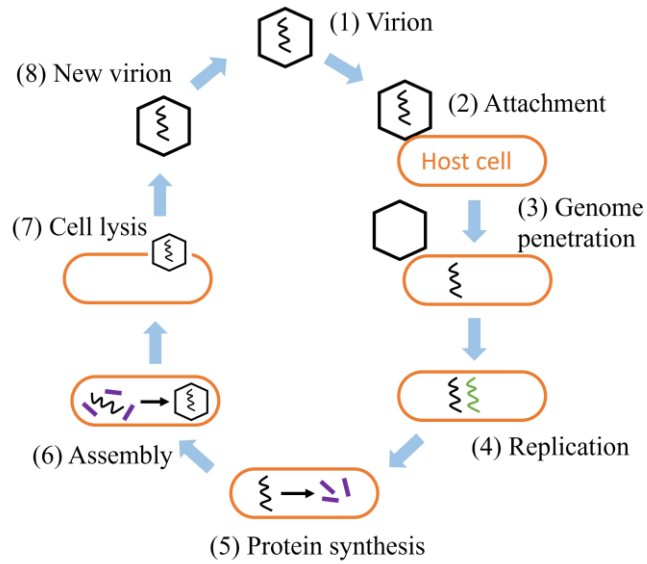
The final chapter, Chapter Eight, summarizes the thesis and offers insights into potential future research directions, building upon the knowledge and discoveries presented throughout the preceding chapters.

## 2 Literature Review

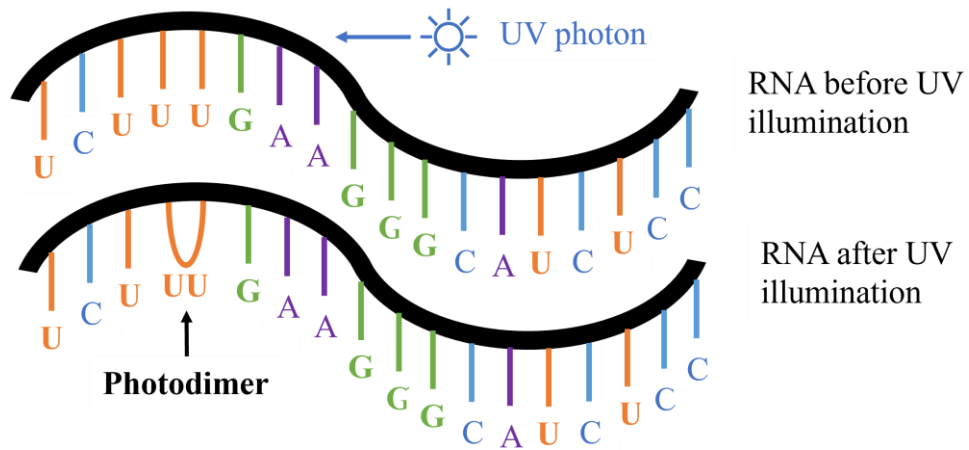
### 2.1 UV inactivation mechanisms

UVGI/GUV uses short-wave ultraviolet energy (UVC, 200 – 280 nm) to inactivate viral, bacterial, and fungal organisms, making them unable to replicate themselves and spread diseases. It has been a validated disinfection technology for microorganisms in water, air, and on the surface for several decades [26,27]. Mainly, the UVC photon absorptions from the intercellular components of microbes (i.e., Deoxyribonucleic acid (DNA), Ribonucleic acid (RNA), and proteins) are responsible for the detrimental effects on microbes [26,28]. Within the UVC range, the germicidal efficiency peaks at about 260 – 265 nm due to the same peak of UV absorption by DNA/RNA [26].

For ssRNA viruses, the main target microorganisms in this thesis, their infection mechanisms are complicated and comprise three main steps (Figure 1): attachment to the host, entry or genome penetration into the host, and genome replication inside the host. During the host attachment and entry or genome penetration processes, viral proteins on capsid are a key component for a successive infection, whereas the viral genome plays a vital role during replication [29,30]. Accordingly, damage caused by UV damage to either of these viral components can inactivate the viruses by interrupting these steps in the infectivity processes.



(a)



(b)

Figure 1 illustrative schematic of (a) virus infection steps and (b) photodimer formations on the RNA upon the UV illumination

In detail, UV effectively inactivates viruses mainly by damaging their genetic materials, thereby inhibiting gene expression and viral replication (steps 4 and 5 in Figure 1 (a)) [31].

The nitrogenous bases in nucleic acids absorb UV radiation and result in photochemical

reactions between adjacent pyrimidine bases (Figure 1 (b)) [26,32]. Commonly characterized photoproducts include cyclobutene pyrimidine dimers (CPD), pyrimidine-pyrimidine adducts (6-4 PP), and their Dewar valence isomers. Among these, CPD photoproducts are the predominant contributors to genome damage due to their high quantum yields [33–37]. The  $UV_{254}$  genome reactivity is influenced by genome size and sequence in several ways: (1) larger genomes lead to more sites for photodimerization and CPD formation, resulting in increased genome damage [26,36,38]; (2) pyrimidine bases (thymine (T), cytosine (C), and uracil (U)) are more photoreactive than purine bases (adenine (A) and guanine (G))[26,32,36]; (3) and pyrimidine dimers display varying degrees of photo-reactivity, in the order  $TT > TC > CT > CC$  [34,38]. While strand breaks, interstrand cross-linking, and protein-nucleic acid linkages are also observed, their quantum yields are comparatively lower than those of CPD photoproducts [36].

In addition to the genome damage, UV radiation also affects capsid proteins, which can obstruct the virus's attachment, entry, and genome integration into host cells, and sometimes even the process of genome integration itself (steps 2 and 3 in Figure 1 (a)) [30,39]. For some particular types of viruses, for instance, double-strand DNA (dsDNA) viruses, there is dark genome repair after the UV illumination. The unique phenomenon is due to twofold reasons: one is because the genome repair enzymes in the host cell, which are meant to repair the host cell, can also be used to repair viral dsDNA once the virus genome is injected into the host cell; and another one is certain viruses encode one or more repair enzymes in their own virus genomes (e.g., *T-even* and *T5 phages*).

## 2.2 UVGI system modeling

### 2.2.1 Characterizing UV inactivation efficiency

UV disinfection is invariably a logarithmic process, as is microbial growth [26]. Quantifying disinfection performance of a UVGI reactor varies widely among different microorganisms and is subject to many complexities, including shoulder effects, second-stage decay, etc. The primary used quantification for disinfection performance is the single-stage inactivation efficacy:

$$\eta = 1 - e^{-kD} = 1 - e^{-kt} \quad (1)$$

where  $k$  is the species-dependent microorganism UV rate constant ( $\text{m}^2/\text{J}$ ),  $D$  is the UV dose ( $\text{J}/\text{m}^2$ ) delivered to the microorganisms,  $I$  is the irradiance ( $\text{W}/\text{m}^2$ ), and  $t$  is the exposure time (s). The single-stage decay model is generally adequate for most in-duct UVGI design purposes, provided the UV dose is within first-order parameters. However, there are a few scenarios that do not entirely comply with the single-stage decay model. For instance, it is commonly observed that during UV disinfection, a tiny fraction of the microbial population exhibits a higher level of resistance than the rest of the microbes [26,40]. This effect will, of course, only be apparent if the inactivation efficiency is very high, sometimes as much as six logs of disinfection. This phenomenon is called two-stage decay, where the susceptible portion of the microbial population will define the first stage of decay (fast decay), and the second stage of decay (slow decay) will be defined by the resistant microbial population. To describe such a case, people defined the inactivation efficiency as:

$$\eta = 1 - \left[ (1 - f_{\text{two-stage}}) e^{-k_1 D} + f_{\text{two-stage}} e^{-k_2 D} \right] \quad (2)$$

where  $f_{\text{two-stage}}$  is fractions of microbial population that is more resistant to UV illumination,  $k_1$  is the first stage (fast decay) UV rate constant ( $\text{m}^2/\text{J}$ ), and  $k_2$  is the section stage (slow decay) UV rate constant ( $\text{m}^2/\text{J}$ ). Besides two-stage decay, there is a potential shoulder effect for some microorganisms that exhibit the lag in response to the UV illumination, which implies that either a threshold dose is necessary before measurable effects occur or that repair mechanisms actively deal with low-level damage at low doses [26]. Correspondingly, the multi-hit model is introduced to address this phenomenon as:

$$\eta = (1 - e^{-kD})^{n_{\text{multitarget}}} \quad (3)$$

where  $n_{\text{multitarget}}$  is the multitarget exponent, which can be found by extrapolating the first-stage data to the y-intercept. It presumably represents the number of discrete critical sites that must be hit to inactivate the microorganism. In theory,  $n$  is an integer, but in practice, this is not always the case. The value of  $n$  is unique to each species. Occasionally, microbial UV disinfection data can display both a shoulder and two stages of decay. The mathematical model for this combined curve can be expressed as [26]:

$$\eta = 1 - \left\{ (1 - f_{\text{two-stage}}) \left[ 1 - (1 - e^{-k_1 D_{UV}})^{n_{\text{multitarget-1}}} \right] + f_{\text{two-stage}} \left[ 1 - (1 - e^{-k_2 D_{UV}})^{n_{\text{multitarget-2}}} \right] \right\} \quad (4)$$

Nevertheless, in the case of ssRNA viruses within the in-duct UVGI system, they predominantly exhibit single-stage inactivation efficiency, as represented by Eq. (1). This is primarily due to their relatively simple inactivation mechanisms and limited UV doses arising from the short UV exposure time inside the duct. Therefore, the UV rate constant

and inactivation efficiency delineated by Eq. (1) are consistently applied throughout the thesis.

### 2.2.2 UV rate constant models

The UV inactivation rate constant ( $k$ ), which describes the UV dose-response behaviors upon UV illumination, differs among viruses [26]. With the UV rate constant known, under any given UV dose, the inactivation efficiency can be estimated using Eqs. (1) – (4) considering different microorganism decay scenarios. To date, various models, spanning empirical, semi-empirical, and experimental models, have been proposed based on the photochemical behaviors of nucleic acid components and compositions. For instance, Lytle et al. [41] introduced the concept of “size-normalized sensitivity” by multiplying the  $D_{37}$  value (UV dose needed for 37% survival) by the genome size. This model revealed relatively constant values for “size-normalized sensitivity” among viruses sharing similar genetic compositions. Taking a semi-empirical approach, both Kowalski et al. [42–44] and Pendyala et al. [38] introduced “dimerization values”, derived by merging the number of counted CPDs on the specific virus genome with dimer proportionality constants. These values were found to correlate closely with  $D_{90}$  values (UV dose yielding 90% inactivation). In addition to these approaches, physics-based models have also been developed to estimate UV-induced damage to specific sequences or entire genomes. These models combine experimentally determined molar absorption coefficients and quantum yields for different CPDs and nucleotide monomers (T, C, U, G) with the counted number of dimers/monomers [32,33]. Alternatively, experimental-based methods have extrapolated whole genome damage from quantitative polymerase chain reaction (qPCR)-detected amplicon damage using a linear correlation

(  $k_{pre,genome} = \frac{total\ genome\ length}{PCR\ region\ length} \times k_{PCR,region}$  ), showing good consistency with viral

infectivity loss [45–48]. Delving into statistical methods, Rockey et al. [31] evaluated four types of statistical learning models, namely, multiple linear regression, elastic net regularization, boosted trees, and random forests. Among these models, multiple linear regressions performed best when trained on a selected subset of predictors, such as virus nucleic acid type, genome length, genome composition, genome repair mode, and host cell type [31].

### 2.2.3 UV dose models

The UV dose is inherently the product of UV irradiance and UV exposure time. It appears quite simple. However, its application can be complicated, being critically affected by the UVGI system designs and operating conditions (e.g., when calculating the dose received by a microorganism following a tortuous path through a device with spatial variations in irradiance). UV irradiance field and airborne microorganism transport (UV exposure time) are the two significant parts of the in-duct UVGI system simulation. CFD simulation has gained popularity in recent years owing to its ability to simulate complex in-duct airflows, providing a microscopic view of the fluid/thermal physical phenomenon and detailed information on the physics quantity field [49].

For the UV irradiance modeling, there are two types of commonly used radiation models: the radiative transfer equation (RTE) physical model and the trigonometric models (point/line-source lamp emission model and view factor model). The former describes radiation propagation with energy loss (absorption), gain (emission), and redistribution (scattering), and the latter predicts UV irradiance based on the inverse square law and

geometric relationship of irradiation surfaces and angles [50]. The RTE approach, which considers varying isothermal conditions, such as absorption, reflection, and refraction, numerically solves the irradiance field and is popular in simulating a complex environment (such as upper-room/whole-room UVGI systems with complex room layouts and light fixtures and louvers) [51–54]. Commonly used RTE models include the P1 model [55], the surface-to-surface model (S2S) [72], and the discrete ordinates (DO) model [55,57–60]. While the trigonometric models obtain analytical solutions of the irradiance distribution and require less computational resources; thus, they can effectively predict the irradiance field in simple scenarios [61–66].

In particular, for in-duct UVGI systems, the view factor model, which was initially derived from calculating the radiative heat transfer between two different areas under different configurations [67], has been widely used to predict the irradiance field within the duct enclosure [61–64]. In detail, the primitive view factor model is developed from the well-addressed theory of the radiation view factor “from a differential planar element perpendicular to a finite cylinder”, which is readily applied for simulating the direct emissive irradiance from a single luminous cylinder UV lamp [62,64]. Then, considering that the ventilation duct walls are commonly made of reflective metals (i.e., galvanized steels) with multiple reflections (specular and diffuse reflections) within the duct, the reflective irradiation needs to be implemented. Notably, the specular reflection irradiance was considered as the direct emissive irradiance from the mirror-reflected “virtual lamp image” by using the primitive view factor “from a differential planar element perpendicular to a finite cylinder” [61,62]. While the diffuse reflection irradiance was calculated by the theory of radiation view factor “from a differential area parallel to a finite wall element”

and using the direct irradiance on the duct wall as the new diffusely emitting energy source [61,63]. Then, summing the direct emissive irradiation with the specular and diffuse reflective irradiation, the total received irradiation from a single luminous cylinder UV lamp within the duct can be obtained. Further considerations were made for the twin-tube UV lamps, which are constructed with two luminous tubes and a connecting tube at the top. Simplifications were made to treat them as two independent luminous cylinders and two luminous cylinder-end circles, and the final irradiance was combinedly obtained from the four luminous objects [61].

As for airborne microorganism transport, CFD simulation with the discrete phase model (DPM), which solves the particle trajectory based on Newton's second law and accounts for gravity, drag force, and momentum coupling between the particle and the fluid, is commonly used [68]. By solving the DPM equations along with the velocity vector of air, the motions of airborne organisms can be tracked, and the spatial and temporal concentrations (number of particles in each computational cell at any time  $t$ ) can be determined. By further combining the UV irradiance field with the bioaerosol trajectories, the cumulative UV dose of individual particles and the average UV dose (standard deviation) of the system can be computed.

The average UV doses (standard deviations) and dose distributions are the critical indices that CFD simulations provide for UVGI system evaluation. CFD has been successfully applied in the literature to provide an accurate overall average UV dose for a system. For instance, the EPA 600/R-06/050 test [69] experimentally rated the performance of a single-lamp UV system of  $2.47 \text{ J/m}^2$  from *B. atrophaeus*. However, CFD simulation shows that the average UV dose should be  $10.97 \text{ J/m}^2$ , a more accurate dose value that gives closer

disinfection efficacy for *MS2* with the experimental results [70]. In the same manner, the average UV dose for EPA 600/R-06/051 [71] was corrected from 2.95 to 18 [11], 18.3 [72] and 18.45 J/m<sup>2</sup> [70] using CFD simulations. The UV dose differences in the three simulation results are attributed to the particle trajectories within the system, the used wall diffusive reflectivity (25% or 15%), and the different particle characteristics. In addition to estimating the average UV dose of a UVGI system, the CFD simulation with the DPM can reveal the cumulative UV dose distribution with respect to particle counts and the standard deviation of the system's average UV dose, which is particularly important from the perspective of inactivating an individual microorganism. For instance, a study shows that an arrangement of four vertical lamps has an average UV dose and standard deviation of 18.3 and 4.17 J/m<sup>2</sup> [72]. In reality, the overdosed UV irradiance on one particle will not transfer to and average with other underexposed particles, resulting in the wasted energy input for the overdosed bioaerosols and insufficient characterization of a system with the average UV dose. Furthermore, research shows that a system with the highest average UV dose (regardless of the standard deviation) performs better on a strongly resistant microorganism. In contrast, for a weak microorganism, a system with a more evenly distributed UV dose (lower standard deviation) is needed, even with a lower average UV dose [73].

With the provided accurate average UV dose and standard deviation along with its advantages in terms of cost and time compared to experimental investigations, the CFD analysis was applied to conduct the parametric studies and UVGI system design optimizations. For instance, the three-lamp array optimization was conducted in six arrangements (detailed arrangements see Capetillo et al. [73]), which resulted in average

UV doses (standard deviations) of 28.33 (10.06), 28.21 (5.39), 27.91 (16.32), 30.18 (12.60), 26.45 (5.37) and 31.05 J/m<sup>2</sup> (5.45 J/m<sup>2</sup>), respectively [73]. From a UVGI system design perspective, a higher average UV dose and a single sharp peak (lower UV dose standard deviation) with all particles receiving the required UV dose are expected [70,72,73]. Thus, the lamp array with all three lamps located at the center of the duct and distributed across its height provides the best performance (average UV dose of 31.05 J/m<sup>2</sup> and standard deviation of 5.45 J/m<sup>2</sup>). In addition to the lamp array arrangements, other design parameters, such as the number of lamps, lamp orientations, and duct materials, can be numerically evaluated using CFD simulations. Table 1 summarizes the numerical analysis and the design suggestions from CFD simulations in the literature.

Table 1 In-duct UVGI system design suggestions from the CFD studies in the literature

Paper	Duct size W×H×L (m×m×m)	Lamp arrangement (lamp numbers, direction)	Average UV dose (standard deviation) (J/m <sup>2</sup> )	Conclusions
[74]	0.61×0.61 ×2.74	4, perpendicular	53.19-6479.66	1. Without considering the thermal effect on the lamp output, placing UV lamps in a crossflow gives higher UV irradiance. 2. Considering the wind chill effects, arranging lamps in parallel flow provides a higher average irradiance for a system with lower temperatures and higher airflow.
		4, parallel	121.30-3732.26	
[73]	0.61×0.61 ×1.83	1, perpendicular, 6 locations in the duct	7.87-9.51	1. Placing the UV lamp at the duct center (height and length) provides the best average UV dose. 2. The lamp located at the beginning of the duct performs better than that located at the end of the duct.
		1, center of the duct, perpendicular 1, center of the duct, parallel	10.97 (4.39) 17.36 (16.27)	

		3 lamps, perpendicular (six arrangements see Capetillo et al. [73])	28.33 (10.06) 28.21 (5.39) 27.91 (16.32) 30.18 (12.60) 26.45 (5.37) 31.05 (5.45)	1. The best performance is achieved by locating all three lamps at the center of the duct and distributing them across the height of the duct. 2. The more even the UV dose distribution is, the more efficient the system is. 3. Increasing the lamp numbers increases the UV dose distribution uniformity and indicates better energy usage.
[72]	0.61×0.61 ×1.83	4, perpendicular 4, 30 degrees perpendicular 4, 60 degrees perpendicular 4, parallel	18.3 (4.17) 18.49 (4.60) 19.12 (6.75) 18.39 (7.89)	1. UV dose distribution non-uniformity (UV dose standard deviation) increases when changing the lamp array configuration from vertical to horizontal.
[75]	0.02×0.02 ×0.12	48 LEDs (at the floor and ceiling of the duct)	-	1. The use of highly reflective surfaces significantly increases microbial inactivation and minimizes the impact of LED positions on inactivation levels. 2. Four-wall reflection results in higher inactivation rates than solely side-side or top-bottom surface reflection. 3. The number of LEDs controls the maximum inactivation level when there are more than three reflection walls.

## 2.3 Factors affecting the UV inactivation efficiency for airborne microorganisms

As mentioned in Section 2.2.1, the UV inactivation efficiency is critically defined by the UV dose and UV rate constant. This section is aimed at discussing how the critical factors, including the in-duct UVGI system designs, operating conditions, and bioaerosol characteristics, affect the UV dose and UV rate constant, thus determining the inactivation efficiency of a UVGI system.

## 2.3.1 In-duct UVGI system designs

### 2.3.1.1 Germicidal sources

Mercury-based UV lamps, which are filled with mercury and a starting gas (typically argon), have a long history in UVGI devices. The commonly used low-pressure mercury germicidal UV lamp has a peak irradiance of 253.7 nm (more than 90% radiative emissions [76]), which is close to the peak germicidal effectiveness wavelength of 265 nm and out of the ozone-producing region (<240 nm) [11]. Furthermore, to eliminate ozone generation thoroughly, a soft glass coating is used to filter out the ozone-forming irradiance (185 nm here) and avoid potential ozone hazards in the air [77].

The lamp output is a critical influencing factor for UV inactivation as it is directly associated with the UV irradiance distribution in a UVGI system. The output of the low-pressure mercury lamp is determined by the coldest spot on the lamp surface, which controls the mercury vapor pressure of the lamp. For instance, Philips mercury lamps have optimum UV emitting efficiency (100%) when the bulb wall temperature reaches approximately 40 °C and only 20% and 58% efficiency when the lamp surface temperature is 10 °C and 80 °C, respectively [77]. The temperature dependency leads to concerns for the in-duct UVGI apparatus, as the heat transfer between the lamp and the ambient airflow strongly affects the lamp surface temperature and the lamp output, which is commonly called the “wind-chill” phenomenon. Thus, it is critical to identify the relationship between the HVAC operating conditions and the UV lamp working efficiency (lamp surface temperature). A previous study [78] introduced empirical correlations of lamp output for three types of low-pressure mercury lamps (cylindrical hot cathode, twin-tube hot cathode, and cylindrical cold cathode) under common HVAC operating conditions (air temperature:

5–35 °C; air velocity: 0.5–4 m/s). The correlations successfully predicted the lamp output under different air velocity and temperature conditions, where insufficient (low air velocity and high air temperature) or excess (high air velocity and low air temperature) convective heat transfer between the UV lamp and duct airflow results in overheating or overcooling of the lamp, thus lowering its output.

Despite the extensive use of conventional mercury-type UVC devices, they have disadvantages: the short lifespan and frequent replacement (4000-10000 h), large size light fixture, uncertain lamp surface temperature, a requirement of warm-up time (about 5 minutes), and mercury as a toxic environmental contaminant [79,80]. Thus, UVC light-emitting diodes (LEDs) are alternative materials to replace conventional mercury-containing UV lamps.

UVC-LEDs can produce UV light in different wavelengths compared to the peak irradiation (254 nm) produced by conventional mercury-based UV lamps. The lamp-emitting wavelength is another critical influencing factor for UV inactivation, as it is directly associated with the UV rate constant of microorganisms. For instance, we summarized studies in the literature that compare the UV rate constants for airborne microorganisms in UV-LED systems with different emitting wavelengths (Table 2). For bacteria, all the data report higher UV rate constants in the UV-LED system than those in the conventional mercury-type UVGI system, whereas, for two viruses (bacteriophages *MS2* and *ΦX174*), opposite trends are found. This variation is attributed to the different wavelengths in the two systems, where the radiation peaks at 270.8 nm [79,81] and 280 nm [82] for the LEDs compared to 253.7 nm for the conventional mercury-type UV lamps. For bacteria, DNA destruction is the primary reason for inactivation, and the DNA of most

microorganisms has a peak absorption between 260 nm and 270 nm [83]. Thus, one expects that the bacteria show higher UV rate constants within a 271 nm UV-LED system [79,81] than within a 254 nm conventional mercury-type UVGI system. Moreover, 254 nm and 280 nm fall away from the peak UV absorption spectrum. Thus, minor differences are observed for these two wavelengths [83]. As for the bacteriophage, previous research shows that the loss of *MS2* viral infectivity is mainly due to RNA damage [84]. The spectral sensitivity of the *MS2* RNA shows lower UV absorbance and viral infectivity at 280 nm than at 254 nm [10], thus resulting in the lower UV rate constants of *MS2* and  $\Phi X174$  for the 280 nm UV-LED system than for the 254 nm conventional mercury-type UVGI system.

Table 2 UV rate constants for the airborne microorganisms in UV-LED and low-pressure mercury UV lamp systems

	Wavelength (nm)	LED device	D range (J/m <sup>2</sup> )	k <sub>LED</sub> (m <sup>2</sup> /J, LED UV lamps)	k <sub>MV</sub> (m <sup>2</sup> /J, low-pressure mercury UV lamps)	
					From the study [79]	Average from literature <sup>1</sup>
[79,81]	271	10 UVC-LEDs, 9V, 350 mA	24.5-318	1.068 ( <i>E. coli</i> )	0.034 ( <i>E. coli</i> )	0.1958 ( <i>E. coli</i> )
				1.148 ( <i>S.marcescens</i> )	0.0417 ( <i>S.marcescens</i> )	0.3949 ( <i>S.marcescens</i> )
				0.156 ( <i>S.epidermidis</i> ) 0.028 ( <i>MS2</i> )	0.0143 ( <i>S.epidermidis</i> )	0.097 ( <i>S.epidermidis</i> ) 0.3629 ( <i>MS2</i> ) <sup>2</sup>
[82]	280	16 UVC-LEDs, 12V	0-453.9	0.202 ( $\Phi X174$ )	-	0.62 ( $\Phi X174$ )
				0.471 ( <i>E. coli</i> )		0.1958 ( <i>E. coli</i> )
				0.264 ( <i>S.aureus</i> )		0.2303 ( <i>S.aureus</i> )

1: Data extracted from [11].

2: Data averaged from [82,85–89] with outlier excluded.

Furthermore, it is expected that by adjusting the LED peak emitting radiation at 260 -270 nm, a higher UV rate constant can be obtained owing to higher UV absorption. At present, UV-LED-based in-duct UVGI systems exist in the prototype stage only, mainly due to limited LED output power. With the development and production of higher-output LEDs, it is expected that UV-LED devices will take a substantial share of the present market, which is occupied by traditional vapor discharge lamps.

### 2.3.1.2 In-duct UVGI system designs

In-duct UVGI systems with different lamp arrangements (number of lamps, lamp power, lamp placement, etc.) and duct designs (duct size, duct wall materials, etc.) have distinct UV inactivation efficiencies as they are directly associated with the UV irradiance distribution in a UVGI system. In addition to Table 1 which presents in-duct UVGI system design suggestions from the CFD simulations, we summarize all the constructed and tested in-duct UVGI system designs (both full-scale and pilot-scale setups) in the literature in Table 3 to provide insights into the real-life designs.

Thirty-three different designs are listed. These designs encompass typical operating conditions, with air velocities ranging from 0.16 to 6.5 m/s, temperatures from 10 to 30 °C, and RH between 31% and 62%. Notably, the U.S. Environmental Protection Agency (EPA) has conducted comprehensive research on in-duct UVGI (designs #1 – 8 [69,71,90–95]) with varied lamp arrangements, forming critical guidelines for system designs. Generally, to obtain a higher UV inactivation efficiency, a higher UV dose shall be delivered in a UVGI system. Designs #4, 5, 7, 17, 31, 32, and 33 provide high UV doses ( $>13 \text{ mJ/cm}^2$ ), which is ten times the required UV dose for 99% of *SARS-CoV-2* inactivation ( $1.222 \text{ mJ/cm}^2$ ) in air applications as recommended by ASHRAE epidemic task force [9]. Furthermore, these designs share common characteristics as (1) using high-power UV lamps or increasing lamp numbers (3 – 12 UV lamps and 180 – 1100 W total energy input), thereby enhancing UV irradiance within the ductwork; (2) using reflective duct materials to increase UV irradiance in the duct further; and (3) maintaining slow to intermediate air velocities (0.16 – 3 m/s) to prolong the UV exposure time for microorganisms.

Table 3 All available in-duct UVGI system designs in the literature

Design details							Reported inactivation efficiencies in the literature
No.	Duct W×H×L (m×m×m)	Lamp arrangement (numbers, direction)	Power (W)	UV dose (mJ/cm <sup>2</sup> )	Airflow (m/s)	Environmental conditions (T, RH)	
#1[90]		12 <sup>2</sup> , reflective duct material	720	7.651		23.2 - 24.1°C	MS2: 98%
#2[69]		1, perpendicular	58	0.247		22.7 – 22.9°C	MS2: 39%
#3[71]	0.61×0.61	4, perpendicular	100	0.295	2.5	23 – 23.2°C	MS2: 46%
#4[91]	×4.6 <sup>1</sup>	6, perpendicular <sup>3</sup> , reflective	420	19.826		25.3 – 25.8°C	MS2: 99%
#5[92]		5, parallel	1100	16.439		24.4 - 24.8°C	MS2: 99%
#6[93]		4, perpendicular	240	0.582		23- 23.2°C	MS2: 75%
#7[94]	0.3×0.3 ×4.6	6, parallel, reflective	750	42.342	1.56	21.2 - 24.1°C	MS2:100%
#8[95]	0.61×0.61 ×4.6	12, pulsed, perpendicular	7020	0.447	2.72	23.6 – 25.2 °C	MS2: 59%
#9[96]	0.2×0.2 ×1.4	1, perpendicular	9	0.735	3	23°C, 55%	SM: 99.925%; PA: 99.909%; EC: 98.168%; SE1: 93.607%; SE2: 92.935%
#10[96]				0.490	4.5		-
#11[96]				0.368	6		-
#12[97]	0.2×0.2 ×1.4	1, perpendicular	9	0.652	3	20°C, 50%	SE2: 81.73%; PA: 99.75%; EC: 95.92%
#13[97]				0.391	5		-
#14[97]				0.301	6.5		-
#15[19]	0.61×0.61 ×2.74	4, perpendicular	240	6.687	2	20°C	-
#16[19]				4.458	3	10°C	-
#17[19]				13.374	1	30°C	-
#18[19]				5.511	2	20°C	-
#19[19]				3.674	3	10°C	-

#20[19]				11.021	1	30°C	-
#21[98]	0.64×0.64 ×2.44	4, parallel	240	0.630	0.93	22.7°C; 31%	MS2: 99.21%; BB: 99.94%; FH: 43.77%; CD: 96.84%
#22[99]		1, perpendicular	145	1.341			SM: 99%; SE: 81%;
#23[99]	0.61×0.61 ×3.54	3, perpendicular	435	3.197	1.27	24°C, 50%	BS: 50.5%; AV: 10.5%; PC: 0.5%; CS: 9.5%
#24[99]		6, perpendicular	870	7.509			BS: 85%; AV: 74.5%; PC: 13.5%; CS: 16%
#25[16]		1, perpendicular, stainless steel		1.537	0.5		<i>E. coli</i> : 99.98%; MS2: 93.04%
#26[16]		1, perpendicular, stainless steel	5	0.921	0.9		<i>E. coli</i> : 98.36%; MS2: 71.36%
#27[16]	0.127	1, perpendicular, stainless steel		0.607			<i>E. coli</i> : 95.60%; MS2: 61.87%
#28[16]	×0.127	1, perpendicular, galvanized steel		0.897		24°C, 40%	<i>E. coli</i> : 97.25%
#29[16]	×1.16	2, perpendicular, 2 lamps in 2 rows, stainless steel	10	1.426	1.35		<i>E. coli</i> : 99.81%
#30[16]		2, perpendicular, 2 lamps in 1 row, stainless steel		1.279			<i>E. coli</i> : 99.59%
#31[100]	Diameter:			13.92	0.56		PRCV: 99.37%
#32[100]	0.298	3, parallel	180	20.28	0.38	57% - 62%	PRCV: 99.96%
#33[100]	Length: 0.724			49.63	0.16		PRCV: 99.98%

SM: *S.marcescens*; PA: *P.alcaligenes*; SE1: *S.enterrica*; SE2: *S.epidermidis*; EC: *E. coli*; BB: *B.broncbiseptica*; FH: *feline herpesvirus-1*; CD: *canine distemper virus*; BS: *Bacillus subtilis*; AV: *Aspergillus versicolor*; PC: *Penicillum chrysogenum*; CS: *Cladosporium sphaerospermum*; PRCV: *Porcine respiratory coronavirus*

1: Duct length estimated by ASHRAE standard 52.2 [101].

2: Lamp arrangement details in [102].

3: Lamp arrangement details in [86].

### 2.3.2 In-duct UVGI system operating conditions

For the same UVGI system operating under different conditions, e.g., air velocity, temperature, RH, and bioaerosol characteristics, the inactivation efficiency varies in several ways.

The effect of air velocity is well-recognized and twofold. Air velocity determines the microorganisms' UV exposure time; thus, the higher the air velocity, the lower the UV reaction time and inactivation efficiency [16]. On the other hand, air velocity also affects UV lamp output. As mentioned in Section 2.3.1.1, low air velocity and high air temperature or excess high air velocity and low air temperature results in overheating or overcooling of the low-pressure mercury lamp, thus lowering its output [16].

The primary effect of air temperature is regulating the UV lamp output along with air velocity, as mentioned [17–19]. While there is a potential effect that high indoor temperatures combined with high humidity may affect the survivability, infectivity, and UVC susceptibility of airborne microorganisms [20–23], most building ventilation systems maintain air temperatures in a narrow range (23–26 °C and 20– 23.5 °C for the cities in North America during the summer and winter seasons [103,104]). Thus, air temperature itself has a negligible impact on the microorganisms' UV rate constants in real-life applications.

Air RH may vary significantly in the duct environment (below 60% RH and around 20% - 30% RH for the room recirculating air during the summer and winter seasons [103,104] to over 90% in proximity to cooling coil locations [105]), which impact on the airborne microorganisms' the UV rate constants. It is widely recognized that higher RH levels tend

to reduce the UV rate constant, particularly in moderate to humid environments with over 50% RH [22,26,106–109]. Conversely, in dry conditions where RH is less than 30% RH, the UV rate constant appears to decrease as RH decreases [22,106]. The diminished inactivation rate at high RH levels is attributed to increased UV absorption by the water content in bioaerosols [20,23,26,109]. However, the literature does not explain the decreased UV susceptibility in low RH conditions.

### 2.3.3 Bioaerosol characteristics

Overall, bioaerosol characteristics, including their composition, size, and the contained microorganism species, determine the received UV radiation and how susceptible a microorganism is to UV illumination. For example, (i) UV absorption properties vary with different bioaerosol compositions, affecting the UVGI efficiency [20,24,25], (ii) bioaerosol particle size impacts UV absorption, but the effect varies with different suspending media [25], (iii) potential cell aggregations in the bioaerosol particles increase resistance to UV inactivation [20,110], and (iv) different microorganisms exhibit varying levels of susceptibility to UV radiation [17,26].

#### 2.3.3.1 Bioaerosol particle size

For the bioaerosol particle size, several studies have investigated its impact on the performance of UVGI systems, demonstrating varying trends with different airborne microorganisms in the various suspending media. For airborne *Serratia Marcescens*, the inactivation efficiencies increased as the particle size increased (aerodynamic diameter: 0.65–3.3  $\mu\text{m}$ ) when suspended in phosphate-buffered saline (PBS) [25] or synthetic saliva [25], yet when the bacterium was aerosolized from serum or beef-broth culture, the

inactivation efficiencies decreased with an increasing particle size (aerodynamic diameter: 0.65–2.1  $\mu\text{m}$  for serum [25] and aerodynamic diameter: 0.65–10  $\mu\text{m}$  for beef-broth culture [111]). In contrast, for *vaccinia virus* aerosolized from water or synthetic respiratory fluid, the virus's susceptibility did not appear to be a function of particle size (aerodynamic diameter: 0.7–3.3  $\mu\text{m}$ ); the particle size distribution remained unchanged before and after UV illumination [107].

### 2.3.3.2 Airborne microorganism species

Microorganisms are inherently susceptible to UVC light, and the term UV rate constant ( $k$ ,  $\text{m}^2/\text{J}$ ) has been widely used to characterize the microorganisms' susceptibility to UV illumination. The higher the UV rate constant of a microorganism is, the more reactive it is to UV light. Different microorganism species, with different genetic materials and structures, inherently react differently upon UV illumination. This, in return, results in different UV rate constants. Generally, it is recognized that fungi tend to be the most resistant to UV illumination, followed by bacteria spores, bacteria vegetative cells, and viruses as the most sensitive to UV light [26].

Several studies have summarized the UV rate constants of different bacteria, viruses, and fungi, and a comprehensive UV rate constant database was established [11]. However, most of the collected data are liquid matrix-based. In general, the susceptibility of airborne microbes to UV is much greater than that of microbes in liquid suspensions or in films on the surfaces. This phenomenon is attributed to (1) the UV absorptivity of liquid media, which impacts the effectiveness of UV exposure; (2) the increased turbulence and diffusion in the air compared to water, resulting in more evenly exposed microorganisms; (3) the aerosolization process, which reduces the microbial survival potential through physical

damage; (4) the presence of oxygen in the air, which contributes to increased vulnerability [17,26]; and (5) potential differences in virion aggregation in bioaerosols and in liquid [20,112]. Thus, aiming at UV inactivation of airborne ssRNA viruses, the core target microorganisms for this thesis, we summarize the available UV rate constant data in the literature in Table 4, and as expected, it shows very distinct UV rate constants for different microorganisms.

Table 4 UV rate constants for the infectivity loss of airborne ssRNA viruses

Microorganisms	UV rate constant $k$ (cm <sup>2</sup> /mJ)	
	Average	Studies in the literature
<i>Phage MS2</i>	1.604±1.780	5.45 [113]
		1.133 [69,71,90–95]
		0.43 [114]
		1.361 [112]
		1.119 [115]
<i>Coxsackievirus</i>	1.110	0.057 [116]
		1.110 [117]
<i>Sindbis virus</i>	1.040	1.04 [117]
		2.9 [108]
<i>Influenza A virus</i>	2.248±0.661	2.7 [108]
		2.2 [108]
<i>Porcine reproductive and respiratory syndrome virus</i>	4.507	4.507 [106]
<i>Porcine respiratory coronavirus*</i>	0.186	0.186 [100]
<i>SARS-CoV-2</i>	9.904	9.904 [118]
<i>Murine hepatitis virus</i>	3.77	3.77 [114]
<i>Bovine coronavirus*</i>	1.105	1.105 [115]

\*: The reported UV rate constant was underestimated due to the virus titers under UV-on conditions falling below the detection limits.

## 2.4 Critical research gaps

A thorough literature review regarding the UV inactivation mechanisms, UVGI system modeling, and factors affecting the UV inactivation efficiency is provided. Despite extensive research on the characterization of the UV disinfection for airborne

microorganisms, several research gaps have been defined in alignment with the primary objectives of this thesis.

### 2.4.1 The UV irradiance model

As mentioned in Section 2.2.3, the current view factor model can characterize well for some in-duct UVGI systems. However, it faces several challenges, such as duct wall reflections and multiple-lamp arrangements, which must be addressed to predict the UV irradiance distribution inside the duct for real-world applications. Notably, different duct walls have different dominating reflection types, and the effects of each reflection type have not been thoroughly discussed. Furthermore, multiple UV lamps must be installed to increase the germicidal effects within the duct, where shadowing effects between the UV lamps (luminous cylinders) occur. However, no view-factor model has quantified the shadowing effects of multiple UV-lamp scenarios inside the duct enclosure. Thus, in this thesis (Section 4.1), a new view-factor-based mathematical model was developed to calculate the irradiation distribution for a typical twin-tube UV lamp, in which the contributions from direct emissive irradiance, specular reflection irradiance, and diffuse reflection irradiance were quantified. Furthermore, the “projection area” method was introduced to mathematically estimate the shadowing effects between the two lamps by considering multiple-lamp scenarios in in-duct UVGI system designs.

### 2.4.2 The UV rate constant model

As mentioned in Section 2.2.2, several UV rate constant models have been introduced, using different approaches such as physical-based, empirical, and semi-empirical methods. However, these models each have their strengths and weaknesses. For instance, empirical

and semi-empirical models excel in correlating genome features (such as sequence length and base compositions) directly with viral infectivity loss [31,38,41–44]. However, they sideline the contributions from protein (capsid) damage. Moreover, model parameters obtained from data fitting often lack interpretable physical meaning. On the other hand, the physics-based approaches that attempt to predict genome damage and CPDs with experimentally measured quantum yield values for different photoreactions [32,33] suffer from lower accuracy, possibly due to the limited availability and significant variations in quantum yield data and the oversimplified assumption that genome damage equals infectivity loss. Thus, in response to these challenges, this thesis (Section 5.1) introduces a UV rate constant prediction model that integrates both genome damage (estimated by an improved genomic model) and capsid protein damage and strives to ensure that the model parameters resonate with physical interpretation.

### 2.4.3 The effect of RH on UV inactivation efficiency

As mentioned in Section 2.3.2, the effect of RH on airborne virus UV inactivation is complex, and the mechanisms behind it are unclear. Additionally, there is inconsistency in the reported UV inactivation behaviors of *MS2* at different RH levels in the literature. One study found that the UV rate constant of *MS2* (aerosolized from deionized water) decreased with increasing RH (from 55% to 85% at 25 – 28 °C) [109], while another study reported the increased UV rate constant for *MS2* (aerosolized from PBS with 0.01% Tween) with increasing RH (32% - 50% to 74% - 82%, with the temperature not reported) [114]. Both studies had limitations; the former did not examine the dry environment [109] and the latter used only a single UV dose to determine the UV rate constant, not reporting air temperature [114]. These limitations hinder providing informed recommendations for implementing

UVGI systems in complex in-duct environments (i.e., below 60% RH and around 20% - 30% RH for the room recirculating air during the summer and winter seasons [103,104] to over 90% in proximity to cooling coil locations [105]). Thus, we conducted UV disinfection experiments on airborne *MS2* and compared the UV rate constants for airborne *MS2* under three RH conditions (25%, 40%, and 60%) with a detailed analysis of potential mechanisms behind this phenomenon.

#### 2.4.4 The effect of bioaerosol particle size on the UV inactivation efficiency

As mentioned in Section 2.3.3.1, the airborne microorganisms carried by bioaerosol particles with different sizes have distinct sensitivity towards UV illumination. In practice settings, the bioaerosol concentrations peak at different particle sizes. For instance, *SARS-CoV-2* RNA was primarily detected in both sub-micrometer (0.25–1.0  $\mu\text{m}$ ) and super-micrometer ( $>2.5$   $\mu\text{m}$ ) bioaerosols (in aerodynamic diameter) in Wuhan hospitals[119]. Similarly, a Singapore hospital reported a higher or equivalent particle concentration in size  $>4$   $\mu\text{m}$  than the 1–4  $\mu\text{m}$  size range (aerodynamic diameter) [120]. Moreover, more positive *SARS-CoV-2* were found in the samples of 2.5–10  $\mu\text{m}$  particles than in  $<2.5$   $\mu\text{m}$  or  $>10$   $\mu\text{m}$  particles (aerodynamic diameter) in Kuwait hospitals[121]. Hence, when we use the UV rate constants reported in labs for bioaerosol particle sizes that do not match the target size, one can expect differences in inactivation efficiency. Importantly, no available UV rate constant data exists in the literature for virus-containing bioaerosols with a particle size larger than 3.3  $\mu\text{m}$ . Therefore, this thesis investigates the effect of particle size on the UV inactivation of airborne *MS2* across a broad particle size range (0.65 – 7  $\mu\text{m}$ ).

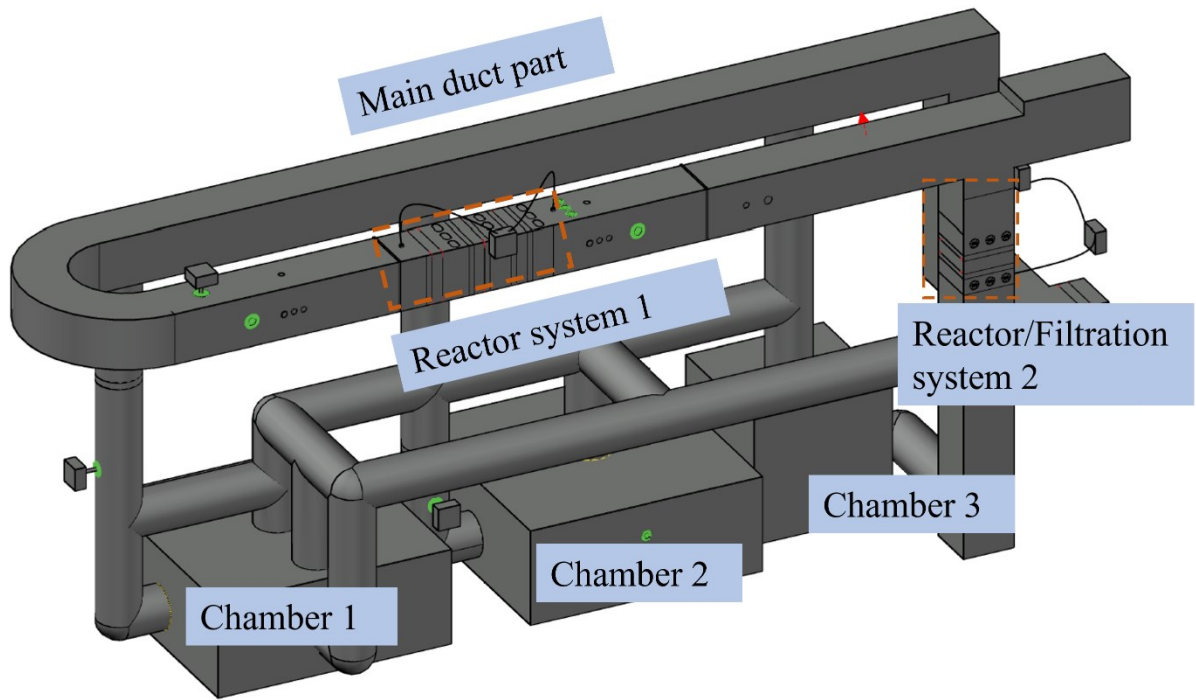
## 3 Experimental Evaluation of the In-duct UVGI System

### 3.1 Pilot HVAC system and in-duct UVGI reactor design

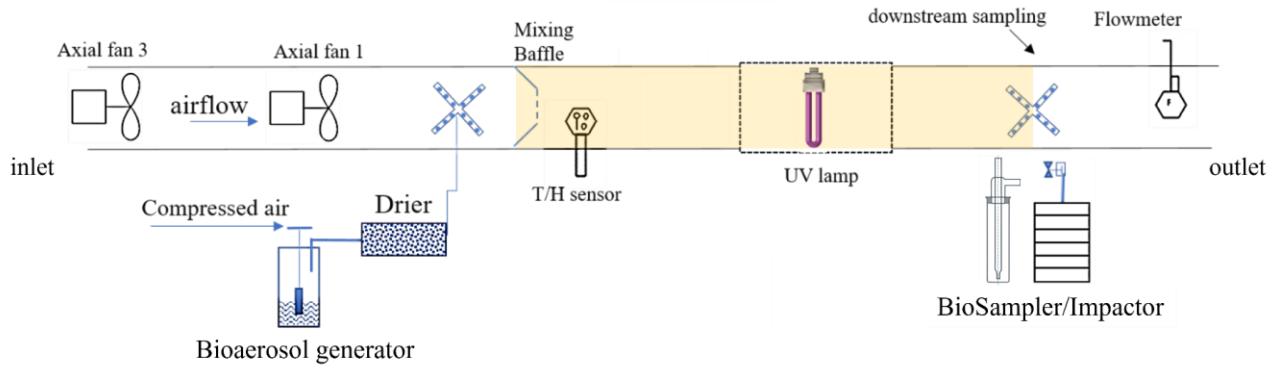
American Society of Heating Refrigeration and Air Conditioning Engineers (ASHRAE) has developed a standard testing method for evaluating UV-C lights for use in air-handling units or air ducts to inactivate airborne microorganisms (ASHRAE Standard 185.1-2020 [122]). In this research, a pilot HVAC system (Figure 2(a) and Figure H1) was designed and constructed at the Built Environment Technology Lab following the guidance of ASHRAE Standard 185.1-2020 [122]. It consists of a main duct section, three chambers, and round ducts that connect chambers and main ducts. The in-duct UVGI reactor (Figure 2(b)) was installed in the main duct section at the location of reactor system #1. It had a cross-sectional area of  $12.70 \times 12.70 \text{ cm}^2$  and a length of 1.35 m, allowing the installation of necessary devices (such as fans, UV lamps, and injection and sampling ports) and sensors (such as the humidity/temperature sensor and flowmeters).

A feedback control system (Opto 22) was developed to record and control ventilation conditions (airflow velocity, temperature, and RH) inside the duct system. It allows the precise control of the airflow rate from 0 to 95 L/s, the relative humidity from room RH to 100%, and the temperature from the room temperature to 50 °C. Furthermore, cross-shaped injection and sampling probes (each tube consisting of four branches and five sampling holes on each branch) were designed to maximize the injection and sampling uniformity across the duct cross-section [123]. Moreover, the mixing baffle was designed to have 40% open area in its plate surface, in accordance with the ASHRAE Standard 52.2-2017 [124], to provide good mixing of the airflow.

For the bioaerosol's UVGI test, a 1-jet nebulizer (Collision Nebulizer, BGI) and diffusion dryer (Silikagel, DDU 570, TOPAS) were connected before the injection tube, and the six-stage Andersen cascade impactors (TE-10-800, TISCH Environmental, USA) or SKC BioSamplers (20ml, BioLite + Pump, SKC Inc, USA) were connected to the downstream sampling probes for simultaneous bioaerosol generation and sampling. Prior to testing the UVGI device, the UV lamps (OSRAM GCF5DS 5 W) were operated for a standard 100 h “burn-in” period to obtain a stable output.



(a)



(b)

Figure 2 The schematic of (a) the pilot HVAC system and (b) in-duct UVGI reactor

## 3.2 In-duct UVGI system prequalification tests

Prequalification tests of the in-duct UVGI system have been conducted to quantitatively verify that the test rig is able to be used to test bioaerosol UV disinfection technology following the requirements of ASHRAE Standard 185.1-2020 [122].

### 3.2.1 Leakage Test

Keeping leakage within an acceptable range is vital for quality control of the experiment and operator safety. Therefore, leakage of the main duct section was assessed in this research. The diagram of the leakage test of the main duct section is illustrated in Figure 3. All sensors and tubes were removed from the main duct, and all round-ducts were disconnected from the square main duct section. All holes, inlet, and outlet of the duct system, and the edge of the duct were sealed by aluminum foil and paper boards.

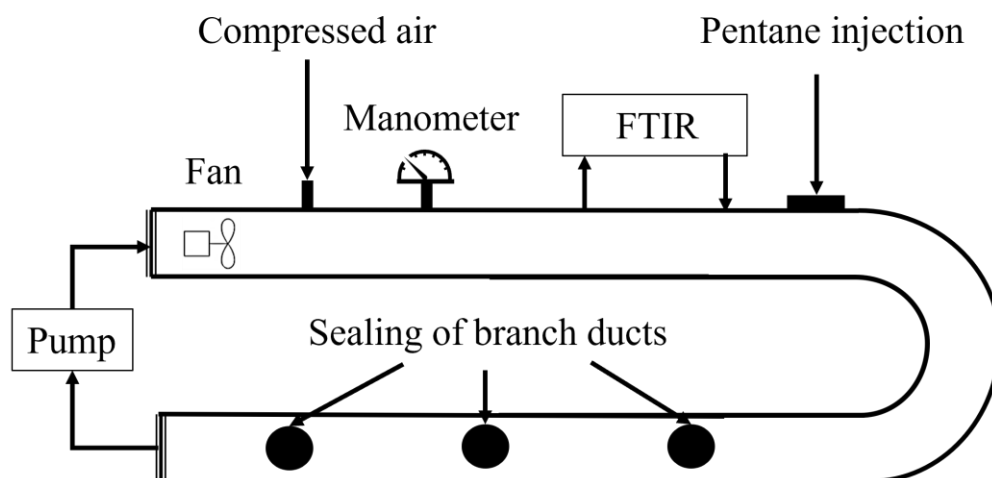


Figure 3 Schematic of the leakage test

Firstly, the maximum operating velocity and pressure drop were measured based on the components installed inside the setup. Specifically, pressure drops of all components, such as the mixing baffle, prefilters, and HEPA filters, were detected by a manometer (TSI/Alnor Model 5825) when installed inside the UVGI reactor. During the leakage test, the compressed air was fed into the duct to keep the system under the targeted pressure (obtained maximum pressure drop). To reach the concentration uniformity of the tracer gas, the inlet and outlet of the duct were connected by a pump running at 28 L/min. Besides, the inlet and outlet of the Fourier transform infrared spectroscopy (FTIR iS50, Thermal Fisher Scientific) were connected to the setup. Thus, the whole system could be a closed-loop system.

Once the system reached the desired pressure, 2  $\mu\text{L}$  pentane was injected into the system by a syringe. The FTIR analyzed concentrations of pentane in the duct system when the gas samples were passing through it. Concentration decay was recorded by 40 mins to obtain the decay curve. Assuming the natural decay of pentane in the duct system is

negligible, the leakage airflow ( $Q_{leak}$ ) and leakage ratio ( $R_L$ ) could be obtained by the following equations:

$$C = C_0 \times e^{-\frac{q_{leak}}{V}t}$$

$$leakage\ ratio = \frac{q_{leak}}{q_{max}} \times 100\% \quad (5)$$

where  $C_0$  is the initial concentration (ppm),  $C$  is the concentration (ppm) at time  $t$  (min), and  $V$  is the duct volume (110.6 L).  $q_{Max}$  is the maximum operating flow rate (1.30 m<sup>3</sup>/min) of the developed setup.

The maximum pressure drop of the in-duct UVGI reactor is mainly from filters and a mixing baffle in the system. According to ASHRAE Standard 185.1-2020 [122], setups used in the bio-experiments should include at least one HEPA filter (prefilter) and one mixing baffle. They have 170 Pa and 160 Pa pressure drops at the maximum operation flow rate of 1.30 m<sup>3</sup>/min in this research. With the consideration of adding one HEPA filter at the outlet of the system (final filter) and potential pressure drop for UV lamp and injection/sampling tubes, the most significant pressure drop requirement in the single-pass mode should be larger than 500 Pa. Figure 4 shows decay curves of the pentane concentration under the duct testing pressure of 652 Pa. According to Eq. (5), leakage was determined as 0.94%, which was within the leakage ratio requirement of the ASHRAE Standard 185.1-2020 (<1.0%) [122].

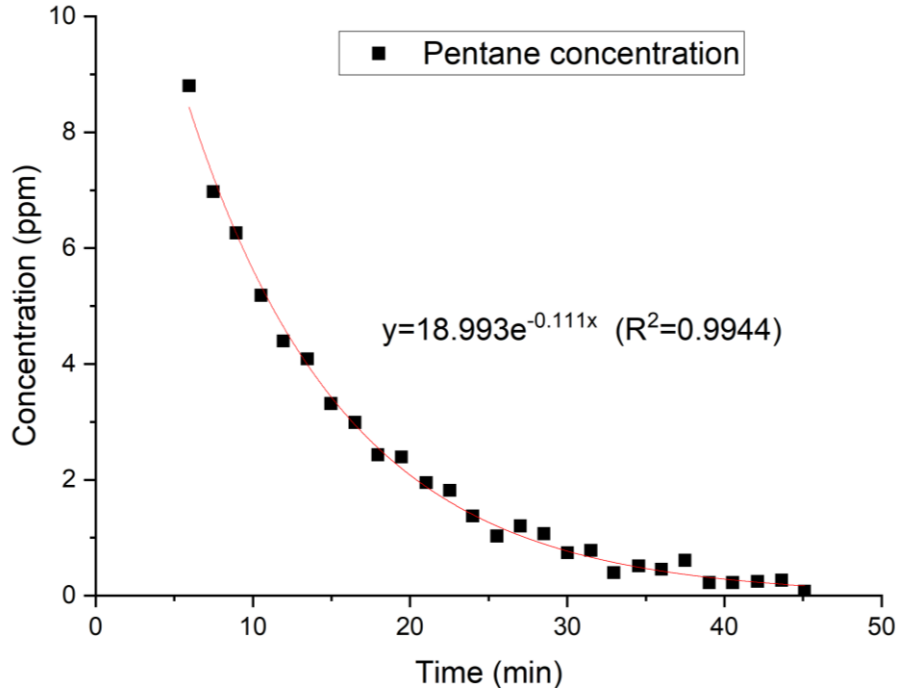


Figure 4 Pentane decay curves during the leakage test

### 3.2.2 Aerosol uniformity test

The aerosol uniformity test was conducted using KCl aerosols. The aerosols were generated by the particle generation system composed of compressed air, a 1-jet Collision nebulizer (Collision Nebulizer, BGI), a Kr-85 charge neutralizer (3077A, TSI Inc., USA), and a diffusion dryer (Silikagel, DDU 570, TOPAS), then introduced into the duct system through the injection tube. In addition, an optical particle sizer (OPS Model 3330, TSI Inc., USA) was used to detect particle concentration with sizes ranging from 0.3  $\mu\text{m}$  to 10.0  $\mu\text{m}$ , referring to ASHRAE Standard 52.2-2017 [124]. It should be noted instead of following the single-point sampling procedure as set forth in the ASHRAE Standard 52.2-2017 [124], we designed cross-shaped sampling probes (45° and 90°, design details can be seen in our previous work [123] and Figure H2) to facilitate the uniform sampling of the bioaerosols across the duct cross-section. Each sampling tube contains four columns with five-hole

openings, and the hole sizes vary along the column to maintain the approximate pressure drop of each hole (difference < 15%) under the desired sampling flow rate (28.3 L/min) according to the preliminary CFD simulations [123]. Therefore, the aerosol uniformity was determined by measuring concentration differences of using 45° and 90° sampling probes at 0.6m/s, 1.0 m/s, and 1.35m/s air velocity.

Table 5 Aerosol concentration differences between 45° and 90° sampling tubes in the duct system

Air velocity (m/s)	Aerosol diameter range (µm)											
	0.3-0.4	0.4-0.55	0.55-0.7	0.7-1.0	1.0-1.3	1.3-1.6	1.6-2.2	2.2-3.0	3.0-4.0	4.0-5.5	5.5-7.0	7.0-10.0
0.6	3%	4%	5%	4%	4%	6%	6%	5%	8%	10%	4%	20%
1.0	1%	3%	1%	1%	1%	5%	4%	7%	9%	10%	1%	18%
1.35	2%	2%	4%	5%	5%	7%	2%	3%	8%	7%	4%	32%

The aerosol concentration differences between the two sampling tubes for each aerosol size range were included in Table 5. All differences were smaller than 15% (requirement of ASHRAE Standard 185.1-2020 [122]), except for aerosols larger than 7.0 µm. This is attributed to the relatively low aerosol concentration for this size inside the duct (lower than 10 particles/cm<sup>3</sup>) and, thus, cannot be detected steadily. For this reason, the large bioaerosols (> 7.0 µm) were not collected nor analyzed in this thesis.

### 3.2.3 Isokinetic sampling test

The isokinetic sampling at upstream and downstream sampling tubes was evaluated by connecting a flow calibrator (Defender 510H, Measalabs) with the isokinetic sampling probes and optical particle sizer (OPS Model 3330, TSI Inc., USA) or six-stage Andersen

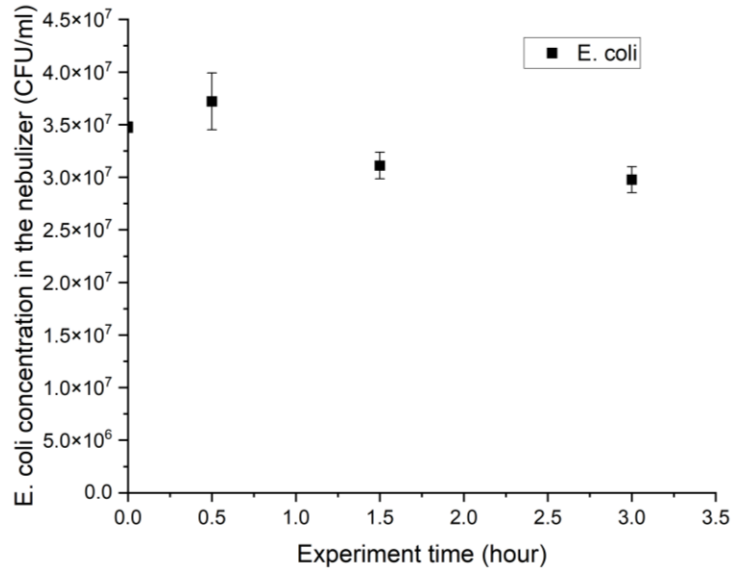
cascade impactor (TE-10-800, TISCH Environmental, USA). The PBS aerosols were used, and the tests were conducted under 0.5m/s, 0.9m/s, and 1.35m/s. The results showed a smaller than 0.7% difference (when using an optical particle sizer) and 1.6% difference (when using an impactor) between the upstream and downstream samplings for all three velocities, indicating the sampling system can maintain isokinetic sampling (<10% as required by ASHRAE Standard 185.1-2020 [122]).

### 3.2.4 Microorganisms' decay in the nebulizer

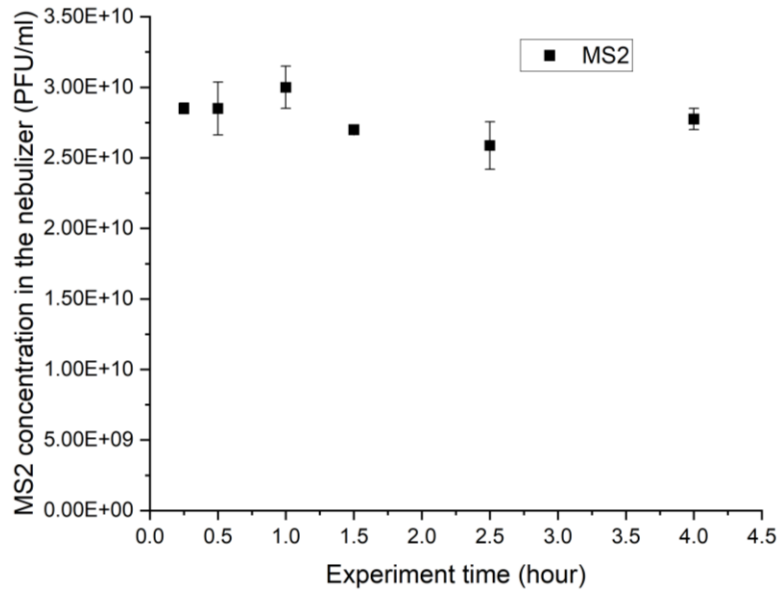
There is potential inactivation for microorganisms during the aerosolization due to the physical stress resulting from the acceleration/deceleration and impaction inside the nebulizer [125]. Thus, despite not being required by the ASHRAE standard, prequalification tests quantifying the microorganisms' (*MS2* and *E. coli*) concentration changes inside the nebulizer during the long-time aerosolization were conducted.

In detail, the nebulization suspension was prepared by adding 200  $\mu\text{L}$  of purified *MS2* stock (concentration around  $10^{11} - 10^{12}$  PFU/mL, preparation method sees in Section 3.3.2.1) into 50 mL PBS or 10 mL of purified *E. coli* stock (concentration around  $10^8 - 10^9$  CFU/mL, preparation method sees in Section 3.3.2.1) into 40 mL PBS. The nebulization (with 20 psi compressed air) was initiated once the duct system stabilized. At around 0 minutes, 25 minutes, 30 minutes, 1 hour, 1.5 hours, 2.5 hours, and 4 hours, the compressed air was turned off, and samples (1000  $\mu\text{L}$ ) were aseptically extracted from the nebulizer using a pipette. Then, the titers of *MS2* or *E. coli* were obtained through serial tenfold dilution and compared. The results showed small changes (Figure 5, maximum 13.5% for *MS2* and maximum 16.1% for *E. coli*) in microorganisms' concentration in the nebulizer.

Thus, we assume insignificant *MS2* and *E. coli* decay during the 4 hours of nebulization in this research.



(a)



(b)

Figure 5 The (a) *E. coli* and (b) *MS2* concentration in the nebulizer during the nebulization

### 3.2.5 Aerosols particle size distribution stability

The aerosol particle size distribution stability prequalification test was conducted to determine if there were variations of PBS aerosols at the downstream sampling port during a 3-hour experiment period under the UV light-off condition. In detail, the test was conducted under the operation conditions of 1.35m/s, 25°C, 25% RH, and UV-off. Once the duct system stabilized, nebulization (with 20 psi compressed air) commenced using the PBS solution and allowing for 10 min of the system equilibration. The sampling was conducted downstream using the TSI 3330 and measured the aerosol concentration across the 0.3 – 10 µm particle size range. The samplings were repeated continuously 10 times, and each sample lasted 15 minutes, thus covering a 3-hour experiment period.

The results showed insignificant variations (Figure 6, the maximum difference between the ten samples was 5.2%) of the PBS aerosol concentrations for the particle sizes < 7.0 µm, indicating the PBS aerosol concentrations and particle size distributions were stable during the test.

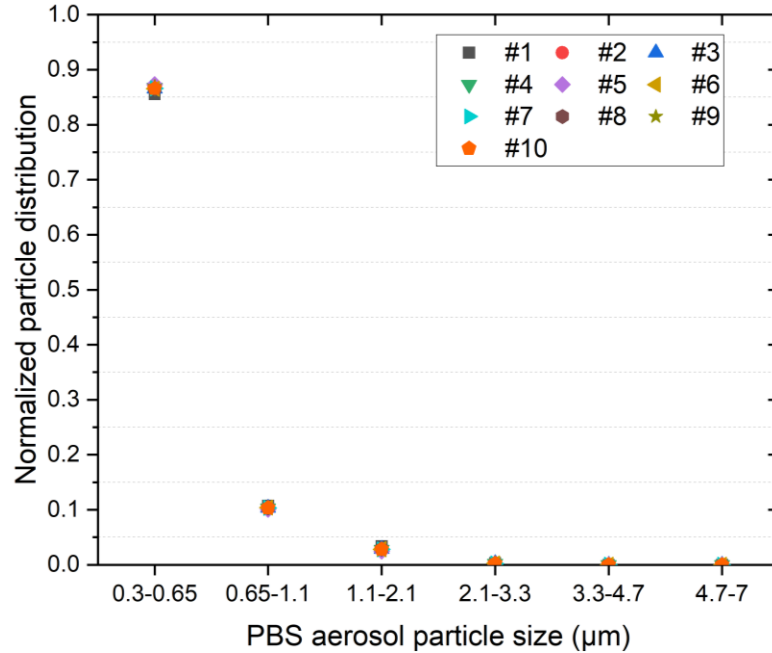


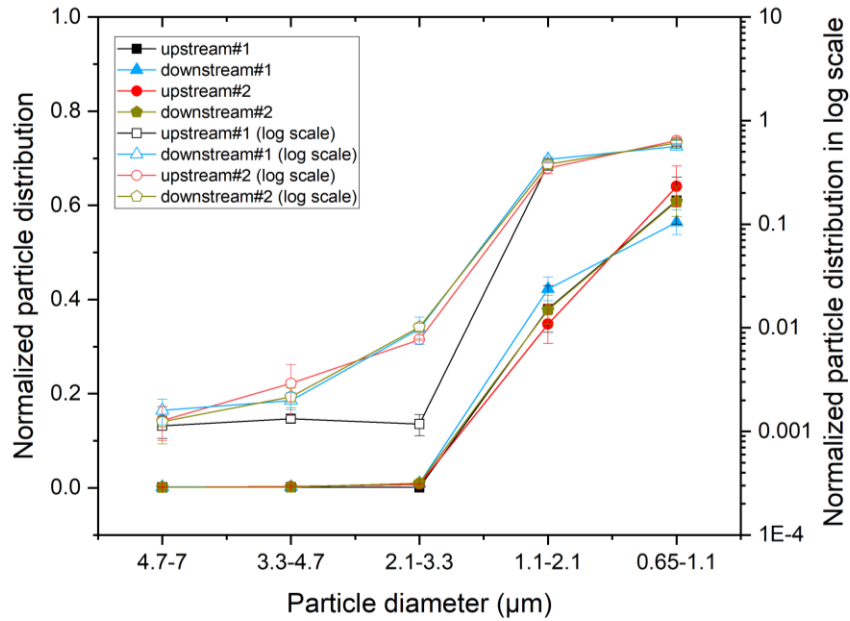
Figure 6 The normalized PBS aerosol particle size distributions for ten samples that are collected for a 3-hour experiment period

### 3.2.6 Bioaerosols light-off loss (correlation ratio test)

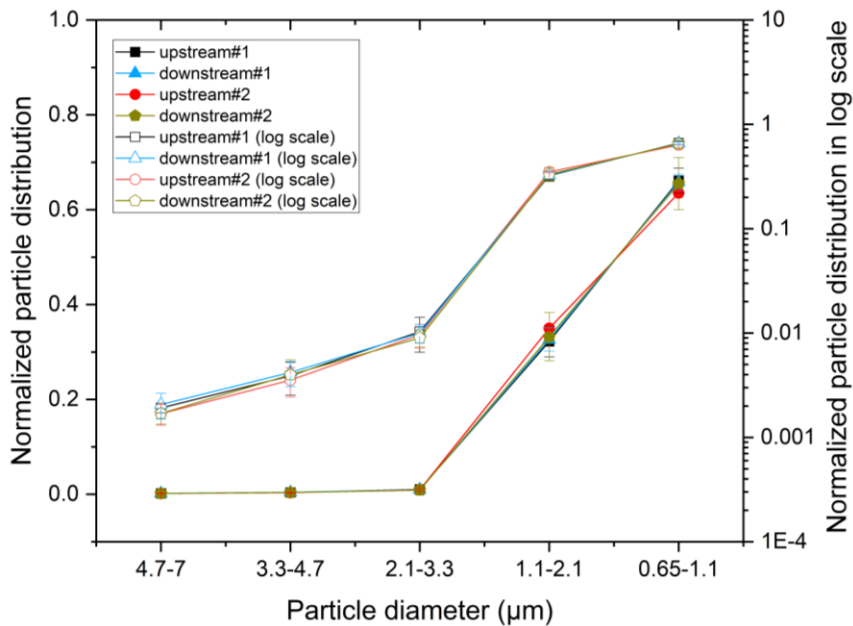
Another prequalification test was conducted to determine if there were variations of *E. coli* or *MS2* bioaerosol concentrations along the duct (upstream and downstream samplings) and throughout the 2.5-hour testing period. In detail, the test was conducted under the operation conditions of 0.5m/s, 25°C, 25% RH, and UV-off. Once the duct system stabilized, nebulization (with 20 psi compressed air) commenced using the mixture suspension media (10 mL purified *E. coli* stock into 40 mL PBS solution or 100 μL purified *MS2* stock into 50 mL PBS solution, preparation method seen in Section 3.3.2.1), allowing for 10 min of the system equilibration. Upstream and downstream samplings were conducted simultaneously using two 6-stage impactors with sterile double nutrient-agar-layer plates inserted. As mentioned before, the bioaerosols with particle sizes greater than

7.0  $\mu\text{m}$  (*MS2*, stage 1) and greater than 2.1  $\mu\text{m}$  (*E. coli*, stages 1, 2, 3, and 4) were not studied. Thus, the sampling times of each stage for *MS2* bioaerosols were 0.5 min (stage 6), 0.5 min (stage 5), 7 min (stage 4), 30 min (stage 3), and 30 min (stage 2) due to the concentration difference of various *MS2* bioaerosol sizes, and for *E. coli* bioaerosols were 0.5 min for both stages 6 and 5. The first sampling occurred 25 minutes after nebulization began, followed by subsequent sampling at 1 hour and 45 minutes. The total experimental time was around 2.5 hours. Then, the sampled agar plates were incubated overnight at 37°C, and the numbers of colonies or plaques formed on the plates were counted and compared.

The results showed insignificant variations of bioaerosol concentrations between the upstream and downstream sampling ports for both *E. coli* (Figure 7(a), maximum 17.7% and 11.7% for stages 5 and 6 between all four sampling scenarios) and *MS2* bioaerosols (Figure 7(b), maximum 18.5%, 15.7%, 19.4%, 12.6%, and 11.5% for stages 2, 3, 4, 5, and 6 between all four sampling scenarios). It should be noted that the particle size distribution for *E. coli* with bioaerosol size greater than 2.1  $\mu\text{m}$  and for *MS2* with bioaerosol size greater than 7  $\mu\text{m}$  were unstable or low concentration during the test, thus not discussed in this research. The results met the requirements of ASHRAE Standard 185.1-2020 [122] for the correlation ratio test and showed the stable operation of the pilot HVAC system during the UVGI experiment.



(a) *E. coli*



(b) *MS2*

Figure 7 Particle size distributions for (a) *E. coli* and (b) *MS2* bioaerosols at the upstream and downstream of the UVGI reactor (0.5m/s and 25% RH), with #1 and #2 representing the testing times of 25 minutes and 1 hour and 45 minutes since the start of nebulization

### 3.2.7 Other prequalification tests

Previous sections have presented the details of the tests that are related to the UV disinfection of the bioaerosols, including the leakage test, aerosol concentration uniformity, isokinetic sampling, microorganisms' decay in the nebulizer, aerosols concentration and particle size distribution stability inside the duct, and bioaerosols light-off correlation ratio test. There are a few other tests that control the pilot HVAC system operation yet are not directly related to the bioaerosols, including air velocity uniformity test, 100% efficiency test, airflow verification test, flow control verification test, etc., which can be referred to our previously published work [123,126]. Furthermore, all the prequalification test results and brief introductions are summarized in Table 6.

Table 6 Pilot HVAC system pre-qualification test results

Parameter	Requirements <sup>1</sup>	Results	Comments
Air velocity uniformity <sup>2</sup>	CV (coefficient of variation) < 10%	<7.7%	Based on traverse measurements taken across a 9-point equal-area grid (UV lamp location) at velocities of 0.585 m/s, 2.487 m/s, and 3.745 m/s.
Aerosol uniformity <sup>2</sup>	< 15%	<10.3% for particle size <7 µm; <32.3% for particle size > 7 µm	Based on the KCl aerosol concentration difference (averaged from upstream and downstream sampling) using two types of sampling tubes (45° and 90°) at velocities of 0.6 m/s, 1.0 m/s, and 1.35 m/s.
100% efficiency test <sup>2</sup>	>99%	>99.0%	Based on the HEPA filter test of the removal efficiency for KCl aerosols (upstream and downstream sampling) at 0.585 m/s, 2.487 m/s, and 3.745 m/s.
Duct leakage <sup>2</sup>	< 1.0	<0.9%	The leak rate ratio was assessed at the max velocity (1.35 m/s) and pressure (652 Pa) in a closed-loop mode.
Isokinetic sampling	< 10%	<0.7% for TSI 3330; <1.6% for Impactor	Based on the downstream sampling airflow rate measurements of the samplers (TSI 3330 or 6-stage Andersen impactor) at velocities of 0.5 m/s, 0.9m/s, and 1.35 m/s.
Virus decay in the nebulizer	–	<13.5%	Based on the titration of the MS2 suspension in the nebulizer during the 4-hour testing period, samples were collected at 15 minutes, 30 minutes, 1 hour, 1.5 hours, 2.5 hours, and 4 hours after initiating the system.
Aerosol generator response time <sup>2</sup>	–	2 min	Based on the continuous sampling at the upstream sampling point to examine the time interval for aerosol concentrations to transition from background to steady test levels.
Aerosol concentration and particle size distribution stability	–	< 5.2% for particle size <7 µm; no readings for particle size > 7 µm	Based on the continuous sampling (sampling ten times, each sample 15 minutes) of the PBS aerosol concentration at the upstream sampling port during a 3-hour experiment period under the UV light-off condition. The TSI 3330 measured the aerosol concentration across 0.3 – 10 µm particle sizes.

---

Bioaerosols light-off loss  
(correlation ratio test)

0.7 – 1.3

0.81 – 1.14

Based on the sampled bioaerosols at upstream and downstream sampling ports for all five impactor stages under the UV light-off condition. This test assessed the no-light loss within the duct and the system's stability during the 2.5-hour experiment period. Samples were taken at 20 minutes and, 1 hour and 45 minutes after initiating the system. The sampling durations for each stage were: 0.5 min (stage 6), 0.5 min (stage 5), 7 min (stage 4), 30 min (stage 3), and 30 min (stage 2).

---

1: Per the requirements of ASHRAE Standard 52.2-2017[124] and ASHRAE Standard 185.1-2020[127].

2: For details, refer to our previous study[126].

---

### 3.3 Experimental evaluation of the in-duct UVGI system

The performance of an in-duct UVGI system was evaluated by the engineering metrics of the UV irradiance and the biological metrics of the airborne microorganism's inactivation efficiency. The following sections give the details of the investigating cases, experimental methodology, and the results and discussions of the experimental evaluations.

Briefly, the effects of duct system designs (UV lamp arrangements and duct wall materials) were investigated based on the UV irradiance distribution and bioaerosol (airborne *E. coli*) inactivation efficiency, the effects of operating conditions (RH) and bioaerosol characteristics (particle size and target genome sequence) were evaluated based on the bioaerosol (airborne *MS2*) inactivation efficiency for infectivity loss and genome damage.

#### 3.3.1 UV irradiance measurement

For a start, the emission wavelength distribution of the used twin-tube UV lamp was measured using a spectrometer (ILT960, International Light, USA).

Then, the UV irradiance inside the duct was measured using a Radiometer RM-12 at multiple locations and was used for irradiance model validations in Section 4.3.1. The irradiance was measured at a total of 36-points (Figure 8), which were uniformly distributed in four cross-sections.

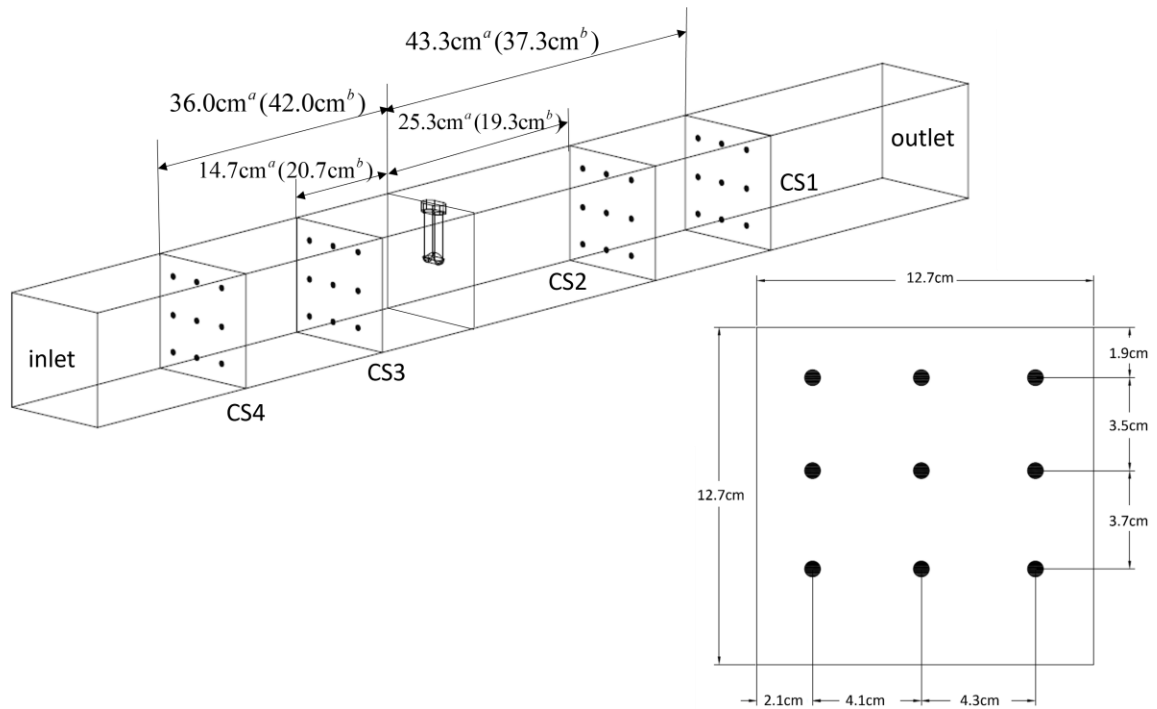
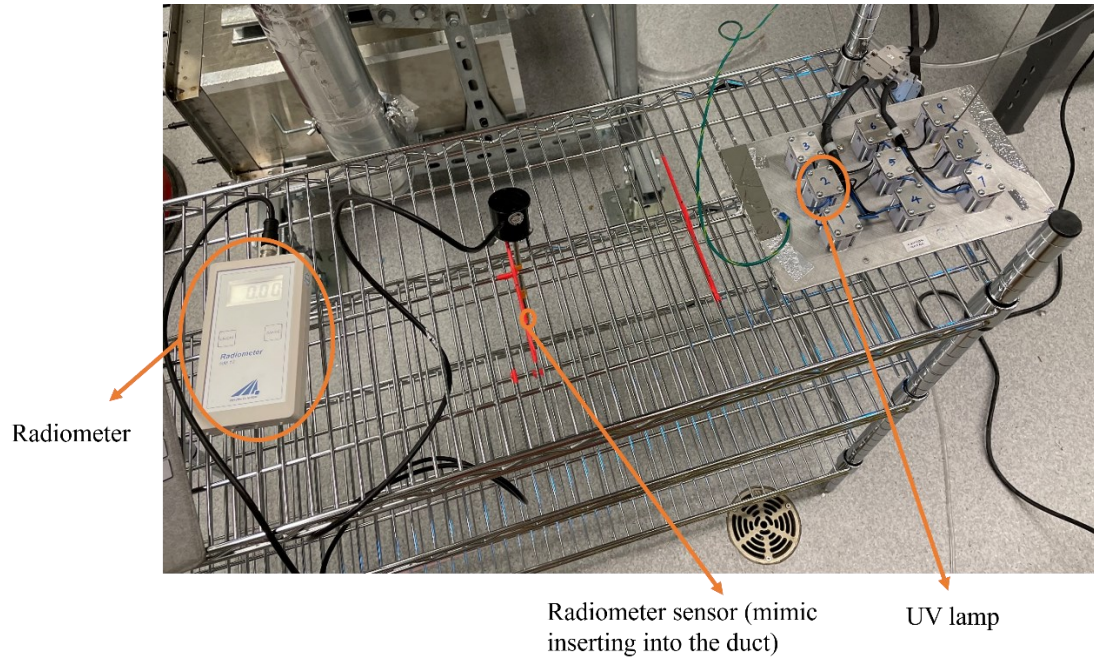


Figure 8 Schematic illustration of the irradiance measurement locations inside the duct (a: measured four cross-sections under the one-lamp stainless steel scenario, b: measured four cross-sections under the one-lamp galvanized steel and multiple-lamps scenarios)

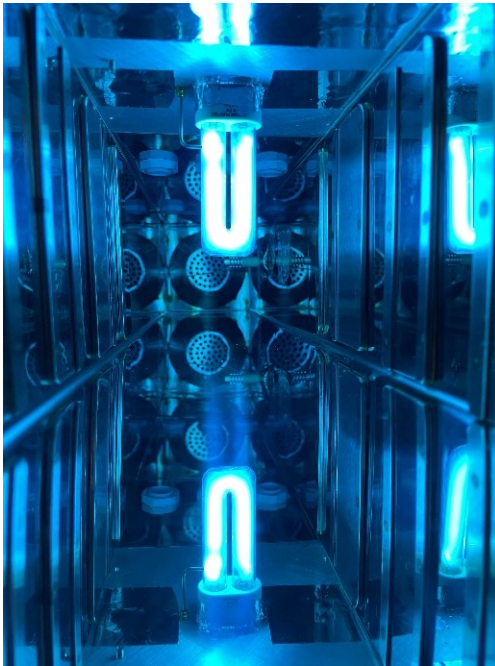
Since the spatial irradiance inside the duct is the sum of the direct emissive irradiance from the UV lamp and the reflected irradiance from the duct walls, the irradiance measurements consist of two parts. First, the direct emissive irradiance was measured in an open-air lab environment ( $19.5^{\circ}\text{C} \pm 2^{\circ}\text{C}$  and  $25\% \pm 5\%$  RH) without duct wall enclosures and reflections (Figure 9(a)). Then, the overall total irradiance at the relative exact spatial locations was measured inside the duct with the wall reflections (Figure 9(b)).

To ensure the same lamp output during the measurements of the direct emissive irradiance and the overall total irradiance, we directly applied the radiometer probe to the UV lamp surface (Figure 9(c)). We measured the lamp surface emitting irradiance for both open-air lab environment and in-duct environment under different ventilation conditions. It was

found that the in-duct environment under T ( $25^{\circ}\text{C}\pm 0.2^{\circ}\text{C}$ ), U ( $0.9\text{ m/s}\pm 0.06\text{ m/s}$ ), and RH ( $40\%\pm 5\%$ ) has the same lamp emission irradiance (lamp output) as the open-air lab environment ( $19.5^{\circ}\text{C}\pm 2^{\circ}\text{C}$  and  $25\%\pm 5\%$  RH). Thus, the measurements of the overall total in-duct irradiance were conducted under the airflow conditions of T ( $25^{\circ}\text{C}\pm 0.2^{\circ}\text{C}$ ), U ( $0.9\text{ m/s}\pm 0.06\text{ m/s}$ ) and RH ( $40\%\pm 5\%$ ).



(a)



(b)



(c)

Figure 9 (a) The direct emissive irradiance measurement in an open-air environment setup; (b) the overall total irradiance measurement inside the duct; and (c) lamp surface emitting irradiance at the bottom point

In addition to the measurements of the one lamp at the duct center scenario, the overall total irradiance of other duct system designs, including different lamp arrangements (one lamp at the center, two lamps in two rows, and two lamps in one row) and duct wall materials (specular reflection-dominated mirror-like stainless steel and diffuse reflection-dominated galvanized steel), were studied. The schematic of the lamp arrangement can be seen in Figure 10.

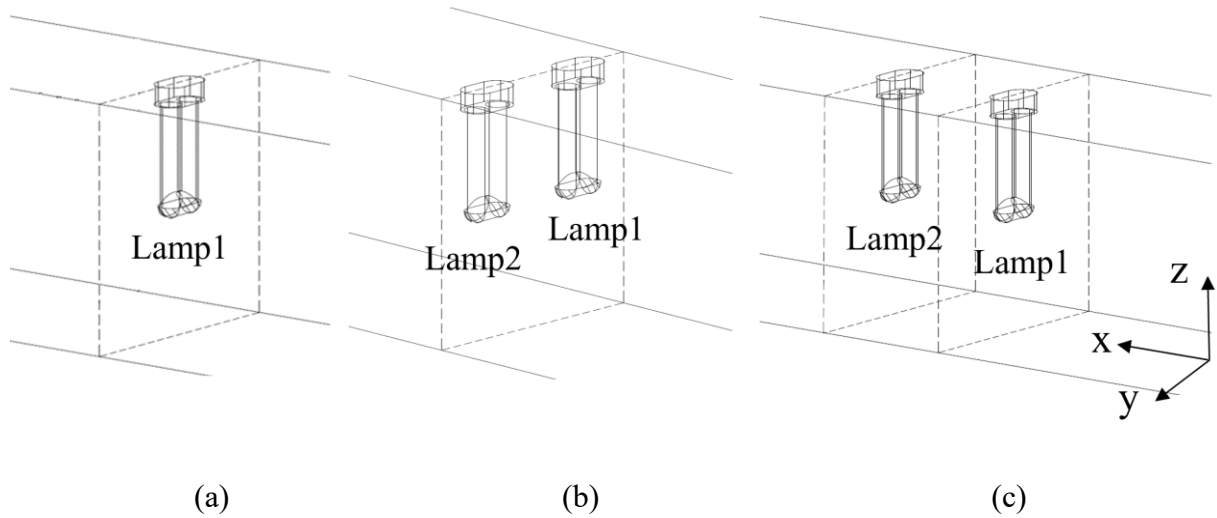


Figure 10 Schematic of lamp arrangements inside a duct: (a) one lamp at the center, (b) two lamps per row (one row), and (c) one lamp per row (two rows)

### 3.3.2 UVGI disinfection tests

In addition to the UV irradiance measurements, the performance of an in-duct UVGI system was evaluated by the inactivation efficiency as well, which was characterized by the genome damage (qPCR assay) and infectivity loss (culturing assay). In this study, airborne *E. coli* and *MS2* were chosen as target microorganisms in the UVGI tests. They are average-size Gram-negative bacterium ( $\sim 1.0 - 2.0 \mu\text{m}$  long and  $0.5 \mu\text{m}$  radius cylinder) and small-size non-enveloped single-stranded viruses (23 – 28 nm diameter sphere), which were commonly used as surrogates for pathogenic viruses and bacterium in the literature [16,17,26,128,129]. Note that airborne *E. coli* UVGI tests were conducted to investigate the effects of the UVGI system designs, and the airborne *MS2* UVGI tests were conducted to investigate the effects of system operating conditions and bioaerosol characteristics.

### 3.3.2.1 Microorganisms' preparation

*E. coli* strain (C3000, ATCC 15597) was cultured in lysogeny broth (LB) within a constant temperature shaking incubator (Corning 6750) at 37 °C and 170 rpm for 16 hours. Then, the stock was harvested by centrifuging the overnight suspension at 1920 relative centrifugal force (rcf) for 5 min and washing it three times with PBS solution. The final pellet was resuspended in 10 mL PBS, corresponding to approximately  $10^8$ – $10^9$  CFU/mL [16] and ready for microbial nebulization in the aerosol generator.

The *MS2* bacteriophage (ATCC 15597-B1) was propagated using *E. coli* C3000 in an LB solution. Initially, freeze-dried *MS2* phage stock was dissolved in  $1 \times$  PBS at 1 mg/mL. Then, 50  $\mu$ L of the resulting *MS2* suspension was added to a 10 mL log-phase *E. coli* LB culture, which was prepared by inoculating the *E. coli* strain in LB and incubating in a constant temperature shaking incubator (Corning 6750) at 37 °C and 170 rpm for 2 – 4 hours with an optical density at 600 nm wavelength ( $OD_{600}$ ) 0.1 – 0.4. Then, the *MS2* culture was incubated at 170 rpm and 37 °C for 16 hours. After propagation, the mixture was centrifuged at 4300 rpm (1750 rcf) for 25 mins to separate the *MS2* suspension from bacterial cells and the debris. The supernatant (*MS2* suspension) was then filtered through a 0.22  $\mu$ m pore membrane filter (Syringe Filter PES, Fisher brand, USA) and stored in a 4°C refrigerator for future use. The filtered *MS2* stock has a concentration of around  $10^{11}$  –  $10^{12}$  PFU/mL and was ready for microbial nebulization in the aerosol generator.

### 3.3.2.2 Bioaerosols preparation

Microbial nebulization was performed using a 1-jet nebulizer (Collision Nebulizer, BGI), in which high-velocity compressed airflow generated aerosols from liquid suspensions.

The aqueous solution in the nebulizer was prepared by adding the microbial suspension from the previous step to PBS (details see in Table 7). The resulting bioaerosols passed through a dryer and were introduced into the duct via an injection tube. Note that the starting microbial concentrations in the nebulizer for the UVGI infectivity loss test and the UVGI genome damage test were different, which were due to different detection limits of the culturing assay (using Andersen impactor) and qPCR assay (using Biosampler).

### 3.3.2.3 Bioaerosols sampling

For the UVGI infectivity loss test, the culturing assay was used to count the functional microorganisms and calculate the UV inactivation efficiency. Bioaerosols were collected using six-stage Andersen cascade impactors (TE-10-800, TISCH Environmental, USA) downstream of the UVGI reactor at a flow rate of 28.3 L/min. The Andersen impactor had six ranges of aerodynamic diameters:  $\geq 7$   $\mu\text{m}$  (stage 1, not included in this study), 4.7–7  $\mu\text{m}$  (stage 2), 3.3–4.7  $\mu\text{m}$  (stage 3), 2.1–3.3  $\mu\text{m}$  (stage 4), 1.1–2.1  $\mu\text{m}$  (stage 5), and 0.65–1.1  $\mu\text{m}$  (stage 6), thus, able to capture the particle size-resolved UV inactivation efficiency. During UVGI experiments, separate sterile impactors were used for UV-off and subsequent UV-on samplings to prevent cross-contamination. Different sizes of bioaerosols were deposited on the Glass Petri dishes inside the impactors. The Glass Petri dishes were prepared with nutrient agar (for *E. coli* cultivation) or double nutrient agar layers based on the plaque assay method in ISO 10705-1 (for MS2 cultivation) [130]. In brief, for preparing the single nutrient agar layer, 27 mL of 1.5% broth agar was directly poured onto a sterile glass Petri dish and allowed to solidify. While preparing the double nutrient agar layer, 22 mL of 1.5% broth agar was poured onto a sterile glass Petri dish and allowed to solidify first. Then, a 5 mL mixture of 0.5% broth agar (50 mL) and *E. coli* C3000 culture

suspension (1875  $\mu\text{L}$ , cultivated for 2–4 h and  $\text{OD}_{600}$  0.1–0.4) was uniformly spread on the 1.5% broth agar surface and left to solidify. Note that the Andersen Cascade Impactor operation manual [131] requires 27 mL of solidified agar in the Glass Petri dishes to maintain the correct distance between the jet orifice and the collection surface of each stage. Once the glass Petri dishes were prepared, they were placed beneath the impactor stages for sampling. The sampled agar plates were then incubated overnight at 37°C, and the number of colonies or plaques formed on the plates was counted and converted to the corresponding corrected particle counts using the positive-hole conversion table [132].

For the UVGI genome damage test, the qPCR assay was used for relative quantification of the undamaged viral genome and to calculate the UV inactivation efficiency. Bioaerosols were collected using SKC BioSamplers (20ml, BioLite + Pump, SKC Inc, USA) at the downstream sampling port at a flow rate of 12.5 L/min for 30 minutes, which had the cutoff size around 0.3  $\mu\text{m}$ [133]. Separate sterile Biosamplers were used for UV-off and subsequent UV-on samplings to prevent cross-contamination. After sampling, the microbial suspension in the Biosampler was aseptically pipetted into 1.5 mL microcentrifuge tubes and stored in a -80 °C freezer for further qPCR analysis.

In addition to bioassay sampling, *MS2* bioaerosols (from stage 4) were also collected for Transmission Electron Microscopy (TEM) imaging and Energy-Filtered Transmission Electron Microscopy (EFTEM) analysis to provide insights into the bioaerosol internal structures. Formvar/Carbon 75 mesh (Advanced microscopy facility, University of Alberta, Canada) was placed on a polytetrafluoroethylene (PTFE) filter (SKC Inc., USA) inside an agar Petri dish (27 mL of nutrient agar) (Figure 11). These were then inserted into stage 4 of the Andersen impactor and sampled for 30 min. After sampling, the TEM grid

was air-dried overnight, stained with 4% uranyl acetate, and prepared for imaging analysis. This study utilized two TEM devices because the electron beam damages the bioaerosol salt crystals (alkali halide crystals are highly beam-sensitive [134]). One device, with a lower electron beam density (Morgagni 268, Philips-FEI, with Gatan Orius charge-coupled detector camera), operated at 80 kV and was used to observe the internal structure of the bioaerosols. The other device, with a high electron beam density (JEOL F2100, Gatan Orius camera with a digital micrograph), operated at 200 kV and was employed for the energy-filtered TEM (EFTEM) analysis to show the elemental distributions of sodium (Na), potassium (K), and chlorine (Cl) ions (main components of PBS aerosols) in the bioaerosol.

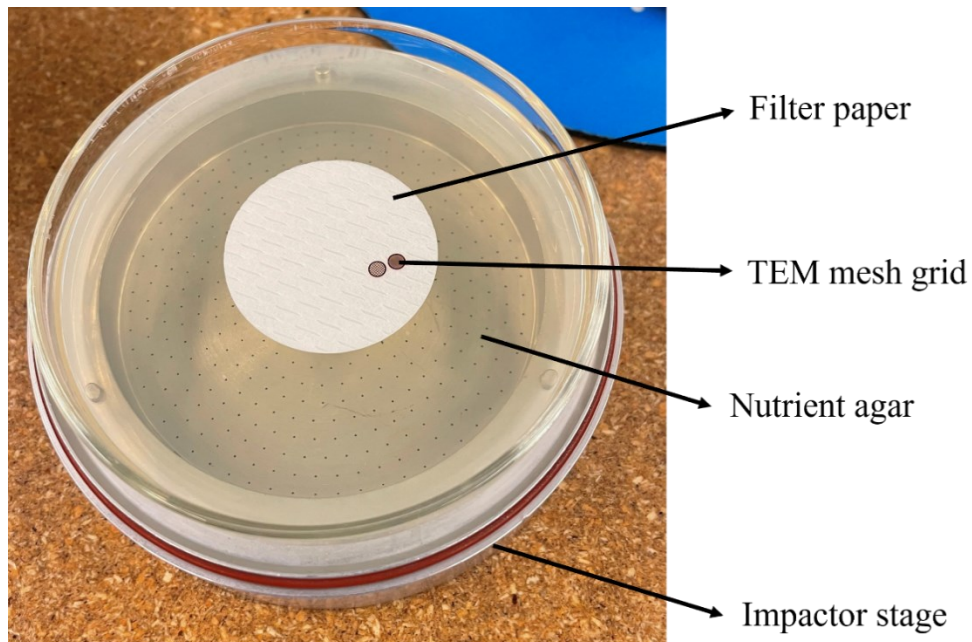


Figure 11 The setup of sampling bioaerosols on the TEM grid

### 3.3.2.4 UVGI test procedures

There was a total of eighteen UVGI tests conducted to investigate the effects of the in-duct UVGI system designs, operating conditions, and bioaerosol characteristics on the UV-induced airborne microorganism infectivity loss and genome damage. Each UVGI test was conducted with three replicates. Detailed information for the system design, environmental conditions, nebulizer solution concentrations, and sampling times are tabulated in Table 7.

Before and after each UVGI test, 50 mL of 70% ethanol was added to the nebulizer to generate an ethanol mist, which disinfected the entire duct system along with the clean air stream (1 h disinfection) [16,97,135]. For each experiment, nebulization commenced after the pilot HVAC system had stabilized under the desired operating condition. The system was then equilibrated for 10 min with the UV lamp turned off.

Due to the different microorganism concentrations across different particle sizes, prior to UVGI experiments, the *MS2* bioaerosol aerodynamic diameter distributions for each RH condition (at 0.5 m/s and 25°C) were initially determined using a six-stage Andersen impactor. The obtained bioaerosol concentrations at different stages were then used to adjust the sampling times in the UVGI test to improve statistical reliability. In addition, multiple sampling times were conducted in each UVGI test for the UV lamp-on condition due to the unknown efficiency of the UVGI system and to decrease the observational error.

During the UVGI tests, samplings were collected downstream of the UV device for the UVC-off and subsequent UVC-on conditions (10 mins UV lamp warmup before sampling). Consequently, the effective UV disinfection region is between the mixing baffle and the downstream sampling port (Figure 2(b)). Due to the varying sampling times with different stages to account for the virus concentration difference, sequential sampling was conducted

in this study. Taking experiment #15 UV-off condition as an example, the initial samplings of stages 5 and 6 were carried out for one minute, followed by the sampling of stage 4 for 15 minutes, and finally, sampling of stages 2 and 3 for 30 minutes. Additionally, it should be noted that during the sampling, agar plates were inserted in all the stages to ensure the aerosol flow inside the impactor was not affected by the absence of plates. For instance, when sampling on stages 5 and 6, agar plates were also inserted in stages 4, 3, 2, and 1, which would not be incubated and counted. Moreover, to ensure the stability of the entire system during the experiment, the duration of each bio-experiment was kept within 2.5 hours.

Table 7 The operating conditions and the sampling times for the *E. coli* and *MS2* UVGI experiment

No.	Test type (microorganisms)	UVGI system designs (lamp arrangements, duct wall materials)	Operating conditions			Nebulizer solution (mL) <sup>a</sup>		Sampling time (min) <sup>b</sup>						
			T (°C)	U (m/s)	RH	Microbial suspension	PBS	Stages 2 & 3		Stage 4		Stages 5 & 6		
								UV off	UV on	UV off	UV on	UV off	UV on	
#1	Infectivity loss ( <i>E. coli</i> )	One lamp at the center, stainless steel		0.49 ± 0.03								0.5	15	
#2				0.88 ± 0.08								1	10	
#3				1.34 ± 0.10								1	10	
#4		One lamp at the center, galvanized steel	25.1 ± 0.2	1.35 ± 0.12	40.7% ± 5.0%	10	40					1	10	
#5		Two lamps per row (one row), stainless steel		1.35 ± 0.13								1	10	
#6		One lamp per row (two rows), stainless steel		1.35 ± 0.11								1	10	
#7	Infectivity loss ( <i>MS2</i> )	One lamp at the center, stainless steel		0.49 ± 0.02			0.025 – 0.035		30	30	15	15, 30	0.67	0.5, 1
#8				0.92 ± 0.05	24.9% ± 1.2%		0.06 – 0.065		30	30	10	15, 30	1	0.5, 1
#9				1.34 ± 0.07			0.075		30	30	10	15, 30	1	0.5, 1
#10				0.51 ± 0.03			0.02 – 0.03		30	30	15	15, 30	0.67	2, 5
#11				0.93 ± 0.06	41.2% ± 4.7%		0.03 – 0.05	50	30	30	3	5, 10	1	1, 2
#12				1.33 ± 0.08			0.04 – 0.05		30	30	6	5, 10	1	0.5, 1
#13				0.51 ± 0.03			0.02 – 0.04		30	30	15	15, 30	0.67	2, 4
#14				0.92 ± 0.07	62.1% ± 5.0%		0.01 – 0.02		30	15, 30	15	15, 30	1	1, 2
#15				1.35 ± 0.07			0.015 – 0.02		30	15, 30	15	15, 30	1	1, 2
#16	Genome damage ( <i>MS2</i> )	One lamp at the center, stainless steel		0.31 ± 0.03										
#17			24.9 ± 0.3	0.49 ± 0.04	39.5% ± 4.3%	2	48	Biosampler <sup>c</sup> : lamp off: 30 min; lamp on: 30 min						
#18				0.92 ± 0.06										

a: The volume of added filtered *MS2* suspension varies according to the recovered plaque results from the previous day's experiment.

b: The sampling time varies according to the change in the *MS2* concentration in the nebulizer. At least two sampling times were conducted for UVC-on downstream sampling to account for the unknown UVGI efficiency and to decrease the observational error.

c: The biosamplers were used for the sample collection in the UVGI genome damage test due to the requirement of the qPCR assay.

### 3.3.2.5 qPCR assay

#### **RNA extraction**

RNA was extracted from 200  $\mu$ L samples of *MS2* using the GeneJET Viral DNA and RNA Purification Kit (Thermo Scientific, USA) following the manufacturer's instructions. In particular, 2  $\mu$ L in vitro transcribed green fluorescent protein (GFP) mRNA from pCDNA3.1-GFP plasmid using T7 RNA Polymerase (Invitrogen™ 18033019) was spiked into the lysis buffer in each batch prior to adding *MS2* samples. The GFP transcript is assayed by a pair of primers (forward: GGAGCGCACCATCTTCTTCA, reverse: AGGGTGTCGCCCTCGAA) and serves as an external reference to normalize the variation of RNA extraction efficiency and sample loading. Extracted RNA was eluted using 50  $\mu$ L of RNase-/DNase-free water (supplied with the kit).

#### **Primers**

Seventeen sets of primers (Table 8) that cover the entire *MS2* coding region were designed to assay the UV-induced genome damage in different regions of the *MS2* genome. All the primers used in this study were designed using the Primer Blast (<https://www.ncbi.nlm.nih.gov/tools/primer-blast/>) and synthesized by Integrated DNA Technologies (IDT, USA). A qPCR standard curve was generated to determine the amplification efficiency of each primer pair. A standard curve program with a melting curve was used to determine the amplification efficiency and specificity of the primers. The complete genome of *MS2* was taken from the NCBI GeneBank database (accession number NC\_001417.2).

Table 8 Seventeen primer sets used for airborne *MS2* UV inactivation tests

Primer set	Direction	Primer sequence	Target location/ encoding proteins	
1	Forward	GTGCGAGCTTTTAGTACCCTTG	130 – 337	A-protein
	Reverse	TCGATGTGACACTTAACGCCC		
2	Forward	GGGGCGTTAAGTGTCACATC	315 – 530	A-protein
	Reverse	TGGGTGACCTTTTGCAGGAC		
3	Forward	CCTGCAAAAGGTCACCCAGGG	513 – 728	A-protein
	Reverse	TGCAACTCCAACCACCTGCCG		
4	Forward	TTGGAGTTGCAGTTCGGTTGG	718 – 923	A-protein
	Reverse	AACCATATCACGATACGTCGCG		
5	Forward	GATGCACGTTTGGCATGGTTG	934 – 1133	A-protein
	Reverse	ACGCTTATGATGGACTCACCCG		
6	Forward	ATAAGCGTTGACGCTCCCTAC	1126 – 1340	A-protein
	Reverse	AGCCATGCTTCAAACCTCCGG		
7	Forward	ACTGTCGCCCCAAGCAACTTC	1392 – 1581	Coat protein
	Reverse	ATGCGGCTACAGGAAGCTCTAC		
8	Forward	CGCAGAATCGCAAATACACCATC	1495 – 1725	Coat protein
	Reverse	AGTAGATGCCGGAGTTTGCTG		
9	Forward	ATTCCCTCAGCAATCGCAGC	1689 – 1885	Lysis protein/ Replicase protein
	Reverse	AAGTCGTCAGTGTGCGGATC		
10	Forward	TTCTCGCGATCTTTCTCTCG	1804 – 1959	Lysis protein/ Replicase protein
	Reverse	TCGCCTCGTCATTACCAGAAC		
11	Forward	CTATCGCTAAGCTACGGGAGG	1975 – 2164	Replicase protein
	Reverse	ATAGGAGCACCGTTGGAGAAC		
12	Forward	GATCGTCGTTGTTTGGGCAATG	2119 – 2340	Replicase protein
	Reverse	ACACTCCGTTCCCTACAACGAG		
13	Forward	ATAGATCGGGCTGCCTGTAAG	2364 – 2561	Replicase protein
	Reverse	GGAGATGGAATCGGATGCAGAC		
14	Forward	TCTGCATCCGATTCCATCTCC	2541 – 2781	Replicase protein
	Reverse	CCCCGTAGATGCCTATGGTTC		
15	Forward	TCCATTTTGGTAACGCCGGAAC	2743 – 2970	Replicase protein
	Reverse	GGGCGAAGAGATTGTCAACAG		
16	Forward	CAATCTCTTCGCCCTGATGCTG	2957 – 3151	Replicase protein
	Reverse	TTGGTGTATACCGAGACTGCC		
17	Forward	TTCCGTCTTGCTCGTATCGCTC	3195 – 3372	Replicase protein
	Reverse	ACTCCTGAGGGAATGTGGGAAC		

### qPCR

A one-step reverse transcription (RT)-qPCR assay was used to measure the RNA damage.

Briefly, 10  $\mu$ L reactions were set up using the EXPRESS One-Step SYBR GreenER kits

(Thermo Scientific, USA) according to the manufacturer's instruction with 0.2  $\mu$ M primers

and 2.5  $\mu\text{L}$  RNA template. The RT-qPCR reactions were run on a QuantStudio 7 Pro Real-Time PCR instrument (Applied Biosystems) using a fast-cycling program: 5 minutes at 25  $^{\circ}\text{C}$  for uracil DNA glycosylase (UDG) digestion, 5 minutes at 50  $^{\circ}\text{C}$  for reverse transcription, 20 seconds at 95  $^{\circ}\text{C}$  for initial denaturation, 40 cycles of 1 second at 95  $^{\circ}\text{C}$  and 20 seconds at 60  $^{\circ}\text{C}$  for amplification and followed by melting curve step. No-template-controls were included for each primer set during the qPCR, and sample cycle threshold (Ct) values were obtained under 30 to ensure positive results.

### 3.3.2.6 Data analysis

For the UVGI tests using Andersen Impactor and subsequent culturing method, the disinfection efficiency of each stage and the UV rate constant are defined as [109,135,136]:

$$\eta_{s,\text{exp}} = \left( 1 - \frac{\overline{C_{s,\text{downstream,light-on}}}}{\overline{C_{s,\text{downstream,light-off}}}} \right) \times 100\% \quad (6)$$

$$k_{s,\text{exp}} = - \frac{\ln(1 - \eta_{s,\text{exp}})}{D} \quad (7)$$

Here,  $\eta_{s,\text{exp}}$  is the experimentally measured disinfection efficiency;  $\overline{C_{s,\text{downstream,light-on}}}$  and  $\overline{C_{s,\text{downstream,light-off}}}$  are the average cultivable bioaerosol concentrations (PFU/ $\text{m}^3$ ) from different downstream sampling times under light-on and light-off conditions, respectively;  $s$  represents the impactor stage number;  $D$  denotes the UV dose received by airborne microorganisms during UV exposure ( $\text{J}/\text{m}^2$ ), which is obtained using CFD simulation; and  $k_{s,\text{exp}}$  presents the UV inactivation rate constant ( $\text{m}^2/\text{J}$ ), which is obtained using regression analysis. In addition to each stage, the overall disinfection efficiencies and UV rate

constants for stages 2 – 6 (*MS2*) or stages 5 – 6 (*E. coli*) are calculated using total cultivable bioaerosol concentrations summed from all the target stages [25] as:

$$\eta_{overall} = \left( 1 - \frac{\overline{C_{s2,down,UV-on}} + \overline{C_{s3,down,UV-on}} + \overline{C_{s4,down,UV-on}} + \overline{C_{s5,down,UV-on}} + \overline{C_{s6,down,UV-on}}}{\overline{C_{s2,down,UV-off}} + \overline{C_{s3,down,UV-off}} + \overline{C_{s4,down,UV-off}} + \overline{C_{s5,down,UV-off}} + \overline{C_{s6,down,UV-off}}} \right) \quad (8)$$

Furthermore, one-way ANOVA followed by Tukey's multiple comparisons tests was performed to evaluate the statistical significance of differences in UV rate constants across different particle sizes and RHs.

As for the UVGI tests using the Biosampler and subsequent qPCR method, the disinfection efficiency (genome damage) and corresponding UV rate constants of the target genome regions were obtained based on the single-stage decay model with the internal reference correction included:

$$\eta_{i,qPCR} = \left( 1 - \frac{AF_{iprimer}^{\Delta Ct_i}}{AF_{GFP}^{\Delta Ct_{GFP}}} \right) \times 100\% \quad (9)$$

$$k_{i,qPCR} = - \frac{\ln(1 - \eta_{i,qPCR})}{D} \quad (10)$$

where AF is the amplification factor of the primer set,  $\Delta Ct$  is the difference of cycle threshold between the UV-off and -on samples, k is the UV rate constant ( $\text{cm}^2/\text{mJ}$ ), D is the UV dose ( $\text{mJ}/\text{cm}^2$ ), and iprimer and GFP represent the primer sets for *MS2* samples and GFP, respectively. Since the biosample is a non-particle-size resolved sampling device, the obtained disinfection efficiency was the overall disinfection efficiency.

## 3.4 Results and discussions

### 3.4.1 UV irradiance distribution inside the duct

#### 3.4.1.1 UV lamp emitting wavelength distribution

The emitting UV wavelength spectra of the UV lamp in this study were measured and confirmed the irradiance wavelength peaks at 253.7 nm, as expected for the low-pressure mercury UV lamp.

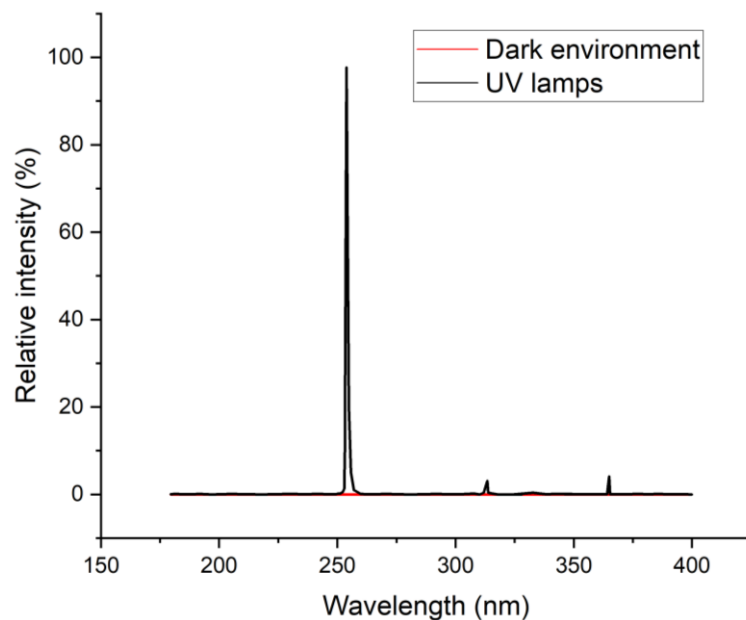


Figure 12 The emitting UV wavelength spectra of the low-pressure mercury UV lamp in this thesis

#### 3.4.1.2 Effects of lamp arrangements and duct wall materials

Three lamp arrangements, one lamp at the duct center, two lamps per row (one row), and one lamp per row (two rows), were investigated with stainless steel plates. Furthermore, two duct wall materials, including stainless steel plate and galvanized steel plate, were

investigated under the one lamp at the center arrangement. Table 9 presents the experimental data of the measured irradiance inside the duct for different scenarios.

The experimental data of irradiance at 36 points will be primarily used for model validations in Section 4.3.1, and a more detailed discussion of the effects of the lamp arrangements and duct wall materials on the irradiance distribution inside the duct will be included in Section 6.1 as well. In this section, several conclusions can still be drawn from the preliminary analysis. Firstly, regardless of the lamp arrangement and duct wall materials, the irradiance decreased along the duct length away from the UV lamp, i.e., the average irradiances of sections 2 and 3 were consistently higher than those of sections 1 and 4. Secondly, comparing the two lamp arrangements, the average irradiance of all 36-points for placing two lamps in the same row ( $0.695 \text{ mW/cm}^2$ ) is slightly higher than placing them in two rows ( $0.682 \text{ mW/cm}^2$ ), indicating a better irradiance distribution and potential better disinfection performance.

Table 9 Experimental data of the measured irradiance (direct emissive irradiance and overall total irradiance) under different lamp arrangements and duct wall materials

CS1			CS2			CS3			CS4		
<b>One lamp at the center, open-air lab environment (direct emissive irradiance), <math>\text{mW/cm}^2</math></b>											
0.07	0.07	0.07	0.20	0.21	0.20	0.64	0.80	0.59	0.12	0.12	0.12
0.07	0.07	0.07	0.21	0.23	0.21	0.66	0.82	0.72	0.12	0.12	0.12
0.07	0.07	0.07	0.20	0.22	0.20	0.53	0.65	0.69	0.12	0.12	0.12
<b>One lamp at the center, in-duct environment, stainless steel (total irradiance), <math>\text{mW/cm}^2</math></b>											
0.22	0.27	0.27	0.45	0.39	0.41	1.06	1.09	1.09	0.38	0.38	0.41
0.22	0.26	0.27	0.53	0.48	0.43	0.99	1.06	1.04	0.34	0.34	0.40
0.24	0.26	0.26	0.51	0.47	0.43	0.88	0.95	0.93	0.34	0.36	0.40
<b>One lamp at the center, in-duct environment, galvanized steel (total irradiance), <math>\text{mW/cm}^2</math></b>											
0.30	0.27	0.26	0.54	0.59	0.55	0.46	0.54	0.54	0.27	0.24	0.23

0.30	0.27	0.25	0.59	0.61	0.57	0.49	0.55	0.57	0.27	0.25	0.23
0.28	0.27	0.25	0.53	0.59	0.55	0.49	0.55	0.54	0.25	0.24	0.22
<b>Two lamps per row (one row), in-duct environment, stainless steel (total irradiance), mW/cm<sup>2</sup></b>											
0.47	0.44	0.43	0.98	1.00	0.94	0.90	0.92	0.93	0.42	0.40	0.39
0.49	0.44	0.45	1.03	1.02	0.97	0.92	0.93	1.01	0.44	0.40	0.41
0.50	0.46	0.46	0.95	0.96	0.91	0.91	0.91	0.95	0.45	0.41	0.41
<b>One lamp per row (two rows), in-duct environment, stainless steel (total irradiance), mW/cm<sup>2</sup></b>											
0.48	0.42	0.48	1.23	1.15	1.18	0.74	0.66	0.71	0.43	0.38	0.43
0.47	0.43	0.47	1.18	1.12	1.18	0.78	0.68	0.73	0.43	0.39	0.42
0.47	0.46	0.49	1.03	1.03	1.04	0.76	0.68	0.72	0.44	0.41	0.44

### 3.4.2 UV inactivation efficiencies

The effects of the UVGI system designs (lamp arrangements and duct wall materials), operating conditions (RH), and bioaerosol characteristics (bioaerosol particle size and genome sequence) on the inactivation efficiency were investigated using airborne *E. coli*, airborne *MS2*, and airborne *MS2*, respectively.

#### 3.4.2.1 Effects of lamp arrangements and duct wall materials

The airborne *E. coli* inactivation efficiencies under different UVGI system configurations and supply air velocities are listed in Table 11. Generally, the *E. coli* disinfection experiment showed the same conclusions as the UV irradiance measurements.

Under the same duct system operating conditions (T, U, and RH), increasing UV lamp numbers increased the inactivation efficiency regardless of the lamp arrangements and duct wall materials (from 95.60% ~ 97.25% to 99.59% ~ 99.81%). As for multiple-lamp scenarios, placing UV lamps in the same row (99.81%) resulted in higher inactivation efficiency than placing them in two rows (99.59%), which agrees with the observation of the measured average irradiance inside the duct (0.695 mW/cm<sup>2</sup> compared to 0.682

mW/cm<sup>2</sup>). With respect to the duct wall materials, it was noticed that diffuse reflection-dominated galvanized steel plates (97.25%) provided a better bacterial inactivation efficiency than the specular reflection-dominated stainless-steel plates (95.60%). A detailed discussion will be included in Section 6.1.

### 3.4.2.2 Effect of RH

The effect of RH on the UVGI system inactivation efficiency was investigated using airborne *MS2* under three RH conditions (24.9% ± 1.2%, 41.2% ± 4.7%, and 62.1% ± 5.0%) at a temperature of 24.8°C ± 0.4°C and velocities of 0.50 ± 0.03, 0.92 ± 0.06, and 1.34 ± 0.07 m/s. The environmental RH impacted the UV inactivation efficiency. As seen from Figure 13, for a given temperature, velocity, and particle size, the inactivation efficiency showed an initial increase and then a decrease as the environmental RH rose from 25% to 60%. A detailed discussion of the mechanisms behind it will be included in Section 6.2.2.

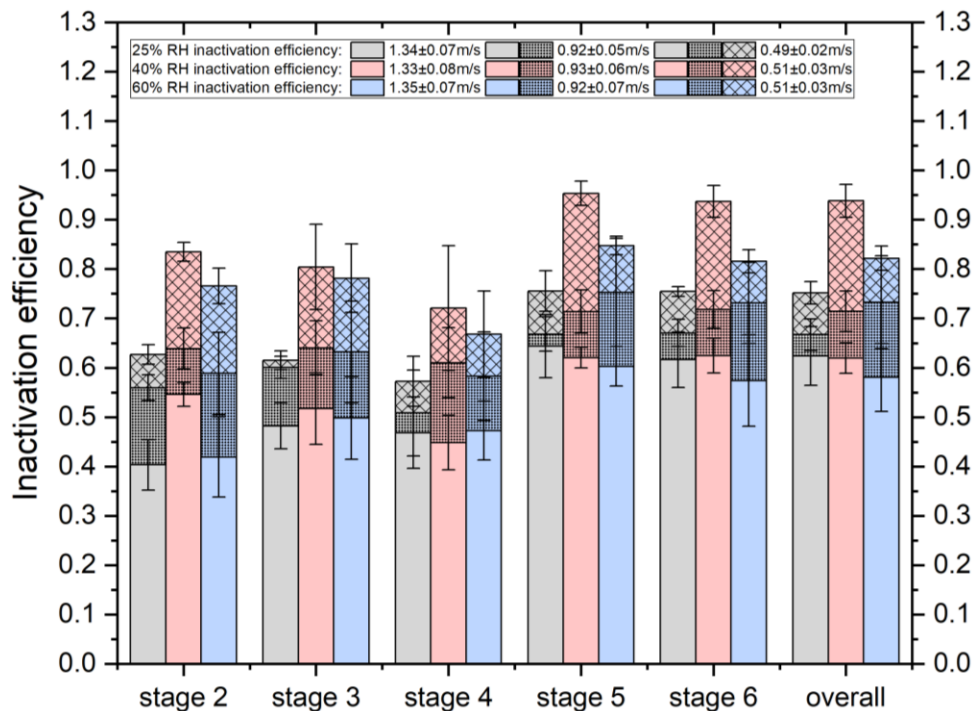


Figure 13 Experimental data of inactivation efficiencies for airborne *MS2* across different impactor stages at different RHs at a temperature of  $24.8^{\circ}\text{C} \pm 0.4^{\circ}\text{C}$  (error bars represent the standard deviations from the triplicate experiments)

#### 3.4.2.3 Effect of bioaerosol particle size

The effect of bioaerosol particle size on the UVGI system inactivation efficiency was investigated using airborne *MS2* with PBS as the suspending medium at RH levels of  $24.9\% \pm 1.2\%$ ,  $41.2\% \pm 4.7\%$ , and  $62.1\% \pm 5.0\%$ , a temperature of  $24.8^{\circ}\text{C} \pm 0.4^{\circ}\text{C}$ , and velocities of  $0.50 \pm 0.03$ ,  $0.92 \pm 0.06$ ,  $1.34 \pm 0.07$  m/s. Bioaerosol particle size impacted the UV inactivation efficiency as well. As shown in Figure 13, for a given temperature, velocity, and RH, Larger bioaerosols (2.1–7  $\mu\text{m}$ , stages 2, 3, and 4) exhibited lower inactivation efficiency compared to smaller ones (0.65–2.1  $\mu\text{m}$ , stages 5 and 6). A detailed discussion of the mechanisms behind it will be included in Section 6.3.1.

#### 3.4.2.4 Effect of genome sequence

The effect of genome sequence on the UV-induced genome damage was investigated using airborne *MS2* with PBS as the suspending medium at RH of  $39.5\% \pm 4.3\%$ , temperature of  $24.9^{\circ}\text{C} \pm 0.3^{\circ}\text{C}$ , and velocities of  $0.31 \pm 0.03$ ,  $0.49 \pm 0.04$ ,  $0.92 \pm 0.06$  m/s. The genome damage on seventeen primer sets that covered different *MS2* genome fractions, thus different genome sequences, were experimentally obtained through qPCR analysis. The genome sequence impacted the UV-induced genome damage (results see in Table 10). The experimental data will be primarily used for validating the genome damage model in Section 5.3.2.

Table 10 Experimental data of inactivation efficiencies of seventeen primer sets used for airborne *MS2* UVGI tests

Primer set	Locations	Encoding proteins	Genome damage		
			0.3m/s	0.5m/s	0.9m/s
1	130 – 337	A-protein	40.56%±28.78%	27.15%±6.24%	26.97%±19.48%
2	315 – 530	A-protein	42.44%±9.50%	22.66%±8.70%	15.48%±26.36%
3	513 – 728	A-protein	46.54%±23.93%	51.83%±3.98%	11.62%±7.87%
4	718 – 923	A-protein	48.69%±15.80%	33.90%±3.63%	19.90%±33.02%
5	934 – 1133	A-protein	29.94%±37.86%	12.87%±9.10%	8.64%±5.80%
6	1126 – 1340	A-protein	40.52%±12.85%	19.46%±14.03%	11.21%±6.23%
7	1392 – 1581	Coat protein	22.26%±33.04%	20.58%±12.81%	13.17%±6.57%
8	1495 – 1725	Coat protein	37.60%±23.30%	23.06%±18.21%	30.26%±28.83%
9	1689 – 1885	Lysis protein/ Replicase protein	36.47%±17.07%	37.73%±6.67%	12.04%±23.43%
10	1804 – 1959	Lysis protein/ Replicase protein	43.22%±13.99%	33.72%±3.60%	9.80%±6.53%
11	1975 – 2164	Replicase protein	19.24%±51.91%	10.58%±18.24%	5.42%±2.46%
12	2119 – 2340	Replicase protein	42.34%±27.84%	21.08%±9.94%	7.90%±16.09%
13	2364 – 2561	Replicase protein	23.32%±24.32%	26.5%±15.96%	16.39%±33.91%
14	2541 – 2781	Replicase protein	41.47%±24.09%	26.50%±15.96%	16.39%±20.47%
15	2743 – 2970	Replicase protein	42.40%±15.68%	31.04%±15.84%	21.97%±20.47%
16	2957 – 3151	Replicase protein	18.74%±58.87%	14.55%±20.06%	-0.51%±21.37%
17	3195 – 3372	Replicase protein	18.73%±37.26%	10.05%±26.97%	5..57%±54.66%

Table 11 Experimental data of inactivation efficiencies of UVGI tests under different UVGI system designs and operating conditions  
for airborne *E. coli* and *MS2*

Micro organism	T (°C)	U (m/s)	RH	Lamp configuration	Inactivation efficiency						
					Stage 2	Stage 3	Stage 4	Stage 5	Stage 6	Overall (Eq. (8))	
<i>E. coli</i>	25.1 ± 0.2	0.49 ± 0.03	40.7%±5.0%	One lamp at the center, stainless steel				99.99%±0.03%	99.98%±0.01%	99.98%±0.02%	
		0.88 ± 0.08					99.34%±0.17%	96.84%±0.28%	98.36%±0.27%		
		1.34 ± 0.10					96.40%±0.54%	95.12%±1.34%	95.60%±1.31%		
		1.35 ± 0.12		One lamp at the center, galvanized steel	-	97.99%±0.33%	97.05%±0.64%	97.25%±0.53%			
		1.35 ± 0.13		Two lamps per row (one row), stainless steel		99.97%±0.13%	99.50%±0.29%	99.81%±0.46%			
		1.35 ± 0.11		One lamp per row (two rows), stainless steel		99.64%±0.10%	99.37%±0.26%	99.59%±0.75%			
<i>MS2</i>	24.8 ± 0.4	0.49 ± 0.02	41.2% ± 4.7%	One lamp at the center, stainless steel	62.71%±1.99%	61.50%±1.91%	57.25%±5.06%	75.55%±4.11%	75.46%±1.01%	75.18%±2.26%	
		0.92 ± 0.05			24.9% ± 1.2%	55.95%±2.60%	60.04%±2.24%	50.82%±8.73%	66.83%±3.51%	67.03%±2.76%	66.70%±3.19%
		1.34 ± 0.07			40.31%±5.08%	48.22%±4.68%	46.83%±7.25%	64.37%±6.41%	61.63%±5.61%	62.38%±5.98%	
		0.51 ± 0.03			83.49%±1.92%	80.42%±8.65%	72.12%±12.65%	95.34%±2.47%	93.71%±3.21%	93.83%±3.36%	
		0.93 ± 0.06			63.88%±4.17%	64.04%±5.45%	61.01%±7.09%	71.40%±4.40%	71.77%±3.82%	71.43%±4.11%	
		1.33 ± 0.08			54.61%±2.44%	51.74%±7.27%	44.82%±5.50%	62.05%±2.11%	62.47%±3.54%	61.94%±3.09%	
		0.51 ± 0.03			76.59%±3.62%	78.15%±6.97%	66.81%±8.74%	84.76%±1.86%	81.56%±2.35%	82.19%±2.48%	
		0.92 ± 0.07			62.1% ± 5.0%	58.83%±8.35%	63.20%±10.32%	58.25%±8.97%	75.26%±10.97%	73.13%±8.23%	73.26%±9.42%
1.35 ± 0.07	41.90%±8.12%	49.83%±8.35%	47.23%±5.96%	60.28%±4.01%	57.38%±9.27%	58.05%±6.87%					

## 4 UVGI Modeling: Prediction of the UV Doses for the In-duct UVGI Systems

The disinfection of airborne microorganisms through ultraviolet (UV) light is a sophisticated procedure encompassing physical, chemical, and biological interactions. Ensuring the optimal design and enhanced application of in-duct UVGI systems within indoor spaces necessitates a precise understanding and characterization of these multifaceted interactions. In this chapter, we focus on modeling the average cumulative UV dose of the in-duct UVGI system and estimating the UV rate constant with the experimental data of inactivation efficiency from the previous chapter.

Section 4.1 presents a view-factor approach-based UV irradiance model to predict the irradiance distribution inside the duct. Further incorporating CFD simulations (Section 4.2), the UV dose of an in-duct UVGI system can be computed, and the UV rate constant can be estimated through the regression analysis. The proposed models are validated by the experimental data in this research and in the literature (Section 4.3). Finally, the predicted UV doses and estimated UV rate constants with different in-duct UVGI system designs, operating conditions, and bioaerosol characteristics are presented in Section 4.4.

### 4.1 UV irradiance model

The UV irradiance model consists of the lamp output prediction and the spatial irradiance distribution prediction. In this research, we introduced a new concept of the “ratio of convective heat dissipation to radiative heat dissipation” to predict the UV output of the low-pressure mercury lamp. Then, we developed a new mathematical model based on the view factor approach to predict the irradiance field (direct emissive irradiance and diffuse

and specular reflection irradiance) of a pilot in-duct UVGI system. The spatial irradiance distribution for different UVGI system configurations, including the number of lamps, multiple lamp positions, and duct wall materials, were predicted and validated using experimental measurements.

#### 4.1.1 Lamp output prediction: r method

To generalize the correlation between different lamp characteristics and wind-chill effects (i.e., different lamp diameters, lengths, and working powers), this thesis introduced the concept of the “ratio of convective heat dissipation to radiative heat dissipation” for the low-pressure mercury UV lamps. The dimensionless ratio  $r_Q$  is written as follows:

$$r_Q = \frac{Q_{conv}}{Q_{rad}} \quad (11)$$

where  $Q_{conv}$  and  $Q_{rad}$  are the lamp’s convective and radiative heat losses, which are calculated by:

$$Q_{conv} = \frac{Nu \cdot k}{d} A(T_{sur} - T_{amb}) \quad (12)$$

$$Q_{rad} = \varepsilon A \sigma \left[ (T_{sur} + 273)^4 - (T_{amb} + 273)^4 \right]$$

$Nu$  is the Nusselt number, which has different forms for different flow regimes and lamp shapes. For a cylindrical UV lamp (type 1), the Nusselt numbers of natural and forced convection [74,137,138] are given as:

$$Nu_{N1} = 0.47(\text{Pr} \cdot Gr)^{1/4} \quad (13a)$$

$$Nu_{F1} = 0.3 + \frac{0.62 \text{Re}^{0.5} \text{Pr}^{1/3}}{(1 + (0.4 / \text{Pr})^{2/3})^{1/4}} \left[ 1 + \left( \frac{\text{Re}}{282000} \right)^{5/8} \right]^{4/5} \quad (13b)$$

For the twin-tubes UV lamp (type 2), the Nusselt numbers for the natural and forced convections were approximated by the correlation for an ellipse [74,139] as:

$$Nu_{N2} = \left[ \left( \frac{1.85}{\ln \left( 1 + \frac{1.85}{0.897C_1 Ra^{1/4}} \right)} \right)^{10} + (0.103 Ra^{1/3})^{10} \right]^{1/10} \quad (13c)$$

$$Nu_{F2} = 0.27 Pr^{0.37} Re^{0.6} \quad (13d)$$

Based on natural and forced convection, the Nusselt numbers for the mixed convection are obtained by introducing the “effective Reynolds number” ( $Re_{eff}$ ), which is calculated as the geometric mean of the imaginary Reynolds number ( $Re_i$ ) for natural convection and real duct  $Re$  [74]:

$$\begin{aligned} Re_i &= \left[ \frac{Nu_N}{0.583} \right]^{1/0.471} \\ Re_{eff} &= \sqrt{Re_i^2 + Re^2} \\ Nu_M &= 0.583 Re_{eff}^{0.471} \end{aligned} \quad (13e)$$

With the Nusselt number known, implementing Eqs. (12) – (13) into Eq. (11), we have:

$$r_Q = \frac{Nu \cdot k \cdot A (T_{sur} - T_{amb})}{dQ_{rad}} \quad (14)$$

Once the lamp surface temperature is known, the  $r$  can be calculated using Eq. (14). It should be noted that the ratio  $r_Q$  contains the characteristics of both the lamps and duct airflow field; thus, it is expected that for the same type of UV lamps (even different dimensions) under the same ventilation conditions (air velocity and temperature), the  $r$  remains the same. That is to say, if the ratio  $r_Q$  of a UV lamp under a ventilation condition

is known, the lamp surface temperature of another same type of UV lamp under the same ventilation condition can be estimated using the following equation:

$$T_{sur} = T_{amb} + \frac{r_Q Q_{rad}^d}{Nu \cdot k \cdot A} = T_{amb} + \frac{r_Q Q_{total}^d}{Nu \cdot k \cdot A(1+r)} \quad (15)$$

where  $Q_{total}$  is the total heat dissipated by the lamp, which equals the input power minus the fraction of input emitted as UVC and other non-thermal radiation. Once the lamp surface temperature is known, the corresponding UV lamp output can be obtained using the manufacturer's data sheet (Figure 14).

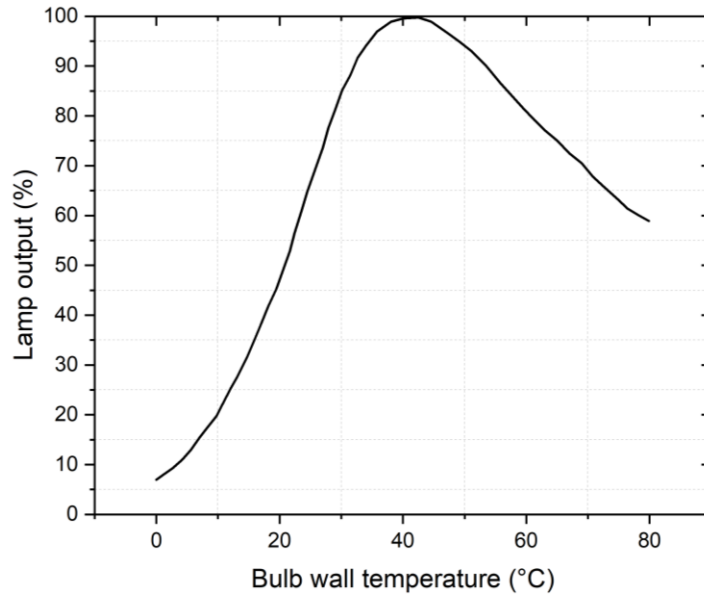


Figure 14 UV lamp output as a function of lamp surface temperature

## 4.1.2 Mathematical model of in-duct spatial irradiance

### 4.1.2.1 One lamp scenario

A new mathematical model based on the view-factor approach to predict the spatial irradiance distribution inside a duct was developed. The complex twin-tube-shaped UVC

lamp (OSRAM GCF5DS 5W) was simplified to a combination of three short luminous cylinders and two luminous circles, with dimensions of 51 mm length ( $L_1$ ) and 12 mm diameter ( $d_{\text{cylinder}}$ ) for the vertical luminous tubes (cylinders 1 and 2), and 3 mm length ( $L_2$ ) and 12 mm diameter ( $d_{\text{cylinder}}$ ) for the horizontal luminous tube (cylinder 3) (Figure 15). The luminous parts were installed inside the duct, and the transformer of the lamp and other accessories were placed outside the duct. However, the lamp manufacturer's installation guideline requires part of the unilluminated lamp base within the duct to minimize duct air leakage (cuboid #4 in Figure 15). A UV lamp was installed at the center of the duct to maximize irradiance uniformity within the duct. Because a mirror finish-polished stainless steel plate and galvanized steel plate were used to construct the duct, both specular reflection and diffuse reflection were considered in the model. Thus, the spatial irradiance ( $I_i$ ) for a given grid cell  $i$  in the computational duct domain can be expressed as the sum of the direct emissive irradiance ( $I_{e,i}$ ) from the UV lamp and the specular reflection irradiance ( $I_{rs,i}$ ) and diffuse reflection irradiance ( $I_{rd,i}$ ) from the duct walls as follows:

$$I_i = I_{e,i} + a_s I_{rs,i} + a_d I_{rd,i} \quad (16)$$

where  $a_s$  and  $a_d$  are the fractions of the specular and diffusive reflection irradiances, respectively, out of the total reflection irradiance.

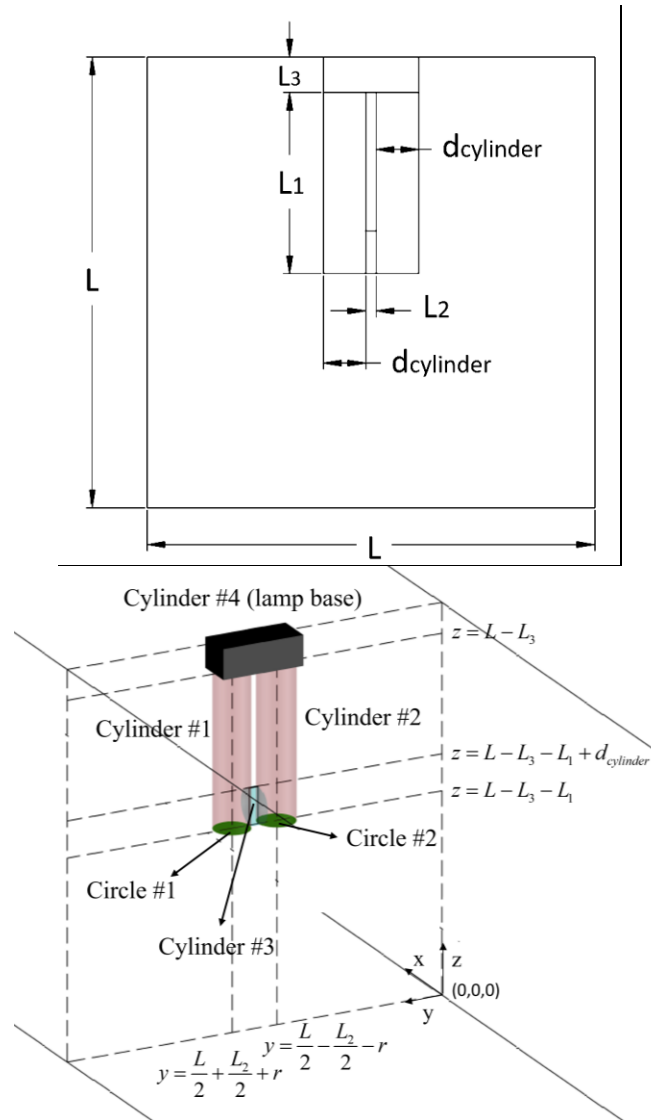


Figure 15 One UV lamp scenario layout in the duct and the schematic illustration of the view factor calculations

#### 4.1.2.1.1 Direct emissive irradiance from the UV lamp

Yang et al.'s study predicted the irradiance field of a similar twin-tube lamp by simplifying it to a double configuration of UV luminous tubes, neglecting the short tube (cylinder #3) that connects the twin tubes [61]. However, in our study, part of the lamp base was inside the duct because of the installation requirement, which is different from that in the previous

study. Thus, this study completes the view factor model for a more complicated lamp structure by considering the lamp-connecting tube and lamp base. Therefore, the received direct-emissive irradiance at any viewpoint (P) at cell *i* from a single luminous tube has the following form [61,63]:

$$I_{e,i} = \frac{W_{cylinder}}{A_{cylinder}} F_P \quad (17)$$

where  $W_{cylinder}$  is the power of each cylinder (W),  $A_{cylinder}$  is the surface area of the cylinder ( $m^2$ ), and  $F_P$  is the view factor from point P to the luminous cylinders (cylinders #1, #2, and #3) or the circles (circles #1 and #2). Analytical solutions of the view factor between a spatial viewpoint and a single cylinder or a circle were well developed and adopted here (see Appendix A). Thus, the overall direct emissive view factor of the twin-tube lamp could be built by “brick-stacking” of the three single cylinders and two circles. For the one-lamp case, there were four scenarios (Table 12, “One-lamp case: direct emissive irradiance”) for an arbitrary viewpoint P receiving the irradiance from the twin-tube UV lamp, which are combinations of the three-cylinder view classifications (Appendix A).

#### 4.1.2.1.2 Specular reflection from the duct walls

Specular reflection dominates in the duct walls that are highly polished with a mirror-like finish, wherein the incident light is reflected from the wall with functions of both surface location and orientation. Furthermore, when all four duct walls are specularly reflective, the radiation reflection bounces between the surfaces and contributes to the final irradiance field in the duct. A previous study [11] introduced a theory of the virtual image model that treats the specular reflection from an object as a direct emission from a virtual image that is symmetrically formed in a mirror (Figure 16), thus converting the specular reflection to

direct emissive radiation. The total specular reflection irradiance is the summation of the final steady reflections from the four walls.

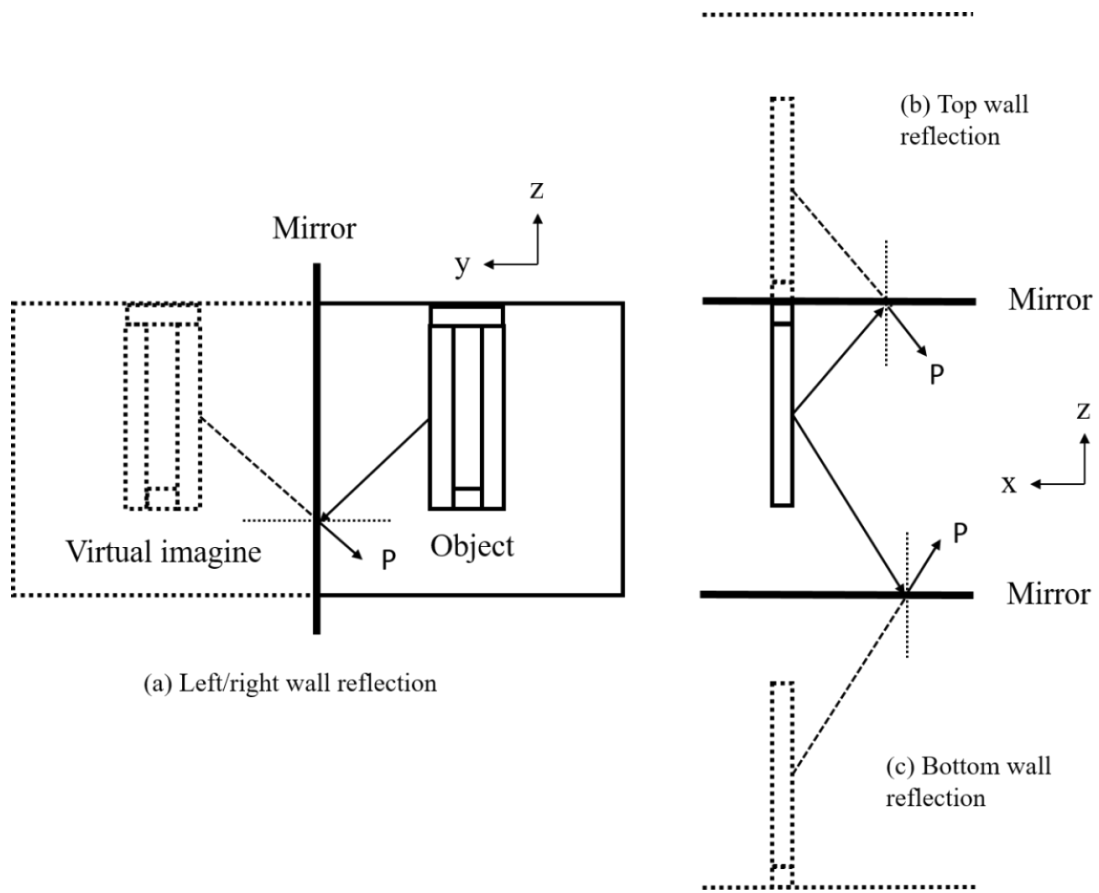


Figure 16 A specular reflector shows a virtual image of a lamp at an equivalent distance behind the reflector surface

Analogous to the direct emissive radiation from the UV lamp, specular reflection is calculated as the direct emissive radiation from the virtual UV lamp with virtual distance and surface reflectivity. More specifically, the surface reflectivity is considered to be the reduction of the virtual lamp output; that is, 90% wall reflectivity results in 90% virtual lamp output. In addition, as mentioned before, the reflections bounce between the surfaces, go through absorption/reflection, and finally become stable. Lastly, the theoretical

calculation yields the final specular reflection between two parallel surfaces as follows [140,141]:

$$I_{R,final} = I_{R1} \frac{R}{1-R^2} \quad (18)$$

where  $I_{R,final}$  is the final stable irradiance,  $I_{R1}$  is the irradiance contributed by the first reflection, and  $R$  is reflectivity. Thus, by summing the specular reflection from all four duct sidewalls and applying the stable specular reflection correlation, we obtain the spatial irradiance from the reflection at any point  $P$ , expressed as follows:

$$I_{rs,i} = \sum_{dw=1}^4 I_{R1} \frac{R}{1-R^2} = \sum_{dw=1}^4 \frac{w_{tube} R^2 F_{(dw)P-virtual\ tube}^s}{A_{tube} (1-R^2)} \quad (19)$$

where  $dw$  represents the four sidewalls,  $R$  is the duct wall reflectivity, and  $F_{(dw)P-virtual\ tube}^s$  is the specular view factor from the virtual tube ( $dw^{th}$  wall reflection) to viewpoint  $P$  (grid  $i$ ).

#### 4.1.2.1.3 Diffuse reflection from the duct walls

Diffuse reflection was considered as the secondary diffusely emitting irradiance from the finite wall element to the spatial point differential area, using the primary direct emissive irradiance from the lamp transported to the duct wall element as the energy source. The view factors  $F_{(we)P-we}^d$  for any two differential elements are organized in Supplementary Material Appendix A. Thus, the diffuse reflection from the duct wall surfaces to a given spatial cell  $i$  can be written as follows:

$$I_{rd,i} = \sum_{dw=1}^4 \sum_{we=1}^{te} R I_{we,wall-direct} F_{(we)P-we}^d \quad (20)$$

where  $w_e$  and  $t_e$  are the  $w_e^{\text{th}}$  face grid cell and the total number of face grid cells of the  $d_w^{\text{th}}$  duct wall, respectively.  $I_{w_e, \text{wall-direct}}$  is the primary emissive irradiance of the first grid cell adjacent to the  $w_e^{\text{th}}$  wall face grid, which is directly obtained from the UV lamp.  $F_{(w_e)P-w_e}^d$  is the view factor of P and the  $w_e^{\text{th}}$  wall face cell. The radiometer RM-12 (Opsytec, Germany) was used in the irradiance measurement, which is capable of  $160^\circ$  radiation detection. Thus, only the forward diffuse reflection from the face boundary cells that were in front of the sensor could be detected, whereas the backward diffuse reflection from the face boundary cells behind the sensor was blocked. Thus, the radiometer rotated  $180^\circ$  to measure the backward incident reflection irradiance at all four measuring cross-sections (nine points at each cross-section see Figure 8), and the readings were  $0 \text{ W/m}^2$  ( $\pm 0.1 \text{ W/m}^2$  for the detection limitation) for both mirror-like stainless steel plates and galvanized steel plates, indicating negligible contributions from the backside reflection. Hence, the contributions from the face boundary cells behind viewpoint P were neglected in the model calculation. The direct emissive irradiance and specular reflection irradiance were not affected by the  $180^\circ$  radiation detection because these irradiances only traveled forward without direction reversal as diffuse reflection.

Finally, analogous to specular wall reflection, inter-reflected diffuse wall reflections were considered using the overall first-time diffuse reflection irradiance at the duct wall as the energy source to compute the second-time in-duct spatial irradiance, as well as the third-time diffuse reflection. Due to each reflection's energy loss, less than 10% of the energy remained after the fifth diffuse reflection [141]. Thus, up to the sixth diffuse reflections were computed sequentially in this study.

#### 4.1.2.1.4 Total irradiance received at the spatial viewpoint P

Summing the direct emissive irradiance, specular reflection irradiance, and diffuse reflection irradiance, we obtain the total irradiance received at viewpoint P as follows:

$$\begin{aligned}
 I_i = & \frac{W_{tube}}{A_{tube}} F_{P-tube} + \sum_{dw=1}^4 \frac{W_{tube} R^2 F_{(dw)P-virtual\ tube}^s}{A_{tube} (1-R^2)} + \sum_{dw=1}^4 \sum_{we=1}^{te} RI_{we,wall-direct} F_{(we)P-we}^d \\
 & + \sum_{dw=1}^4 \sum_{we=1}^{te} RI_{we,wall-1st} F_{(we)P-we}^d + \dots + \sum_{dw=1}^4 \sum_{we=1}^{te} RI_{we,wall-nth\ reflection} F_{(we)P-we}^d
 \end{aligned} \tag{21}$$

However, the view factor method only considers the geometric transmission between the two surfaces while neglecting the radiation transport (absorption and scattering) along the path within the transport medium. Thus, adding the extinction coefficient for the non-negligible media absorption and scattering effects is essential to consider both geometric and transportation light losses [142,143]. Eq. (21) is modified using the Beer-Lambert law as follows:

$$\begin{aligned}
 I_i = & \frac{W_{tube}}{A_{tube}} e^{-\alpha_\lambda PL_{P-tube}} F_{P-tube} + \sum_{dw=1}^4 \frac{W_{tube} e^{-\alpha_\lambda PL_{P-virtual\ tube}} R^2 F_{(dw)P-virtual\ tube}^s}{A_{tube} (1-R^2)} \\
 & + \sum_{dw=1}^4 \sum_{we=1}^{te} RI_{we,wall-direct} e^{-\alpha_\lambda PL_{P-we}} F_{(we)P-we}^d + \sum_{dw=1}^4 \sum_{we=1}^{te} RI_{we,wall-1st} e^{-\alpha_\lambda PL_{P-we}} F_{(we)P-we}^d \\
 & + \dots + \sum_{dw=1}^4 \sum_{we=1}^{te} RI_{we,wall-nth\ reflection} e^{-\alpha_\lambda PL_{P-we}} F_{(we)P-we}^d
 \end{aligned} \tag{22}$$

where  $\alpha_\lambda$  is the UV extinction coefficient ( $\text{cm}^{-1}$ ) at a specific wavelength,  $PL_{P-tube}$ ,  $PL_{P-virtual\ tube}$ , and  $PL_{P-we}$  are the radiation transport path length of viewpoint P and luminous tube, viewpoint P and specular reflection virtual image tube, and viewpoint P and wall surface element, respectively. The path length was calculated as the distance between point P and

the midpoint of the cylinder to simplify the path-length calculation between the cylinder and infinitesimal area P.

#### 4.1.2.2 Two lamps' scenarios

Multiple lamps are often present inside the duct to deliver more UV energy for sufficient antiviral disinfection. However, spatial radiation is not a simple summation of the emitting irradiance from each lamp owing to the inter-lamp shadowing effects. Therefore, this study considered the geometrical shadowing effects between the two lamps and validated them using experimental data for the two commonly used lamp arrangements inside the ductwork (Figure 17).

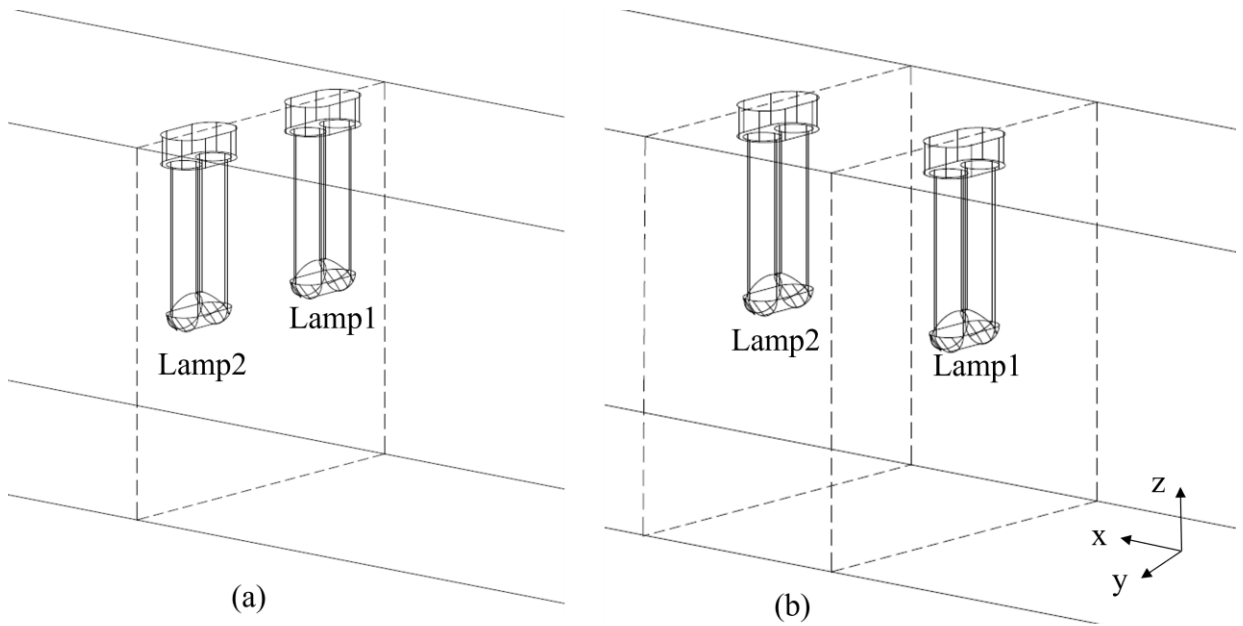


Figure 17 Schematic of two-lamp arrangements inside a duct: (a) two lamps per row (one row) and (b) one lamp per row (two rows)

#### 4.1.2.2.1 Two lamps per row (one row)

Two twin-tube UV lamps were placed inside the duct and arranged in one row, facing the incoming airflow, as shown in Figure 17(a). There were no shadowing effects between the two lamps in most of the regions. Thus, the total irradiance can be considered the simple sum of the two single-lamp irradiances (direct emissive irradiance, specular reflection irradiance, and diffuse reflection irradiance). For the region  $-r < x < r$  &  $L - L_3 - L_1 < z < L - L_3$  indicated in Figure 19(f), partial shadowing effects must be considered, and the schematic illustration and mathematical equations are presented in Table 12.

#### 4.1.2.2.2 One lamp per row (two rows)

Two twin-tube UV lamps were placed at the duct center and arranged in two rows along the airflow direction, as shown in Figure 17(b). Shadowing effects must be considered owing to the geometrical relationships. The “projection area” method was introduced to compute the shadow effects of lamp #1 on lamp #2. For viewpoint P in front of lamp #1, the projections of lamp #1 from P create a shadow area on the lamp #2 plane (shadowed area in Figure 18). For different P locations, the shadow varied, and different sections of lamp #2 were blocked (yellow area in Figure 18). Thus, the projected shadow areas from viewpoint P to the lamp #2 plane were calculated and compared with the luminous area of lamp #2, and the attenuation ratios (fraction of the luminous cylinder that was not blocked) were estimated accordingly. A schematic illustration of the shadow area calculation for different viewpoint P scenarios is presented in Table 12. The shadowing effect-corrected irradiance from lamp #2 due to the presence of lamp #1 was calculated as follows:

$$I_{i,lamp2} = e^{-\alpha_\lambda PL_{p-cy1}} I_{e,i,lamp2cy1} + e^{-\alpha_\lambda PL_{p-cy2}} I_{e,i,lamp2cy2} + a_d e^{-\alpha_\lambda PL_{p-we}} I_{rd,i,lamp2} + a_s e^{-\alpha_\lambda PL_{p-virtual\ tube}} \left( I_{rs\_left,i,lamp2'} + I_{rs\_right,i,lamp2'} + I_{rs\_top,i,lamp2'} + I_{rs\_bottom,i,lamp2'} \right) \quad (23)$$

where  $I_{e,i,lamp2cy1}$  and  $I_{e,i,lamp2cy2}$  are the direct emissive irradiances from cylinders 1 and 2 of lamp #2,  $I_{rs\_left,i,lamp2'}$ ,  $I_{rs\_right,i,lamp2'}$ ,  $I_{rs\_top,i,lamp2'}$  and  $I_{rs\_bottom,i,lamp2'}$  are the left-wall reflection irradiance from lamp #2, and  $I_{rd,i,lamp2}$  is the diffuse reflection irradiance from lamp #2. They are represented as follows:

$$I_{e,i,lamp2cy1} = \frac{W_{lamp2cy1}}{A_{lamp2cy1}} F_{P-lamp2cy1} f_{block\_lamp1} = \frac{W_{lamp2cy1}}{A_{lamp2cy1}} F_{P-lamp2cy1} \times \begin{cases} \text{if } z_p > z_{30} : \frac{l_{y\_block}}{d_{cy}} \\ \text{else} : \frac{l_{y\_block} l_{z\_cy1cy2\_block} + (d_{cyl} - l_{y\_block}) l_{z\_cy3\_block}}{d_{cyl} L_{cyl}} \end{cases} \quad (24)$$

$I_{e,i,lamp2cy2}$  has a symmetrical distribution with  $I_{e,i,lamp2cy1}$ .

$$I_{rs\_left,i,lamp2'} = \frac{W_{lamp2'cy1'}}{A_{lamp2'cy1'}} F_{(left)P-lamp2'cy1'}^s f_{block\_lamp1} + \frac{W_{lamp2'cy2'}}{A_{lamp2'cy2'}} F_{(left)P-lamp2'cy2'}^s f_{block\_lamp1} = \frac{W_{lamp2'cy1'}}{A_{lamp2'cy1'}} F_{(left)P-lamp2'cy1'}^s \times \begin{cases} \text{if } z_p > z_{32} : \frac{l_{y\_block\_cy1'}}{d_{cy}} \\ \text{else} : \frac{l_{y\_block\_cy1'} l_{z\_cy1cy2\_block}}{d_{cyl} L_{cyl}} \end{cases} + \frac{W_{lamp2'cy2'}}{A_{lamp2'cy2'}} F_{(left)P-lamp2'cy2'}^s \times \begin{cases} \text{if } z_p > z_{32} : \frac{l_{y\_block\_cy2'}}{d_{cy}} \\ \text{else} : \frac{l_{y\_block\_cy2'} l_{z\_cy1cy2\_block}}{d_{cyl} L_{cyl}} \end{cases} \quad (25)$$

$I_{rs\_right,i,lamp2'}$  has a symmetrical distribution with  $I_{rs\_left,i,lamp2'}$ .

$$\begin{aligned}
I_{rs\_top,i,lamp2'} &= \frac{W_{lamp2'cy1'}}{A_{lamp2'cy1'}} F_{(top)P-lamp2'cy1'}^s f_{block\_lamp1} + \frac{W_{lamp2'cy2'}}{A_{lamp2'cy2'}} F_{(top)P-lamp2'cy2'}^s f_{block\_lamp1} \\
&= \frac{W_{lamp2cy1}}{A_{lamp2cy1}} F_{(top)P-lamp2'cy1'}^s \times \frac{l_{y\_block} l_{z\_lamp2'\_block}}{d_{cyl} L_{cyl}} + \text{symmetrical distribution with cyl}
\end{aligned}
\tag{26}$$

$$\begin{aligned}
I_{rs\_bottom,i,lamp2'} &= \frac{W_{lamp2'cy1'}}{A_{lamp2'cy1'}} F_{(bottom)P-lamp2'cy1'}^s f_{block\_lamp1} + \frac{W_{lamp2'cy2'}}{A_{lamp2'cy2'}} F_{(bottom)P-lamp2'cy2'}^s f_{block\_lamp1} \\
&= \frac{W_{lamp2cy1}}{A_{lamp2cy1}} F_{(bottom)P-lamp2'cy1'}^s \times \frac{l_{y\_block} l_{z\_lamp2'\_block}}{d_{cyl} L_{cyl}} + \text{symmetrical distribution with cyl}
\end{aligned}
\tag{27}$$

Summing the total irradiance from lamp#1 (Eq.(22)), we obtain the total irradiance for the case of one lamp per row (two rows).

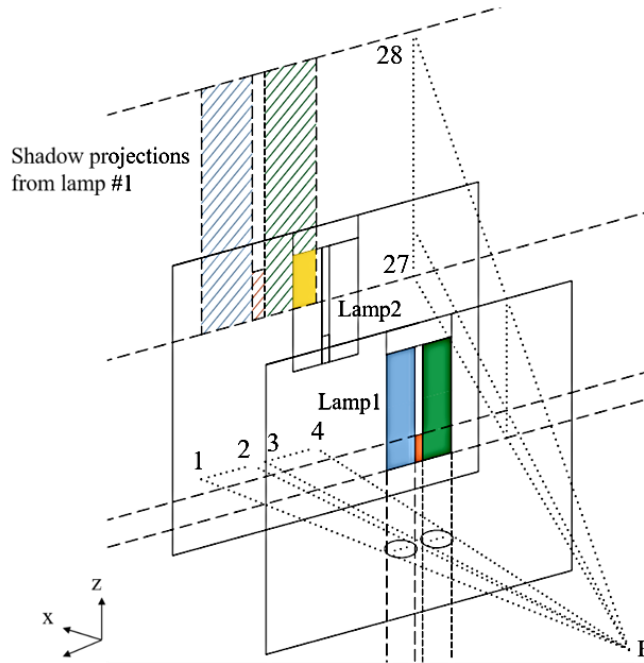


Figure 18 Schematic illustration of the shadowing effects between Lamp1 and Lamp2 placed in two rows

Table 12 Schematic diagram and model equations of the viewpoint P receiving the radiation from the twin-tube UV lamp

**Scenarios**

**View factor model equations<sup>1</sup>**

Figure 19 (a) – (k) Schematic of the view factor calculations for different lamp arrangements and scenarios

One-lamp case: direct emissive irradiance

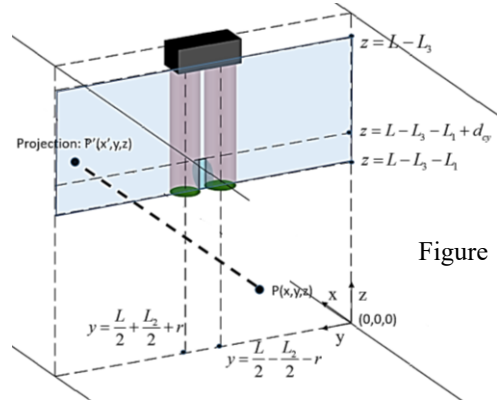


Figure 19(a)

P is above the bottom of the UV lamp and below the lamp base. Only the emissive irradiance from the three cylinders (classification) is considered.

$$\begin{cases}
 \frac{L}{2} - \frac{L_2}{2} - r < y < \frac{L}{2} : F_{P-lamp} = F_{P-cy1}(|z - (L - L_3 - L_1)|, D_{P-c1}) + F_{P-cy1}(|L - L_3 - z|, D_{P-c1}) + F_{P-cy2}(|z - (L - L_3 - L_1)|, D_{P-c2}) \\
 \quad + F_{P-cy2}(|L - L_3 - z|, D_{P-c2}) + F_{P-cy3}\left(\left|\frac{L_2}{2} - \left(\frac{L}{2} - y\right)\right|, D_{P-c3}\right) + F_{P-cy3}\left(\left|\frac{L_2}{2} + \left(\frac{L}{2} - y\right)\right|, D_{P-c3}\right) & (28a) \\
 y < \frac{L}{2} - \frac{L_2}{2} - r : F_{P-lamp} = F_{P-cy1}(|z - (L - L_3 - L_1)|, D_{P-c1}) + F_{P-cy1}(|L - L_3 - z|, D_{P-c1}) + F_{P-cy2}(|z - (L - L_3 - L_1)|, D_{P-c2}) \\
 \quad + F_{P-cy2}(|L - L_3 - z|, D_{P-c2}) + F_{P-cy3}\left(\left|y - \frac{L}{2} + \frac{L_2}{2}\right|, D_{P-c3}\right) - F_{P-cy3}\left(\left|y - \frac{L}{2} - \frac{L_2}{2}\right|, D_{P-c3}\right) & (28b) \\
 -r < x < r : \begin{cases}
 \frac{L}{2} - \frac{L_2}{2} - r < y < \frac{L}{2} : F_{P-lamp} = F_{P-cy1}(|z - (L - L_3 - L_1)|, D_{P-c1}) + F_{P-cy1}(|L - L_3 - z|, D_{P-c1}) + F_{P-cy2}(|z - (L - L_3 - L_1)|, D_{P-c2}) \\
 \quad + F_{P-cy2}(|L - L_3 - z|, D_{P-c2}) + F_{P-cy3}\left(\left|\frac{L_2}{2} - \left(\frac{L}{2} - y\right)\right|, D_{P-c3}\right) + F_{P-cy3}\left(\left|\frac{L_2}{2} + \left(\frac{L}{2} - y\right)\right|, D_{P-c3}\right) & (28c) \\
 y < \frac{L}{2} - \frac{L_2}{2} - r : F_{P-lamp} = F_{P-cy2}(|z - (L - L_3 - L_1)|, D_{P-c2}) + F_{P-cy2}(|L - L_3 - z|, D_{P-c2}) & (28d)
 \end{cases} \\
 \text{where } D_{P-c1} = \sqrt{x^2 + (L/2 - L_2/2 - r - y)^2}; D_{P-c2} = \sqrt{x^2 + (L/2 + L_2/2 + r - y)^2}; D_{P-c3} = \sqrt{x^2 + (z - (L - L_3 - L_1 + r))^2} & (28e)
 \end{cases}$$

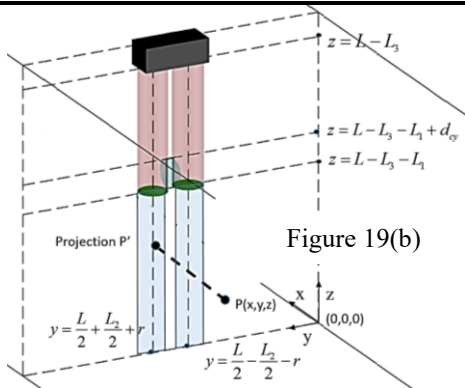


Figure 19(b)

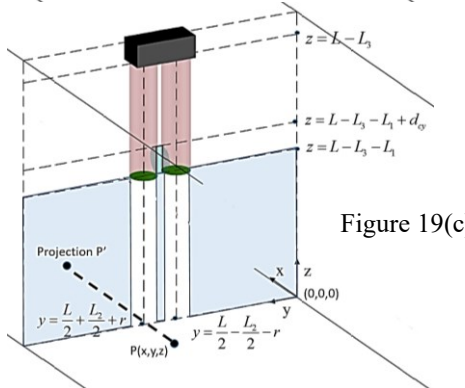


Figure 19(c)

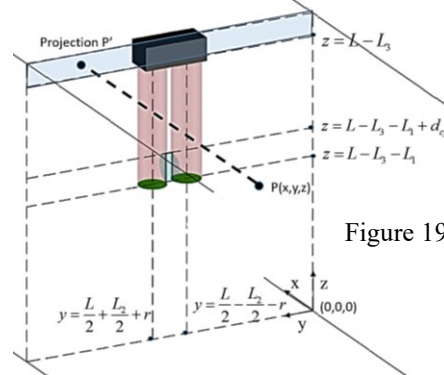


Figure 19(d)

For the cases of P is vertically below cylinder #1 or #2's (Figure 19(b)), above the top of the UV lamp (Figure 19(c)), and below the bottom of the UV lamp, and vertically beside cylinders #1 and #2 (Figure 19(d)), the model equations are concluded in the Appendix A Table A4.

Note: I: Only the equations of the right half of the computational domain are listed here, where the left half of the computational domain is symmetrical to the right half.

One-lamp case: Specular reflection irradiance (direct emissive irradiance from the virtual lamp)

One-lamp case: Diffuse reflection irradiance (refer to Supplementary Material Appendix A)

Two lamps per row (one row) case: direct emissive irradiance

$x > r \parallel x < -r$	Summation of the total direct emissive irradiance from the two UV lamps
$-r < x < r$	$z > L - L_3 - L_1$ Total direct irradiance from lamp #2 cyl

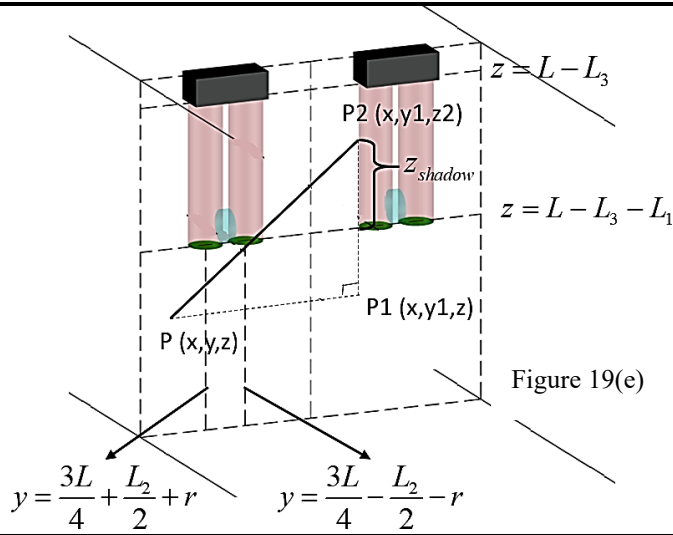


Figure 19(e)

$$y > \frac{3L}{4} + \frac{L_2}{2} + r$$

$$z < L - L_3 - L_1$$

Full direct irradiance from lamp #2 cy1, lamp #2 cy3 and partial lamp #1 cy1 ( $\frac{z_{light}}{L_1} I_{lamp\#1cy1}$ ), where  $z_{light} = (L - L_3 - L_1 - z) \times \frac{L/2 - L_2 - 4r}{y - (3L/4 - L_2/2 - 2r)}$  for  $L - L_3 - L_1 < z_2 < L - L_3$  and  $z_{light} = L_1$  for  $z_2 > L - L_3$

$$\frac{3L}{4} - \frac{L_2}{2} - r < y < \frac{3L}{4} + \frac{L_2}{2} + r$$

$$z < L - L_3 - L_1$$

Full direct irradiance from lamp #2 cy1, lamp #2 cy2 and lamp #2 cy3  
Full direct irradiance from lamp #2 cy1, lamp #2 cy3 and partial lamp #1 cy1 ( $\frac{z_{light}}{L_1} I_{lamp\#1cy1}$ ), where  $z_{light} = (L - L_3 - L_1 - z) \times \frac{L/2 - L_2 - 4r}{y - (3L/4 - L_2/2 - 2r)}$  for  $L - L_3 - L_1 < z_2 < L - L_3$  and  $z_{light} = L_1$  for  $z_2 > L - L_3$

$$\frac{L}{2} < y < \frac{3L}{4} - \frac{L_2}{2} - r$$

$$z > L - L_3 - L_1$$

Full direct irradiance from lamp #2 cy2 and lamp #1 cy1

$$z < L - L_3 - L_1$$

Full direct irradiance from lamp #2 cy2, lamp #2 cy3, lamp #2 circle1, lamp #2 circle2, lamp #1 cy1, lamp #1 cy3, lamp #1 circle1 and lamp #1 circle 2.

### Two lamps per row (one row) case: left wall specular reflection irradiance

$$x > r \parallel x < -r$$

Summation of the total direct emissive irradiance from the two virtual UV lamps

$$z > L - L_3 - L_1 \begin{cases} y > 3L/4 + L_2/2 + r \\ y < 3L/4 + L_2/2 + r \end{cases}$$

Total direct irradiance from lamp #2' cy2  
No specular reflection irradiance from the lamp #1' and lamp #2'  
Total direct irradiance from lamp #2' cy2, lamp #2' cy3, lamp #2' circle1, lamp #2' circle2, lamp1' cy3 and partial lamp #1' cy2 ( $\frac{z_{light}}{L_1} I_{lamp\#1'cy2}$ ), where

$$y > 3L/4 + L_2/2 + r$$

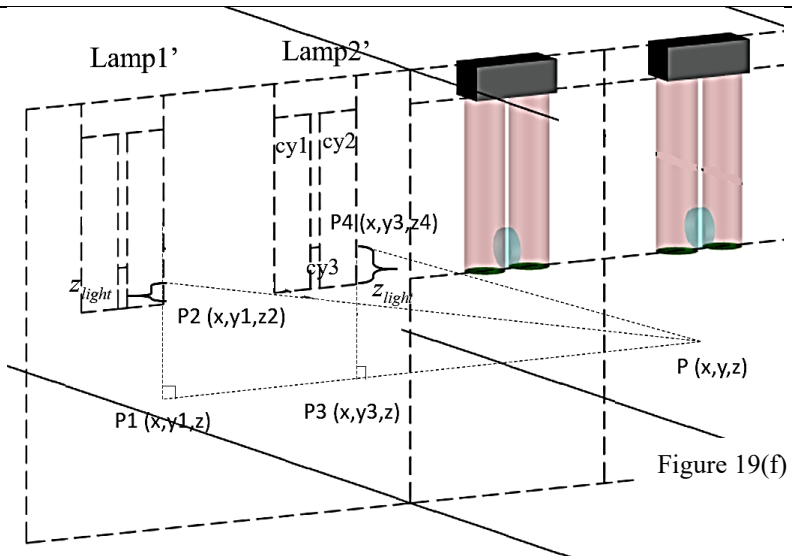
$z_{light} = (L - L_3 - L_1 - z) \times \frac{L/2 - L_2 - 4r}{5L/4 + L_2/2 + 2r - y}$  for  $L - L_3 - L_1 < z_2 < L - L_3$  and  $z_{light} = L_1$  for  $z_2 > L - L_3$

$$-r < x < r$$

$$z < L - L_3 - L_1$$

Full direct irradiance from lamp2' cy3, lamp1' cy3, lamp2' circle1 and 2, lamp2' circle1 and 2, partial lamp1' cy2 ( $\frac{z_{light}}{L_1} I_{lamp\#1'cy2}$ ), where

$$y < 3L/4 + L_2/2 + r$$



$$z_{light} = (L - L_3 - L_1 - z) \times \frac{L/2 - L_2 - 4r}{5L/4 + L_2/2 + 2r - y} \text{ for } L - L_3 - L_1 < z_2 < L - L_3 \text{ and}$$

$$z_{light} = L_1 \text{ for } z_2 > L - L_3 \text{ and partial lamp2' cy2 } \left( \frac{z_{light}}{L_1} I_{lamp\#2',cy2} \right), \text{ where}$$

$$z_{light} = (L - L_3 - L_1 - z) \times \frac{L/2 - L_2 - 4r}{3L/4 + L_2/2 + 2r - y} \text{ for } L - L_3 - L_1 < z_4 < L - L_3 \text{ and}$$

$$z_{light} = L_1 \text{ for } z_4 > L - L_3$$

Two lamps per row (one row) case: right wall specular reflection irradiance has the symmetrical distribution as the left wall specular reflection irradiance

Two lamps per row (one row) case: top wall specular reflection irradiance is the summation of the total direct emissive irradiance from the two virtual UV lamps

Two lamps per row (one row) case: bottom wall specular reflection irradiance is the summation of the total direct emissive irradiance from the two virtual UV lamps

Two lamps per row (one row) case: diffuse reflection irradiance is the summation of the diffuse reflection irradiance from the two UV lamps

One lamp per row (two rows) case: Direct emissive irradiance

$$|x| < L_{10} - r$$

$L_{10}$  is the distance between the center of lamp1 and the mid of lamp1 and lamp2 along the x-axis

Summation of the total direct emissive irradiance from the two UV lamps.

Note: for the region between the two cylinders of the UV lamp1 or lamp2, which only receives the direct emissive from the two cylinders without the contributions from lamp2 or lamp1 due to the narrowed gap (significant shadowing effects).

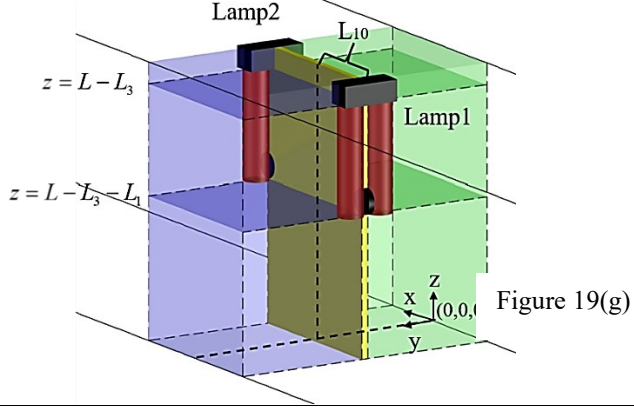


Figure 19(g)

$|x| > L_{10} - r$  : Fraction of  $z$  blocked by cylinders #1 and #2 (the viewpoint P is either vertically within the lamp length or below the lamp).

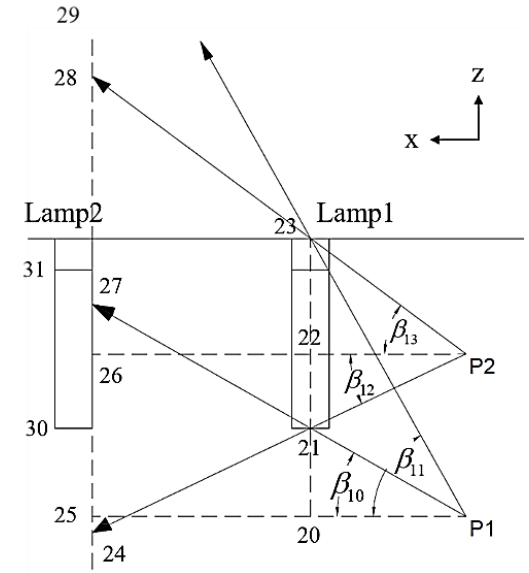


Figure 19(h)

$$z_{27} = z_{P1} + \frac{L_{20\_21} \times L_{P1\_25}}{L_{P1\_20}}$$

$$z_{24} = z_{P2} - \frac{L_{21\_22} \times L_{P2\_26}}{L_{P2\_22}}$$

$z_{28}$  and  $z_{29}$  are consistently above the top of the duct.

$$\begin{aligned} z_P < z_{30}; z_{30} < z_{27} < z_{31} \\ l_{z\_cyl1cyl2\_block} &= L_{31\_27} \end{aligned} \quad (29)$$

$$\begin{aligned} z_P < z_{30}; z_{27} > z_{31} \\ l_{z\_cyl1cyl2\_block} &= 0 \end{aligned} \quad (30)$$

$$\begin{aligned} z_P > z_{30} \\ l_{z\_cyl1cyl2\_block} &= L_{cylinder} \end{aligned} \quad (31)$$

$|x| > L_{10} - r$  : Fraction of  $z$  block by cylinder #3 (the viewpoint P is vertically below the UV lamp). For other cases, refer to Supplementary Material Table S4.

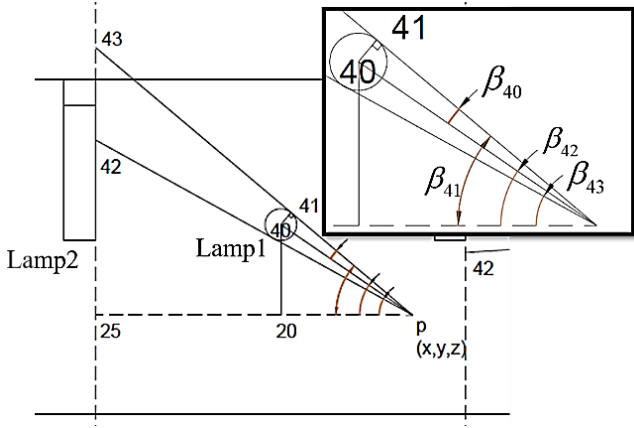


Figure 19(i)

$$(a) : z_{42} = z + (x_{25} - x) \tan \left( \arctan \left( \frac{z_{40} - z}{x_{20} - x} \right) - \arcsin \left( \frac{r_{cylinder}}{\sqrt{(x_{40} - x)^2 + (z_{40} - z)^2}} \right) \right)$$

$$z_{43} = z + (x_{25} - x) \tan \left( \arctan \left( \frac{z_{40} - z}{x_{20} - x} \right) + \arcsin \left( \frac{r_{cylinder}}{\sqrt{(x_{40} - x)^2 + (z_{40} - z)^2}} \right) \right)$$

$$z_{42} > z_{31} \quad (32)$$

$$l_{z\_cy3\_block} = 0$$

$$z_{30} < z_{42} < z_{31}; z_{43} > z_{31}$$

$$l_{z\_cy3\_block} = L_{31\_42} \quad (33)$$

$$z_{30} < z_{42} < z_{31}; z_{30} < z_{43} < z_{31}$$

$$l_{z\_cy3\_block} = L_{43\_42} \quad (34)$$

$|x| > L_0 - r$  : Fraction of y block by cylinders #1 and #2 (the viewpoint P is on the right side of the lamp1). For other cases, refer to Supplementary Material Table S4.

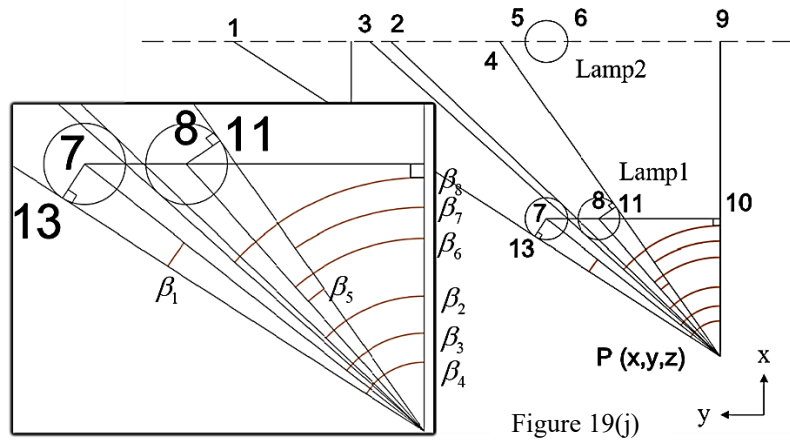


Figure 19(j)

$$\beta_1 = \arcsin \left( \frac{r_{cylinder}}{\sqrt{(x_7 - x)^2 + (y_7 - y)^2}} \right); \quad y_1 = y_4 > y_5 : l_{y\_block} = 0$$

$$\beta_3 = \arctan \left( \frac{abs(y_7 - y)}{abs(x_7 - x)} \right); \quad y_2 = y_6 < y_4 < y_5; y_3 > y_5 : l_{y\_block} = L_{4\_5}$$

$$\beta_4 = \beta_1 + \beta_3; \quad \beta_2 = \beta_3 - \beta_1; \quad y_3 = y_4 < y_6; y_3 > y_5 : l_{y\_block} = d_{cylinder}$$

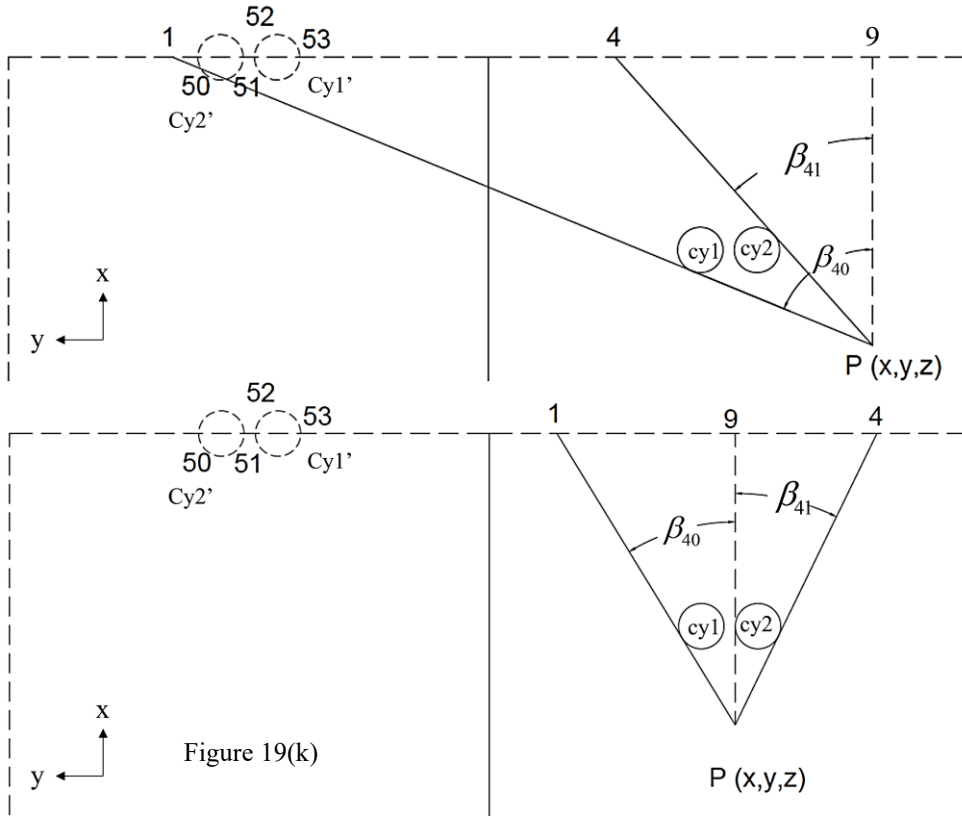
$$\beta_5 = \arcsin \left( \frac{r_{cylinder}}{\sqrt{(x_8 - x)^2 + (y_8 - y)^2}} \right); \quad l_{y\_block} = L_{3\_6}$$

$$\beta_6 = \arctan \left( \frac{abs(y_8 - y)}{abs(x_8 - x)} \right); \quad y_4 < y_6; y_3 < y_6; y_2 > y_5 : l_{y\_block} = 0$$

$$\beta_7 = \beta_6 - \beta_5; \quad \beta_8 = \beta_6 + \beta_5;$$

(35)

One lamp per row (two rows) case: left wall specular reflection irradiance



$$\begin{aligned}
 y_1 &= y + (x_{lamp2} - x) \tan \beta_{40} \\
 y_4 &= y + (x_{lamp2} - x) \tan \beta_{41} \\
 y_4 > y_{50} : l_{y\_block\_cy2'} &= 0 \& l_{y\_block\_cy1'} = 0 \\
 y_{50} < y_4 < y_{51}, y_1 > y_{50} : l_{y\_block\_cy2'} &= L_{50-4} \& l_{y\_block\_cy1'} = 0 \\
 y_{51} < y_4 < y_{52}, y_1 > y_{50} : l_{y\_block\_cy2'} &= d_{cylinder} \& l_{y\_block\_cy1'} = 0 \\
 y_{53} < y_4 < y_{52}, y_1 > y_{50} : l_{y\_block\_cy2'} &= d_{cylinder} \& l_{y\_block\_cy1'} = L_{52-4} \\
 y_{53} < y_4 < y_{52}, y_{50} < y_1 < y_{51} : l_{y\_block\_cy2'} &= L_{1-51} \& l_{y\_block\_cy1'} = L_{52-4} \\
 y_4 < y_{53}, y_1 > y_{50} : l_{y\_block\_cy2'} &= d_{cylinder} \& l_{y\_block\_cy1'} = d_{cylinder} \\
 y_4 < y_{53}, y_{50} < y_1 < y_{51} : l_{y\_block\_cy2'} &= L_{1-51} \& l_{y\_block\_cy1'} = d_{cylinder} \\
 y_4 < y_{53}, y_{51} < y_1 < y_{52} : l_{y\_block\_cy2'} &= 0 \& l_{y\_block\_cy1'} = d_{cylinder} \\
 y_4 < y_{53}, y_{52} < y_1 < y_{53} : l_{y\_block\_cy2'} &= 0 \& l_{y\_block\_cy1'} = L_{1-53} \\
 y_1 < y_{53} : l_{y\_block\_cy2'} &= 0 \& l_{y\_block\_cy1'} = 0
 \end{aligned}$$

(36)

One lamp per row (two rows) case: right wall specular reflection irradiance has the symmetrical distribution as the left wall specular reflection irradiance

One lamp per row (two rows) case: top wall specular reflection irradiance is the summation of the total direct emissive irradiance from the two virtual UV lamps

One lamp per row (two rows) case: bottom wall specular reflection irradiance is the summation of the total direct emissive irradiance from the two virtual UV lamps

One lamps per row (two rows) case: diffuse reflection irradiance is the summation of the diffuse reflection irradiance from the two UV lamps

## 4.2 UV dose and inactivation efficiency simulation

### 4.2.1 CFD models for UV dose estimation

CFD simulations were conducted to obtain the detailed flow field and track the bioaerosol trajectories within the duct. Further, combining the computed in-duct spatial irradiance distribution (using the mathematical model from Section 4.1), the average accumulated UV dose at the duct outlet and the corresponding UVGI disinfection efficiencies can be calculated.

The Eulerian-Lagrangian method was used to model the transport of air and airborne microorganisms, and the CFD model used in this research has been widely used and validated in other previous studies in the literature [144]. The steady state conservation equations of mass and momentum have the forms:

$$\nabla \cdot (\rho \vec{u}) = S_m \quad (37a)$$

$$\nabla \cdot (\rho \vec{u} \vec{u}) = -\nabla p + \nabla \cdot (\vec{\tau}) + \rho \vec{g} + \vec{F}$$
$$\text{where } \vec{\tau} = \mu \left[ \left( \nabla \vec{u} + \nabla \vec{u}^T \right) - \frac{2}{3} \nabla \cdot \vec{u} I_{unit} \right] \quad (37b)$$

where  $\rho$ ,  $\vec{u}$ ,  $S_m$ ,  $p$ ,  $\vec{\tau}$ ,  $\rho \vec{g}$ ,  $\vec{F}$ ,  $\mu$ , and  $I_{unit}$  denote air density, air velocity, source term, static pressure, stress tensor, gravitational body force, external body forces, molecular viscosity, and unit tensor, respectively. In addition, realizable k- $\varepsilon$  model was employed to close the governing equations [145]:

$$\begin{aligned}
\frac{\partial}{\partial x_j} (\rho k_{turbulent} u_j) &= \frac{\partial}{\partial x_j} \left[ \left( \mu + \frac{\mu_t}{\sigma_k} \right) \frac{\partial k_{turbulent}}{\partial x_j} \right] + G_k + G_b - \rho \varepsilon_t - Y_M + S_k \\
\frac{\partial}{\partial x_j} (\rho \varepsilon_t u_j) &= \frac{\partial}{\partial x_j} \left[ \left( \mu + \frac{\mu_t}{\sigma_{\varepsilon_t}} \right) \frac{\partial \varepsilon_t}{\partial x_j} \right] + \rho C_1 S \varepsilon_t - \rho C_2 \frac{\varepsilon_t^2}{k_{turbulent} + \sqrt{\nu \varepsilon_t}} + C_{1\varepsilon_t} \frac{\varepsilon_t}{k_{turbulent}} C_{3\varepsilon_t} G_b + S_{\varepsilon_t} \\
\text{where } C_1 &= \max \left[ 0.43, \frac{\eta}{\eta + 5} \right], \quad \eta = S \frac{k_{turbulent}}{\varepsilon_t}, \quad S = \sqrt{2 S_{ij} S_{ij}}
\end{aligned}
\tag{38}$$

where  $k_{turbulent}$ ,  $\varepsilon_t$ ,  $u_j$ ,  $\mu$ ,  $\mu_t$ ,  $G_k$ ,  $G_b$ ,  $Y_M$ ,  $S_k$ , and  $S_\varepsilon$  are the turbulent kinetic energy, turbulent dissipation rate, velocity, molecular viscosity, turbulent viscosity, generation of turbulence kinetic energy due to the mean velocity gradients, generation of turbulence kinetic energy due to buoyancy, contribution of the fluctuating dilatation in compressible turbulence to the overall dissipation rate, source term for  $k_{turbulent}$ , and source term for  $\varepsilon_t$ . And  $C_{1\varepsilon_t} = 1.44$ ,  $C_2 = 1.9$ ,  $C_{3\varepsilon_t} = -0.33$ ,  $\sigma_k = 1.0$ ,  $\sigma_{\varepsilon_t} = 1.2$ . Once the flow field is solved, the routes of pathogen carriers are computed by discrete phase modeling (DPM) on the base of the obtained flow map. Each pathogenic particle trajectory is calculated in the Lagrangian reference frame as [68]:

$$\begin{aligned}
\frac{d\vec{u}_p}{dt} &= D_p (\vec{u}_f - \vec{u}_p) + \frac{\vec{g} (\rho_p - \rho_f)}{\rho_p} + \vec{F}_a \\
D_p &= \frac{18\mu}{\rho_p d_p^2} \frac{C_D \text{Re}}{24}
\end{aligned}
\tag{39}$$

where  $u$  is the fluid phase velocity,  $u_p$  is the particle velocity,  $\mu$  is the molecular viscosity of the fluid,  $\rho$  is the fluid density,  $\rho_p$  is the density of the particle,  $d_p$  is the particle diameter,  $D_p (\vec{u}_f - \vec{u}_p)$  is the drag force per unit particle mass of which  $C_D$  is the drag

coefficient, Re is the relative Reynolds number, and  $\overline{F_a}$  is the additional forces such as the thermophoretic force, Saffman's lift force, Brownian force, which are neglected here [145–147]. The steady particle tracking was conducted with the maximum number of time steps as 50,000 to avoid termination of particles' tracking too early before reaching the walls or outlet. With the known bioaerosols trajectories and spatial irradiance distributions inside the duct, the accumulative UV dose for each particle and the average accumulative UV dose of all the tracked particles (arithmetic mean) at the duct outlet were given as [148]:

$$D_{UV} = \sum_{i=1}^{i=n_t} \frac{dt \times (I_i + I_{i+1})}{2} \quad (40a)$$

$$\overline{D_{UV}} = \frac{\sum_i^N D_{UV}}{N} \quad (40b)$$

where dt is the time interval,  $n_t$  is the number of total time steps that a particle moves from the inlet (start of UV illumination) to the outlet (end of UV illumination) of the duct,  $I_i$  and  $I_{i+1}$  are the UV intensities in the computational cell at the beginning and end of the time step, and N is the total bioaerosol particles in the UVGI system, respectively.

#### 4.2.2 UV rate constant calculation

With the average cumulative UV dose of the in-duct UVGI system known, combined with the experimentally obtained disinfection efficiencies under different UV doses (under different air velocities in this research), the UV rate constant for an airborne microorganism can be estimated as:

$$k = -\frac{\ln(1 - \eta_{\text{experiment}})}{D_{UV}} \quad (41)$$

where  $k$  is the microorganism-specific UV rate constant ( $\text{m}^2/\text{J}$ ) upon the UV irradiation. On the other hand, if the  $k$  is and  $\overline{D_{UV}}$  of a UVGI system are known, the average UV inactivation efficiency of the system can be predicted as:

$$\eta_{prediction} = 1 - e^{-k\overline{D_{UV}}} \quad (42)$$

### 4.2.3 Numerical methodology

Based on the design of the ductwork for the in-duct UVGI system, the structured mesh was generated for the effective UVGI reactor region ( $1.16\text{m} \times 0.127\text{m} \times 0.127\text{m}$ , length from the mixing baffle to the downstream sampling port) using ANSYS ICEM 19.2. Three grid resolutions, 126k (coarse), 273k (medium), and 501k (fine), were generated for the mesh independence test, and the grid convergence index (GCI) was tested for the average air velocity and average irradiance at the outlet plane for operating condition #3 (Table 7). The calculated GCIs (Table 13) with safety factor ( $F_s=1.25$ ) were within 5%, and the refinement was in the asymptotic range of convergence ( $\approx 1$ ). Thus, the grid convergence was reached, and the medium mesh (273k) was adopted to reduce the calculation time while ensuring accurate results, and the numerical grid is shown in Figure 20.

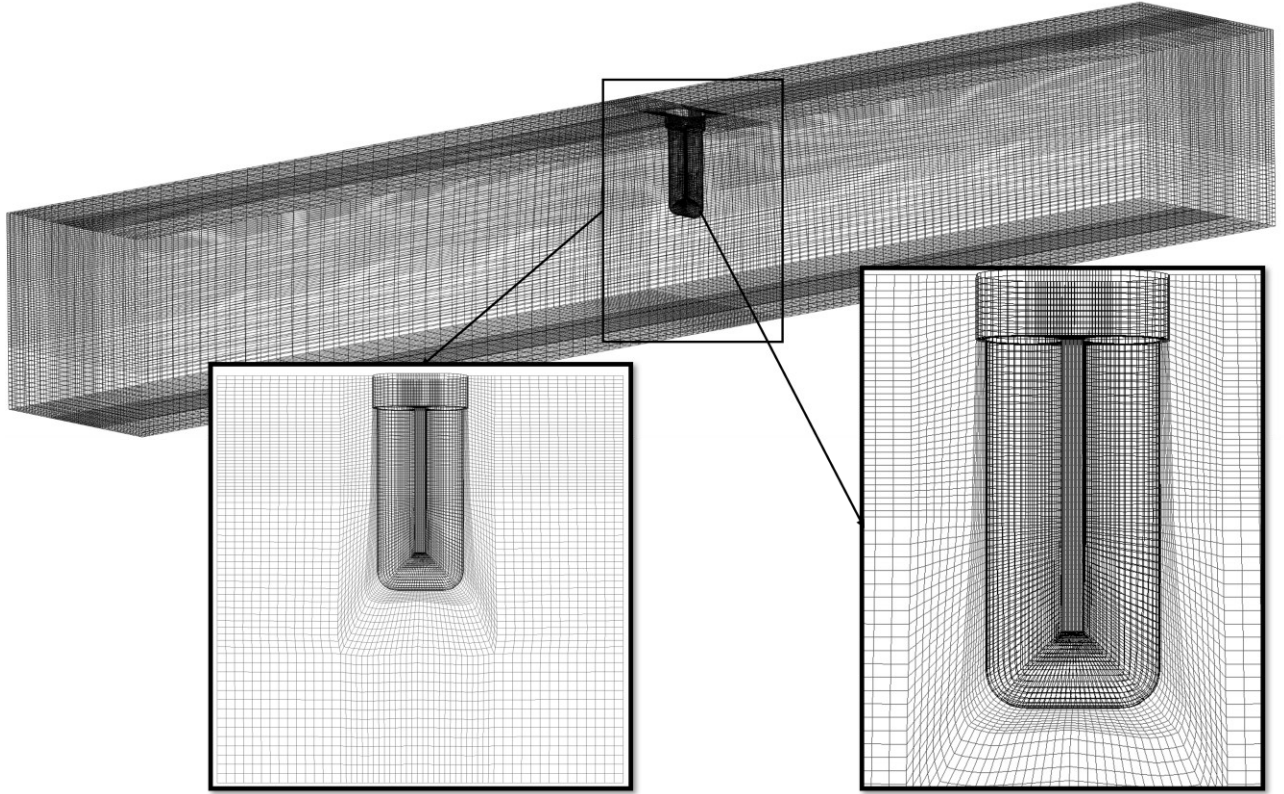


Figure 20 Numerical grid of the in-duct UVGI system with a single lamp

Table 13 Mesh independence test

Mesh	Number of mesh elements	Grid independence analysis for the average velocity at the outlet			
		Average velocity (m/s)	Order of convergence (p)	Grid convergence index (GCI)	Asymptotic range of convergence
Fine (1)	501k	1.3504		-	
Medium (2)	273k	1.3494	1.74	0.040%	0.9982
Coarse (3)	126k	1.3497		0.012%	
Mesh	Number of mesh elements	Grid independence analysis for average incident radiation at the outlet			
		Incident radiation (W/m <sup>2</sup> )	Order of convergence (p)	Grid convergence index (GCI)	Asymptotic range of convergence
Fine (1)	501k	3.2191		-	
Medium (2)	273k	3.1423	1.76	1.280%	1.0142
Coarse (3)	126k	3.1201		0.373%	

Calculating example for average velocity:

$$r = \frac{\Delta x_3}{\Delta x_2} = \frac{\Delta x_2}{\Delta x_1} = 2; \quad p = \ln \left( \frac{\overline{v_3 - v_2}}{\overline{v_2 - v_1}} \right) / \ln r; \quad GCI_{2,3} = \frac{F_s \left| \frac{\overline{v_2 - v_3}}{\overline{v_2}} \right|}{r^p - 1}; \quad \text{asymptotic convergence: } \frac{GCI_{2,3}}{r^p GCI_{1,2}} \approx 1$$

The in-duct airflow field was obtained by solving the continuity, momentum, and turbulence equations. Subsequently, the air velocity was monitored at the center of the duct, and the simulation stopped once a converged flow field was obtained. The trajectory of the airborne particles was then obtained by integrating the Lagrangian force balance equations (Eq. (38)) based on the computational airflow field [149]. The spatial irradiance within each numerical grid cell was calculated using the view factor model implemented into the ANSYS Fluent solver as a user-defined function (UDF, example see in Appendix B). Finally, the accumulated UV dose received by each particle as it passed through the UV field and the corresponding UVGI inactivation efficiency were calculated using the ANSYS Fluent solver by implementing Eqs. (39) – (40) as UDFs. The UDF codes for the UV irradiance model and UV dose calculation were included in Appendix C.

In detail, the steady-state CFD simulations with steady particle tracking were conducted. The airflow was assumed to be isothermal, with turbulence approximated using the realizable k-epsilon model with standard wall functions [70,72,149]. For the airflow boundary conditions, supply air was introduced at the inlet at the prescribed inlet velocity according to the experimental conditions (Table 7). The outlet was set as the outflow, and all the other walls were set as stationary walls with no-slip boundary conditions.

With respect to the DPM particle tracking, one thing to be noted is that the simulated bioaerosols have particle sizes ranging from 0.65 – 7  $\mu\text{m}$  and 0.65 – 2.1  $\mu\text{m}$  for airborne *MS2* and *E. coli*, respectively. Therefore, preliminary CFD simulations with different bioaerosol particle sizes were conducted to determine how variations in particle size impact the average accumulative UV dose at the UVGI reactor outlet (details see in Appendix D). The results (Table D1) indicate that variations in particle size within the submicrometer

scale ( $< 10 \mu\text{m}$ ) have a minimal effect, accounting for less than 5.1% of the average accumulative UV dose at the UVGI reactor outlet. Thus, the bioaerosols were treated as liquid droplets with a representative diameter of  $1 \mu\text{m}$  and were injected at the duct inlet with a total of 11250 injection particles for each CFD simulation. Furthermore, for the particle tracking boundary conditions, the duct inlet and outlet were set as “escaped,” and all other boundaries, including the duct walls and UV lamp walls, were set as “trapped”, respectively.

## 4.3 Model validations

### 4.3.1 UV irradiance model

#### 4.3.1.1.1 Lamp output prediction: r method

As we mentioned before, the dimensionless  $r$  contains the characteristics of both UV lamps and the duct airflow field. Thus, it is expected that the  $r$  remains the same for the same type of lamps (single cylinder, twin tube, etc.) with different dimensions that are working under the same ventilation conditions. To verify the hypothesis, we selected three studies in the literature that conducted UVGI tests under similar ventilation conditions [19,97,99] and compared their calculated  $r$  by using Eqs. (11) – (14). Then, to verify the predicted lamp output using the  $r$  method, we extracted the  $r$  of a twin-tube UV lamp from the study of Lau et al. [19] and reversely calculated the lamp surface temperature of the twin-tube UV lamp that is used in this research, and compared the measured the lamp surface temperature with the prediction.

For validating  $r$ , three studies in the literature [19,97,99] with two types of UV lamps under two types of convection scenarios were compared (Figure 21). It is observed that the lamp

surface temperature varies significantly with different lamp characteristics (lamp length, diameter, power input, and UVC output) even under the same ventilation conditions, resulting in lamp output variation. However, the convective heat loss ratio  $r_Q$  remains constant among different studies under the same operating conditions (variations from 0.03% to 7.04%). This result is reasonable, as the ratio  $r_Q$  is a dimensionless parameter that incorporates the lamp shape and working power. Furthermore, the ratio  $r_Q$  is much larger for a lamp operating under forced convection (Figures 21(b) and 21(c)) than for that under mixed convection (Figure 21(a)), which indicates more substantial convective heat transfer. This observation is confirmed by the higher lamp surface temperature in Figure 21(a), which shows that overheating is an issue for mixed convection, whereas the wind-chill effects are dominant for forced convection (Figures 21(b) and 21(c)). However, uncertainty may arise when applying the  $r$  method correlating lamps from different manufacturers, as the  $r$  difference in Figures 21(a) and 21(b) (one lamp from Philips and one lamp from Steril-Aire) is higher than that in Figure 21(c) (both lamps are from Philips). Overall, it is promising to bridge the performance of the same type of UV lamps by the ratio  $r_Q$ . In other words, for each type of UV lamp, once the convective heat loss ratio  $r_Q$  under different operating conditions is experimentally or numerically determined, variations in lamp characteristics (diameter, length, and power) can easily be converted to the new  $T_s$  using Eq. (15). Thus, the corresponding performance of each type of lamp can be estimated using the manufacturer's technical data.

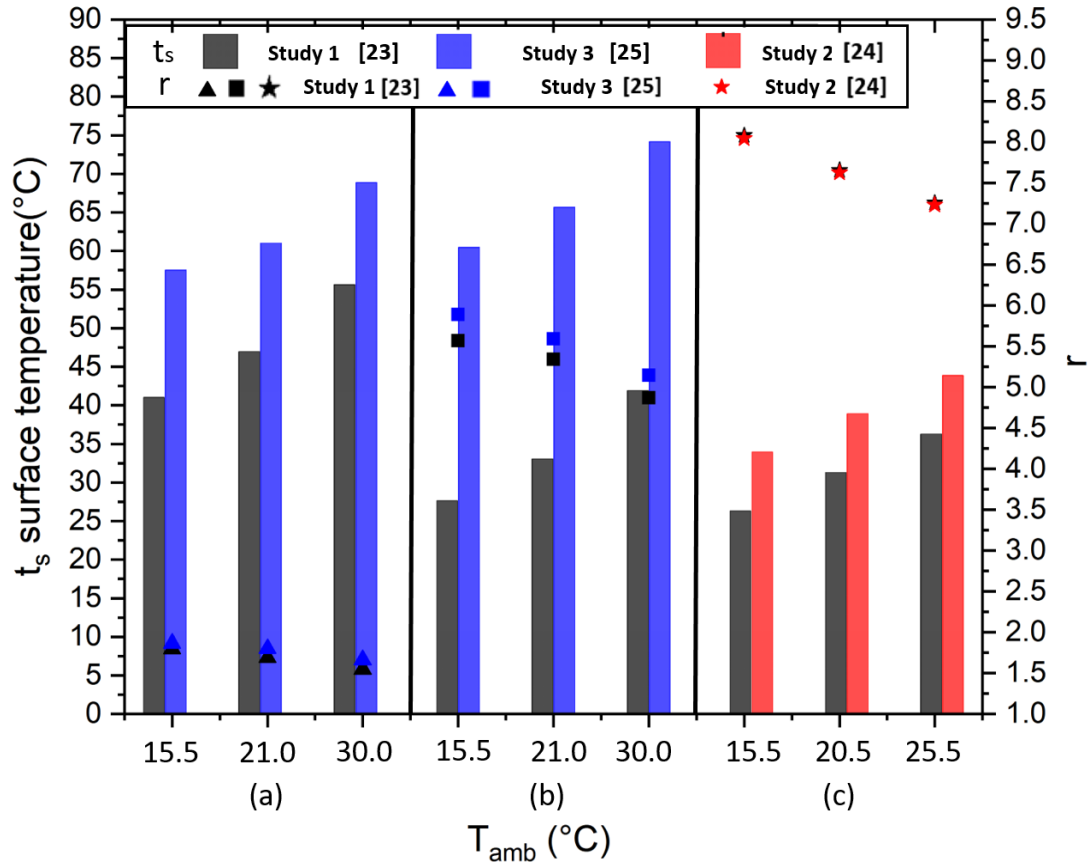


Figure 21 Predicted lamp surface temperature and convective heat loss ratio  $r_Q$  for (a) mixed convection ( $U = 0.31$  m/s) with lamp type 1; (b) forced convection ( $U = 2.5$  m/s) with lamp type 1; and (c) forced convection ( $U = 3$  m/s) with lamp type 2

(Note: (a) Study 1: Cylindrical hot cathode (Philips TUV 25W) with  $L = 437$ mm,  $D = 28$ mm,  $P_{input} = 25$ W, and  $P_{UVCoutput} = 7$ W; Study 3: Cylindrical hot cathode (GTS 24 VO, P/N 21000300) with  $L = 610$ mm,  $D = 16$ mm,  $P_{input} = 70$ W, and  $P_{UVCoutput} = 24$ W; (b) Study 1: Cylindrical hot cathode (Philips TUV 25W) with  $L = 437$ mm,  $D = 28$ mm,  $P_{input} = 25$ W, and  $P_{UVCoutput} = 7$ W; Study 3: Cylindrical hot cathode (GTS 24 VO, P/N 21000300) with  $L = 610$ mm,  $D = 16$ mm,  $P_{input} = 70$ W, and  $P_{UVCoutput} = 24$ W; (c) Study 1: Twin tube hot cathode (Philips TUV PLL 60W 4P/HO) with  $L = 385$ mm,  $D = 18$ mm,

$P_{\text{input}} = 60\text{W}$ , and  $P_{\text{UVCoutput}} = 18\text{W}$ ; Study 2: Twin tube hot cathode (Philips PL-S TUV 9W) with  $L = 120\text{mm}$ ,  $D = 10\text{mm}$ ,  $P_{\text{input}} = 9\text{W}$ , and  $P_{\text{UVCoutput}} = 2.3\text{W}$ )

Then, to examine this hypothesis and validate the predicted  $T_s$ , we extracted the  $r_Q$  for the UV lamp from the Study 1 [19] (Twin tube hot cathode (Philips TUV PLL 60W 4P/HO) with  $L = 385\text{mm}$ ,  $D = 18\text{mm}$ ,  $P_{\text{input}} = 60\text{W}$ , and  $P_{\text{UVCoutput}} = 18\text{W}$ ) under the ventilation conditions of  $1\text{m/s}$  and  $26^\circ\text{C}$  and  $35^\circ\text{C}$ , which were  $2.4391$  and  $2.2372$ , respectively. Implementing the calculated  $r_Q$  into Eq. (15), the lamp surface temperatures of the twin-tube UV lamp in this research (Twin tube hot cathode (OSRAM GCF5DS 5W) with  $L = 51\text{mm}$ ,  $D = 27\text{mm}$ ,  $P_{\text{input}} = 5\text{W}$ , and  $P_{\text{UVCoutput}} = 1.3\text{W}$ ) were estimated as  $35.67^\circ\text{C}$  and  $43.94^\circ\text{C}$ . The predictions agree well with the measured lamp surface temperature as  $34.9^\circ\text{C}$  and  $43.6^\circ\text{C}$ , indicating the applicability of using the  $r$  method to bridge the lamp surface temperature and output for the same types of UV lamps.

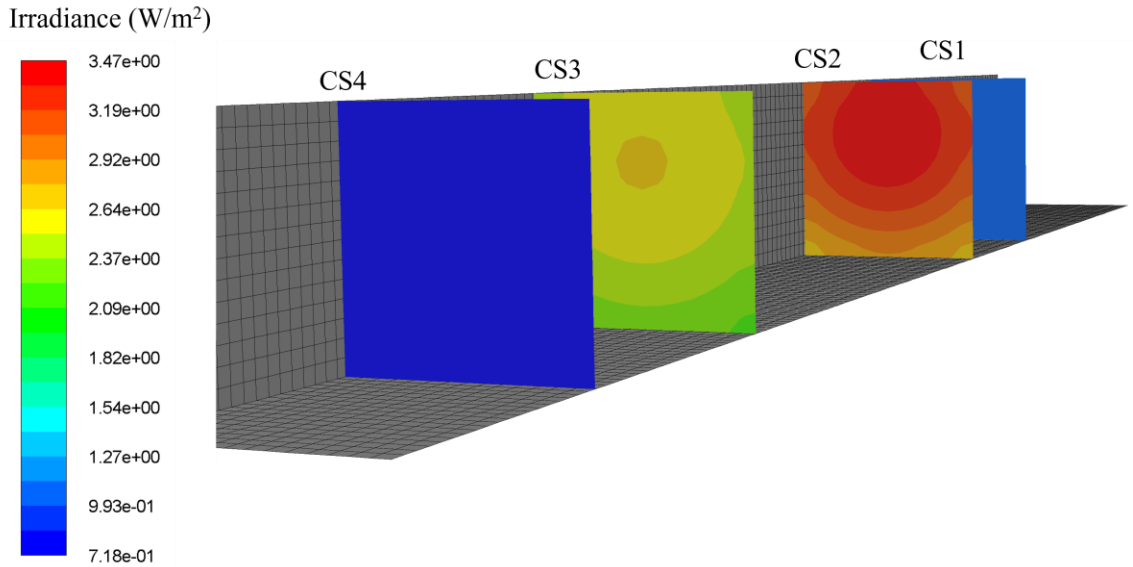
#### 4.3.1.1.2 One-lamp setup with stainless steel duct walls

Initially, the view factor model for the direct emissive irradiation and total irradiation were validated by the measured irradiance for the one-lamp scenario in an open-air environment ( $T: 19.5^\circ\text{C} \pm 2^\circ\text{C}$  and  $\text{RH}: 25\% \pm 5\%$ ) and in-duct environment under  $T (25^\circ\text{C} \pm 0.2^\circ\text{C})$ ,  $U (0.9 \text{ m/s} \pm 0.06 \text{ m/s})$  and  $\text{RH} (40\% \pm 5\%)$ . Using the  $r_Q$  value ( $2.2941$ ) extracted from Study 1 [19] under the temperature of  $25^\circ\text{C}$  and velocity of  $0.9\text{m/s}$ , the output for the twin tube lamp in this research was determined to be around  $94\%$ . Implementing the obtained lamp output into the UV irradiance model, the irradiance distribution inside the duct was estimated.

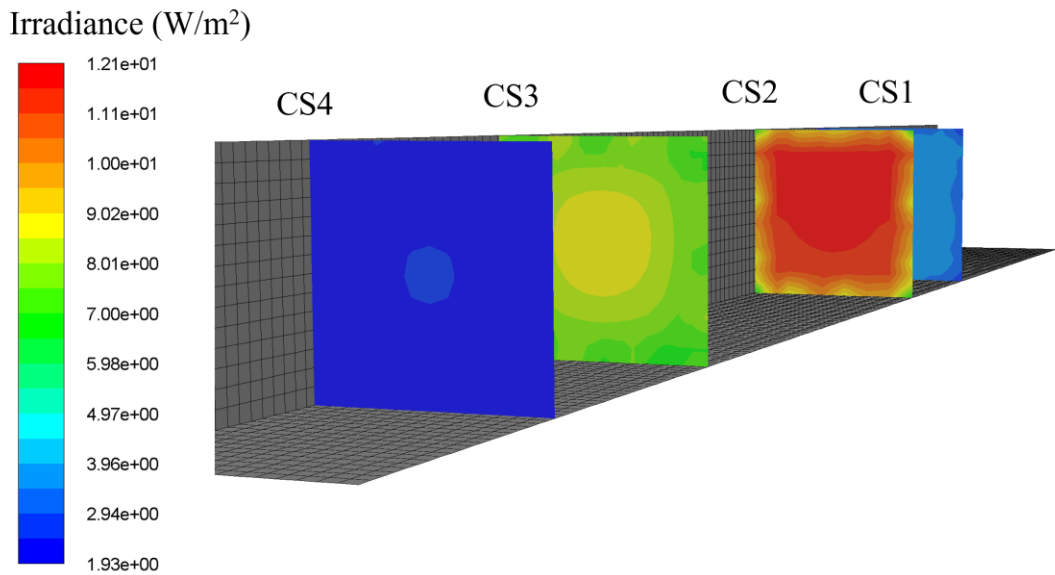
Figure 22(a) shows the contour maps of direct emissive irradiance ( $I_{e,i}$ ) at the four measured cross-sections, demonstrating decreased irradiance with increasing radial distance from the UV lamp, as expected. Despite the gradually decreasing irradiance along the duct length, the spatial distributions within the same cross-section were relatively uniform for direct emissive irradiation from the UV lamp. Comparisons between the experimental data and simulated results for the direct emissive irradiance at 36 points are tabulated in Table 14, demonstrating good agreement (average difference of  $7.2\% \pm 5.0\%$ ). Figures 22(b) and 22(c) show the contour maps of pure specular reflection irradiance ( $I_{rs,i}$ ) and pure diffuse reflection irradiance ( $I_{rd,i}$ ), respectively. The pure specular reflection irradiance demonstrated a significant non-uniform distribution on all cross-sections, in which the irradiance peaked along the z-direction at the center of the duct ( $y=L/2$ ) owing to the superposition of four “virtual images” from the four duct walls. Contrastingly, the pure diffuse reflection irradiance presented a uniform, well-mixed distribution within the duct owing to the diffuse emitting nature of the radiation on the duct walls.

Furthermore, the total irradiance, which includes direct emissive irradiance and specular and diffuse reflection irradiance, was considered. The fractions of specular and diffuse reflections were tested by a trial-and-error method, and the best combination was obtained as 78% and 22% for specular and diffuse reflections, respectively. Figure 22(d) shows the total irradiance field for the four cross-sections. A moderate non-uniformity distribution was observed owing to the high contributions from the natural specular reflection of the mirror-like finish stainless steel. Following the direct emissive irradiance and specular reflection irradiance (two major contributions), the total irradiance contour demonstrated the highest irradiance (ellipse) at the duct center, which decreased with the radial distance

and circumferential area. Table 14 compares the simulation results and experimental data for the total irradiance with a good agreement (average difference:  $8.9\% \pm 6.5\%$ ).

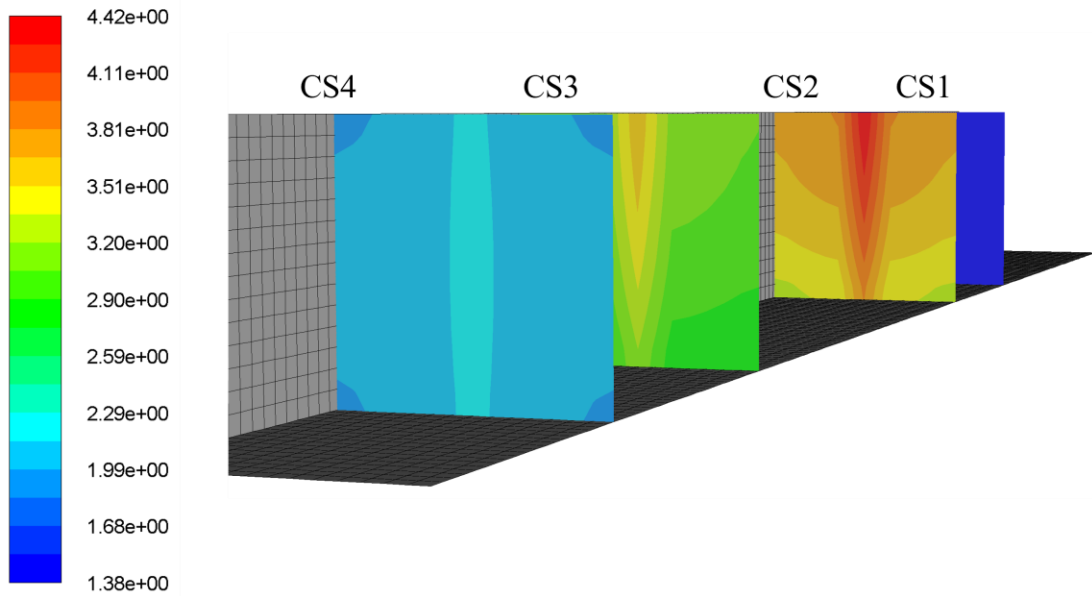


(a) Contour of direct emissive irradiance at the four cross-sections within the duct



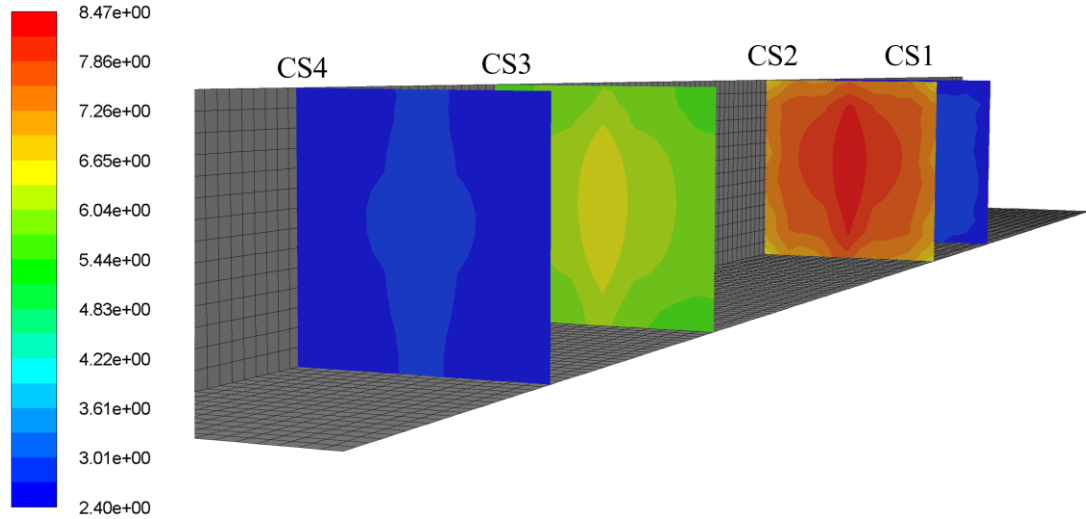
(b) Contour of diffuse reflection irradiance at the four cross-sections within the duct

Irradiance ( $\text{W}/\text{m}^2$ )

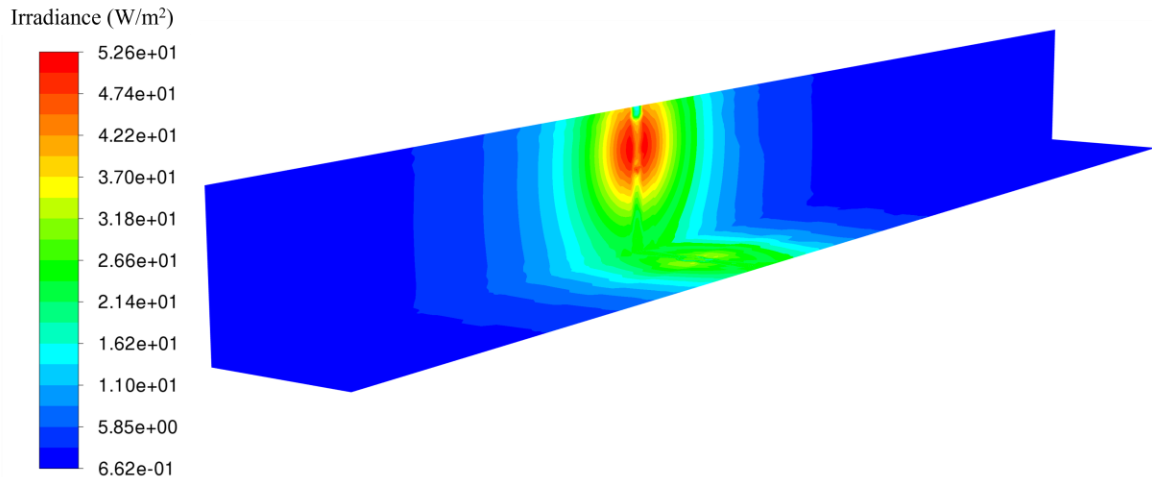


(c) Contour of specular reflection irradiance at the four cross-sections within the duct

Irradiance ( $\text{W}/\text{m}^2$ )



(d) Contour of total irradiance at the four cross-sections within the duct



(e) Contour of total irradiance at the left and bottom walls within the duct

Figure 22 Contours of the numerical results for the irradiance distribution within the stainless steel duct for one lamp

#### 4.3.1.1.3 One-lamp scenario with galvanized steel duct walls

The in-duct irradiance field was measured with a galvanized steel duct enclosure. The direct emissive irradiance remained the same as in the stainless steel case, while the duct reflectivity and the specular and diffuse reflection ratios changed accordingly. The UVC reflectivity of the galvanized steel duct was 0.57, as reported in the literature [11,61,64], while the specular and diffuse reflection fractions were determined to be 22% and 78% through trial-and-error testing. Comparisons of the experimental data and simulation results are tabulated in Table 14, demonstrating good agreement (average difference: 6.9%  $\pm$  3.3%). The total irradiance field is presented in Figure 23, and the distribution is much more uniform than that of the stainless-steel duct owing to the high contributions of the diffuse reflection. Moreover, the average irradiance of the four cross-sections for the galvanized steel (2.72, 5.83, 5.65, and 2.53 W/m<sup>2</sup>) was higher than the stainless steel (2.54,

4.96, 5.03, and 2.41 W/m<sup>2</sup>) even though the duct wall reflectivity is low. This was attributed to the diffusely emitted (reflected) irradiance from the duct walls. Every wall segment contributed to viewpoint P, while for specular reflection, only the emitting irradiance from the “virtual lamp” contributed to viewpoint P, resulting in lower reflected irradiation.

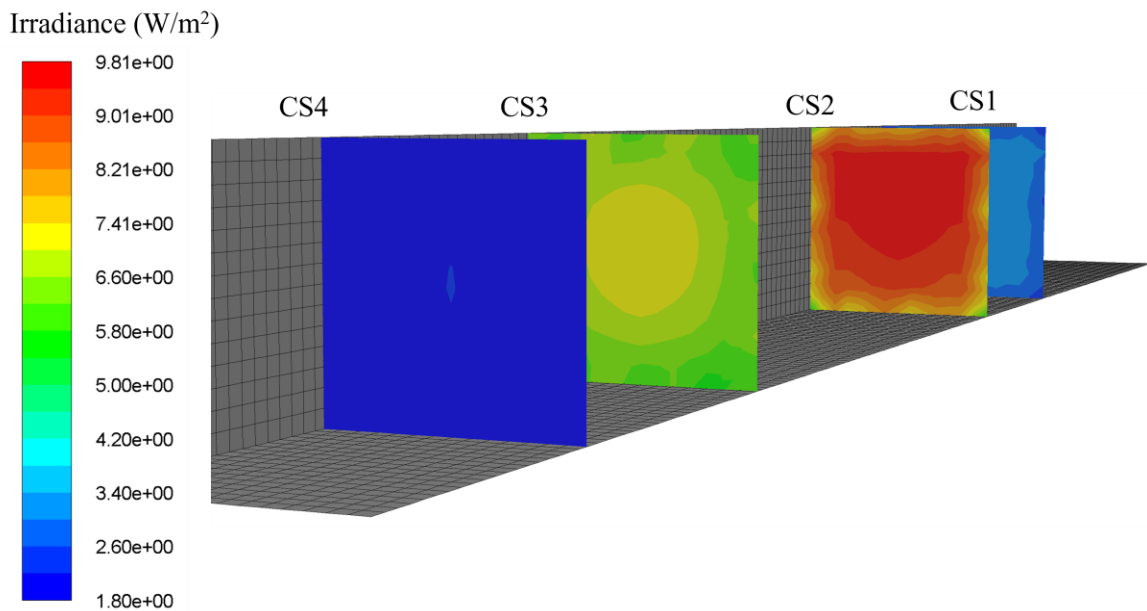


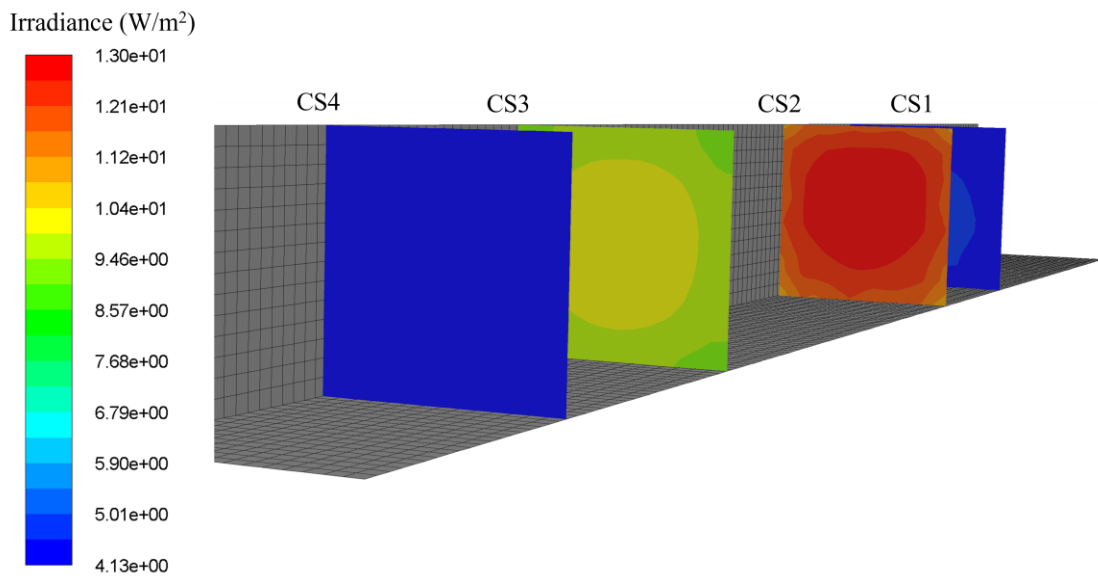
Figure 23 Contour of the numerical results for the total irradiance distribution within the galvanized steel duct for one lamp

#### 4.3.1.1.4 Multiple lamp scenarios with stainless steel duct walls

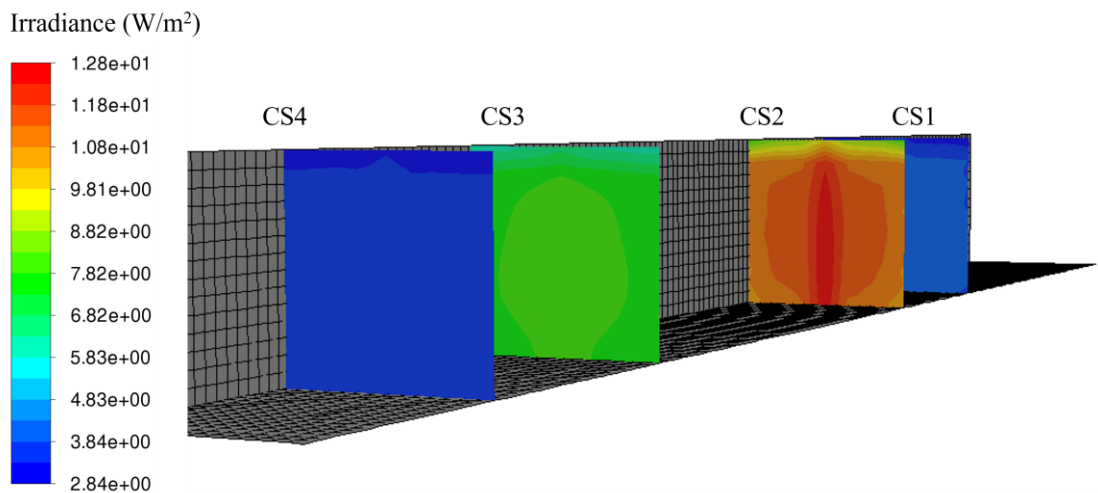
Two lamps per row (one row) and one lamp per row (two rows) were constructed with stainless steel plates. Thus, the total irradiance fields were computed by implementing the reflectivity and the ratios of the specular (0.75) and diffuse (0.25) reflections. Table 14 presents the comparisons of the experimental data and simulation results for the two multiple-lamp scenarios demonstrating good agreement (average differences of 10.5% ± 14.8% and 14.6% ± 3.4% for the two lamps per row (one row) and one lamp per row (two rows) cases). Figures 24(a) and 24(b) show the contour maps of these two scenarios, where

a more uniform distribution was observed when two lamps were placed in one row. Figure 24(c) compares the irradiance distributions of cross-section #2 (CS2, location see Figure 8, 19.3 cm away from lamp center) under different duct arrangements. For the stainless steel one-lamp scenario (specular reflection dominates), an apparent ellipse brighter region was observed at the duct center, and the radiation decreased with an increase in the radial distance from the UV lamp. While for the galvanized steel one-lamp scenario (diffuse reflection dominates), the bright region uniformly occupied a more extensive region at the cross-section and decreased when approaching the duct wall, resulting in a higher average irradiance. With respect to the multiple lamp scenarios, placing two lamps in one row provided a relatively uniform radiation distribution with a radial decrease from the duct center bright circle region. The placement of two lamps in two rows (one lamp per row) resulted in three bright elliptical regions located at the duct center and close to the left and right walls. In other words, the irradiance decreased and then increased from the duct center to the left or right wall along the y-direction. The irradiance peaked at the duct center, attributed to the shortest distance between viewpoint P and the three cylinders of UV lamp #1 (lamp in front), and was further contributed by fractions of irradiance from UV lamp #2 (lamp behind) that traveled through the gap between the three cylinders of lamp #1. The high irradiance at the duct walls was due to the fewer shadowing effects between the two lamps. Further, due to more shadowing effects between the two UV lamps for the case of one lamp in two rows, the average irradiance within the duct was smaller as well ( $5.74 \text{ W/m}^2$  compared to  $6.65 \text{ W/m}^2$  for two lamps per row case). However, lamp #1 was placed closer to CS2 in the case of one lamp in two rows compared to lamp #2 (the lamp used for the other three cases), resulting in higher irradiation at CS2, as shown in Figure 24(c), but

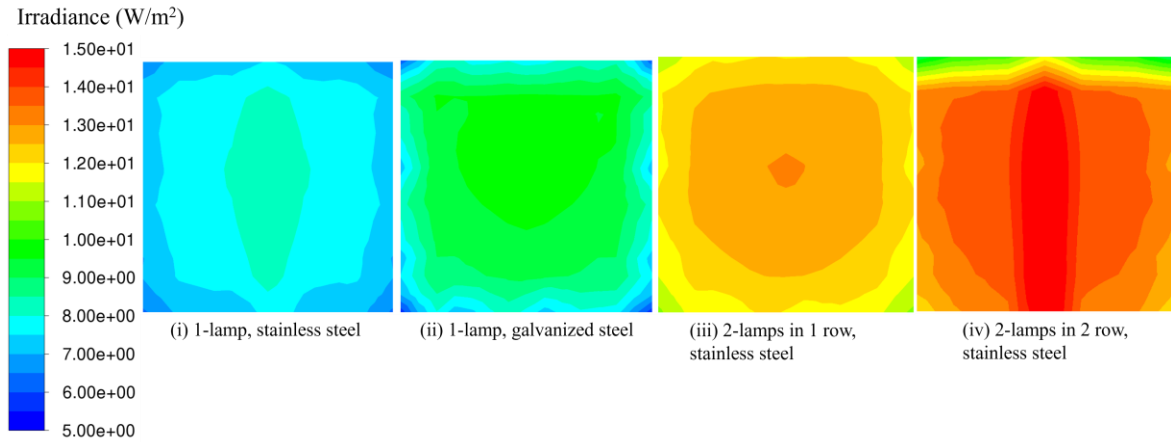
the total average irradiance within the duct was smaller than when two lamps were placed in one row. Finally, the irradiance prediction for the one lamp per row (two rows) case was higher than the experimental data, and the difference was larger than other lamp arrangements, which is attributed to the simplification of shadowing effects (such as the shadowing effects from the top and bottom walls specular reflections were not considered). Therefore, further improvement is required.



(a) Contour of the total irradiance distribution for two lamps per row (one row)



(b) Contour of the total irradiance distribution for one lamp per row (two rows)



(c) Contour of the total irradiance distribution at cross-section 2 for different lamp arrangements

Figure 24 Contours of the numerical results for the cross-sectional total irradiance distributions under different lamp arrangements

Table 14 Comparisons of the model predictions and experimental data of one-lamp with galvanized steel duct walls and multiple lamps with stainless steel duct walls

Total irradiance	CS1			CS2			CS3			CS4		
<b>One lamp at the center, open-air lab environment (direct emissive irradiance)</b>												
Experimental data (W/m <sup>2</sup> )	0.7	0.7	0.7	2.0	2.1	2.0	6.4	8.0	5.9	1.2	1.2	1.2
	0.7	0.7	0.7	2.1	2.3	2.1	6.6	8.2	7.2	1.2	1.2	1.2
	0.7	0.7	0.7	2.0	2.2	2.0	5.3	6.5	6.9	1.2	1.2	1.2
Model predictions (W/m <sup>2</sup> )	0.74	0.75	0.73	1.79	1.91	1.77	6.08	6.43	5.87	1.19	1.20	1.18
	0.74	0.75	0.73	1.79	1.95	1.77	6.09	6.45	5.88	1.19	1.20	1.18
	0.73	0.74	0.73	1.74	1.89	1.72	5.51	5.80	5.34	1.16	1.18	1.16
Differences	5.7%	7.1%	4.3%	10.5%	9.0%	11.5%	5.0%	13.1%	0.5%	0.8%	0.0%	1.7%
	5.7%	7.1%	4.3%	14.8%	15.2%	17.7%	7.7%	14.5%	12.2%	0.8%	4.0%	1.7%
	4.3%	5.7%	2.7%	13.0%	14.1%	14.0%	4.0%	10.8%	12.5%	3.3%	5.6%	3.3%
<b>One lamp at the center, in-duct environment, stainless steel (total irradiance)</b>												
Experimental data (W/m <sup>2</sup> )	2.2	2.7	2.7	4.5	3.9	4.1	10.6	10.9	10.9	3.8	3.8	4.1
	2.2	2.6	2.7	5.3	4.8	4.3	9.9	10.6	10.4	3.4	3.4	4.0
	2.4	2.6	2.6	5.1	4.7	4.3	8.8	9.5	9.3	3.4	3.6	4.0
Model predictions (W/m <sup>2</sup> )	2.06	2.13	2.06	4.57	4.84	4.46	10.42	11.83	10.38	3.16	3.59	3.25
	2.11	2.17	2.14	4.89	4.97	4.71	10.18	11.41	10.40	3.44	3.73	3.42
	2.08	2.15	2.12	4.75	4.88	4.62	9.33	10.49	9.22	3.33	3.68	3.17
Differences	6.4%	21.1%	14.2%	1.6%	24.1%	8.8%	1.7%	8.5%	4.8%	16.8%	5.5%	20.7%
	4.1%	16.5%	10.8%	7.7%	3.5%	9.5%	2.8%	7.6%	0.0%	1.2%	9.7%	14.5%

	13.3%	17.3%	7.8%	6.9%	3.8%	7.4%	6.0%	10.4%	0.9%	2.1%	2.2%	20.8%
<b>One lamp at the center, in-duct environment, galvanized steel (total irradiance)</b>												
Experimental data (W/m <sup>2</sup> )	3.0	2.7	2.6	5.4	5.9	5.5	4.6	5.4	5.4	2.7	2.4	2.3
	3.0	2.7	2.5	5.9	6.1	5.7	4.9	5.5	5.7	2.7	2.5	2.3
	2.8	2.7	2.5	5.3	5.9	5.5	4.9	5.5	5.4	2.5	2.4	2.2
Model predictions (W/m <sup>2</sup> )	3.10	2.70	2.66	5.49	6.19	5.92	4.76	5.90	5.82	2.95	2.65	2.53
	3.18	2.75	2.57	6.43	6.85	6.31	5.29	5.94	6.10	2.89	2.69	2.47
	2.94	2.73	2.31	5.60	6.10	6.16	5.37	5.89	5.84	2.75	2.59	2.51
Differences	3.3%	0.0%	2.3%	1.7%	4.9%	7.6%	3.5%	9.3%	7.8%	9.3%	10.4%	10.0%
	6.0%	1.9%	2.8%	9.0%	12.3%	10.7%	8.0%	8.0%	7.0%	7.0%	7.6%	7.4%
	5.0%	1.1%	7.6%	5.7%	3.4%	12.0%	9.6%	7.1%	8.1%	10.0%	7.9%	14.1%
<b>Two lamps per row (one row), in-duct environment, stainless steel (total irradiance)</b>												
Experimental data (W/m <sup>2</sup> )	4.7	4.4	4.3	9.8	10.0	9.4	9.0	9.2	9.3	4.2	4.0	3.9
	4.9	4.4	4.5	10.3	10.2	9.7	9.2	9.3	10.1	4.4	4.0	4.1
	5.0	4.6	4.6	9.5	9.6	9.1	9.1	9.1	9.5	4.5	4.1	4.1
Model predictions (W/m <sup>2</sup> )	4.81	4.61	4.45	11.2	10.5	11.1	9.9	10.6	10.9	4.32	4.26	3.95
	5.02	4.53	4.68	10.17	11.3	11.2	9.8	12.1	11.4	4.62	4.27	4.21
	5.07	4.72	4.85	9.9	10.9	10.1	10.1	10.5	9.8	4.75	4.65	4.26
Differences	10.2%	12.6%	13.5%	8.5%	14.3%	7.2%	20.1%	17.0%	17.2%	12.6%	14.5%	20.2%
	10.0%	11.9%	12.8%	16.1%	14.7%	8.9%	15.8%	21.0%	17.0%	15.1%	14.1%	15.2%
	12.1%	12.2%	11.6%	13.1%	16.7%	12.3%	17.8%	21.0%	17.5%	16.6%	15.6%	17.7%
<b>One lamp per row (two rows), in-duct environment, stainless steel (total irradiance)</b>												
Experimental data (W/m <sup>2</sup> )	4.8	4.2	4.8	12.3	11.5	11.8	7.4	6.6	7.1	4.3	3.8	4.3
	4.7	4.3	4.7	11.8	11.2	11.8	7.8	6.8	7.3	4.3	3.9	4.2
	4.7	4.6	4.9	10.3	10.3	10.4	7.6	6.8	7.2	4.35	4.1	4.4
Model predictions (W/m <sup>2</sup> )	5.29	4.73	5.45	13.35	13.14	12.65	8.89	7.72	8.32	4.84	4.35	5.17
	5.17	4.81	5.3	13.70	12.85	12.85	9.03	8.23	8.54	4.95	4.45	4.84
	5.27	5.16	5.47	11.65	12.02	11.68	8.95	8.23	8.46	5.07	4.74	5.18
Differences	10.2%	12.6%	13.5%	8.5%	14.3%	7.2%	20.1%	17.0%	17.2%	12.6%	14.5%	20.2%
	10.0%	11.9%	12.8%	16.1%	14.7%	8.9%	15.8%	21.0%	17.0%	15.1%	14.1%	15.2%
	12.1%	12.2%	11.6%	13.1%	16.7%	12.3%	17.8%	21.0%	17.5%	16.6%	15.6%	17.7%

Note: Nine testing points are presented in Figure 8.

### 4.3.2 CFD simulation validation

Despite the CFD models in this research being well-developed and validated in the literature, additional validations for the CFD simulation were conducted. With the airflow field and particle trajectories obtained from the CFD simulations and the in-duct irradiance

field from the view factor model, the cumulative UV dose can be estimated using Eq. (39) - (40). To validate the accuracy of the UV dose computed by CFD simulations, the *E. coli* UV rate constant was obtained using the disinfection efficiency and UV dose correlation (Eq. (41)) in a one-lamp setup under different supply air velocities (operating conditions #1–3) and compared with the data in the literature (Figure 25). Further, the obtained UV rate constant was implemented in the UV doses for the case of different lamp arrangements and wall materials (operating conditions #4–7), and the estimated disinfection efficiencies were compared with the experimental data (Eq. (42)). For the one-lamp setup, the average accumulated UV doses at the duct outlet were 15.37 J/m<sup>2</sup>, 9.21 J/m<sup>2</sup>, and 6.07 J/m<sup>2</sup> for the supply air velocities of 0.5 m/s, 0.9 m/s, and 1.35 m/s, respectively. By incorporating the corresponding *E. coli* disinfection efficiencies of 99.98%, 98.36%, and 95.60% (Table 11), the UV rate constant  $k$  was obtained by regression analysis [22,23,96] as 0.5245 m<sup>2</sup>/J under environmental conditions of T (25°C) and RH (40%). By plotting the  $k$  value in this study and the *E. coli* UV rate constant data in the literature (with the x-axis as the humidity ratio) [150–155], good agreement was observed, and an increase in the UV rate constant was observed with a decrease in the humidity ratio.

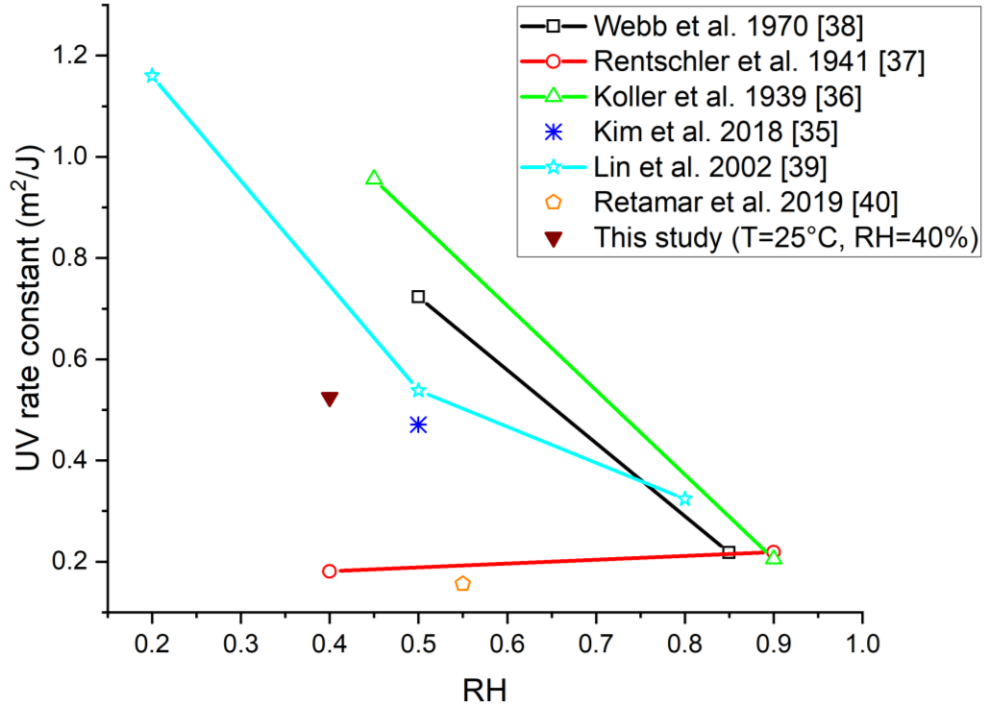


Figure 25 Comparison of the UV rate constant for airborne *E. coli* in this study and literature

Further incorporating the obtained UV rate constant ( $0.5245 \text{ m}^2/\text{J}$ ) into the predicted UV dose of operating conditions #4-6 (14.26, 12.79, and  $8.97 \text{ J/m}^2$  for two lamps per row (one row), one lamp per row (two rows) and 1 lamp at center with galvanized steel), we have the *E. coli* disinfection efficiencies of 99.79%, 99.61%, and 97.97%, demonstrating good agreement with the experimental data (Table 11, 99.81%, 99.59% and 97.25%) with an error of 0.02%, 0.02% and 0.72%. Thus, both the UV irradiance and UV dose predictions from the CFD simulation agreed well with the experimental data and can be further used to simulate the in-duct UVGI performance with other designs.

#### 4.4 Results and discussions

With the validated UV irradiance model CFD simulations, the effects of the duct system design (UV lamp arrangements and duct wall materials), operating conditions (RH), and

bioaerosol particle size on the average accumulative UV dose and UV rate constant are presented in this section. A detailed analysis of the underlying mechanisms will be included in Section 6.

#### 4.4.1 Effects of the in-duct UVGI system designs

##### 4.4.1.1 Effects of lamp arrangements

Different lamp arrangements result in different irradiance distribution inside the duct, thus, different UV doses. In this research, despite using the same airborne microorganism (*E. coli*) for the UVGI tests, different inactivation efficiencies were reported (Table 15). The results of the *E. coli* disinfection efficiency agreed with the average in-duct irradiance under the same operating conditions. The higher the in-duct irradiance and the more uniform the irradiance distribution, the better the UVGI disinfection performance. More specifically, increasing UV lamps resulted in higher UVC irradiance, thus improving the UVGI system inactivation performance. For multiple-lamp scenarios, placing UV lamps in the same row resulted in less shadowing effects and more uniform spatial irradiance distribution (Figure 24(c)), resulting in better UV-C energy utilization and higher inactivation efficiency.

Table 15 Airborne *E. coli* inactivation efficiencies under various conditions

T (°C)	U (m/s)	RH	Lamp configuration	Lamp output <sup>a, b</sup>	Duct average irradiance (W/m <sup>2</sup> ) <sup>b</sup>	UV dose (J/m <sup>2</sup> ) <sup>b</sup>	Inactivation efficiency <sup>c</sup>
25±0.2	0.5±0.04	40%±5%	One lamp at the center, stainless steel	94%	15.41	15.37	99.98%±0.02%
	82%			13.46	9.21	98.36%±0.27%	
	1.35±0.12				12.78	6.07	95.60%±1.31%
	1.35±0.12		One lamp at the center, galvanized steel	78%	13.01	8.97	97.25%±0.53%

1.35±0.13	Two lamps per row (one row), stainless steel	22.02	14.26	99.81%±0.46%
1.35±0.11	One lamp per row (two rows), stainless steel	21.57	12.79	99.59%±0.75%

a: The lamp outputs under different velocities were calculated using the r method model from [156].

b: Results from irradiance model calculations and CFD simulations.

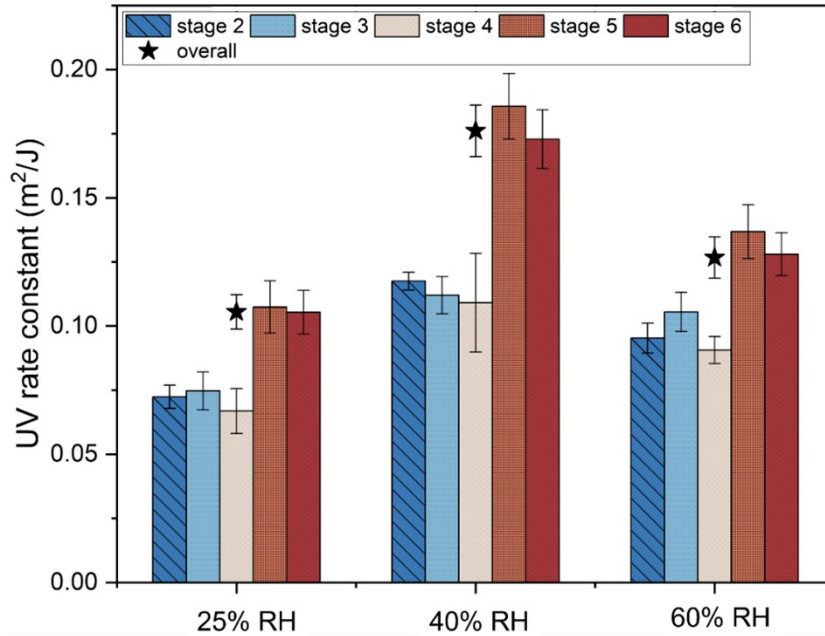
c: Results from the experiment.

#### 4.4.1.2 Effects of duct wall materials

The duct wall material property is an essential parameter defining inactivation efficiency in the in-duct UVGI systems, owing to the improvements in the UV energy utilization (duct wall reflections) with the use of highly reflective duct wall materials [11,50,51,61,64,157–162]. This study discovered that diffuse reflection-dominated galvanized steel plates provided a more uniform in-duct irradiance distribution (Figure 24(c)) and a higher average irradiance (Table 14), thus resulting in a better bacterial inactivation efficiency (Table 15), even with lower UVC reflectivity.

#### 4.4.2 Effects of the in-duct UVGI system operating conditions (RH)

The effect of environmental RH on the UV inactivation efficiency and the UV rate constant was studied using airborne *MS2* under three RH conditions (24.9% ± 1.2%, 41.2% ± 4.7%, and 62.1% ± 5.0%) at a temperature of 24.8°C ± 0.4°C and velocities of 0.50 ± 0.03, 0.92 ± 0.06, and 1.34 ± 0.07 m/s. The reported UV rate constants showed an initial increase and then a decrease as the environmental RH rose from 25% to 60% across all impactor stages (Figure 26 (a)). Significant differences were noted between the three RH conditions, except for stage 3 under 41.2% and 62.1% RH. The highest and lowest UV rate constants were recorded at 41.2% RH and 24.9% RH, respectively (Figure 26 (b) – (g)).



(a) stage 2: 4.7–7 $\mu$ m, stage 3: 3.3–4.7 $\mu$ m, stage 4: 2.1–3.3 $\mu$ m, stage 5: 1.1–2.1 $\mu$ m, stage 6: 0.65–1.1 $\mu$ m, overall: 0.65–

7 $\mu$ m

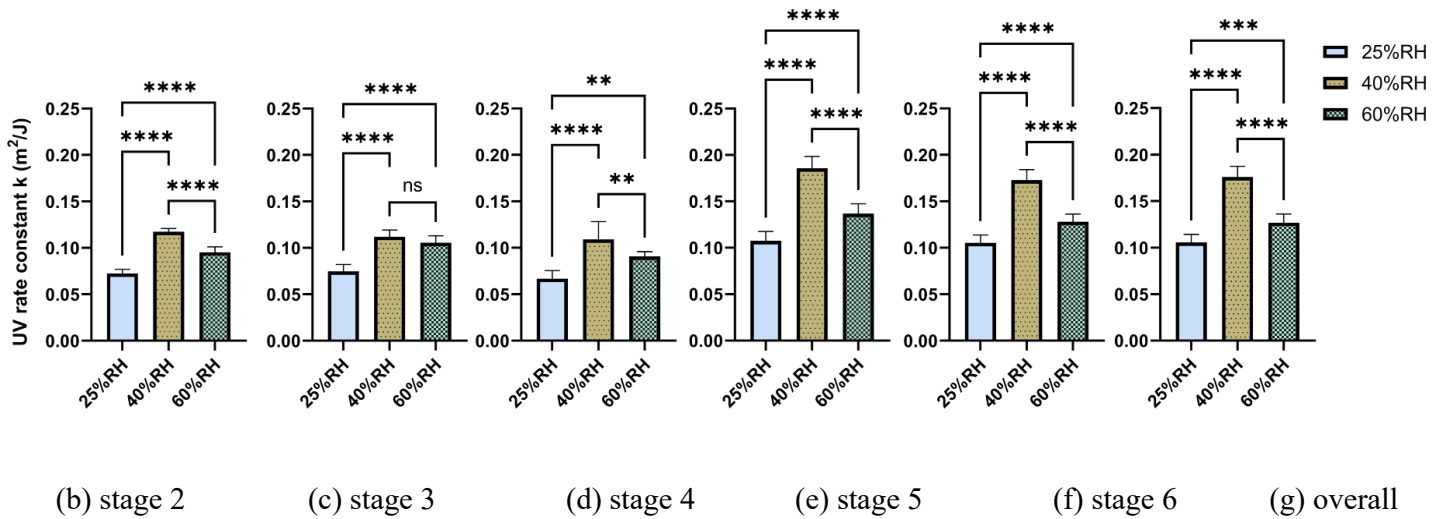


Figure 26 (a) UV rate constants of airborne *MS2* exposed to UVGI across three RH levels, categorized by particle sizes and (b) – (g) UV rate constants and statistical analysis from the one-way ANOVA followed by Tukey’s multiple comparisons tests

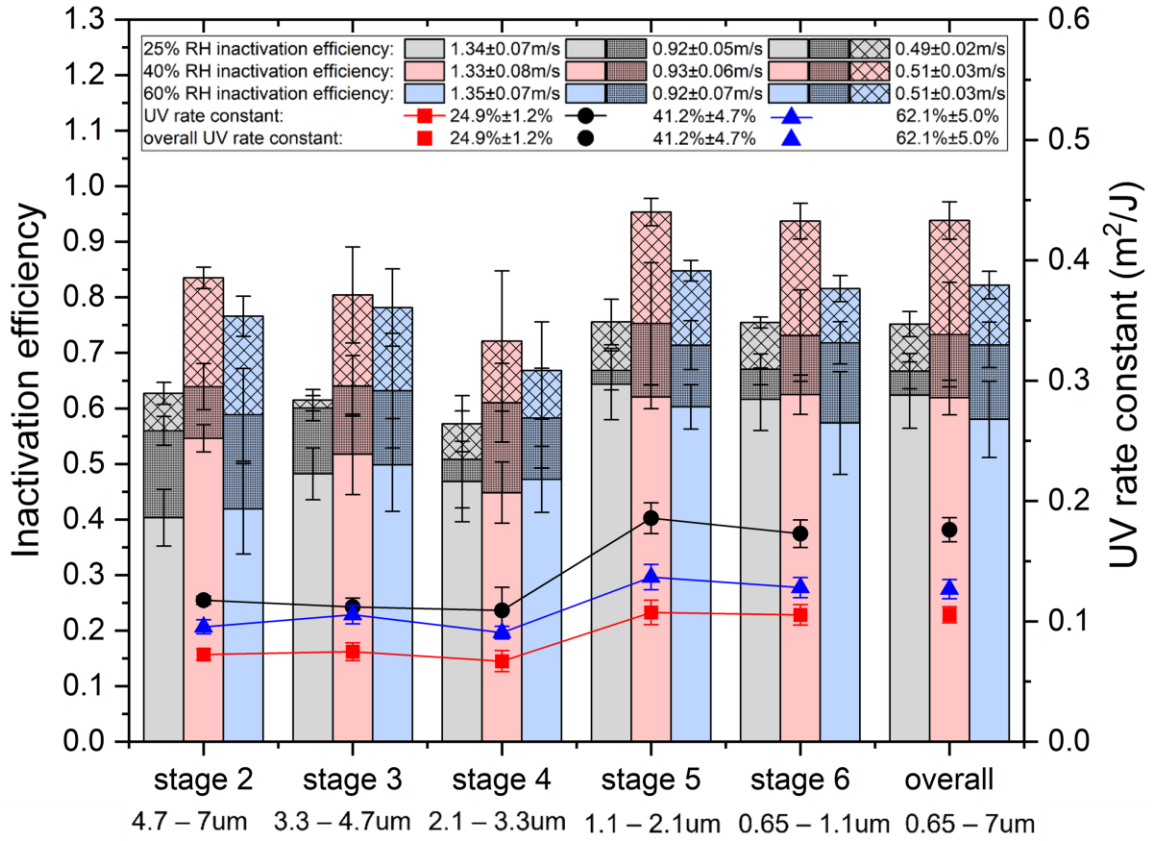
(Appendix E)

(Note: (a) error bars represent the standard deviations from the triplicate experiments and

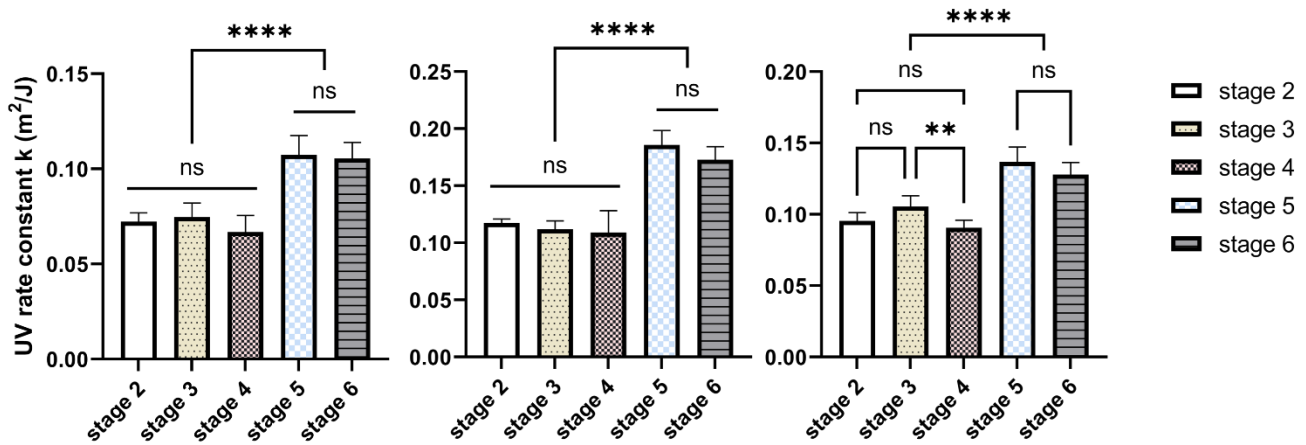
(b) \*\*\*\*:  $P \leq 0.0001$ , \*\*\*:  $P \leq 0.001$ , \*\*:  $P \leq 0.01$ , ns:  $P > 0.05$ )

#### 4.4.3 Effects of the bioaerosol characteristics (particle size)

The effect of bioaerosol particle size on UVGI inactivation efficiencies was investigated using PBS as the suspending medium at RH levels of  $24.9\% \pm 1.2\%$ ,  $41.2\% \pm 4.7\%$ , and  $62.1\% \pm 5.0\%$ , a temperature of  $24.8^\circ\text{C} \pm 0.4^\circ\text{C}$ , and velocities of  $0.50 \pm 0.03$ ,  $0.92 \pm 0.06$ ,  $1.34 \pm 0.07$  m/s. Bioaerosol particle size impacted the UV rate constants. Larger bioaerosols (2.1–7  $\mu\text{m}$ , stages 2, 3, and 4) exhibited significantly lower UV rate constants compared to smaller ones (0.65–2.1  $\mu\text{m}$ , stages 5 and 6) ( $p < 0.0001$ , Figure). There were no significant differences between stages 2, 3, and 4 (except between stages 3 and 4 at  $62.1\% \pm 5.0\%$  RH), nor significant differences between stages 5 and 6 under all three RH levels (Figure 27 (b) – (d)).



(a)



(b) 24.9% ± 1.2% RH

(c) 41.2% ± 4.7% RH

(d) 62.1% ± 5.0% RH

Figure 27 (a) Inactivation efficiencies and UV rate constants for airborne *MS2* across different impactor stages at different RHs and a temperature of  $24.8^{\circ}\text{C} \pm 0.4^{\circ}\text{C}$  and (b) –

(d) UV rate constants and statistical analysis from the one-way ANOVA followed by Tukey's multiple comparisons tests (Appendix E)

(Note: (a) error bars represent the standard deviations from the triplicate experiments and

(b) \*\*\*\*:  $P \leq 0.0001$ , \*\*:  $P \leq 0.01$ , ns:  $P > 0.05$ )

## **5 UVGI Modeling: Prediction of the UV Rate Constants for ssRNA Viruses**

The disinfection of airborne microorganisms through ultraviolet (UV) light is a sophisticated procedure encompassing physical, chemical, and biological interactions. Ensuring the optimal design and enhanced application of in-duct UVGI systems within indoor spaces necessitates a precise understanding and characterization of these multifaceted interactions. In this chapter, we focus on the modeling of an in-duct UVGI system from the biological perspective, illustrating how to predict the UV rate constant of ssRNA viruses with the correct reflection of UV-induced genome and structure damage. For this purpose, a UV rate constant prediction model was introduced, which integrated both genome damage (estimated by an improved genomic model) and capsid protein damage and striving to ensure the model parameters resonate with physical interpretation. Sections 5.1 and 5.2 present the model development for the UV rate constant for characterizing the infectivity loss of ssRNA viruses upon the UV illumination in both liquid matrix and airborne states. The prediction model goes through both quantitative and qualitative validation (Section 5.3) using the experimental data from this study (presented in Section 3.4.2.4) and existing literature. Finally, the results for the UV rate constants of various ssRNA viruses are presented in Section 5.4.

### **5.1 UV rate constant model**

This thesis introduces an improved UV rate constant prediction model that integrates both genome damage (estimated by an improved genomic model) and capsid protein damage and strives to ensure that the model parameters resonate with physical interpretation. Two

independent databases containing UV inactivation data on ssRNA viruses in liquid media were collected. One database contained genome damage data (from qPCR tests) for determining the genomic model parameters through multivariable regression analysis. The other contained viral infectivity loss data (from culturing assays) for validating the genomic model-based UV rate constant prediction model. Additionally, the “UV rate constant ratio of aerosol and liquid” was employed to predict UV rate constants for airborne viruses.

### 5.1.1 Literature mining

To gather data on UV<sub>254</sub> ssRNA virus inactivation, we performed a systematic literature review. Data were extracted from studies that met the following criteria: (1) targets were ssRNA viruses in liquid suspensions; (2) the emitting UV wavelength was set at 253.7 nm (or within the range of 253, 254, 255 nm); (3) the implemented UV doses were reported; (4) infectious viruses were quantified either through qPCR (for determining genome damage) or culture-based approaches (for determining overall infectivity loss); (5) the first-order inactivation rate constant or log-removal dose (e.g., D<sub>90</sub>) was provided or could be determined with the data in the paper; and (6) primers or target genome sequence information were given for the qPCR experiment. For studies that reported multiple UV inactivation data for the same virus (e.g., in different solutions), the average UV rate constant was used. If the UV rate constant was not reported in the studies, the Chick-Watson model was applied for calculation:

$$\ln\left(\frac{C_t}{C_0}\right) = -kD \quad (43)$$

where  $C_t$  and  $C_0$  are the virus concentrations at specific sampling times and time zero, respectively;  $k$  is the UV rate constant ( $\text{cm}^2/\text{mJ}$ ); and  $D$  is the UV dose ( $\text{mJ}/\text{cm}^2$ ). In total,

261 data records (57 characterizing genome damage and 204 characterizing total infectivity loss) for 36 viruses were included. The complete list of data is provided in Tables 16 and 18 (Section 5.3.1), which tabulates the data for characterizing genome damage from qPCR assays and total infectivity loss from culture assays, respectively.

Table 16 Summary of the model parameter information and genome damage UV rate constants in the literature for various genome segments of ssRNA viruses in liquid

Microorganisms	Genome location	UU	UC	CU	CC	YR	length	GC	$k_{\text{genome}}$ ( $\text{cm}^2/\text{mJ}$ )
<i>MS2</i> [163]	24 – 134	11	10	7	7	17	111	54	0.0064
	1534 – 1644	9	7	5	7	14	111	54	0.0046
	1534 – 2225	52	48	48	38	86	692	332	0.0152
	1534 – 3442	114	123	142	116	235	1909	974	0.044
	2145 – 2225	5	5	4	5	8	81	43	0.003
	2145 – 3442	67	80	98	83	157	1298	688	0.0196
<i>MS2</i> [164]	344 – 678	17	24	21	27	44	335	194	0.008
<i>MS2</i> [39]	344 – 678	17	24	21	27	44	335	194	0.0092
	1530 – 1818	22	20	20	19	35	289	130	0.0097
	1809 – 2125	24	25	25	15	41	317	152	0.015
	2724 – 3033	24	16	20	20	42	310	155	0.014
	657 – 959	22	12	20	13	38	303	145	0.017
<i>MS2</i> [30]	632 – 708	4	4	5	6	10	77	43	0.008
<i>MS2</i> [165]	657 – 959	22	12	20	13	38	303	145	0.01
<i>MS2</i> [48]	657 – 959	22	12	20	13	38	303	145	0.0133
<i>MS2</i> [166]	1255 – 1423	11	14	14	8	22	169	86	0.0186
<i>GA</i> [167]	967 – 1559, 1587 – 1945, 2143 – 2523, 2533 – 2926, 2958 - 3343 <sup>1</sup>	174	165	165	105	283	2121	997	0.0373
<i>MS2</i> [167]	344 – 678, 657 – 959, 1530 – 1818, 1809 – 2125, 2724 – 3033, 3285 – 3528 <sup>1</sup>	115	121	121	122	226	1798	935	0.0388
<i>Hepatitis E virus</i> [168]	5261 – 5330	6	7	7	11	9	70	38	0.018
<i>MS2</i> [169]	657 – 959	22	20	20	13	38	303	145	0.0142
<i>Poliovirus 1</i> [170]	444 – 638	17	11	11	16	28	195	99	0.0113
<i>Feline calicivirus</i> [171]	2452 – 2534	8	8	8	2	14	83	42	0.0188
<i>SARS-CoV-2</i> [172]	15431 – 15530	9	4	4	3	13	100	41	0.0129

<i>SARS-CoV-2</i> [172]	26269 – 26381	16	6	6	2	15	113	46	0.0142
<i>SARS-CoV-2</i> [173]	192 – 8196	841	353	353	229	1009	8005	3042	0.1546
	7838 – 16080	908	360	360	219	1072	8243	3132	0.1575
	15862 – 23813	865	372	372	242	1027	7952	2942	0.1768
	22782 – 29738	744	399	399	237	913	6957	2783	0.1134
	21620 – 25366	450	206	206	126	498	3747	1386	0.0955
	28274 – 29533	67	71	71	68	146	1260	592	0.0242
	28706 – 28833	6	11	11	7	13	128	67	0.0142
<i>SARS-CoV-2</i> [174]	15431 – 15530	9	4	4	3	13	100	41	0.0233
<i>Coxsackievirus</i> <i>B5</i> [47]	272 – 876	44	28	28	39	79	605	290	0.02835
	1069 – 1681	42	23	23	33	63	613	294	0.02785
	1866 – 2377	28	23	23	32	65	512	251	0.01759
	2654 – 3051	22	23	23	26	47	398	195	0.02459
	3470 – 3924	29	29	29	28	58	455	228	0.02782
	4665 – 5177	33	24	24	26	59	513	236	0.02575
	6072 – 6582	32	21	21	23	58	511	225	0.02099
<i>Human</i> <i>norovirus</i> [47]	390 – 887	41	29	29	36	63	498	229	0.02436
	1360 – 1864	20	32	32	37	61	505	268	0.01837
	2044 – 2557	16	22	22	28	60	514	252	0.01456
	3273 – 3778	10	20	20	45	60	506	283	0.01173
	4098 – 4593	29	41	41	39	53	496	248	0.0209
	5097 – 5565	32	21	21	52	60	469	239	0.01689
	5842 – 6343	22	27	27	47	61	502	256	0.0178
6925 – 7424	24	36	36	34	62	500	260	0.01826	
<i>MS2</i> [32]	944 – 1439	22	38	38	28	59	496	263	0.011
	2693 – 3189	30	35	35	35	64	497	263	0.024
<i>Poliovirus 1</i> [163]	452 – 596	13	7	7	11	19	145	75	0.0127
	5573 – 5648	3	5	5	2	8	76	36	0.00714
	5573 – 7440	118	104	104	82	220	1868	822	0.1036
<i>Tulane virus</i> [175]	3514 – 3637	6	11	11	10	20	124	58	0.0018
<i>GA</i> [176]	1778 – 1889	11	15	15	4	18	112	52	0.0061
<i>Human</i> <i>norovirus</i> [176]	5012 – 5109	5	8	8	2	8	89	45	0.00223
<i>Tulane virus</i> [177]	2774 – 4097	76	72	72	99	172	1324	622	0.0461
<i>Human</i> <i>norovirus</i> [178]	4930 – 5028	4	7	7	4	8	98	52	0.0047
Mean and standard deviation of the genomic variables for preliminary standardization in principal components analysis (mean/standard deviation)		94.95/ 216.73	57.11/ 95.76	58.05/ 95.99	46.04/ 60.43	134.93/ 255.84	1062.18/ 1978.68	454.46/ 753.50	-

1. The genome damage is the sum of the individual genome damages from multiple genome segments.

## 5.1.2 The UV rate constant prediction model of the infectivity loss for liquid-based viruses

In this study, we consider the UV-mediated infectivity loss rate constant to be the sum of contributions from genome damage and protein damage, as expressed by:

$$k_{\text{viral infectivity loss}} = k_{\text{genome damage}} + k_{\text{protein damage}} \quad (44)$$

where  $k_{\text{viral infectivity loss}}$ ,  $k_{\text{genome damage}}$ , and  $k_{\text{protein damage}}$  are the UV rate constants ( $\text{cm}^2/\text{mJ}$ ) for the overall virus infectivity loss, genome damage, and protein damage upon the UV illumination, respectively.

### 5.1.2.1 Genome damage prediction

The genome damage rate constant  $k_{\text{genome damage}}$  is predicted by a modified genome sequence-based composition model, following several simple rules for DNA/RNA photoreactivity [26,31–33,179,180]: (1) Photoreactions occur with two or more adjacent pyrimidines; (2) nonadjacent pyrimidines, surrounded on both sides by purines, exhibit little or no photoreactivity; and (3) purines produce UV photoproducts when flanked on their 5' side by two or more contiguous pyrimidine residues. Thus, the bioinformatics parameters of the genomic model are preliminarily determined as adjacent pyrimidines (UU, UC, CU, and CC), purines flanked by pyrimidine doublets on the 5' side (UUA, UUG, UCA, UCG, CUA, CUG, CCA, CCG, collectively referred to as YR), genome length, and guanine-cytosine (GC) content. The molecular weight parameter is excluded since it is highly collinear with genome length. In addition, we assume the probability of forming a photoproduct in a long chain of pyrimidine bases (such as uracil quintuplets (UUUUU), uracil sextuplets (UUUUUU), etc.) is the summation of individual pyrimidine

doublets (UU). Thus, uracil/cytosine triplets, quadruplets, quintuplets, and sextuplets are counted as two, three, four, and five uracil/cytosine doublets, respectively.

While the determinants of UV-induced genome damage are well recognized, the empirical mathematical forms in the literature lack consensus, varying from multiple linear equations [32,33] to multiple nonlinear equations (summation with exponents [181] or multiplication with exponents [38,42,43]). Thus, this thesis explores different regression methods and compares prediction results with experimental data to identify the best fit with reasonable physical and statistical significance. Here, multiple linear regression, multiple nonlinear regression, and principal component regression were compared for the UV rate constant model for genome damage. The model parameters, adjacent pyrimidines (UU, UC, CU, and CC), purines flanked by pyrimidine doublets on the 5' side (UUA, UUG, UCA, UCG, CUA, CUG, CCA, CCG, counted together as YR), and guanine-cytosine (GC) content, were expressed in either the counted number or the occupied ratio. Along with the bioinformatics parameter genome length, the tested genome damage models have the following equation forms:

$$k_{\text{multiple linear}} = a \times UU + b \times UC + c \times CU + d \times CC + e \times YR + f \times \text{length} + g \times GC + h \quad (45a)$$

$$k_{\text{multiple nonlinear-summation with exponents}} = h \times (UU^a + UC^b + CU^c + CC^d + YR^e + \text{length}^f + GC^g) + i \quad (45b)$$

$$k_{\text{multiple nonlinear-multiplication with exponents}} = h \times (UU^a \times UC^b \times CU^c \times CC^d \times YR^e \times \text{length}^f \times GC^g) + i \quad (45c)$$

$$k_{PCR} = a \times PC1 + b \times PC2 + c \times \text{length} + d \quad (45d)$$

where UU, UC, CU, and CC are the number or the ratio of adjacent pyrimidines, YR represents the number or the ratio of purines flanked by pyrimidine doublets on the 5' side, GC is the number or the ratio of guanines and cytosine, length is the length of the target genome segment, PC1 and PC2 are the first and second principal components obtained from principal component analysis (PCA) which was performed on the abovementioned features UU, UC, CU, CC, YR, GC, and length (if the parameters are expressed in the forms of number), and  $a, b, c, d, e, f, g, h,$  and  $i$  are the empirical constants obtained through multivariable regression analysis. Note that to ensure the statistical significance of the fitted equation, the coefficients that had p values greater than 0.05 were excluded one by one from the highest p values until all the remaining coefficients were statistically significant ( $p < 0.05$ ).

Since the regression models (Eqs. (45a) – (45d)) are derived from qPCR data, where the amplicon length is typically only a few hundred bases, it would be inappropriate to apply these equations directly to whole genomes (such as *SARS-CoV-2*, which comprises 29.9k base pairs). To address this issue, the entire genome shall be divided into smaller fractions with lengths within the database range, and we assume the total genome damage for the entire virus is the sum of individual damages from different fractions, expressed as:

$$k_{total\ genome\ damage} = \sum_{i=1}^N k_{genome\ damage\_i} \quad (46)$$

where N and i stand for the total number and index of genome fractions, respectively. Despite different genome fractions having values of dinucleotide counts, genome lengths, and GC contents, the model parameters ( $a, b, c, d, e, f, g, h,$  and  $i$ ) remain consistent across all fractions. Considering the nonlinear nature of Eqs. (45a) – (45d), the fraction length is treated as a hyperparameter. A range of values (500, 1000, 2000, 3000, 4000, 5000, 6000,

7000, 8000, and no division) were tested to optimize the prediction based on experimental data (Section 5.2.1).

### 5.1.2.2 Infectivity loss prediction

In addition to genome damage, the contribution from protein damage to the overall virus infectivity loss ( $k_{protein\ damage}$ ) is generally minor but nonnegligible when treated with UV [26]. Thus, the contribution ratio for protein damage can be represented as:

$$k_{protein\ damage} = hk_{viral\ infectivity\ loss} \quad (47)$$

where  $h$  stands for the relative contribution of protein damage to the total viral functional loss. Thus, the prediction model for the overall UV rate constant of the virus infectivity loss is formulated as:

$$k_{viral\ infectivity\ loss} = \frac{\sum_{i=1}^N k_{genome\ damage\_i}}{1-h} \quad (48)$$

Generally, for a virus with a known genome sequence and a contribution ratio of genomic/protein damage, the overall UV rate constant for virus infectivity loss can be estimated using Eq. (48). However, some groups of viruses with distinct genome structure features require specific adjustments to the genome damage model. For instance, retroviruses are pseudodiploid, meaning that each virion contains two complete copies of the single-stranded RNA genome. This feature increases the probability of successful DNA synthesis under UV illumination: if one of the two RNAs is UV-damaged, reverse transcription can switch templates and utilize the co-packaged RNA, thereby allowing DNA synthesis through the lesion sites [182]. Considering this unique characteristic and assuming a 50% probability of successful genome damage (while protein damage remains unaffected), Eq. (48) can be rewritten for retroviruses as:

$$k_{\text{viral infectivity loss\_retroviruses}} = \frac{\sum_{i=1}^N k_{\text{genome damage\_i}}}{1-h} - \frac{\sum_{i=1}^N k_{\text{genome damage\_i}}}{2} \quad (49)$$

In addition, the *Orthomyxoviridae* family consists of naturally segmented RNA viruses (each segment is approximately 1000–2000 bp). Since these naturally occurring segments are small enough, artificial genome fraction divisions are not applied to them. Instead, the genome damage prediction model (Eq. (45)) is directly applied to their original segmented RNAs.

### 5.1.3 The UV rate constant prediction model of the infectivity loss for airborne viruses

It is important to note that the abovementioned prediction model provides UV rate constants for viruses suspended in liquid. While the intrinsic inactivation mechanisms remain the same, UV inactivation data for airborne viruses differ due to several factors: (1) the UV absorptivity of liquid media, which impacts the effectiveness of UV exposure; (2) the increased turbulence and diffusion in the air compared to water, resulting in more evenly exposed microorganisms; (3) the aerosolization process, which reduces the microbial survival potential through physical damage; (4) the presence of oxygen in the air, which contributes to increased vulnerability [17,26]; and (5) potential differences in virion aggregation in bioaerosols and in liquid [20,112]. To convert the UV rate constants from those based on liquid suspension to airborne ones, the method “UV rate constant ratio of aerosol and liquid” was used as follows [87,183]:

$$k_{\text{genome damage\_air}} = r_{UV} k_{\text{genome damage\_liquid}} \quad (50)$$

and

$$k_{\text{viral infectivity loss}_{\text{air}}} = r_{UV} k_{\text{viral infectivity loss}_{\text{liquid}}} = r_{UV} \frac{\sum_{i=1}^N k_{\text{genome damage}_{\text{liquid}_i}}}{1-h} \quad (51)$$

where  $r_{UV}$  is the UV rate constant correction ratio for converting from water-borne to airborne viruses.

## 5.1.4 Model validation

### 5.1.4.1 Quantitative validation of the infectivity loss UV rate constant model for liquid-based and airborne viruses

In this study, the proposed UV rate constant model underwent both quantitative and qualitative assessments. Initially, the prediction of the overall infectivity loss, as described by Eqs. (6) and (9), were quantitatively validated. This was accomplished by comparing the model's results with experimental data from the literature, encompassing both liquid-based and airborne viruses (Table 18 with 36 ssRNA viruses in liquid and Table 19 with 9 airborne ssRNA viruses).

### 5.1.4.2 Qualitative validation of the genome damage UV rate constant model using liquid-based *MS2*

Subsequently, the genome damage models' (Eqs. (45) and (50)) abilities to predict variations in UV-induced genome damage across different sequences were qualitatively evaluated using experimental data of *MS2* UV inactivation. For the liquid-based applications, due to all the available genome damage UV rate constant data from experiments ( $k_{\text{genome damage}}$ ) were already used in regression analysis. Thus, inactivation efficiency was compared instead. Herein, we selected the experimental data reported by Pecson et al. [184], which measured UV-induced genome damage for various *MS2* genome

segments under a single UV dose (590 mJ/cm<sup>2</sup>) condition, and the detailed specifics of the experimental procedures can be found in their original paper [184]. Information on the twelve primer sets is included in Table 20, with each targeting approximately 300 nucleotides. Note that data from primer #3 [184] met the inclusion criteria for Table 16 (see Section 5.1.1), thus, were used for model regression analysis, while data measured using other primers were excluded from the training set and served as the validation set.

#### 5.1.4.3 Qualitative validation of the genome damage UV rate constant model using airborne *MS2*

For the genome damage prediction validation in airborne applications (Eq. (50)), due to the lack of existing research in investigating the genome damage variations with different sequences for airborne viruses, we conducted UV inactivation tests using airborne *MS2*. Seventeen sets of primers were designed to assay genome damage under three different UV dose conditions to obtain UV rate constants. The detailed experimental setup and experimental results are included in Sections 3.3.2 and 3.4.2.4. Thus, the model-predicted UV rate constant variations were qualitatively compared with the experimental data.

## 5.2 Determination of model parameters

### 5.2.1 Genome damage prediction model for liquid-based viruses

Table 16 tabulates the available genome damage UV inactivation data for ssRNA viruses, along with the corresponding genome sequence information. In particular, the nucleotide sequences were retrieved directly from the accessible NCBI genome database. The information for the model variables, including the numbers and the occupied ratios of pyrimidines and purines flanked by pyrimidine doublets, were extracted using RStudio

version 1.2.475 with R software version 4.2.2 [185] (for the coding script, see Appendix F). Then, multiple variable curve fitting was conducted in Origin 2022 for Eq. (45), yielding the following results:

$$k_{\text{genome damage\_summation\_number}} = -4.2144 \times 10^{-4} UU_{\text{number}} + 1.3316 \times 10^{-4} \text{length} - 1.8074 \times 10^{-4} GC_{\text{number}} + 0.0100 \quad (52a)$$

$$k_{\text{genome damage\_summation\_ratio}} = 1.7362 \times 10^{-5} \text{length} - 0.0855 GC_{\text{ratio}} + 0.0523 \quad (52b)$$

$$k_{\text{genome damage\_summation with exponents\_number}} = 0.0026 (UU_{\text{number}}^{0.6046}) \quad (52c)$$

$$k_{\text{genome damage\_summation with exponents\_ratio}} = 7.3029 \times 10^{-5} (\text{length}^{0.8494}) + 0.0053 \quad (52d)$$

$$k_{\text{genome damage\_multiplication with exponents\_number}} = 8.6568 \times 10^{-4} (CU_{\text{number}}^{-0.6248} \times YR_{\text{number}}^{1.2822}) \quad (52e)$$

$$k_{\text{genome damage\_multiplication with exponents\_ratio}} = YR_{\text{ratio}}^{3.9995} \times \text{length}^{0.7013} \quad (52f)$$

$$k_{\text{genome damage\_principal components regression\_number}} = 0.0140 \times PC1_{\text{number}} + 0.0293$$

where  $PC1_{\text{number}} = 0.3754 UU_{\text{number}} + 0.3794 UC_{\text{number}} + 0.3791 CU_{\text{number}} + 0.3717 CC_{\text{number}} + 0.3798 YR_{\text{number}} + 0.3798 \text{length} + 0.3805 GC$

(52g)

$$k_{\text{genome damage\_principal components regression\_ratio}} = -0.0021 PC1_{\text{ratio}} + 1.7773 \times 10^{-5} \text{length} + 0.0104$$

where  $PC1_{\text{ratio}} = -0.4085 UU_{\text{ratio}} + 0.4203 UC_{\text{ratio}} + 0.4172 CU_{\text{ratio}} + 0.4103 CC_{\text{ratio}} - 0.0237 YR_{\text{ratio}} + 0.5560 GC_{\text{ratio}}$

(52h)

These fittings across all equation forms demonstrated strong compatibility with the existing data (with  $R^2 > 0.88$ ) and statistical significance (all remaining coefficients  $p < 0.05$ , except for the intercept and multiplier in Eq. (52d), as either removing the intercept or letting the multiplier equal 0 would lead to a significantly reduced  $R^2 < 0.68$ ). The detailed data-fitting results are presented in Appendix G (Tables G1 and G2). Note that in principal component

regressions (Eqs. (52g) and (52h)),  $UU'$ ,  $UC'$ ,  $CU'$ ,  $CC'$ ,  $YR'$ ,  $length'$ , and  $GC'$  represent the standardization of genomic variables to unit variance prior to principal component analysis to eliminate dissimilarities in the magnitude of variable values. For instance,

$$UU_{number}' = \frac{UU_{number} - \overline{UU_{number}}}{\sigma_{S_{UU_{number}}}},$$

where  $\overline{UU_{number}}$  and  $\sigma_{S_{UU_{number}}}$  are the mean and standard

deviation of the number of UUs calculated from the database in Table 16. Thus, when applying Eqs. (52g) and (52h) to predict other genome fractions, preliminary standardization using the same values of  $\overline{UU_{number}}$  and  $\sigma_{S_{UU_{number}}}$  are needed (reported in Table 16).

To determine the optimal model forms for genome damage prediction, comparisons between the model predictions and the experimental data for the overall infectivity loss UV rate constants were subsequently conducted in Section 5.2.3.

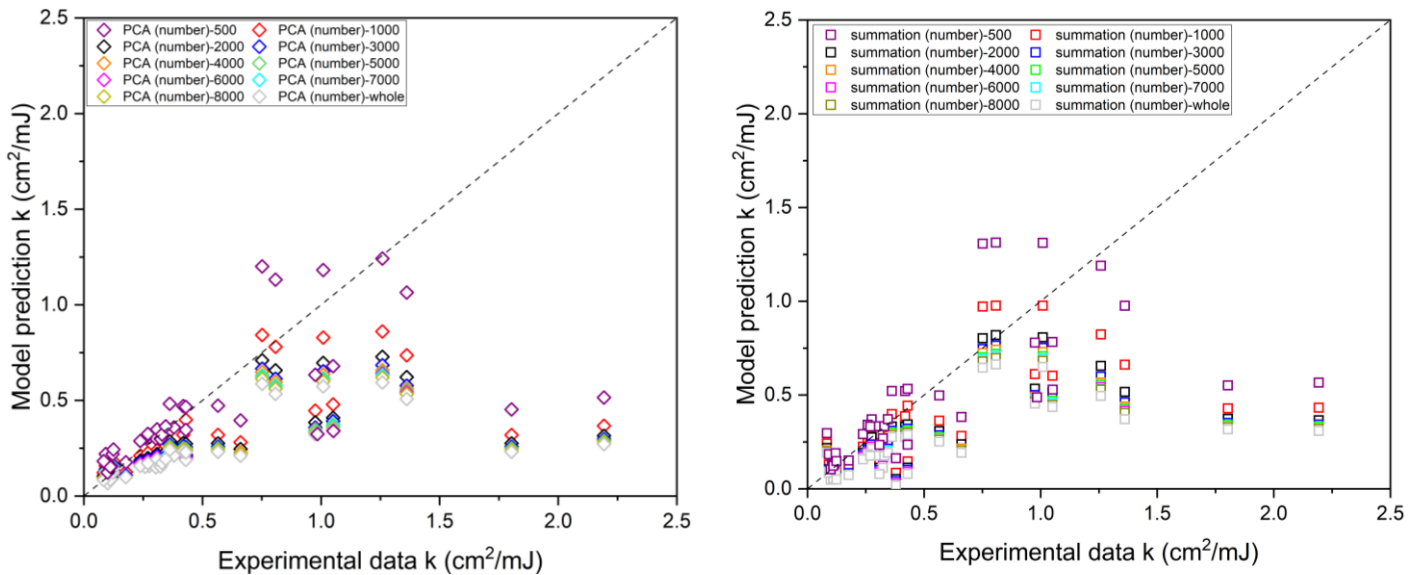
## 5.2.2 Protein damage prediction model for liquid-based viruses

Building upon the genome damage prediction model, the contribution ratio of protein damage, denoted as  $h$ , shall be established to calculate the final virus infectivity loss. Various studies in the literature have reported that protein damage contribution ratios display minor variations across ssRNA viruses, ranging between 6% and 17% for different families and classes. For instance, experimental results revealed an average protein damage contribution of 17% for *MS2*, leading to disruption of the viral genome's injection into the host cell [30,39], and an average of 11.7% for the *mouse hepatitis virus (MHV, strain A59)*, resulting in the failure of virus attachment and genome penetration into the host cell [186]. Analogously, theoretical calculation of protein capsid damage contribution (based on the amino acid composition) yielded values of 6%, 6%, 7%, 6%, 11%, 10%, 14%, and 17%

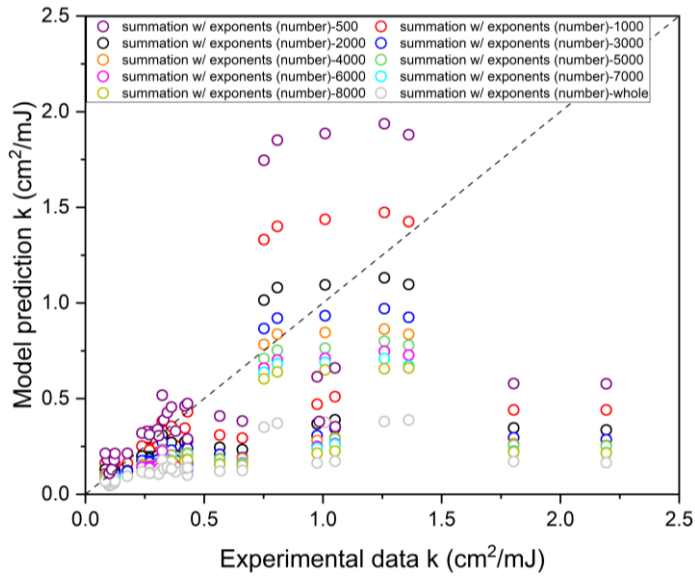
for *MS2 bacteriophage*, *fr bacteriophage*, *poliovirus type 1*, *coxsackievirus B6*, *echovirus 12*, *norovirus*, *murine norovirus*, and *feline calicivirus* [187]. In light of the absence of accurate estimations for the contribution ratios of protein damage across all ssRNA viruses, we assume that the value can vary from 0% to 20%. The model's results are presented in boxplot form, providing a visual comparison with the experimental data.

### 5.2.3 Infectivity loss prediction model for liquid-based viruses

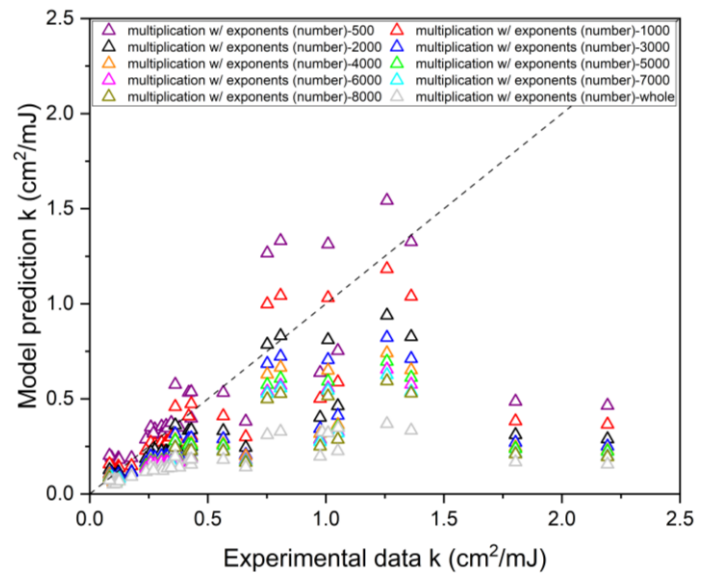
The optimal form of the infectivity loss prediction model was determined through comparisons between the model predictions and experimental data for UV rate constants across various ssRNA viruses. These tests include eight different genome damage equation forms (Eqs. (52a) – (52h)) with ten possible genome fraction division lengths (500, 1000, 2000, 3000, 4000, 5000, 6000, 7000, 8000, and no division). Considering a contribution of protein damage set at 10% and using known genome fraction sequences, the UV rate constants of infectivity loss for 36 different viruses were estimated and compared with experimental data (as shown in Figure 28).



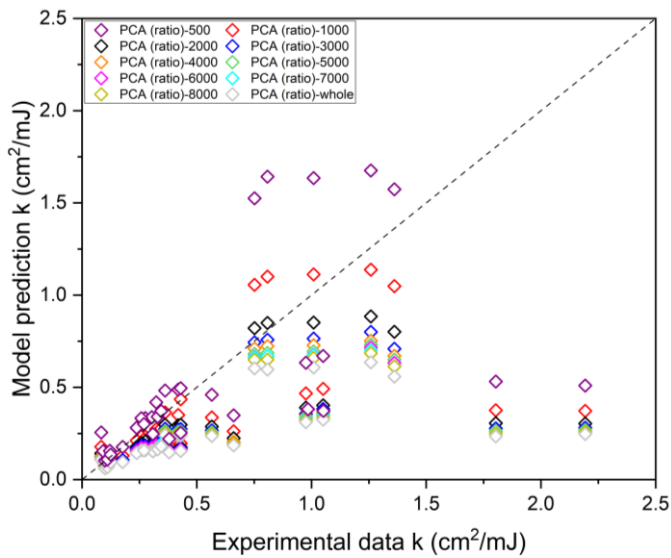
(a)



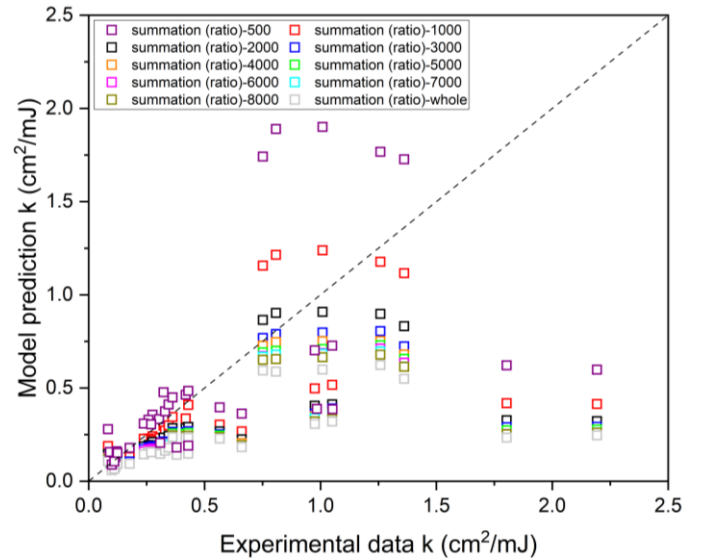
(b)



(c)

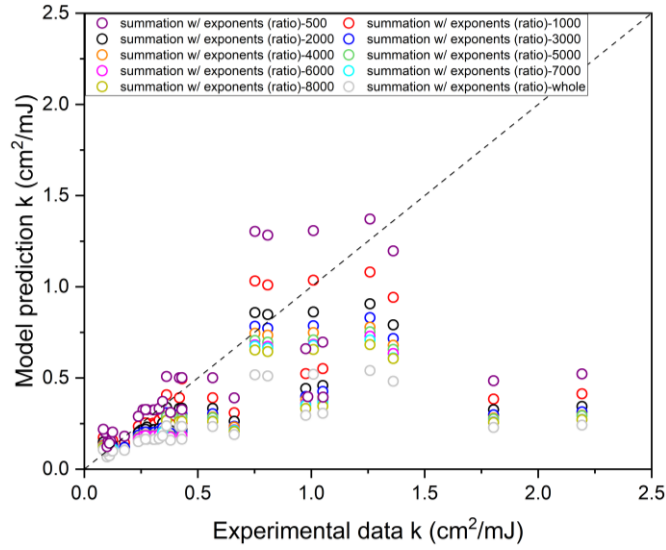


(d)

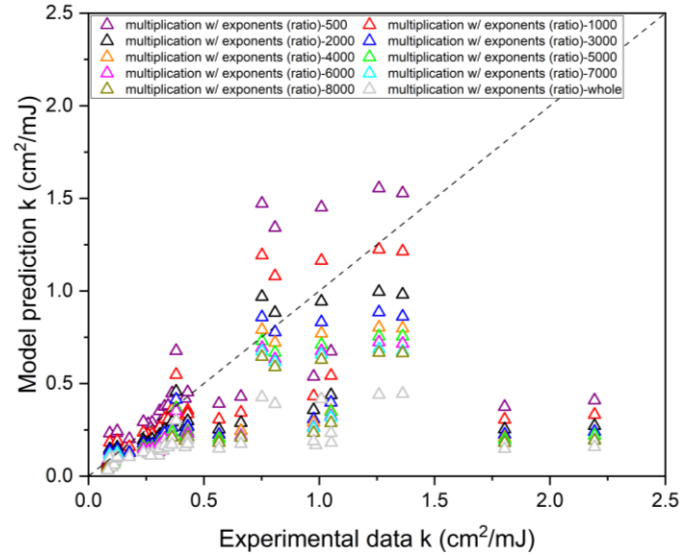


(e)

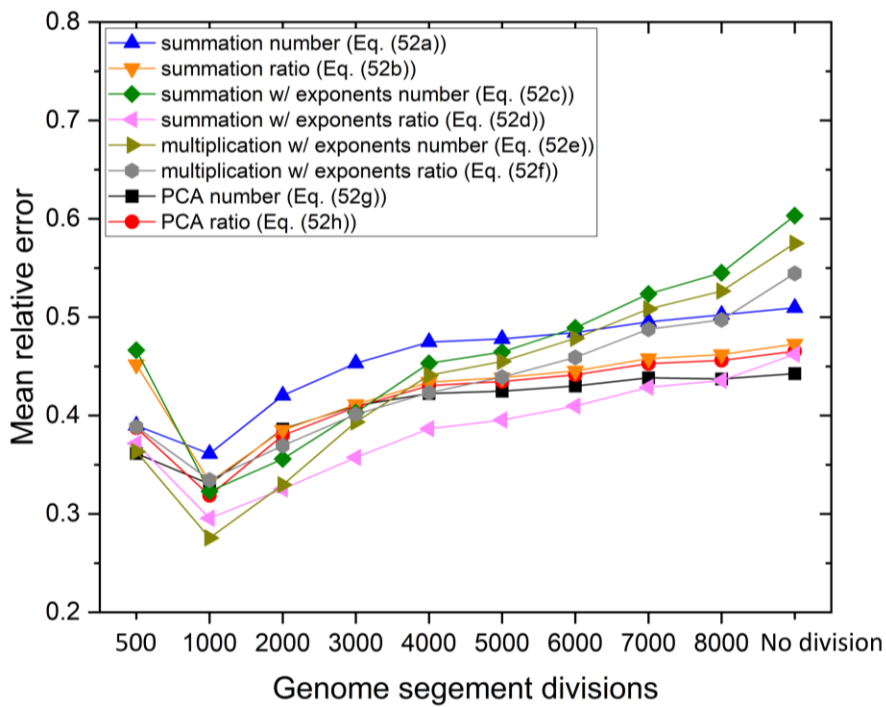
(f)



(g)



(h)



(i)

Figure 28 (a) – (h) Comparisons between the model predictions and experimental data of the infectivity loss UV rate constants for 36 viruses using eight genome damage equation

forms (Eq. (9a) – (9h)) with ten genome segment division lengths (500, 1000, 2000, 3000, 4000, 5000, 6000, 7000, 8000, and no division), and (i) Mean relative errors of the predicted infectivity loss UV rate constants (36 ssRNA viruses) for eight genome damage equations with ten segment division lengths

The equation form that multiplied with exponents expressed as a number value (Eq. (52e)) and employed a 1000 genome length division exhibited the lowest mean relative error (MRE) between the model's predictions and experimental data. Thus, the chosen UV rate constant models for genome damage and infectivity loss for ssRNA viruses in liquid-based applications were represented by:

$$k_{\text{genome damage\_liquid}} = 8.6568 \times 10^{-4} \left( CU_{\text{number}}^{-0.6248} \times YR_{\text{number}}^{1.2822} \right) \quad (53)$$

$$k_{\text{infectivity loss\_liquid}} = \frac{\sum_{i=1}^{N_{\text{integer}}} 8.6568 \times 10^{-4} \left( CU_{\text{number\_}i}^{-0.6248} \times YR_{\text{number\_}i}^{1.2822} \right)}{1 - h} \quad (54)$$

where  $N_{\text{integer}}$  is the number of genome fractions obtained by dividing the total length of genome size by 1000, and  $i$  represents each genome fraction. The optimal equation form does not incorporate the terms UU, UC, CC, length, and GC due to their lack of statistical significance, and the exponent of the term CU is negative. This can be explained by the experimental findings in the literature, which concluded that different nucleotide bases had UV sensitivity in the order of TT>TC>CT>CC [26]. In the case of ssRNA viruses, this corresponds to UU>UC>CU>CC, considering the similarities between thymine and uracil. Thus, the negative exponent in the term of CU indicates the negative contribution of an increasing number of CU pairs to genome damage, as this occupies sites for the more UV-sensitive pyrimidines, such as UU. Moreover, another remaining term is YR, which is reasonable as it contains various kinds of purines flanked by pyrimidine doublets on the 5'

side (UUA, UUG, UCA, UCG, CUA, CUG, CCA, CCG). These combinations have colinear effects with pure pyrimidine doublets. Studies in the literature suggest that the presence of flanking pyrimidines next to other pyrimidines can increase UV reactivity [180,188–190].

#### 5.2.4 Infectivity loss prediction model for airborne viruses

When estimating the UV rate constants for airborne viruses, the method of “UV rate constant ratio of aerosol and liquid” plays a crucial role. This method involves determining the ratio of the UV rate constant of a specific virus between airborne and liquid-based applications. Upon examining the literature, we observed that the majority of the available data indicated a ratio of approximately greater than 3 (Table 17). Thus, a ratio of 3 was adopted in this study as the conservative estimation. The UV rate constant models for genome damage and infectivity loss for airborne ssRNA viruses are presented as follows:

$$k_{\text{genome damage\_air}} = 2.5970 \times 10^{-3} \left( CU_{\text{number}}^{-0.6248} \times YR_{\text{number}}^{1.2822} \right) \quad (55)$$

$$k_{\text{infectivity loss\_air}} = \frac{\sum_{i=1}^{N_{\text{integer}}} 2.5970 \times 10^{-3} \left( CU_{\text{number\_}i}^{-0.6248} \times YR_{\text{number\_}i}^{1.2822} \right)}{1 - h} \quad (56)$$

It is worth noting that for viruses that exhibit larger ratios, employing a smaller value, such as 3, in the model will offer conservative estimations of both the UV rate constants and the subsequent inactivation performance.

Table 17 UV rate constant ratio of aerosol and liquid for different ssRNA viruses

Microorganisms	UV rate constant (cm <sup>2</sup> /mJ)		Ratio (aerosol/liquid)
	Water-borne viruses	Airborne viruses	
<i>Murine hepatitis virus</i>	1.26 [191–195]	3.77 [136]	3.0

<i>SARS-CoV-2</i>	1.01 [192,196–206]	9.90 [118]	9.8
<i>MS2</i>	0.12 [26,30,39,48,184,207–240]	1.60 [69,71,90–95,109,115,116,136]	13.3
<i>Coxsackie virus</i>	0.30 [47,219,221,241–249]	1.11 [117]	3.7
<i>Sindbis virus</i>	0.36 [250–252]	1.04 [117]	2.9
<i>Influenza A virus</i>	1.01 [253–260]	2.78 [108,261]	2.8

## 5.3 Model validations

### 5.3.1 UV rate constant model for overall infectivity loss

Comparisons between the model predictions and the experimental data of the UV rate constant for the liquid-based (Eq. (54)) and airborne (Eq. (56)) ssRNA viruses are plotted in Figure 29 and concluded in Tables 18 and 19.

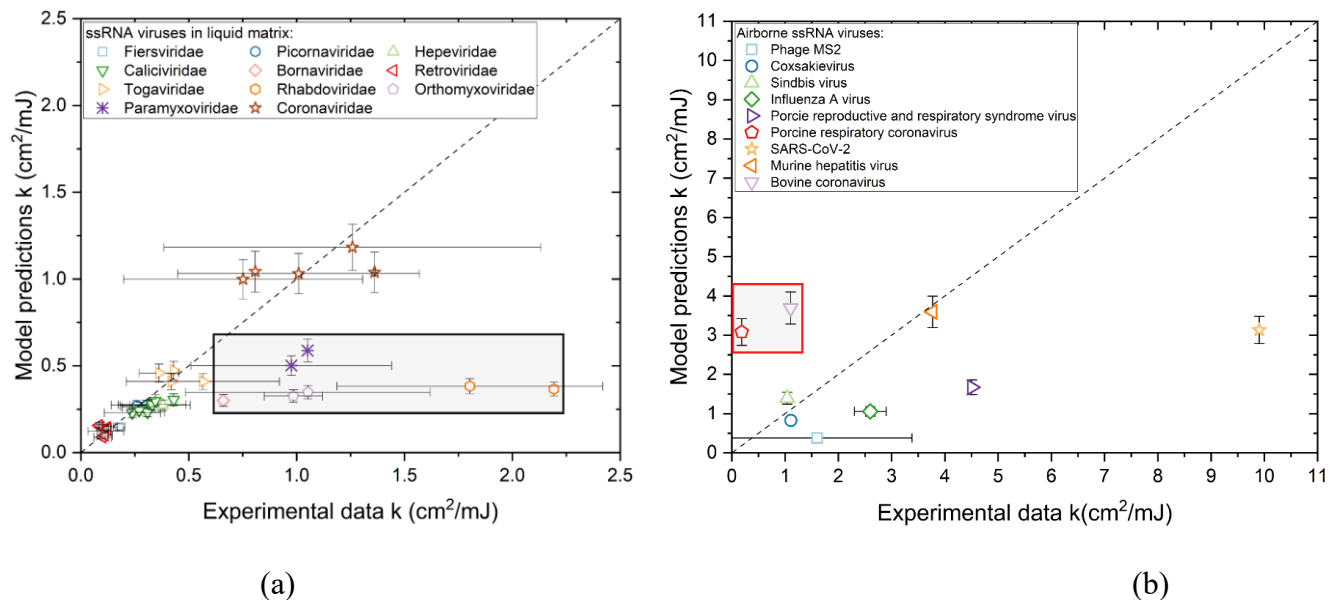


Figure 29 Comparisons between model predictions and experimental data for the infectivity loss UV rate constant of ssRNA viruses in (a) liquid-based and (b) airborne applications.

(Note: The x-axis error bar represents the standard deviation of the experimental UV rate constant data from the literature, while the y-axis error bar represents the range of model predictions accounting for 0% - 20% variations in protein damage. The black and red squares represent the outliers in the model predictions.)

For liquid-based ssRNA viruses, 36 viruses were categorized into 11 families, which showed MREs of 9.68% (*Fiersiviridae*), 9.00% (*Picornaviridae*), 28.19% (*Hepeviridae*), 16.12% (*Caliviridae*), 54.59% (*Bornaviridae*), 20.32% (*Retroviridae*), 16.66% (*Togaviridae*), 81.04% (*Rhabdoviridae*), 66.94% (*Orthomyxoviridae*), 46.29% (*Paramyxoviridae*), and 18.73% (*Coronaviridae*). Interestingly, the model predictions for positive-sense (+) RNA viruses (*Fiersiviridae*, *Picornaviridae*, *Hepeviridae*, *Caliviridae*, *Retroviridae*, *Togaviridae*, and *Coronaviridae*, MRE: 17.56%) displayed better predictions than negative-sense (-) RNA viruses (*Bornaviridae*, *Rhabdoviridae*, *Orthomyxoviridae*, and *Paramyxoviridae*, MRE: 61.22%). This discrepancy is marked in Figure 29(a), with negative-sense RNA viruses enclosed in a black square.

Table 18 Model predictions and experimental data (in the literature) of the infectivity loss

UV rate constants for ssRNA viruses in liquid

Microorganisms	Experimental data k (cm <sup>2</sup> /mJ)		Model predictions (cm <sup>2</sup> /mJ, 0% protein damage – 20% protein damage)
	Average	Studies in the literature	
<i>Phage GA</i>	0.1055±0.010	0.115 [163] 0.096 [167] 0.0971 [163] 0.0554 [262] 0.094 [164] 0.062 [39]	0.0999 – 0.1249
<i>Phage ms2</i>	0.1155±0.082	0.1027 [30] 0.048 [165] 0.066 [48] 0.1296 [166] 0.1707 [263] 0.086 [167]	0.1116 – 0.1396

		0.101 [169]	
		0.131 [214]	
		0.075 [215]	
		0.132 [216]	
		0.0792 [217]	
		0.1423 [218]	
		0.1398 [219]	
		0.0921 [220]	
		0.056 [221]	
		0.038 [222]	
		0.171 [223]	
		0.0539 [224]	
		0.119 [225]	
		0.055 [226]	
		0.0625 [227]	
		0.078 [228]	
		0.576 [229]	
		0.133 [26]	
		0.106 [230]	
		0.1063 [231]	
		0.108 [232]	
		0.123 [233]	
		0.136 [234]	
		0.1402 [235]	
		0.116 [236]	
		0.101 [237]	
		0.1452 [238]	
		0.1495 [239]	
		0.1262 [240]	
		0.1563 [163]	
		0.2025 [264]	
		0.1972 [265]	
		0.1386 [240]	
<i>Phage Qbeta</i>	0.1773±0.027	0.1129 [266]	0.1333 – 0.1667
		0.1840 [267]	
		0.1932 [268]	
		0.19 [269]	
		0.17 [270]	
		0.19 [271]	
		0.2387 [170]	
		0.2752 [163]	
		0.141 [241]	
		0.2798 [272]	
		0.2977 [242]	
		0.285 [273]	
<i>Poliovirus</i>	0.26778±0.089	0.4292 [218]	0.2351 – 0.2938
		0.276 [219]	
		0.3359 [243]	
		0.323 [274]	
		0.325 [275]	
		0.242 [276]	

		0.446 [277]	
		0.32 [26]	
		0.24 [278]	
		0.184 [233]	
		0.103 [279]	
		0.096 [234]	
		0.208 [244]	
		0.191 [244]	
		0.224 [244]	
		0.401 [280]	
		0.206 [281]	
		0.375 [218]	
		0.252 [220]	
		0.35 [47]	
		0.112 [241]	
		0.339 [245]	
		0.2553 [242]	
		0.2837 [242]	
		0.3926 [219]	
<i>Coxsackievirus</i>	0.3044±0.076	0.3962 [243]	0.2444 – 0.3055
		0.3278 [221]	
		0.2 [244]	
		0.2684 [246]	
		0.333 [247]	
		0.2746 [248]	
		0.3685 [248]	
		0.36 [249]	
		0.112 [241]	
		0.31 [245]	
		0.209 [214]	
		0.2785 [242]	
<i>Echovirus</i>	0.2586±0.076	0.3313 [242]	0.2432 – 0.3040
		0.2076 [243]	
		0.219 [244]	
		0.38 [282]	
		0.28 [283]	
		0.141 [241]	
		0.593 [221]	
		0.512 [250]	
<i>Hepatitis A virus</i>	0.3237±0.183	0.461 [229]	0.2463 – 0.3079
		0.25 [284]	
		0.234 [26]	
		0.075 [234]	
<i>Hepatitis E virus</i>	0.38	0.38 [285]	0.2456 – 0.3070
		0.1051 [175]	
<i>Tulane virus</i>	0.2382±0.130	0.41454 [177]	0.2065 – 0.2582
		0.1949 [286]	
		0.154 [241]	
<i>Murine norovirus</i>	0.3088±0.08	0.315 [214]	0.2096 – 0.2620
		0.423 [215]	

		0.3436 [216]	
		0.2971 [248]	
		0.32 [47]	
<i>Human norovirus</i>	0.27	0.27 [47]	0.2191 – 0.2739
<i>Bovine calicivirus</i>	0.43	0.43 [287]	0.2735 – 0.3419
		0.3442 [171]	
		0.136 [241]	
		0.368 [214]	
		0.2644 [217]	
<i>Feline calicivirus</i>	0.3296±0.157	0.3276 [217]	0.2493 – 0.3116
		0.053 [234]	
		0.576 [231]	
		0.527 [280]	
		0.37 [47]	
<i>Canine calicivirus</i>	0.345	0.345 [231]	0.2691 – 0.3363
<i>Borna virus</i>	0.661	0.661 [288]	0.2702 – 0.3377
<i>Avian sarcoma virus</i>	0.1	0.14 [289]	0.0726 – 0.0908
		0.06 [290]	
<i>Murine sarcoma virus</i>	0.1113±0.035	0.097 [291]	0.0810 – 0.1012
		0.16 [292]	
		0.077 [293]	
<i>Friend murine leukemia virus</i>	0.092	0.092 [293]	0.1196 – 0.1495
		0.2 [175]	
<i>Moloney murine leukemia virus</i>	0.1216±0.048	0.128 [292]	0.1187 – 0.1484
		0.082 [293]	
		0.062 [294]	
		0.136 [291]	
<i>Bovine leukemia virus</i>	0.1245±0.004	0.121 [294]	0.1124 – 0.1406
		0.128 [295]	
<i>Human immunodeficiency virus type I</i>	0.084±0.002	0.082 [296]	0.1087 – 0.1209
		0.086 [297]	
<i>Sindbis virus</i>	0.3623±0.092	0.386 [298]	0.4128 – 0.5159
		0.24 [250]	
		0.461 [252]	
<i>Venezuelan equine encephalomyelitis virus</i>	0.419	0.419 [299]	0.3681 – 0.4601
<i>Western equine encephalomyelitis virus</i>	0.43	0.43 [300]	0.4261 – 0.5327
<i>Semliki forest virus</i>	0.5655±0.356	0.21 [301]	0.3687 – 0.4608
		0.921 [302]	
<i>Vesicular stomatitis virus</i>	1.8033±0.617	1.9 [275]	0.3448 – 0.4310
		2.3 [303]	
		1.92 [295]	
		2.3 [304]	
		1.92 [235]	
		0.48 [305]	

<i>Rabies virus</i>	2.193	2.193 [251]	0.3291 – 0.4114
		0.91 [253]	
		0.92 [254]	
		1.82 [254]	
		0.11 [254]	
<i>Influenza A virus</i>	1.052±0.589	2.1 [255]	0.3130 – 0.3912
		0.69 [256]	
		1.27 [258]	
		1.17 [259]	
		0.48 [260]	
<i>Infectious salmon anaemia virus</i>	0.9849±0.135	1.1197 [306]	0.29331 – 0.3664
		0.85 [307]	
<i>Newcastle disease virus</i>	0.9755±0.464	0.511 [308]	0.4518 – 0.5648
		1.44 [309]	
<i>Measles</i>	1.051	1.051 [285]	0.5293 – 0.6616
<i>Human coronavirus 229E</i>	1.3611±0.0026	1.3585 [310]	0.9347 – 1.1684
		1.3637 [192]	
<i>Canine coronavirus</i>	0.808	0.808 [193]	0.9385 – 1.1732
		0.4167 [172]	
		0.7769 [173]	
		0.6144 [199]	
		0.85 [199]	
		2.034 [174]	
		0.37 [174]	
		1 [200]	
		0.88 [200]	
		0.1506 [201]	
		1.2853 [192]	
<i>SARS-CoV-2</i>	1.0358±0.5656	0.3511 [202]	0.9277 – 1.1596
		1.3361 [203]	
		1.854 [203]	
		1.819 [311]	
		1.21 [205]	
		0.26 [205]	
		0.8655 [199]	
		2.098 [206]	
		1.35 [312]	
		1.09 [312]	
		1.14 [312]	
<i>SARS-CoV</i>	0.752±0.585	0.575 [313]	0.8986 – 1.1232
		0.141 [314]	
		1.54 [315]	
<i>Murine hepatitis virus</i>	1.259±0.873	2.1414 [192]	1.0160 – 1.3312
		0.228 [193]	
		2.1666 [310]	
		0.224 [194]	
		1.535 [195]	

For airborne viruses, the model predictions were compared to the UV rate constants for nine available viruses. Since a conservative value of 3 was chosen for the “UV rate constant ratio of aerosol and liquid”, most of the model predictions resulted in a more conservative estimation of UV rate constants for airborne viruses. The two outliers are identified in a red square (porcine respiratory coronavirus and bovine coronavirus, enclosed by a red square). They exhibited significantly smaller experimental values than model predictions, attributed to the underestimation in the experimental data where the virus titers under UV- on conditions fell below detection limits.

Table 19 UV rate constants for the infectivity loss of airborne ssRNA viruses

Microorganisms	UV rate constant $k$ ( $\text{cm}^2/\text{mJ}$ )		Model predictions ( $\text{cm}^2/\text{mJ}$ , 0% protein damage – 20% protein damage)
	Average	Studies in the literature	
<i>Phage MS2</i>	1.604±1.780	5.45 [113]	0.3349 – 0.4187
		1.133 [69,71,90–95]	
		0.43 [114]	
		1.361 [112]	
		1.119 [115]	
<i>Coxsakiavirus</i>	1.110	0.057 [116]	0.7333 – 0.9166
		1.110 [117]	
<i>Sindbis virus</i>	1.040	1.04 [117]	1.2383 – 1.5478
<i>Influenza A virus</i>	2.248±0.661	2.9 [108]	0.9389 – 1.1736
		2.7 [108]	
		2.2 [108]	
<i>Porcine reproductive and respiratory syndrome virus</i>	4.507	4.507 [106]	1.4854 – 1.8568
<i>Porcine respiratory coronavirus</i>	0.186	0.186 [100]	2.7363 – 3.4204
<i>SARS-CoV-2</i>	9.904	9.904 [118]	2.7831 – 3.4788
<i>Murine hepatitis virus</i>	3.77	3.77 [114]	3.1949 – 3.9936
<i>Bovine coronavirus</i>	1.105	1.105 [115]	3.2810 – 4.1012

### 5.3.2 Genome damage model

The genome damage model (Eqs. (53) and (55)) was further evaluated regarding its ability to predict UV-induced genome damage concerning different genome compositions.

Predictions of the UV inactivation efficiency for liquid-based *MS2* (12 genome fractions)

and UV rate constant for airborne *MS2* (17 genome fractions) were compared with the experimental data from the literature (Table 20) and in this study (Table 21), and the results are plotted in Figure 30.

T tests, followed by Bonferroni correction, were conducted to compare the model predictions with experimental data concerning the genome fractions targeted by each primer pair. The results revealed no statistically significant differences (adjusted p values > 0.05, Tables 20 and 21). This finding underscores a broad consensus between the model's predictions and experimental observations regarding UV-induced genome damage at different *MS2* genome locations for both liquid-based and airborne applications. It is worth noting that while certain specific locations displayed discrepancies between the model predictions and experimental data, such as a protein-encoding region (~ 300–600), coat protein-encoding region (~ 1200–1800), and 3' untranslated region (~ 3300–3500), these localized misalignments, spanning a few hundred base pairs, did not exert a significant influence on the overall validation of virus infectivity loss UV rate constants (Section 5.3.1), which encompasses thousands of base pairs, reaffirming the model's robust performance.

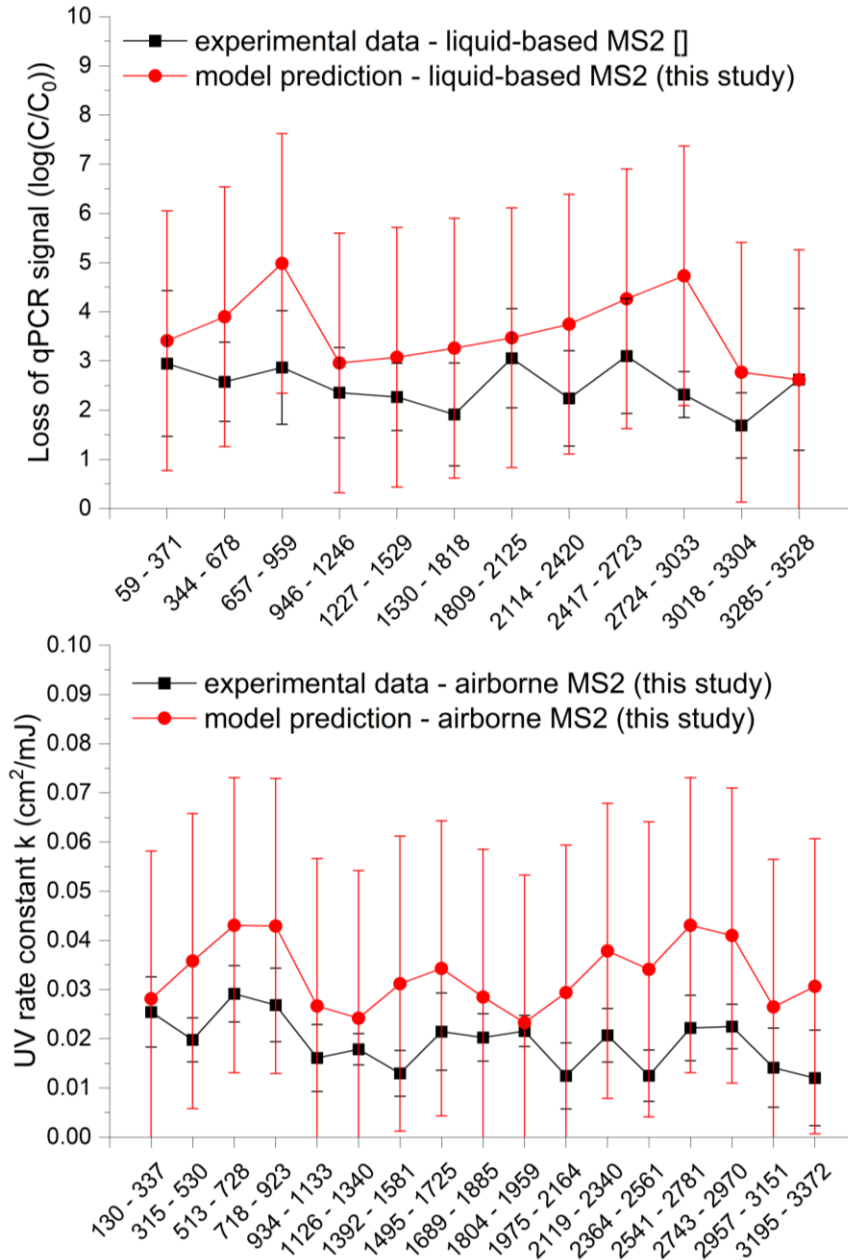


Figure 30 Comparisons of the model predictions of the genome damage (inactivation efficiency and UV rate constant) for liquid-based and airborne *MS2* inactivation.

(Note: The error bar for experimental data represents the standard deviations from three replicates, and the error bar for model predictions represents the root-mean-square deviations from the data fitting)

Table 20 Twelve primer sets used for MS2 UV inactivation tests in liquid and the experimental data of inactivation efficiencies[165]

Primer set	Direction	Primer sequence	Target location/encoding proteins		Loss of qPCR signal (log reduction)		
					Experimental data	Prediction	Adjusted p value
1	Forward	TGTCTTTAGCGAGACGCTACC	59 – 371	A-protein	2.945±1.482	3.411±0.01	1
	Reverse	GATGACCCACTTCGCTTGTAG					
2	Forward	AAGGTGCCTACAAGCGAAGT	344 – 678	A-protein	2.573±0.805	3.898±0.01	1
	Reverse	TTCGTTTAGGGCAAGGTAGC					
3	Forward	CCGCTACCTTGCCCTAAAC	657 – 959	A-protein	2.866±1.155	4.981±0.01	0.3865
	Reverse	GACGACAACCATGCCAAAC					
4	Forward	GCATGGTTGTCGTCTCTAGGT	946 – 1246	A-protein	2.354±0.917	2.957±0.01	1
	Reverse	ACTTTACGTACGCGCCAGTT					
5	Forward	AACTGGCGCGTACGTAAAGT	1227 – 1529	Coat protein	2.267±0.683	3.072±0.01	1
	Reverse	CACCTCGACTTTGATGGTGTA					
6	Forward	CCTAAAGTGGCAACCCAGAC	1530 – 1818	Coat protein	1.911±1.047	3.258±0.01	1
	Reverse	AAAGATCGCGAGGAAGATCA					
7	Forward	CGCGATCTTTCTCTCGAAAT	1809 – 2125	Lysis protein/Replicase protein	3.054±1.008	3.471±0.01	1
	Reverse	GACGATCGGTAGCCAGAGAG					
8	Forward	CTACCGATCGTCGTTGTTTG	2114 – 2420	Replicase protein	2.236±0.969	3.745±0.01	1
	Reverse	GACCCCTTTCTGGAGGTACA					
9	Forward	GGTCGGTGCTTTCATCAGA	2417 – 2723	Replicase protein	3.099±1.169	4.262±0.01	1
	Reverse	TGCCCAGAATATCATGGACTC					
10	Forward	ATAGTCAAAGCGACCCAAATC	2724 – 3033	Replicase protein	2.315±0.466	4.731±0.01	0.2144
	Reverse	GCGTGGATCTGACATACCT					
11	Forward	ATGTCAGATCCACGCCTCTA	3018 – 3304	Replicase protein	1.688±0.664	2.768±0.01	1
	Reverse	TTCATGCTGTCGGTGATTTT					
12	Forward	GAAATCACCGACAGCATGAA	3285 – 3528	Replicase protein	2.622±1.441	2.616±0.01	1
	Reverse	AATCCCGGGTCCTCTCTTA					

Table 21 Seventeen primer sets used for airborne *MS2* UV inactivation tests and the experimental data of the genome damage UV rate

constant

Primer set	Direction	Primer sequence	Target location/ encoding proteins		Amplification factor	UV rate constant (cm <sup>2</sup> /mJ)		
						Experimental data	Predictions	Adjusted p value
1	Forward	GTGCGAGCTTTTAGTACCCTTG	130 – 337	A-protein	2.016	0.0254±0.007	0.0281±0.03	1
	Reverse	TCGATGTGACACTTAACGCC						
2	Forward	GGGGGCGTTAAGTGTCACATC	315 – 530	A-protein	2.039	0.0198±0.004	0.0358±0.03	1
	Reverse	TGGGTGACCTTTTGCAGGAC						
3	Forward	CCTGCAAAGGTCACCCAGGG	513 – 728	A-protein	2.028	0.0291±0.006	0.0431±0.03	1
	Reverse	TGCAACTCCAACCACCTGCCG						
4	Forward	TTGGAGTTGCAGTTCGGTTGG	718 – 923	A-protein	2.000	0.0269±0.007	0.0429±0.03	1
	Reverse	AACCATATCACGATACGTCGCG						
5	Forward	GATGCACGTTTGGCATGGTTG	934 – 1133	A-protein	2.134	0.0161±0.007	0.0266±0.03	1
	Reverse	ACGCTTATGATGGACTCACCCG						
6	Forward	ATAAGCGTTGACGCTCCCTAC	1126 – 1340	A-protein	1.997	0.0179±0.003	0.0242±0.03	1
	Reverse	AGCCATGCTTCAAACCTCCGG						
7	Forward	ACTGTCGCCCCAAGCAACTTC	1392 – 1581	Coat protein	2.054	0.0130±0.005	0.0312±0.03	0.6571
	Reverse	ATGCGGCTACAGGAAGCTCTAC						
8	Forward	CGCAGAATCGCAAATACACCATC	1495 – 1725	Coat protein	1.801	0.0214±0.008	0.0343±0.03	1
	Reverse	AGTAGATGCCGGAGTTTGCTG						
9	Forward	ATTCCCTCAGCAATCGCAGC	1689 – 1885	Lysis protein/ Replicase protein	2.087	0.0203±0.005	0.0285±0.03	1
	Reverse	AAGTCGTCACTGTGCGGATC						
10	Forward	TTCCTCGCGATCTTTCTCTCG	1804 – 1959	Lysis protein/ Replicase protein	2.075	0.0216±0.003	0.0233±0.03	1
	Reverse	TCGCCTCGTCATTACCAGAAC						

11	Forward	CTATCGCTAAGCTACGGGAGG	1975 –	Replicase	1.982	0.0124±0.007	0.0294±0.03	0.8876
	Reverse	ATAGGAGCACCGTTGGAGAAC	2164	protein				
12	Forward	GATCGTCGTTGTTTGGGCAATG	2119 –	Replicase	1.756	0.0207±0.005	0.0379±0.03	0.8433
	Reverse	ACACTCCGTTCCCTACAACGAG	2340	protein				
13	Forward	ATAGATCGGGCTGCCTGTAAG	2364 –	Replicase	2.033	0.0125±0.005	0.0341±0.03	0.2893
	Reverse	GGAGATGGAATCGGATGCAGAC	2561	protein				
14	Forward	TCTGCATCCGATTCCATCTCC	2541 –	Replicase	1.993	0.0222±0.007	0.0431±0.03	0.3469
	Reverse	CCCCGTAGATGCCTATGGTTC	2781	protein				
15	Forward	TCCATTTTGGTAACGCCGGAAC	2743 –	Replicase	1.916	0.0225±0.005	0.0410±0.03	0.6157
	Reverse	GGCGAAGAGATTGTCAACAG	2970	protein				
16	Forward	CAATCTCTTCGCCCTGATGCTG	2957 –	Replicase	1.957	0.0141±0.008	0.0265±0.03	1
	Reverse	TTGGTGTATACCGAGACTGCC	3151	protein				
17	Forward	TTCCGTCTTGCTCGTATCGCTC	3195 –	Replicase	1.892	0.0120±0.010	0.0306±0.03	0.5979
	Reverse	ACTCCTGAGGGAATGTGGGAAC	3372	protein				

## 5.4 Results and discussions

### 5.4.1 Prediction of infectivity loss UV rate constants for ssRNA viruses

in liquid and comparisons of different UV rate constant models in the literature

Comparisons between the model predictions and the experimental data of infectivity loss UV rate constants for 36 ssRNA viruses are presented in Figure 31, which shows good agreement for the positive-sense (+) RNA viruses.

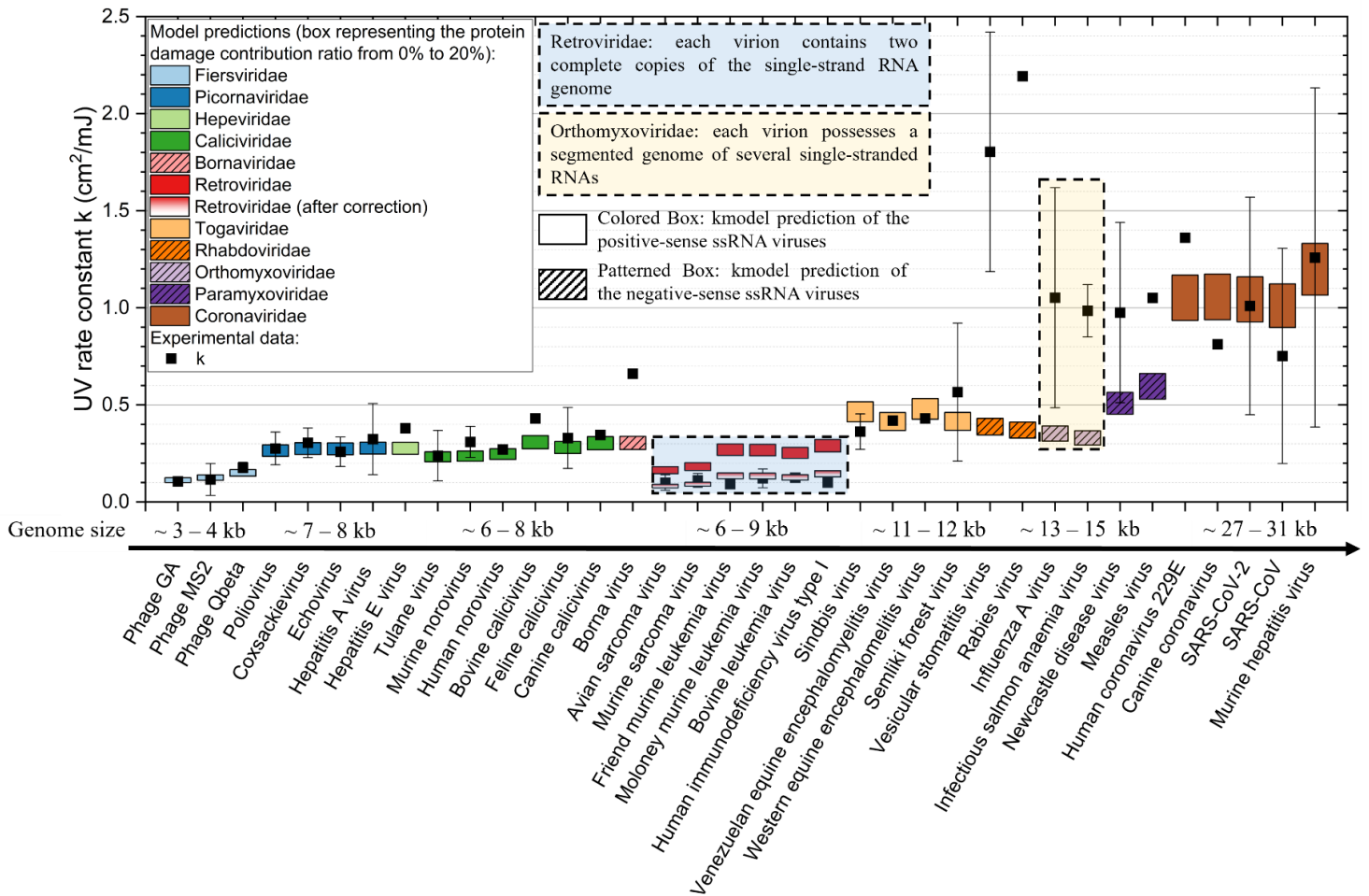


Figure 31 Comparisons between model predictions and experimental data from the literature for the UV rate constants of ssRNA viruses

Detailed MREs of each virus and virus family for this model are included in Section 5.3.1. In this section, we further compare the prediction results of the infectivity loss UV rate constants between different models in the literature, including the one presented in this thesis, as summarized in Table 22 and Figure 32.

The comparisons revealed a nuanced picture of model performance across different viruses. Specifically, no single model was found to excel universally across all viral types. The strengths of each model varied depending on the virus group targeted. In detail, the pure empirical model from Lytle et al. [41] covered 10 virus family groups and was effective in estimating UV rate constants for *Retroviridae*, *Orthomyxoviridae*, and *Paramyxoviridae*. However, it is essential to acknowledge that this model simplistically assumes identical UV rate constants for viruses within the same family group, lacking the resolution to distinguish between individual viruses within the group.

The physics-based model from Cheng et al. [33] covered 10 virus family groups and reported accurate predictions for *Bornaviridae*, *Orthomyxoviridae*, and *Paramyxoviridae*. This model derives its predictions from experimentally measured quantum yield values for various photoreactions, offering strong physical interpretability. Nevertheless, it exhibits low accuracies for several virus family groups, likely attributed to the limited availability and significant variations in quantum yield data.

The semi-empirical approach by Pendyala et al. [38] covered 2 virus family groups and worked well for *Caliciviridae*. However, the model assigned parameters devoid of discernible physical significance, as it assigns identical contribution factors for different

bioinformatics (TT%, TC%, CT%, and CC%) as one. Another semiempirical approach by Rockey et al. [31] covered 6 virus family groups and demonstrated positive outcomes for *Hepeviridae* and *Togaviridae*. Their principal component analysis-based model incorporated multiple collinear genomic variables. However, as they mentioned in their paper, the dataset for model regression analysis was limited and unbalanced [31]. Furthermore, similar to Pendyala et al. [38], they used the leave-one-virus-out cross-validation method, potentially resulting in high-variance performance estimates and overfitting.

The semi-empirical model developed in this work exhibited robust predictive capabilities for *Fiersiviridae*, *Picornaviridae*, and *Coronaviridae*. A notable distinction between our model and previous semiempirical models [31,38] is that it relies on two independent databases for establishment and validation. Model parameters are determined using experimental data from qPCR experiments and demonstrate interpretable statistical and physical significance. Model validation employs infectivity loss experimental data, yielding good agreement for the (+) ssRNA viruses. The utilization of two distinct datasets effectively mitigates data leakage issues and reduces the risk of overfitting. Nevertheless, our model's performance may be influenced by the size of the database as well, potentially contributing to less accurate estimations for (-) ssRNA viruses (*Bornaviridae*, *Rhabdoviridae*, *Orthomyxoviridae*, and *Paramyxoviridae*), as we mentioned before. Furthermore, our database does not strictly exclude experimental data that fail to report UV attenuation in the experimental solutions, unlike a prior study [31]. Consequently, our model may underestimate UV rate constants due to these experimental data utilizing higher UV doses for UV rate constant calculation without UV attenuation correction.

In summary, the comparative analysis of existing models emphasizes the necessity of judiciously selecting the optimal model to predict UV rate constants for specific virus groups in practical applications. Based on our evaluation, we recommend specific models for the 11 ssRNA virus family groups, taking into account their respective performance, as detailed in Table 22 for reference.

Table 22 Comparisons of the model performance for the predicted infectivity loss UV rate constants of ssRNA viruses in liquid

Virus family	Mean relative error (MRE) between model predictions and experimental data				
	This study	Lytle et al. [41]	Cheng et al. [33]	Pendyala et al. [38]	Rockey et al. [31]
<i>Fiersviridae</i>	*	-	†	-	†
<i>Picornaviridae</i>	*	***	†	-	**
<i>Hepeviridae</i>	***	†	-	-	*
<i>Caliciviridae</i>	**	**	†	*	***
<i>Bornaviridae</i>	†	†	*	-	-
<i>Retroviridae</i>	†	**	†	-	-
<i>Togaviridae</i>	**	**	†	-	*
<i>Rhabdoviridae</i>	†	***	†	-	-
<i>Orthomyoviridae</i>	†	*	*	-	-
<i>Paramyxoviridae</i>	†	**	**	-	-
<i>Coronaviridae</i>	**	†	†	***	†

\* : MRE < 10%; \*\* : 10% < MRE < 20%; \*\*\* : 20% < MRE < 30%; † : MRE > 30%; - : data not reported in their studies; and symbol in red: the recommended model for this virus family group

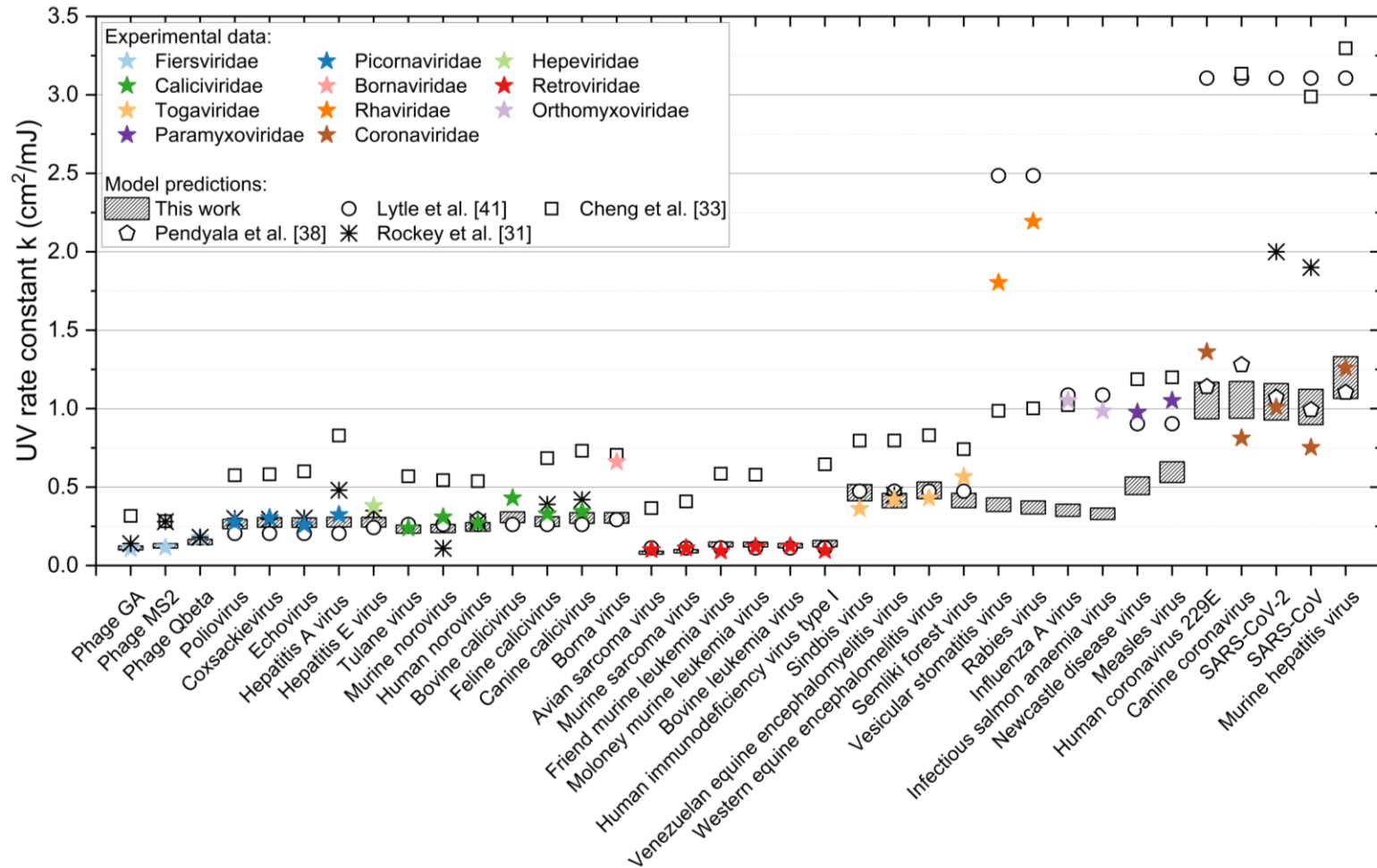


Figure 32 The comparisons between the model predictions (models from the literature [31,33,38,41] and this study) and experimental data for the ssRNA viruses in liquid

## 5.4.2 Prediction of infectivity loss UV rate constants for airborne ssRNA viruses

The UV rate constants of airborne ssRNA viruses were predicted using Eq. (56). Note that some viruses were omitted from the prediction due to their irrelevance to human health or non-airborne transmission methods. These include *bacteriophages* (non-harmful to humans [316]); *Hepatitis A virus* (not airborne [317]); *Hepatitis E virus* (mainly through fecal-oral route [318]); *murine norovirus* (non-harmful to humans [319]); *Bornavirus* (non-harmful to humans[320]); *bovine, feline, and canine caliciviruses* (non-harmful to humans (Dastjerdi et al., 2000; Hofmann-Lehmann et al., 2022; Mochizuki et al., 2002)); *retroviruses* (infections mainly through sexual contact, exposure to contaminated blood, or perinatally[324]); *Togaviridae* (mainly transmitted via insects[325]); *Rhabdoviridae* (mainly through infected mammal bite[326]); *infectious salmon anemia virus* (non-harmful to humans [327]), and *murine hepatitis virus* (non-harmful to humans [328]). An exception is the *canine coronavirus*, which has been reported to transmit to human hosts from dogs [329] and thus was retained in our analysis. The UV rate constant prediction results are included in Table 23.

Table 23 Predicted UV rate constants for potential airborne ssRNA viruses

Microorganisms	<i>Poliovirus</i>	<i>Coxsackievirus</i>	<i>Echovirus</i>	<i>Tulanevirus</i>	<i>Human norovirus</i>	<i>Influenza A virus</i>	<i>Newcastle disease virus</i>	<i>Measles virus</i>	<i>HCoV-229E</i>	<i>Canine coronavirus</i>	<i>SARS-CoV</i>	<i>SARS-CoV-2</i>
UV rate constants (cm <sup>2</sup> /mJ)	0.793	0.825	0.821	0.970	0.739	1.056	1.525	1.786	3.155	3.168	3.033	3.131

The same conclusions were observed for airborne viruses as for those in the liquid-based matrix, which is that viruses with larger genome sizes generally have higher UV rate constants and are easier to inactivate. Moreover, for viruses within the same family, similarities in genome sizes and protein structures resulted in analogous UV rate constants. Furthermore, we assessed the alignment of our model predictions with real-world applications, particularly by estimating the UV rate constant for airborne *SARS-CoV-2* as  $3.131 \text{ cm}^2/\text{mJ}$ . This estimation corresponds to UV doses of  $735 \text{ }\mu\text{J}/\text{cm}^2$  and  $1471 \text{ }\mu\text{J}/\text{cm}^2$ , achieving 90% and 99% inactivation of *SARS-CoV-2*, respectively. Notably, ASHRAE's epidemic task force [9] recommends minimum UV doses of  $611 \text{ }\mu\text{J}/\text{cm}^2$  and  $1222 \text{ }\mu\text{J}/\text{cm}^2$  for 90% and 99% inactivation, respectively. Considering the conservative nature of our UV rate constant estimation in this study, this alignment suggests that our model predictions closely meet real-world requirements for effectively inactivating *SARS-CoV-2*, a critical practical consideration.

## **6 Analysis of influencing Factors affecting the In-duct UVGI System Inactivation Efficiency**

Following the experimental data and model prediction results in the previous chapters, this chapter provides a detailed analysis of how key factors influence the performance of an in-duct UVGI system from the perspective of different system designs, operating conditions, and bioaerosol characteristics. This chapter includes an examination of how elements of duct system designs (UV lamp arrangements and duct wall materials) impact the average accumulated UV dose, and how operating conditions (RH) and bioaerosol characteristics (bioaerosol particle size and microorganism species) influence the UV rate constant for airborne microorganisms. These insights collectively shed light on the factors that affect UV inactivation efficiency in in-duct UVGI systems.

### **6.1 Effects of the in-duct UVGI system designs**

The in-duct UVGI system designs, including the UV lamp arrangements and duct wall materials, are found to impact the UV irradiance distribution inside the duct (Section 3.4.1.2), thus influencing the average accumulative UV dose at the duct outlet (Section 4.4.1) and determine the UV inactivation efficiency (3.4.2.1).

The effect of UV lamp arrangements in the current experimental setup is straightforward in two aspects: (a) the more UV lamps are used, the higher the overall UV irradiance inside the duct (Table 9), thus, the higher UV dose received by the airborne microorganisms (Table 15) and results in higher UV inactivation efficiency (Table 11); and (b) when placing two UV lamps in the two rows at the front and back locations, there are more

shadowing effects between the two lamps (Figure 19 (g) – (k)) compared to placing them in one row side to side (Figure 19 (e) – (f)).

As for the duct wall materials, the effects are two-fold, which are related to the material reflectivity and the reflection type: (a) the higher the material reflectivity is, the higher the overall UV irradiance inside the duct (Table 9), thus, results in higher UV inactivation efficiency (Table 11); and (b) when the reflectivity of two materials are close, highly diffusely reflection provides a more uniform UV irradiance distribution and overall higher average radiation inside the duct, thus better inactivation efficiency (Table 11).

This observation was supported by a previous in-duct UVGI study that compared the disinfection efficiency among the black surface ( $R=0$ ), galvanized iron sheet, and mirrored surface, where galvanized iron sheet showed approximately 1.5% and 20% higher *E. coli* inactivation efficiency than the mirrored surface and black surface, respectively, which was in close agreement with the experimental results in this study (Table 15) [157]. Further, the same observations were made in an annular UV reactor for PCO reactions, where the uniformity of the UV fluence rate distribution was strongly dependent on the diffuse reflection property of the inner wall, and the UV reactor performance was significantly enhanced with an increase in the diffuse reflection fraction under the highly reflective inner wall scenario ( $R=0.8$ ) [159,160]. Another study designed an annular UV reactor for air disinfection and reported that the UV radiation flux increased 20 to 40 times by constructing walls with porous structured, highly diffusely reflective materials, polytetrafluoroethylene (PTFE), and expanded PTFE (ePTFE), and its distribution became uniform and highly symmetric [161]. All evidence in the literature discussing the effects of wall properties on the irradiance distribution within a UV reactor is presented in Table

24. Overall, increasing the wall reflectivity effectively enhances UV energy utilization, mainly when the reflectivity is low or moderate. However, for highly reflective materials or materials with similar reflectivity, diffuse reflection provides a more uniform irradiation distribution within the duct along the duct length (x-direction) and across duct cross-sections (y/z planes). Thus, an overall higher and more uniform irradiance distribution is obtained by increasing the fraction of diffuse reflection irradiance. In conclusion, the commonly used galvanized steel in HVAC systems works well for the UVGI reactor.

Table 24 Effect of duct wall materials on the UVGI efficiency in different reactors

Designs	Wall materials	Conclusions
[157] in-duct UVGI: <i>E. coli</i> inactivation efficiency	Black surface, galvanized iron sheet, and mirrored surface	Black surface: 72.7% (U=3.0 m/s), 62.5% (U=4.5 m/s) and 57% (U=6.0 m/s) Galvanized iron sheet: 96.7% (U=3.0 m/s), 85.2% (U=4.5 m/s) and 84.1% (U=6.0 m/s) Mirrored surface: 95.2% (U=3.0 m/s), 83.1% (U=4.5 m/s) and 82.5% (U=6.0 m/s)
[61] In-duct UVGI: <i>E. coli</i> inactivation efficiency <sup>1</sup>	Steel wall (R=0.37) and galvanized wall (R=0.57) <sup>2</sup>	Steel wall: 70.5% (U=3.0 m/s), 57.3% (U=4.5 m/s), 49.2% (U=6.0 m/s) and 42.5% (U=7.0 m/s) Galvanized steel: 76.3% (U=3.0 m/s), 61.2% (U=4.5 m/s), 54.3% (U=6.0 m/s) and 49.2% (U=7.0 m/s)
[64] In-duct UVGI: radiation	Galvanized steel and black flock paper-lined duct	The cross-sectional average irradiance increases by 1.48 to 3.01 times using reflective galvanized steel walls. Moreover, the further away from the lamp, the more evident are the contributions of the reflection (ratio of total irradiance for galvanized steel and black flock).
[51] Upper-room UVGI: radiation <sup>1</sup>	Lumacept coated reflective room wall	The volume-averaged incident radiation increased by 60% in the presence of UV-reflective walls.
[159] Annular UV reactor: radiation <sup>1</sup>	Highly reflective (R=0.8) and ordinary (R=0.26) inner walls	UV reactors with a highly reflective inner wall (R=0.80) had evidently higher UV fluence rates than those with an ordinary inner wall (R=0.26). Furthermore, the inner-wall diffuse reflection further increased the reactor's overall average UV fluence rate.
[160] Annular UV reactor: radiation	Quartz/aluminum foil (R=0.805), quartz/stainless steel (R=0.261), and quartz/black cloth (R=0.111)	An inner wall with a high reflectivity leads to a marked increase in the UV fluence rate and better reactor efficiency. Furthermore, a more uniform fluence rate inside the UV reactor was achieved with a rough surface, enhancing diffuse reflection.
[161] Annular UVGI reactor: radiation	PTFE and ePTFE	Up to 20 times the amplification of the UV irradiation in the UV reactor was observed, and its distribution became uniform and highly symmetric.
This study	Mirror-like finish stainless steel and galvanized steel	Stainless steel: 95.60% (U=1.35 m/s) Galvanized steel: 97.25% (U=1.35 m/s)

1: The inactivation efficiency and radiation were obtained by simulations.

2: Assumed pure diffuse reflection.

## 6.2 Effect of the in-duct UVGI system operating condition (RH)

### 6.2.1 Underlying mechanisms of the impact of RH on the UV rate constant in the current UVGI system

The environmental RH is found to be a critical factor in influencing the UV rate constant of airborne microorganisms (Section 4.4.2), thus determining the UV inactivation efficiency (Section 3.4.2.2). In this study, the airborne *MS2* UV inactivation was tested under three RH conditions, and the UV rate constant data were found to be an initial increase and then a decrease when the RH rose from 25% to 40% and then to 60% (Section 4.4.2).

The initial increase in the UV rate constant for RH ranging from 40% to 60% is straightforward, which is due to the increased UV absorption by the water in bioaerosols. In this study, salt-based bioaerosols were generated from a PBS solution. The tested RHs (25%, 40%, and 60%) either fell below or similar to the deliquescence RHs of the pure components of PBS (namely, NaCl, KCl, Na<sub>2</sub>HPO<sub>4</sub>, and KH<sub>2</sub>PO<sub>4</sub> with respective deliquescence RHs of 73%–77%, 83%–86%, >96%, and >50% at 25°C [330–332]). Thus, theoretically, no water uptake should occur as the bioaerosols pass through the dryer and are subsequently exposed to the ambient duct environment, which eliminates water's impact on UV absorption and inactivation efficiency. However, in practice, bioaerosols consist of a combination of salt crystals and virions, resulting in varying water sorption and hygroscopic behaviors compared to individual salt aerosol particles [333,334]. For instance, when observing the hygroscopic growth curve for *MS2* aerosolized from a PBS

solution, there is a modest increase (10.68% volume change) as the RH rises from 40% to 60% [335]. Bioaerosols of different bacteria species, such as *E. coli*, *Bacillus subtilis*, *Serratia marcescens*, and *Mycobacterium parafortuitum*, demonstrate a similar trend when aerosolized from deionized water. As RH elevates from 40% to 60%, these bioaerosols display noticeable water sorption and hygroscopic growth, represented by a 3.93% diameter change in *E. coli*, a 1.69% diameter change and a 123.46% mass change in *B. subtilis*, and 80.85% mass change in *S. marcescens*, and an 83.16% mass change in *M. parafortuitum* [22,336]. This evidence suggests that bioaerosols exhibit water sorption when RH increases in the intermediate RH range (40% to 60%). Consequently, the absorbed water may enhance UV attenuation, resulting in a lower UV rate constant at higher RH levels.

Meanwhile, a symmetrical trend was observed where the UV rate constant decreases when the RH is reduced from an intermediate level (40%) to a low level (25%). This finding aligns with the observation of another study in the literature (see Figure 33) that the highest UV rate constant for airborne porcine respiratory and reproductive syndrome viruses are found at an intermediate RH (25% - 79%), regardless of ambient temperatures ( $\leq 15^{\circ}\text{C}$ ;  $16^{\circ}\text{C} - 29^{\circ}\text{C}$ ; and  $\geq 30^{\circ}\text{C}$ ), compared to highly humid ( $>80\%$ ) and dry ( $<24\%$ ) environments [106]. However, the literature does not explain the decreased UV rate constant at low RH. In this study, considering the salt-based bioaerosols, water uptake and the water effect in bioaerosols at low RH are minimal. This conclusion is supported by the reported minimal water sorption/hygroscopic growth of the above-mentioned airborne microorganisms when RH is increased from 25% to 40% (*MS2*: -2.38% volume change; *E. coli*: 2.54% diameter change; *B. subtilis*: 0.6% diameter change; *B. subtilis*: 44.25%

mass change; *S. marcescens*: 34.91% mass change; and *M. parafortuitum*: 14.17% mass change) [22,336]. Furthermore, if water effects are present, minimal water uptake would contribute negatively to the UV rate constant when the RH is varied from 25% to 40%, which contradicts the experimental data. Thus, we suspect another factor exists, potentially interfering with the relationship between ambient RH and viral susceptibility to UV radiation.

A plausible hypothesis is that RH affects airborne viruses' structural integrity and survivability, thereby influencing UV inactivation. This hypothesis was briefly mentioned in a UVGI study on airborne bacteria, which proposed that hydration/rehydration under different RH levels might alter protein structures and cell wall biopolymer conformations. These changes could impact the DNA repair process and control the extent of UV inactivation [22]. As for MS2, as a non-enveloped virus, studies in the literature show better survivability in both dry (<30% RH) and humid (>80% RH) environments, while its survivability is minimal in moderately moist conditions (~50%–60% RH) [337–339]. The underlying mechanisms remain unclear. However, it is suspected that abrupt hydration occurs when bioaerosols pass through the drying process and are exposed to the ambient duct environment. This hydration induces structural rearrangement and damage to the capsid of non-enveloped viruses [340,341]. The level of abrupt hydration is minimal under dry conditions, resulting in higher virus survivability at 25% compared to 40% and 60% RH.

Although the direct influence of environmental RH on virus viability has been considered during UV-off and -on sampling under the same operating conditions, the subsequent indirect interference from structural damage affects the effective utilization of UV energy

within the virion. In detail, more capsid damage occurs at higher RH due to the abrupt hydration, resulting in increased UV light penetration through the capsid and greater UV exposure to the *MS2* nucleic acid. Given that the primary UV inactivation mechanism for *MS2* is RNA damage rather than structural protein damage [30,39], this leads to higher UV inactivation efficiency. In other words, the maximum *MS2* survivability (with less viral structure damage) at 25% RH indirectly inhibits UV inactivation, leading to a relatively lower UV rate constant compared to 40% RH.

Overall, considering the combined effects of the reduced UV penetration (leading to decreased UV irradiation on virus RNA) due to the more intact virus structure at lower RH and the increased UV absorption (resulting in reduced UV irradiation on viruses) due to the higher water content in bioaerosols at higher RH, the UV rate constant for *MS2* exhibits a pattern of initial increase followed by a decrease as environmental RH rises from 25% to 60%.

## 6.2.2 Discussion of the impact of RH on the UV rate constant in the literature

Limited research has explored the impact of environmental RH on the UV rate constants of airborne viruses in the literature. In Figure 33, all available UV rate constant data from the literature are summarized and presented. Despite variations in test microorganisms across existing studies, a consistent observation emerges: there is a reduction in the UV rate constant at intermediate to high RH levels (> 50% - 60% RH). This decline is attributed to the increased water content in bioaerosols, leading to enhanced UV absorption [20,23,26,109]. Particularly in highly humid environments (RHs >80% ~ 90%),

deliquescence occurs (if using salt-based aerosols), causing particles to transition into an aqueous state, significantly boosting UV absorption by water and diminishing inactivation efficiency [342].

However, there is inconsistency in the reported UV rate constant data for conditions with lower to intermediate humidity (< 50% - 60% RH). Three studies [106,114], including our own, observed an increased UV rate constant as RH increased (from ~ 25% RH to ~ 50% RH), while two other studies reported the opposite [107,108]. In retrospect, it is suspected that the structural rearrangement and damage of airborne viruses during the drying and subsequent hydration process contribute to the higher UV rate constant under intermediate humid conditions. Upon examining the detailed experimental setups of these studies, it is noteworthy that the ones reporting a decreasing trend in UV rate constants for *vaccinia virus* (20.5% - 60.5% RH) [107] and *influenza virus* (25% - 50% RH) [108] did not involve a dryer in their experiments. In contrast, both this study (*MS2*, 25% - 40% RH) and the work by Walker et al. [114] (*Adenovirus*, 33.5% - 52.5% RH) used a dryer and reported the opposite trend. However, another study that reported the same trend (porcine respiratory and reproductive syndrome virus, 24% - 52% RH) [106] did not specify whether a dryer was used. Therefore, the inconsistency in conclusions regarding the effect of RH on the UV rate constant may be related to experimental procedures involved in the bioaerosol drying process.

Nonetheless, as mentioned earlier, further increasing RH from intermediate to high RH levels (>60%), the UV rate constant consistently decreases with the increase in RH, regardless of whether a bioaerosol dryer is employed [109] or not [107,108]. This suggests that the impact of structural rearrangement and damage becomes less pronounced

compared to the influence of enhanced UV absorption due to increased water content under high RH conditions.

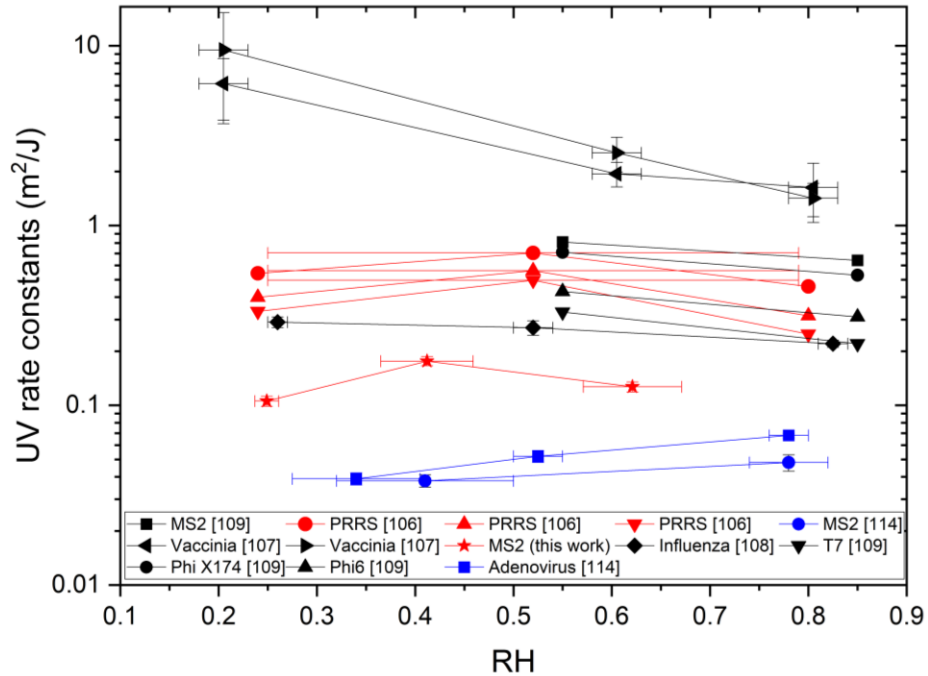


Figure 33 Comparisons of UV rate constants for airborne viruses exposed to UVGI at different RH levels in the literature [106–109,114]

(Note: The x-axis error bar represents the RH variations during the experiment, and the y-axis error bar represents the UV rate constant standard deviations.)

### 6.3 Effect of the bioaerosol characteristics

#### 6.3.1 Impact of bioaerosol particle size on UV rate constant for airborne MS2

Analogous to RH, the bioaerosol particle size is found to be a critical factor in influencing the UV rate constant of airborne microorganisms (Section 4.4.3), thus determining the UV inactivation efficiency (Section 3.4.2.3). In this study, the airborne MS2 UVGI tests were

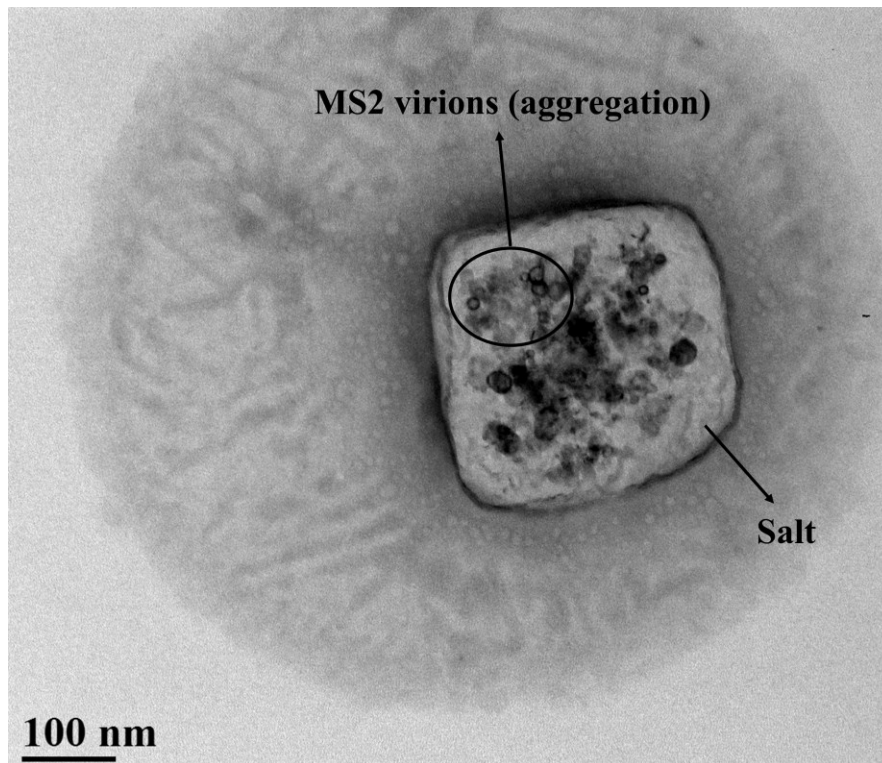
measured in five particle size ranges (stage 2: 4.7–7  $\mu\text{m}$ , stage 3: 3.3–4.7  $\mu\text{m}$ , stage 4: 2.1–3.3  $\mu\text{m}$ , stage 5: 1.1–2.1  $\mu\text{m}$ , and stage 6: 0.65–1.1  $\mu\text{m}$ ; in aerodynamic diameter). The results showed that larger bioaerosols (2.1–7  $\mu\text{m}$ , stages 2, 3, and 4) exhibited significantly lower UV rate constants compared to smaller ones (0.65–2.1  $\mu\text{m}$ , stages 5 and 6) (Section 4.4.3).

A few studies have discussed the effect of particle size on UVGI inactivation efficiency in the literature, and factors such as cell aggregation on bioaerosols [20] and UV protection provided by aerosol particles [111] have been advised as influencing factors. Therefore, in this study, as mentioned in Section 3.3.2.3, the TEM imaging was conducted to observe the internal structure of *MS2* bioaerosols. The image showed that the *MS2* bioaerosol consists of a cubic salt crystal with numerous viral particles attached (20–30 nm) (Figure 34(a)). Moreover, EFTEM analysis (Figure 34(b)) further verified the widespread distribution of Na, K, and Cl ions (main components of the PBS solution) within the *MS2* bioaerosol.

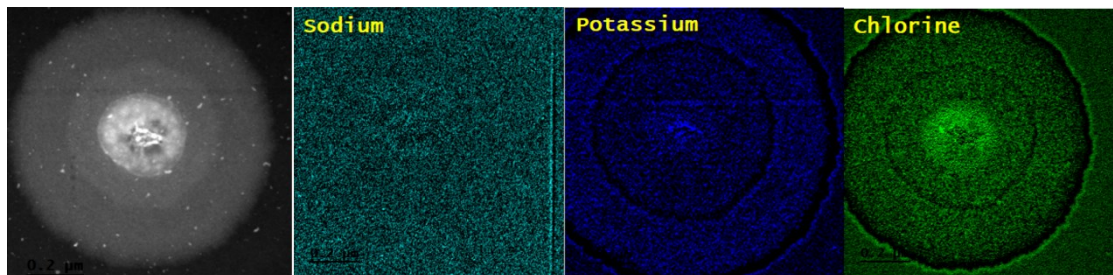
It is well-established that multiple virions reside within a single bioaerosol particle, with the viral load increasing exponentially or following other mathematical relationships (depending on the suspending medium) with the particle size [128,343,344]. These multiple virions may be homogeneously distributed within the particles, accumulate on the particle surface, or form aggregates randomly scattered inside the bioaerosols when aerosolized from the deionized water, beef extract solution, or artificial saliva (comprised of inorganic salts with mucins) [343]. In this study, random *MS2* aggregations were observed in the PBS particle (Figure 34(a)) as an expected outcome, given that the main components of artificial saliva include the elements of PBS [345]. The virion aggregations,

in return, are likely to diminish the UV dose received by each viral particle due to the shadowing effect, a phenomenon associated with clusters of aggregated particles [346,347]. Consequently, as the viral load of *MS2* in a single bioaerosol increases with the particle size, the probability of forming aggregates increases, leading to increased UV shadowing and a subsequent decrease in UV inactivation efficiency.

Beyond virion aggregation within individual particles, clusters can also form among PBS aerosol particles [348]. Therefore, larger bioaerosols may result from either an increase in particle size or the aggregation of particles. Combining the evidence of virions aggregating within bioaerosol particles, both an increase in particle size and particle aggregation lead to greater UV absorption and shadowing as the UV light attempts to penetrate the salt crystals and reaches the internal *MS2* virions. This finding supports the experimental data presented in this study, which observed lower UV rate constants for larger particles than smaller ones.



(a)



(b)

Figure 34 (a) TEM image of an *MS2* bioaerosol (sample comes from stage 4); and (b) EFTEM analysis of an *MS2* bioaerosol from stage 4.

(Note: the distribution of K and Cl ions was found to follow the structure of the original particle, while Na ions expanded beyond the particle and redistributed across the heated TEM substrate. This phenomenon may be attributed to beam damage from the TEM

equipment: the high energy of the electron beam bombarded the sample, reacted with the noncrystalline (likely liquid-containing) material, and redistributed the Na ions[134,349]

### 6.3.2 Impact of microorganism species on UV rate constant

Different airborne virus species, contain nucleic acids with different genome sequences and potentially different protein structures, resulting in different UV rate constants (Section 5.4). This study introduces an improved genomic model to predict the UV rate constants of ssRNA viruses in the liquid-based matrix (Section 5.4.1) or airborne state (Section 5.4.2).

In general, irrespective of liquid-borne or airborne ssRNA viruses, it is observed that viruses with larger genome sizes exhibit greater sensitivity to UV illumination, resulting in higher UV rate constants. This is consistent with the literature, which highlights that a longer genome provides more sites for photodimerization, leading to increased genome damage and infectivity loss [26,38]. For viruses within the same family, similarities in genome sizes and protein structures resulted in analogous UV rate constants.

However, there are some exceptions for viruses with unique genetic structures. For instance, as mentioned in Section 5.1.2.2, the model accounted for the pseudodiploid nature of retroviruses, wherein two complete RNA copies would effectively increase the likelihood of successful DNA synthesis under UV exposure. This adjustment significantly improved the match between model predictions and experimental data, reducing the MRE to 20.32% from an initial 99.11% (assuming the median contribution ratio of protein damage is 10%) by halving the predicted genome damage. This supports the notion that the pseudodiploid nature of the retroviral genomes increases resistance to UV exposure, and a half-reduction correction shall be implemented in the model to estimate the UV rate constants for

retroviruses. Besides the pseudodiploid nature of retroviruses, it is noticed that the current model faces challenges in accurately predicting UV rate constants for segmented RNA viruses (*Orthomyxoviridae*). This discrepancy may arise from the complex UV-RNA interactions resulting from segmented RNA, a feature not considered in our current model. Similarly, as mentioned in Section 5.3.1, the model exhibited better predictions for (+) ssRNA viruses than for (-) ssRNA viruses. This discrepancy is suspected to result from differences in the viral replication process: (+) ssRNA virus consists of viral mRNA that can be directly translated into proteins, whereas (-) ssRNA virus requires an additional step of synthesizing the corresponding positive RNA strand before translation [350]. While the current genomic model does not detail genome replication and translation processes, this observation highlights an area for future exploration and refinement. Furthermore, the database for model parameter determination contains mainly the qPCR tests for the (+) ssRNA viruses. Thus, underestimations were observed for (-) ssRNA viruses.

## **7 Engineering Implications: A Case Study Aiming at Airborne ssRNA Viruses' Inactivation**

The design of a UVGI system for disinfecting airborne microorganisms in a complex duct environment involves careful consideration of various parameters. This thesis conducted comprehensive investigations on the critical influencing factors from the engineering and biological perspective. This section aims to integrate the research outcomes from previous sections, propose a comprehensive UVGI system design flowchart, and illustrate its application for the effective design and implementation of UVGI technology in controlling the bioaerosols in the duct environment.

### **7.1 UVGI system design flowchart**

Based on the water UV treatment guidance manual from the U.S. Environmental Protection Agency [351], this thesis introduced a comprehensive flowchart for the UVGI system designs in the air applications (Figure 35). In detail, the initial step in planning a UV disinfection facility for air treatment is to define its types and goals, including the selection of the UVGI system type (upper-room, in-duct, or portable cleaner), identification of target microorganisms, target inactivation efficiency, and the required UV dose. Next, the impact of applying UV disinfection in the target environment must be evaluated, considering factors such as safety for human beings and the effects of UV on technologies and materials within the irradiated zone. Additionally, the working conditions of the UV facility, such as air temperature, RH, velocity, and bioaerosol characteristics (particle size, compositions, etc.), need to be identified. Subsequently, suitable UV lamps and their arrangement must be chosen to deliver an adequate UV dose. An on-site or off-site evaluation should be

conducted to verify the ability of the UV facility to achieve the desired inactivation efficiency. If the facility does not meet the goals, adjustments should be made in the previous step of designing and sizing the UV reactor until the objectives are achieved. Finally, the construction of the UV facility can be carried out.

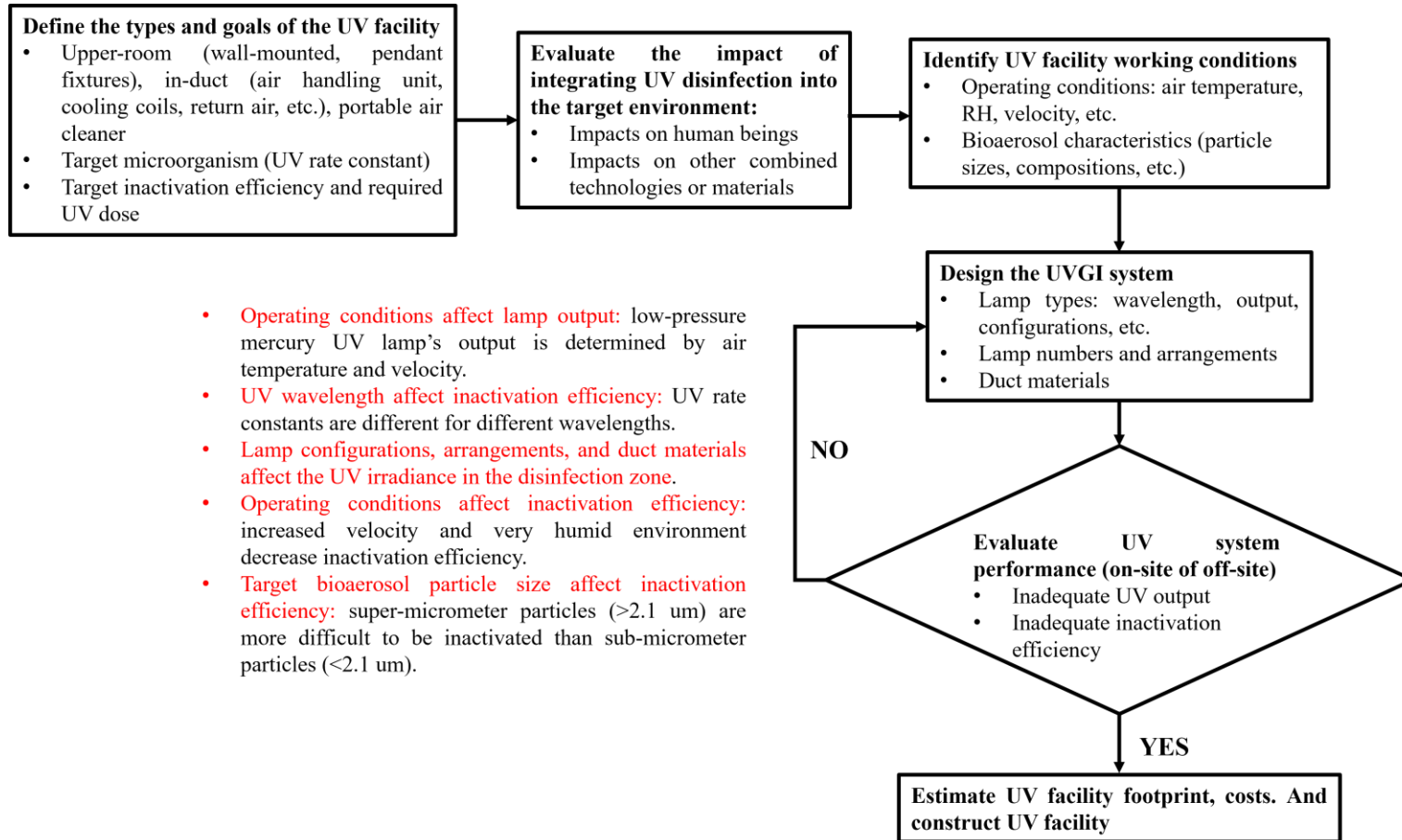


Figure 35 A flowchart describing the process of planning UV facilities for inactivating airborne microorganisms (red highlights: potential causes of system failure during UVGI evaluation)

## 7.2 A case study aiming at airborne ssRNA viruses inactivation

To better illustrate the application of the flowchart with the integration of the research outcomes in this thesis, we will briefly discuss a case study targeting airborne ssRNA viruses' inactivation in HVAC ducts in North American cities.

### 7.2.1 Define the types and goals of the UV facility

Aligning with the research objectives for this thesis, we are aiming at installing UVC lamps in HVAC ducts for disinfecting the building's recirculating air, thus, an in-duct UVGI system. Moreover, the selected targeting microorganisms are the potential airborne ssRNA viruses mentioned in Section 5.4.2, including the *Poliovirus*, *Coxsackievirus*, *Echovirus*, *Tulane virus*, *Human norovirus*, *Influenza A virus*, *Newcastle disease virus*, *Measles virus*, *Human coronavirus 229E (HCoV-229E)*, *Canine coronavirus*, *SARS-CoV*, and *SARS-CoV-2*. The estimated UV rate constants for these viruses are 0.793, 0.825, 0.821, 0.97, 0.739, 1.056, 1.525, 1.786, 3.155, 3.168, 3.033, and 3.131 cm<sup>2</sup>/mJ. Thus, targeting 90% inactivation efficiencies, the required UV doses are 2.904, 2.791, 2.805, 2.374, 3.116, 2.180, 1.510, 1.289, 0.730, 0.727, 0.759, and 0.735 mJ/cm<sup>2</sup> for them.

### 7.2.2 Identify UV facility working conditions

The full air recirculation scenario is considered here to mimic the worst virus transmission cases. Therefore, the environmental conditions in an HVAC system are defined to be the same as those in an indoor environment. That is to say, maintaining the indoor temperature in the range of 23–26 °C (below 60% RH) and 20– 23.5 °C (20%–30% RH) for the cities

in North America during the summer and winter seasons, respectively [103,104]. However, it should be noted that the RH would vary at different locations inside HVAC ducts. For instance, at locations downstream in proximity to cooling coils, the RH could elevate to higher than 90% [105]. Therefore, we consider the operating condition for RH ranges from 20%–30% to > 90% in the HVAC ducts. As mentioned in Section 6.2.2, regarding the impact of RH on the UV rate constant, while there is no consistent conclusion for conditions with low to moderate humidity (<60% RH), a consensus emerges concerning high RH levels (>80%). In detail, as depicted in Figure 33, when environmental RH increases from approximately 50% - 60% to over 80%, the UV rate constant decreases by a factor of 1.5 (averaged data from *MS2* [109], *Porcine respiratory and reproductive syndrome virus* [106], *Vaccinia virus* [107], *Influenza* [108], *Phix174* [109], *Phi6* [109], and *T7* [109]). Consequently, considering the worst-case scenario (UV lamps are installed downstream in proximity to cooling coils with RH > 80%), a safety factor of 1.5 should be applied for the abovementioned UV rate constants for potential airborne ssRNA viruses, assuming the initial UV rate constant values are predicted for the moderate humid environment. The UV rate constants are corrected to 0.529, 0.550, 0.547, 0.647, 0.493, 0.704, 1.017, 1.191, 2.103, 2.112, 2.022, and 2.087 cm<sup>2</sup>/mJ for *Poliovirus*, *Coxsackievirus*, *Echovirus*, *Tulane virus*, *Human norovirus*, *Influenza A virus*, *Newcastle disease virus*, *Measles virus*, *HCoV-229E*, *Canine coronavirus*, *SARS-CoV*, and *SARS-CoV-2*.

Another factor to be considered is the bioaerosol particle size, where it is observed in Section 6.3.1 that inactivation efficiency is lower for large bioaerosols (2.1-7 µm) compared to small ones (0.65-2.1 µm). Specifically, the UV rate constant is 1.59 times smaller for large bioaerosols than for small ones. Considering the worst-case scenario to

disinfect the airborne viruses embedded in the super-micrometer region ( $>2.5 \mu\text{m}$ ) in indoor environments, a safety factor of 1.59 shall be applied to the estimated UV rate constants. This results in the UV rate constants are further corrected to 0.332, 0.346, 0.344, 0.407, 0.310, 0.443, 0.639, 0.749, 1.323, 1.328, 1.272, and 1.313  $\text{cm}^2/\text{mJ}$  for *Poliovirus*, *Coxsackievirus*, *Echovirus*, *Tulane virus*, *Human norovirus*, *Influenza A virus*, *Newcastle disease virus*, *Measles virus*, *HCoV-229E*, *Canine coronavirus*, *SARS-CoV*, and *SARS-CoV-2*.

### 7.2.3 Design the UVGI systems

Instead of designing the new UVGI systems, we summarized all the constructed and tested in-duct UVGI system designs in the literature in Section 2.3.1.2 (Table 3). There are thirty-three real-life in-duct UVGI systems designs that encompass typical operating conditions, with air velocities ranging from 0.16 to 6.5 m/s, temperatures from 10 to 30 °C, and RH between 31% and 62%.

### 7.2.4 Evaluate the UVGI system performance

Instead of conducting the on-site or off-site evaluation for the UVGI system, we estimate the inactivation efficiencies by implementing the UV rate constants for each potential airborne ssRNA virus and the reported UV dose for each design and using the single-stage decay model (Eq. (1),  $\eta = 1 - e^{-kD_{UV}} = 1 - e^{-kt}$ ). The inactivation efficiencies are estimated and detailed in Table 25 and Figure 36.

Ten designs #1, 4, 5, 7, 17, 20, 24, 31, 32, and 33 may be considered suitable for achieving 90% inactivation of all viruses, compared to the fourteen designs (1, 4, 5, 7, 15, 16, 17, 18, 19, 20, 24, 31, 32, and 33) when using the best-scenario without corrected UV rate

constants from Section 7.2.1. These designs share common characteristics: (1) using high-power UV lamps or increasing lamp numbers (3 – 12 UV lamps and 180 – 1100 W total energy input), thereby enhancing UV irradiance within the ductwork; (2) using reflective duct materials to further increase UV irradiance in the duct; and (3) maintaining slow to intermediate air velocities (0.16 – 2.5 m/s) to prolong the UV exposure time for microorganisms.

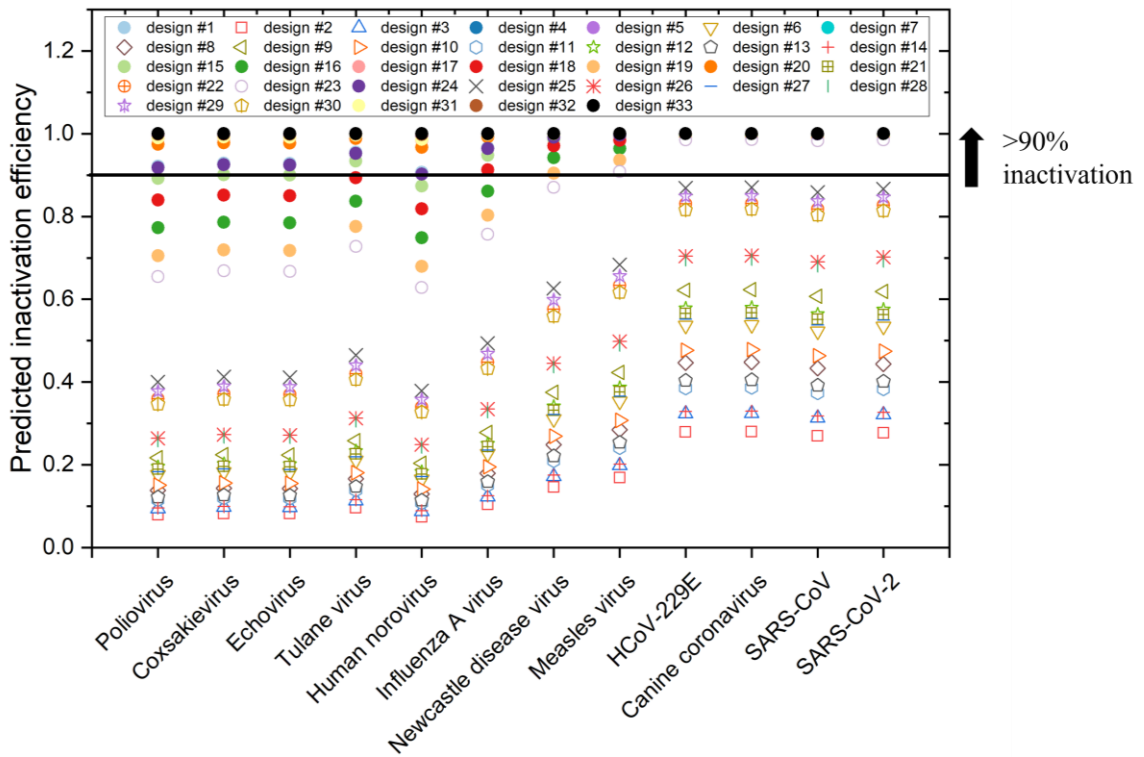


Figure 36 Predicted inactivation efficiencies of airborne ssRNA viruses (potentially harmful to humans) using various in-duct UVGI system designs in the literature (design details see in Table 3)

Table 25 In-duct UVGI system designs in the literature and the estimated airborne ssRNA viruses' inactivation efficiencies

Design details (see Table 3)		Predicted inactivation efficiency											
No.	Reported UV dose (mJ/cm <sup>2</sup> )	Airborne ssRNA viruses (corrected UV rate constant (cm <sup>2</sup> /mJ))											
		<i>Polio-virus</i> (0.332)	<i>Coxsack ie-virus</i> (0.346)	<i>Echo-virus</i> (0.344)	<i>Tulane virus</i> (0.407)	<i>Human norovirus</i> (0.310)	<i>Influenza A virus</i> (0.443)	<i>Newcastle disease virus</i> (0.639)	<i>Measles virus</i> (0.749)	<i>HCoV-229E</i> (1.323)	<i>Canine coronavirus</i> (1.328)	<i>SARS-CoV</i> (1.272)	<i>SARS-CoV-2</i> (1.313)
#1[90]	7.651	92.14%	92.91%	92.82%	95.55%	90.66%	96.62%	99.25%	99.68%	100.00%	100.00%	99.99%	100.00%
#2[69]	0.247	7.88%	8.19%	8.15%	9.56%	7.37%	10.36%	14.61%	16.89%	27.87%	27.97%	26.96%	27.69%
#3[71]	0.295	9.34%	9.70%	9.66%	11.31%	8.74%	12.24%	17.19%	19.82%	32.31%	32.42%	31.28%	32.11%
#4[91]	19.826	99.86%	99.89%	99.89%	99.97%	99.79%	99.98%	100.00%	100.00%	100.00%	100.00%	100.00%	100.00%
#5[92]	16.439	99.58%	99.66%	99.65%	99.88%	99.39%	99.93%	100.00%	100.00%	100.00%	100.00%	100.00%	100.00%
#6[93]	0.582	17.59%	18.23%	18.16%	21.08%	16.50%	22.72%	31.07%	35.33%	53.69%	53.84%	52.29%	53.42%
#7[94]	42.342	100.00%	100.00%	100.00%	100.00%	100.00%	100.00%	100.00%	100.00%	100.00%	100.00%	100.00%	100.00%
#8[95]	0.447	13.81%	14.33%	14.26%	16.62%	12.93%	17.96%	24.86%	28.45%	44.64%	44.77%	43.36%	44.39%
#9[96]	0.735	21.68%	22.45%	22.35%	25.84%	20.37%	27.78%	37.50%	42.33%	62.18%	62.33%	60.73%	61.90%
#10[96]	0.490	15.03%	15.59%	15.52%	18.07%	14.09%	19.50%	26.90%	30.71%	47.70%	47.84%	46.37%	47.44%
#11[96]	0.368	11.52%	11.95%	11.90%	13.90%	10.78%	15.04%	20.97%	24.09%	38.54%	38.66%	37.37%	38.31%
#12[97]	0.652	19.49%	20.19%	20.10%	23.29%	18.29%	25.08%	34.09%	38.63%	57.79%	57.94%	56.36%	57.51%
#13[97]	0.391	12.19%	12.65%	12.59%	14.70%	11.41%	15.90%	22.12%	25.38%	40.38%	40.51%	39.18%	40.15%
#14[97]	0.301	9.52%	9.89%	9.84%	11.52%	8.90%	12.48%	17.51%	20.18%	32.85%	32.96%	31.80%	32.64%
#15[19]	6.687	89.18%	90.10%	89.99%	93.41%	87.41%	94.82%	98.61%	99.33%	99.99%	99.99%	99.98%	99.98%
#16[19]	4.458	77.29%	78.61%	78.45%	83.69%	74.88%	86.11%	94.22%	96.45%	99.73%	99.73%	99.65%	99.71%
#17[19]	13.374	98.83%	99.02%	99.00%	99.57%	98.41%	99.73%	99.98%	100.00%	100.00%	100.00%	100.00%	100.00%
#18[19]	5.511	84.00%	85.14%	85.00%	89.37%	81.87%	91.28%	97.05%	98.39%	99.93%	99.93%	99.91%	99.93%
#19[19]	3.674	70.52%	71.94%	71.77%	77.56%	67.97%	80.34%	90.46%	93.62%	99.23%	99.24%	99.06%	99.20%
#20[19]	11.021	97.44%	97.79%	97.75%	98.87%	96.71%	99.24%	99.91%	99.97%	100.00%	100.00%	100.00%	100.00%

#21[98]	0.630	18.90%	19.58%	19.50%	22.60%	17.73%	24.34%	33.16%	37.61%	56.54%	56.69%	55.12%	56.27%
#22[99]	1.341	35.97%	37.12%	36.97%	42.04%	34.00%	44.77%	57.58%	63.37%	83.03%	83.16%	81.83%	82.80%
#23[99]	3.197	65.46%	66.91%	66.73%	72.75%	62.86%	75.72%	87.05%	90.87%	98.54%	98.57%	98.28%	98.50%
#24[99]	7.509	91.76%	92.55%	92.46%	95.28%	90.24%	96.40%	99.18%	99.64%	100.00%	100.00%	99.99%	99.99%
#25[16]	1.537	40.01%	41.24%	41.09%	46.48%	37.89%	49.37%	62.57%	68.37%	86.91%	87.02%	85.84%	86.70%
#26[16]	0.921	26.38%	27.28%	27.17%	31.24%	24.83%	33.49%	44.51%	49.83%	70.43%	70.58%	69.00%	70.15%
#27[16]	0.607	18.28%	18.94%	18.86%	21.88%	17.15%	23.57%	32.17%	36.53%	55.20%	55.35%	53.79%	54.93%
#28[16]	0.897	25.79%	26.68%	26.57%	30.57%	24.27%	32.78%	43.65%	48.92%	69.47%	69.62%	68.04%	69.20%
#29[16]	1.426	37.76%	38.94%	38.79%	44.01%	35.72%	46.81%	59.82%	65.63%	84.84%	84.96%	83.69%	84.62%
#30[16]	1.279	34.64%	35.75%	35.61%	40.56%	32.72%	43.24%	55.86%	61.63%	81.58%	81.71%	80.34%	81.35%
#31[100]	13.92	99.02%	99.19%	99.17%	99.65%	98.66%	99.79%	99.99%	100.00%	100.00%	100.00%	100.00%	100.00%
#32[100]	20.28	99.88%	99.91%	99.91%	99.97%	99.81%	99.99%	100.00%	100.00%	100.00%	100.00%	100.00%	100.00%
#33[100]	49.63	100.00%	100.00%	100.00%	100.00%	100.00%	100.00%	100.00%	100.00%	100.00%	100.00%	100.00%	100.00%

## 8 Conclusions and Recommendations

Aligning with the principal objectives of the thesis, the following sections summarize the major research outcomes in this research regarding the effects of the in-duct UVGI system designs, duct operating conditions, and bioaerosol characteristics on the inactivation efficiency of an in-duct UVGI system. Then, a conclusion for the limitations and future works is provided accordingly.

### 8.1 Summary and conclusions

#### 8.1.1 The effects of key influencing factors on UV inactivation

This thesis conducted comprehensive experimental and modeling works to investigate the effects of in-duct UVGI system designs, duct operating conditions, and bioaerosol characteristics on the UV inactivation efficiency of airborne microorganisms. A pilot HVAC system was designed to equitably and thoroughly evaluate the performance of the in-duct UVGI system. A new UV irradiance model combined with CFD simulations was developed to simulate the detailed UV irradiance field, airflow field, particle transport, and UV dose in the in-duct UVGI system. Furthermore, an improved UV rate constant model was developed to predict the genome damage and infectivity loss UV rate constants for ssRNA viruses. The following points summarize the major findings:

- For the UVGI system designs, improvements in disinfection performance can be attained by increasing the UV lamps and UV lamp power and using more reflective duct wall materials. Regarding the multiple lamp positions, placing lamps perpendicular to the airflow in the same row results in a more uniform irradiance

distribution and higher overall irradiation than putting them in different rows along with the duct airflow, leading to higher disinfection efficiency. Regarding the duct wall reflection, highly diffuse reflection provides a more uniform UV irradiance distribution and overall higher average radiation, thus better disinfection performance for an in-duct UVGI device.

- For the UVGI system operating conditions (RH), our observation within the current experimental setup (involving *MS2* aerosols generated from PBS and passing through a bioaerosol dryer) revealed that as RH increased from 25% to 60%, the *MS2* UV rate constant initially increased and then decreased, reaching its peak at 40% RH. This can be attributed to the combined effects of direct interference from water sorption behaviors, which may attenuate UV radiation, and indirect interference from structural damage, which may facilitate UV penetration. Furthermore, a consensus has emerged from the available UV rate constant data in the literature, indicating a reduction in the UV rate constant at intermediate to high RH levels (> 50% - 60% RH). This decrease is attributed to the increased water content in bioaerosols, leading to enhanced UV absorption.
- For the bioaerosol particle size, it exhibited the lower UV rate constants for large *MS2* bioaerosols (2.1–7 $\mu\text{m}$ ) compared to small *MS2* bioaerosols (0.65–2.1 $\mu\text{m}$ ), irrespective of the environmental RH. The heterogeneous UV inactivation behaviors for different particle sizes were suspected to result from the increased UV shadowing effects caused by potential virion aggregations and particle aggregations, as well as the increased UV absorption effects when the UV light

penetrated the larger salt crystals and reached the inner *MS2* virions. Overall, larger bioaerosols require a higher UV dose for disinfection in very humid environments.

- As for the airborne microorganism species, generally, viruses with larger genome sizes have larger UV rate constants and are more sensitive to UV illumination. This is attributed to a longer genome providing more sites for photodimerization, leading to increased genome damage and infectivity loss. For viruses within the same family, similarities in genome sizes and protein structures resulted in analogous UV rate constants.

### 8.1.2 Engineering implications

Finally, we proposed a comprehensive design flowchart to integrate the research outcomes in this thesis and illustrate their applications for the effective design and implementation of UVGI technology in controlling the bioaerosols in complex indoor environments. The following point summarizes the major findings:

- We identified ten designs #1, 4, 5, 7, 17, 20, 24, 31, 32, and 33 (Table 25) that may be considered suitable for achieving 90% inactivation of all viruses under the worst-case scenario for the UVGI application in the duct environment (very humid environment (>80% RH) and large bioaerosols (>2.5  $\mu\text{m}$ )). These designs share common characteristics: using high-power UV lamps or increasing lamp numbers, using reflective duct materials to further increase UV irradiance in the duct, and maintaining slow to intermediate air velocities.

## 8.2 Recommendations for future research

Though we have conducted comprehensive experimental and modeling works for characterizing and assessing various the in-duct UVGI system parameters, there remain limitations to be addressed in future works.

### 8.2.1 The mechanisms behind the effects of particle size and environmental RH on the airborne virus UV inactivation

This thesis investigated the impact of particle size and environmental RH on the UV inactivation of *MS2* with PBS as the suspending medium. First, the analysis of the RH effect was based on PBS aerosols; however, real-world bioaerosols contain a mixture of inorganic matter, virions, and proteins from the respiratory fluid. These bioaerosols may exhibit different hygroscopic behaviors and UV protection effects compared to salt, potentially resulting in variations in UVGI system performance. Further research is needed to conduct UVGI tests using other suspending media that mimic saliva and respiratory fluid.

Second, although several studies have examined the effects of RH on airborne viruses, no general conclusion can be drawn due to the complex interactions between virus species/structures and bioaerosol compositions. The connections between virus structural damage and UV penetration in this study were hypothesized based on *MS2*. In this non-enveloped virus, the capsid protein damage contributes insignificantly to the overall viral infectivity loss. However, many other target airborne pathogens, such as *influenza* and *coronavirus*, are enveloped viruses interacting differently as environmental RH changes [352]. Consequently, discrepancies in the RH effect may arise between non-enveloped and

enveloped viruses. Future research should elucidate the impact of RH on UVGI system efficiency, considering different species of microorganisms.

Third, the hypothesis that UV rate constants may be influenced under intermediate humidity due to bioaerosol drying and hydration presents an interesting aspect for consideration, triggering discussion about the testing conditions and broader applicability of the ASHRAE standard 185.1-2020 [127]. This standard, which is pivotal for evaluating and comparing UV-C light's inactivation performance in ventilation systems, mandates the use of a bioaerosol dryer in its generation system [127]. While this approach is standard in the industry, it highlights the need to consider a range of environmental conditions, including those that may not involve drying and additional hydration processes. Therefore, future research should aim to explore UV rate constants for bioaerosols in varying conditions, including scenarios both with and without the dryer process. Such studies would enhance our understanding of the effectiveness of UVGI systems in diverse environments and contribute valuable insights to the existing body of knowledge.

In addition, the factors influencing UV inactivation, such as air velocity, temperature, bioaerosol particle sizes, compositions, environmental RH, etc., are interconnected variables. For instance, it is known that particle size can increase with rising RH levels, particularly under conditions of high humidity [335]. In this thesis, we systematically examined the individual effects of bioaerosol particle size and RH by controlling each variable during the tests. However, to achieve a more comprehensive understanding of UV inactivation, future research should delve deeper into the intricate interplay among these and other influencing factors and identify the controlling factor for UVGI system performance in realistic in-duct environments.

In the end, it is essential to note that the conclusions drawn in this thesis are based on aerodynamic particle diameter.

### 8.2.2 The mechanisms behind the UV rate constant model

First, the model may not be suitable for predicting UV rate constants for other types of viruses, as it does not consider specific UV inactivation mechanisms, such as the dark genome repair that dsDNA viruses might undergo following UV<sub>254</sub> treatment.

Second, due to the semi-empirical genomic model (Eq. (52)) limitations, the model estimates genome damage of large genomes by summing the divided genomes (divided into 1000 nucleotides) and assigning equal weight to different fractions. This approach oversimplifies reality, ignoring the fact that genome damage's effect on infectivity loss might vary according to the target proteins.

Third, the database for model training primarily used qPCR tests of (+) ssRNA viruses, neglecting the complex UV-RNA interactions of (-) ssRNA viruses. As a result, discrepancies emerged in predictions for them. Additionally, the database did not strictly exclude experimental data that failed to report UV attenuation in the experimental solutions. Consequently, the model may underestimate UV rate constants due to these experimental data utilizing higher UV doses for UV rate constant calculation without UV attenuation correction.

Fourth, the inability to accurately determine the contribution ratios of genome/protein damage to the overall infectivity loss led to predictions being based on a range of genome damage, 80% – 100%, using a 90% contribution ratio for comparison with experimental data and the model predictions.

Finally, this study used the “UV rate constant liquid-to-aerosol ratio” to predict UV inactivation data for airborne viruses. However, this purely empirical ratio is dependent on specific microorganism species and the characteristics of liquid suspensions and bioaerosols. Thus, overestimations or underestimations of inactivation efficiencies are inevitable. Future work should strive to refine the model by using UV inactivation data for airborne viruses, including genome damage data from qPCR tests and infectivity loss data from culture methods, rather than relying on the liquid-to-aerosol correction ratio.

### 8.2.3 Engineering implication case study

This thesis proposes a comprehensive UVGI system flowchart and conducts a case study aiming at inactivating potential airborne ssRNA viruses in the in-duct UVGI systems. Ten designs were identified as suitable for achieving a 90% inactivation rate for all considered viruses. However, it is essential to note that since the UV rate constant model and the corrections regarding the effect of RH and bioaerosol particle size tend to underestimate the UV rate constants for airborne ssRNA viruses, the predicted inactivation efficiencies should be regarded as conservative evaluations for the in-duct UVGI system designs. Moreover, it is essential to highlight that the UV dose used for estimating inactivation efficiency was obtained directly from the authors’ respective publications, ensuring its alignment with the specific system design and the prevailing operational and environmental conditions, as summarized in Table 3. In essence, any variations in the operational parameters, such as alterations in air velocity, temperature, RH, and other factors, would inevitably impact the delivered UV dose by the selected in-duct UVGI system, subsequently influencing the anticipated inactivation efficiency.

## Reference

- [1] A.C. Fears, W.B. Klimstra, P. Duprex, A. Hartman, S.C. Weaver, K.S. Plante, D. Mirchandani, J. Plante, P. V. Aguilar, D. Fernandez, A. Nalca, A. Totura, D. Dyer, B. Kearney, M. Lackemeyer, J.K. Bohannon, R. Johnson, R.F. Garry, D.S. Reed, C.J. Roy, Comparative dynamic aerosol efficiencies of three emergent coronaviruses and the unusual persistence of SARS-CoV-2 in aerosol suspensions, *MedRxiv* (2020). <https://doi.org/10.1101/2020.04.13.20063784>.
- [2] J.L. Santarpia, D.N. Rivera, V. Herrera, M.J. Morwitzer, H. Creager, G.W. Santarpia, K.K. Crown, D. Brett-Major, E. Schnaubelt, M.J. Broadhurst, J. V Lawler, St.P. Reid, J.J. Lowe, Transmission Potential of SARS-CoV-2 in Viral Shedding Observed at the University of Nebraska Medical Center, *MedRxiv* (2020). <https://doi.org/10.1101/2020.03.23.20039446>.
- [3] P.Y. Chia, K.K. Coleman, Y.K. Tan, S.W.X. Ong, M. Gum, S.K. Lau, S. Sutjipto, P.H. Lee, T.T. Son, B.E. Young, D.K. Milton, G.C. Gray, S. Schuster, T. Barkham, P.P. De, S. Vasoo, M. Chan, B.S.P. Ang, B.H. Tan, Y.S. Leo, O.-T. Ng, M.S.Y. Wong, K. Marimuthu, Detection of Air and Surface Contamination by Severe Acute Respiratory Syndrome Coronavirus 2 (SARS-CoV-2) in Hospital Rooms of Infected Patients, *MedRxiv* (2020). <https://doi.org/10.1101/2020.03.29.20046557>.
- [4] Y. Liu, Z. Ning, Y. Chen, M. Guo, Y. Liu, N.K. Gali, L. Sun, Y. Duan, J. Cai, D. Westerdahl, X. Liu, K. Xu, K. Ho, H. Kan, Q. Fu, K. Lan, Aerodynamic analysis of SARS-CoV-2 in two Wuhan hospitals, *Nature* (2020). <https://doi.org/10.1038/s41586-020-2271-3>.

- [5] Z. Ding, H. Qian, B. Xu, Y. Huang, T. Miao, H.-L. Yen, S. Xiao, L. Cui, X. Wu, W. Shao, Y. Song, L. Sha, L. Zhou, Y. Xu, B. Zhu, Y. Li, Toilets dominate environmental detection of SARS-CoV-2 virus in a hospital, *MedRxiv* (2020). <https://doi.org/10.1101/2020.04.03.20052175>.
- [6] R.T. 7 Members, The ventilation of buildings and other mitigating measures for COVID-19: a focus on winter 2020, (2020) 1–62.
- [7] P.W. Francisco, S.J. Emmerich, ASHRAE Position Document on Unvented Combustion Devices Approved by ASHRAE Board of Directors, *Ashrae Standard* (2020).
- [8] D.T. Stevens, P. Francisco, S.J. Emmerich, D.A. Baylon, T.M. Brennan, R.R. Crawford, D.C. Delaquila, L.L. Delaura, S.C. Drumheller, P.W. Fairey, D.H. Heberer, R.L. Hedrick, T.P. Heidel, M.C. Jackson, D.E. Jacobs, G.P. Langan, J.W. Lstiburek, J. Malone, S.I. Mason, J.C. Moore, A.B. Musser, J.P. Proctor, P.H. Raymer, M.H. Sherman, I.S. Walker, E.D. Werling, C.S. Barnaby, *ASHRAE 62.1 Ventilation and Acceptable Indoor Air Quality*, 2019 (2019) 58.
- [9] ASHRAE, Filtration and Air Cleaning Summary, 2021 (2021). <https://www.ashrae.org/technical-resources/filtration-disinfection> (accessed October 18, 2023).
- [10] S.E. Beck, R.A. Rodriguez, M.A. Hawkins, T.M. Hargy, T.C. Larason, K.G. Linden, Comparison of UV-induced inactivation and RNA damage in MS2 phage across the germicidal UV spectrum, *Appl Environ Microbiol* 82 (2016) 1468–1474. <https://doi.org/10.1128/AEM.02773-15>.

- [11] W. Kowalski, Ultraviolet Germicidal Irradiation Handbook, 2009.  
<https://doi.org/10.1007/978-3-642-01999-9>.
- [12] W.F. Wells, M.W. Wells, T.S. Wilder, THE ENVIRONMENTAL CONTROL OF EPIDEMIC CONTAGION I. AN EPIDEMIOLOGIC STUDY OF RADIANT DISINFECTION OF AIR IN DAY SCHOOLS, 1942.  
<https://academic.oup.com/aje/article/35/1/97/85502>.
- [13] ULTRAVIOLET AIR AND SURFACE TREATMENT, n.d.
- [14] W.P. Bahnfleth, Cooling coil ultraviolet germicidal irradiation, ASHRAE J 59 (2017) 72–74. <https://www.scopus.com/inward/record.uri?eid=2-s2.0-85031932252&partnerID=40&md5=76599dc7e2ae67f49665a51b888f85d1>.
- [15] P. Wargocki, T.H. Kuehn, H.E.B. Burroughs, C.O. Muller, E.A. Conrad, D.A. Saputa, W.J. Fisk, J.A. Siegel, M.C. Jackson, A. Veeck, P. Francisco, ASHRAE Position Document on Filtration and Air Cleaning, 2015. [www.ashrae.org](http://www.ashrae.org).
- [16] H. Luo, L. Zhong, Development and experimental validation of an improved mathematical irradiance model for in-duct ultraviolet germicidal irradiation (UVGI) applications, Build Environ 226 (2022).  
<https://doi.org/10.1016/j.buildenv.2022.109699>.
- [17] H. Luo, L. Zhong, Ultraviolet germicidal irradiation (UVGI) for in-duct airborne bioaerosol disinfection: Review and analysis of design factors, Build Environ 197 (2021). <https://doi.org/10.1016/j.buildenv.2021.107852>.

- [18] H. Zhang, X. Jin, S.S. Nunayon, A.C.K. Lai, Disinfection by in-duct ultraviolet lamps under different environmental conditions in turbulent airflows, *Indoor Air* 30 (2020) 500–511. <https://doi.org/10.1111/ina.12642>.
- [19] J. Lau, W. Bahnfleth, J. Freihaut, Estimating the effects of ambient conditions on the performance of UVGI air cleaners, *Build Environ* 44 (2009) 1362–1370. <https://doi.org/10.1016/j.buildenv.2008.05.015>.
- [20] L. Abkar, K. Zimmermann, F. Dixit, A. Kheyrandish, M. Mohseni, COVID-19 pandemic lesson learned- critical parameters and research needs for UVC inactivation of viral aerosols, *Journal of Hazardous Materials Advances* 8 (2022) 100183. <https://doi.org/10.1016/j.hazadv.2022.100183>.
- [21] A.C. Lowen, J. Steel, Roles of Humidity and Temperature in Shaping Influenza Seasonality, *J Virol* 88 (2014) 7692–7695. <https://doi.org/10.1128/jvi.03544-13>.
- [22] P. Jordan, H.M. Werth, M. Shelly, H. Mark, Effects of relative humidity on the ultraviolet induced inactivation of airborne bacteria, *Aerosol Science and Technology* 35 (2001) 728–740. <https://doi.org/10.1080/02786820152546770>.
- [23] G. Ko, M.W. First, H.A. Burge, Influence of relative humidity on particle size and UV sensitivity of *Serratia marcescens* and *Mycobacterium bovis* BCG aerosols, *Tubercle and Lung Disease* 80 (2000) 217–228. <https://doi.org/10.1054/tuld.2000.0249>.
- [24] Y.G. Karim, M.K. Ijaz, S.A. Sattar, C.M. Johnson-Lussenburg, Effect of relative humidity on the airborne survival of rhinovirus-14, *Can J Microbiol* 31 (1985) 1058–1061. <https://doi.org/10.1139/m85-199>.

- [25] K.M. Lai, H.A. Burge, M.W. First, Size and UV Germicidal Irradiation Susceptibility of *Serratia marcescens* when Aerosolized from Different Suspending Media, *Appl Environ Microbiol* 70 (2004) 2021–2027. <https://doi.org/10.1128/AEM.70.4.2021-2027.2004>.
- [26] W. Kowalski, *Ultraviolet germicidal irradiation handbook: UVGI for air and surface disinfection*, Springer Berlin Heidelberg, 2009. <https://doi.org/10.1007/978-3-642-01999-9>.
- [27] M. Raeiszadeh, B. Adeli, A Critical Review on Ultraviolet Disinfection Systems against COVID-19 Outbreak: Applicability, Validation, and Safety Considerations, *ACS Photonics* 7 (2020) 2941–2951. <https://doi.org/10.1021/acsp Photonics.0c01245>.
- [28] M. Norval, The Effect of Ultraviolet Radiation on Human Viral Infections, *Photochem Photobiol* 82 (2006) 1495–1504. <https://doi.org/10.1111/j.1751-1097.2006.tb09805.x>.
- [29] L. Harb, K. Chamakura, P. Khara, P.J. Christie, R. Young, L. Zeng, ssRNA phage penetration triggers detachment of the F-pilus, *Proceedings of the National Academy of Sciences* 117 (2020) 25751–25758. <https://doi.org/10.1073/pnas.2011901117>.
- [30] S. Rattanakul, K. Oguma, Analysis of Hydroxyl Radicals and Inactivation Mechanisms of Bacteriophage MS2 in Response to a Simultaneous Application of UV and Chlorine, *Environ Sci Technol* 51 (2017) 455–462. <https://doi.org/10.1021/acs.est.6b03394>.

- [31] N.C. Rockey, J.B. Henderson, K. Chin, L. Raskin, K.R. Wigginton, Predictive Modeling of Virus Inactivation by UV, *Environ Sci Technol* 55 (2021) 3322–3332. <https://doi.org/10.1021/acs.est.0c07814>.
- [32] Z. Qiao, Y. Ye, P.H. Chang, D. Thirunarayanan, K.R. Wigginton, Nucleic Acid Photolysis by UV254 and the Impact of Virus Encapsidation, *Environ Sci Technol* 52 (2018) 10408–10415. <https://doi.org/10.1021/acs.est.8b02308>.
- [33] S. Cheng, Y. Ge, Y. Lee, X. Yang, Prediction of Photolysis Kinetics of Viral Genomes under UV254 Irradiation to Estimate Virus Infectivity Loss, *Water Res* 198 (2021). <https://doi.org/10.1016/j.watres.2021.117165>.
- [34] T. Douki, Low ionic strength reduces cytosine photoreactivity in UVC-irradiated isolated DNA, *Photochemical and Photobiological Sciences* 5 (2006) 1045–1051. <https://doi.org/10.1039/b604517k>.
- [35] S. Premi, S. Wallisch, C.M. Mano, A.B. Weiner, A. Bacchiocchi, K. Wakamatsu, E.J.H. Bechara, R. Halaban, T. Douki, † Douglas, E. Brash, Chemiexcitation of melanin derivatives induces DNA photoproducts long after UV exposure, n.d. <https://www.science.org/doi/10.1126/science.1256022> (accessed August 15, 2023).
- [36] R.P. Sinha, D.P. Häder, UV-induced DNA damage and repair: A review, *Photochemical and Photobiological Sciences* 1 (2002) 225–236. <https://doi.org/10.1039/b201230h>.
- [37] Y. Yoon, M.C. Dodd, Y. Lee, Elimination of transforming activity and gene degradation during UV and UV/H<sub>2</sub>O<sub>2</sub> treatment of plasmid-encoded antibiotic

- resistance genes, *Environ Sci (Camb)* 4 (2018) 1239–1251.  
<https://doi.org/10.1039/c8ew00200b>.
- [38] B. Pendyala, A. Patras, B. Pokharel, D. D’Souza, Genomic Modeling as an Approach to Identify Surrogates for Use in Experimental Validation of SARS-CoV-2 and HuNoV Inactivation by UV-C Treatment, *Front Microbiol* 11 (2020).  
<https://doi.org/10.3389/fmicb.2020.572331>.
- [39] K.R. Wigginton, B.M. Pelson, T. Sigstam, F. Bosshard, T. Kohn, Virus inactivation mechanisms: Impact of disinfectants on virus function and structural integrity, *Environ Sci Technol* 46 (2012) 12069–12078. <https://doi.org/10.1021/es3029473>.
- [40] E.W. Chick, A.B. Hudnell, D.G. Sharp, Ultraviolet sensitivity of fungi associated with mycotic keratitis and other mycoses, *Med Mycol* 2 (1963) 195–200.  
<https://doi.org/10.1080/00362176385190331>.
- [41] C.D. Lytle, J.-L. Sagripanti, Predicted inactivation of viruses of relevance to biodefense by solar radiation., *J Virol* 79 (2005) 14244–52.  
<https://doi.org/10.1128/JVI.79.22.14244-14252.2005>.
- [42] W.J. Kowalski, W.P. Bahnfleth, M.T. Hernandez, A Genomic Model for Predicting the Ultraviolet Susceptibility of Viruses and Bacteria, in: *IUVA Conference Proceedings*, September 21-25. 2009At: Amsterdam, Netherlands, 2009.
- [43] W.J. Kowalski, Ultraviolet Genomic Modeling: Current Research and Applications, in: *IOA IUVA World Congress and Exhibition*, 2011.

- [44] W.J. Kowalski, W.P. Bahnfleth, M.T. Hernandez, A Genomic Model for the Prediction of Ultraviolet Inactivation Rate Constants for RNA and DNA Viruses, 2009.
- [45] S. Young, J. Torrey, V. Bachmann, T. Kohn, Relationship Between Inactivation and Genome Damage of Human Enteroviruses Upon Treatment by UV254, Free Chlorine, and Ozone, *Food Environ Virol* 12 (2020) 20–27. <https://doi.org/10.1007/s12560-019-09411-2>.
- [46] Y. Ye, P.H. Chang, J. Hartert, K.R. Wigginton, Reactivity of Enveloped Virus Genome, Proteins, and Lipids with Free Chlorine and UV254, *Environ Sci Technol* 52 (2018) 7698–7708. <https://doi.org/10.1021/acs.est.8b00824>.
- [47] N. Rockey, S. Young, T. Kohn, B. Pecson, C.E. Wobus, L. Raskin, K.R. Wigginton, UV Disinfection of Human Norovirus: Evaluating Infectivity Using a Genome-Wide PCR-Based Approach, *Environ Sci Technol* 54 (2020) 2851–2858. <https://doi.org/10.1021/acs.est.9b05747>.
- [48] B.M. Pecson, M. Ackermann, T. Kohn, Framework for using quantitative PCR as a nonculture based method to estimate virus infectivity, *Environ Sci Technol* 45 (2011) 2257–2263. <https://doi.org/10.1021/es103488e>.
- [49] H. Luo, L. Zhong, G. Zhang, An improved numerical model of a UV-PCO reactor for air purification applications, (2020).
- [50] A.J. Capetillo, Computational Fluid Dynamic Modeling of In-duct UV Air Sterilisation Systems., (2015).

- [51] G. Krishnamoorthy, B.M. Tande, Improving the effectiveness of ultraviolet germicidal irradiation through reflective wall coatings: Experimental and modeling based assessments, *Indoor and Built Environment* 25 (2016) 314–328. <https://doi.org/10.1177/1420326X14547785>.
- [52] M. Heidarinejad, J. Srebric, Computational fluid dynamics modelling of UR-UVGI lamp effectiveness to promote disinfection of airborne microorganisms, *World Review of Science, Technology and Sustainable Development* 10 (2013) 78–95. <https://doi.org/10.1504/WRSTSD.2013.050788>.
- [53] P.C. Hoi, Validation of discrete ordinate radiation model for application in UV air disinfection modeling, Thesis (2009).
- [54] I.W. and S.H. S.Sadrizadeh, S.Stensson, S.Marashian, Airborne Bacteria Inactivation in a Hospital Ward by Ultraviolet Irradiation, (2018) 1–30.
- [55] S.A. Cuevas, C.A. Arancibia-Bulnes, B. Serrano, Radiation Field in an Annular Photocatalytic Reactor by the P1 Approximation, *International Journal of Chemical Reactor Engineering* 5 (2007). <https://doi.org/10.2202/1542-6580.1589>.
- [56] H. Einaga, J. Tokura, Y. Teraoka, K. Ito, Kinetic analysis of TiO<sub>2</sub>-catalyzed heterogeneous photocatalytic oxidation of ethylene using computational fluid dynamics, *Chemical Engineering Journal* (2015). <https://doi.org/10.1016/j.cej.2014.11.017>.
- [57] F. Denny, J. Scott, V. Pareek, G. Ding Peng, R. Amal, CFD modelling for a TiO<sub>2</sub>-coated glass-bead photoreactor irradiated by optical fibres: Photocatalytic

- degradation of oxalic acid, *Chem Eng Sci* (2009).  
<https://doi.org/10.1016/j.ces.2008.12.021>.
- [58] F.J. Trujillo, T. Safinski, A.A. Adesina, Oxidative photomineralization of dichloroacetic acid in an externally-irradiated rectangular bubble tank reactor: Computational fluid dynamics modeling and experimental verification studies, *Ind Eng Chem Res* (2010). <https://doi.org/10.1021/ie901364z>.
- [59] J.E. Duran, M. Mohseni, F. Taghipour, Computational fluid dynamics modeling of immobilized photocatalytic reactors for water treatment, *AIChE Journal* (2011). <https://doi.org/10.1002/aic.12399>.
- [60] P. Atkins, J. De Paula, *Atkins' Physical chemistry 8th edition*, Chemistry (Easton) (2009). <https://doi.org/10.1021/ed056pA260.1>.
- [61] Y. Yang, H. Zhang, V. Chan, A.C. Lai, Development and experimental validation of a mathematical model for the irradiance of in-duct ultraviolet germicidal lamps, *Build Environ* 152 (2019) 160–171. <https://doi.org/10.1016/j.buildenv.2019.02.004>.
- [62] W. Kowalski, W. Bahnfleth, R.G. Mistrick, A Specular Model for UVGI air Disinfection Systems, *IUVA News* 7 (2005) 19–26.
- [63] W. Kowalski, *Design and Optimization of UVGI Air Disinfection Systems A Thesis in Architectural Engineering by*, Configurations (2001).
- [64] D. VanOsdell, K. Foarde, *Defining the Effectiveness of UV Lamps Installed in Circulating Air Ductwork, Prepared for the Air-Conditioning and Refrigeration Technology Institute under ARTI 21-CR Program Contract Number 610-*

40030. Available to the Public from U.S. Department of Commerce, National Technical Information Service, 5285 Port Royal Road, Springfield (2002).
- [65] C.L. Wu, Y. Yang, S.L. Wong, A.C.K. Lai, A new mathematical model for irradiance field prediction of upper-room ultraviolet germicidal systems, *J Hazard Mater* 189 (2011) 173–185. <https://doi.org/10.1016/j.jhazmat.2011.02.022>.
- [66] Y. Yang, A.C.K. Lai, C. Wu, Study on the disinfection efficiency of multiple upper-room ultraviolet germicidal fixtures system on airborne microorganisms, *Build Environ* 103 (2016) 99–110. <https://doi.org/10.1016/j.buildenv.2016.04.004>.
- [67] M.F. Modest, View Factors, *Radiative Heat Transfer* (2013) 129–159. <https://doi.org/10.1016/b978-0-12-386944-9.50004-2>.
- [68] ANSYS Academic Research, ANSYS Fluent Theory Guide, in: ANSYS Help System, 2018.
- [69] Karin Foarde, Deborah Franke, James Hanley, Kathleen Owen, Tricia Webber, Biological Inactivation Efficiency by HVAC In-Duct Ultraviolet Light Systems Dust Free Bio-Fighter 4Xtreme, Model 21, 2006.
- [70] A. Capetillo, C.J. Noakes, P.A. Sleight, Computational fluid dynamics analysis to assess performance variability of in-duct UV-C systems, *Sci Technol Built Environ* 21 (2015) 45–53. <https://doi.org/10.1080/10789669.2014.968512>.
- [71] Karin Foarde, Deborah Franke, James Hanley, Kathleen Owen, Tricia Webber, Biological Inactivation Efficiency by HVAC In-Duct Ultraviolet Light Systems Atlantic Ultraviolet Corporation AeroLogic Model AD24-4, 2006.

- [72] F. Atci, Y.E. Cetin, M. Avci, O. Aydin, Evaluation of in-duct UV-C lamp array on air disinfection: A numerical analysis, *Sci Technol Built Environ* 4731 (2020). <https://doi.org/10.1080/23744731.2020.1776549>.
- [73] A.J. Capetillo, Computational Fluid Dynamic Modeling of In-duct UV Air Sterilisation Systems., (2015).
- [74] J. Lau, W. Bahnfleth, J. Freihaut, Estimating the effects of ambient conditions on the performance of UVGI air cleaners, *Build Environ* 44 (2009) 1362–1370. <https://doi.org/10.1016/j.buildenv.2008.05.015>.
- [75] C.H. Thatcher, B.R. Adams, Impact of surface reflection on microbial inactivation in a UV LED treatment duct, *Chem Eng Sci* (2020) 116204. <https://doi.org/10.1016/j.ces.2020.116204>.
- [76] Food and Drug Administration (FDA), Ultraviolet Radiation for the Processing and Treatment of Food, (2011) 24–27.
- [77] Philips, UV Purification - Application Information, (2005) 39.
- [78] J. Lau, W. Bahnfleth, J. Freihaut, Estimating the effects of ambient conditions on the performance of UVGI air cleaners, *Build Environ* 44 (2009) 1362–1370. <https://doi.org/10.1016/j.buildenv.2008.05.015>.
- [79] S.S. Nunayon, H. Zhang, A.C.K. Lai, Comparison of disinfection performance of UVC-LED and conventional upper-room UVGI systems, *Indoor Air* 30 (2020) 180–191. <https://doi.org/10.1111/ina.12619>.

- [80] J.Y. Shin, S.J. Kim, D.K. Kim, D.H. Kang, Fundamental characteristics of deep-UV light-emitting diodes and their application to control foodborne pathogens, *Appl Environ Microbiol* (2016). <https://doi.org/10.1128/AEM.01186-15>.
- [81] S.S. Nunayon, H.H. Zhang, A.C.K. Lai, A novel upper-room UVC-LED irradiation system for disinfection of indoor bioaerosols under different operating and airflow conditions, *J Hazard Mater* 396 (2020) 122715. <https://doi.org/10.1016/j.jhazmat.2020.122715>.
- [82] D. Kim, D. Kang, crossm UVC LED Irradiation Effectively Inactivates Aerosolized Viruses , 84 (2018) 1–11.
- [83] T. Koutchma, V. Popović, UV light-emitting diodes (LEDs) and food safety, *Ultraviolet LED Technology for Food Applications: From Farms to Kitchens* (2019) 91–117. <https://doi.org/10.1016/B978-0-12-817794-5.00005-4>.
- [84] J. Simonet, C. Gantzer, Inactivation of poliovirus 1 and F-specific RNA phages and degradation of their genomes by UV irradiation at 254 nanometers, *Appl Environ Microbiol* (2006). <https://doi.org/10.1128/AEM.01106-06>.
- [85] C.C. Tseng, C.S. Li, Inactivation of virus-containing aerosols by ultraviolet germicidal irradiation, *Aerosol Science and Technology* 39 (2005) 1136–1142. <https://doi.org/10.1080/02786820500428575>.
- [86] EPA, Biological inactivation efficiency by HVAC in-duct ultraviolet light. Steril-Aire, Inc. Model SE 1VO with GTS 24 VO emitter, Epa 600/R-06/052 (2006).
- [87] C.M. Walker, G. Ko, Effect of ultraviolet germicidal irradiation on viral aerosols, *Environ Sci Technol* 41 (2007) 5460–5465. <https://doi.org/10.1021/es070056u>.

- [88] J.I. Pearce-Walker, D.J. Troup, R. Ives, L.A. Ikner, J.B. Rose, M.A. Kennedy, M.P. Verhougstraete, Investigation of the effects of an ultraviolet germicidal irradiation system on concentrations of aerosolized surrogates for common veterinary pathogens, *Am J Vet Res* 81 (2020) 506–513. <https://doi.org/10.2460/ajvr.81.6.506>.
- [89] S. Ge, *Viral Aerosol Survivability, Transmission, and Sampling in an Environmental Chamber*, (2014).
- [90] Karin Foarde, Deborah Franke, Tricia Webber, James Hanley, Kathleen Owen, *Biological Inactivation Efficiency by HVAC In-Duct Ultraviolet Light Systems UltraViolet Devices, Inc. Altru-V V-Flex*, 2006.
- [91] Karin Foarde, Deborah Franke, Tricia Webber, James Hanley, Kathleen Owen, *Biological Inactivation Efficiency by HVAC In-Duct Ultraviolet Light Systems Steril-Aire, Inc. Model SE 1 VO with GTS 24 VO Emitter*, 2006.
- [92] Karin Foarde, Deborah Franke, Tricia Webber, James Hanley, Kathleen Owen, *Biological Inactivation Efficiency by HVAC In-Duct Ultraviolet Light Systems Sanuvox Technologies Inc. UV Bio-Wall 50 Outwardly Projecting Air Purifier*, 2006.
- [93] Karin Foarde, Deborah Franke, Tricia Webber, James Hanley, Kathleen Owen, *Biological Inactivation Efficiency by HVAC In-Duct Ultraviolet Light Systems American Ultraviolet Corporation ACP-24/HO-4*, 2006.
- [94] Karin Foarde, Deborah Franke, Tricia Webber, James Hanley, Kathleen Owen, *Biological Inactivation Efficiency by HVAC In-Duct Ultraviolet Light Systems Novatron, Inc. BioProtector BP114i*, 2006.

- [95] Karin Foarde, Deborah Franke, Tricia Webber, James Hanley, Kathleen Owen, Biological Inactivation Efficiency by HVAC In-Duct Ultraviolet Light Systems Abracair, LLC In-Duct System, 2006.
- [96] Y. Yang, H. Zhang, S.S. Nunayon, V. Chan, A.C.K. Lai, Disinfection efficacy of ultraviolet germicidal irradiation on airborne bacteria in ventilation ducts, *Indoor Air* 28 (2018) 806–817. <https://doi.org/10.1111/ina.12504>.
- [97] H. Zhang, X. Jin, S.S. Nunayon, A.C.K. Lai, Disinfection by in-duct ultraviolet lamps under different environmental conditions in turbulent airflows, *Indoor Air* 30 (2020) 500–511. <https://doi.org/10.1111/ina.12642>.
- [98] J.I. Pearce-Walker, D.J. Troup, R. Ives, L.A. Ikner, J.B. Rose, M.A. Kennedy, M.P. Verhougstraete, Investigation of the effects of an ultraviolet germicidal irradiation system on concentrations of aerosolized surrogates for common veterinary pathogens., *Am J Vet Res* 81 (2020) 506–513.
- [99] D. Vanosdell, K. Foarde, DEFINING THE EFFECTIVENESS OF UV LAMPS INSTALLED IN CIRCULATING AIR DUCTWORK Final Report, 2002.
- [100] Y. Qiao, M. Yang, I.A. Marabella, D.A.J. McGee, H. Aboubakr, S. Goyal, C.J. Hogan, B.A. Olson, M. Torremorell, Greater than 3-Log Reduction in Viable Coronavirus Aerosol Concentration in Ducted Ultraviolet-C (UV-C) Systems, *Environ Sci Technol* 55 (2021) 4174–4182. <https://doi.org/10.1021/acs.est.0c05763>.
- [101] M.D. Corbat, K. Owen, T.A. Mcgrath, R.B. Burkhead, D.M. Feddersen, C. Fischer, P. Maybee, S.W. Nicholas, C.Q. Sun, R.M. Harrold, S.J. Emmerich, J.D. Aswegan,

K.I. Emerson, J.M. Ferguson, M.W. Gallagher, W.T. Grondzik, S.S. Hanson, R.L. Hedrick, Method of testing general ventilation air-cleaning devices for removal efficiency by particle size, ASHRAE Standard 2017 (2007) 1–64.

- [102] EPA, Biological inactivation efficiency by HVAC in-duct ultraviolet light. UltraViolet Devices, Inc. Altru-V V-Flex, Epa 600/R-06/049 (2006).
- [103] ANSI/ASHRAE Addendum d to ANSI/ASHRAE Standard 55-2017, 2020. [www.ashrae.org](http://www.ashrae.org).
- [104] Canada. Healthy Environments and Consumer Safety Branch., Relative humidity indoors : factsheet., Health Canada, 2016.
- [105] C. Grimes, K. Quinn Hart, M. Hodgson, V. Health Administration Washington, D. Lan Chi Nguyen Thi, W. Rose, ASHRAE Position Document on Limiting Indoor Mold and Dampness in Buildings, 2012.
- [106] T.D. Cutler, C. Wang, S.J. Hoff, J.J. Zimmerman, Effect of temperature and relative humidity on ultraviolet (UV 254) inactivation of airborne porcine respiratory and reproductive syndrome virus, *Vet Microbiol* 159 (2012) 47–52. <https://doi.org/10.1016/j.vetmic.2012.03.044>.
- [107] J.J. McDevitt, M.L. Ka, S.N. Rudnick, E.A. Houseman, M.W. First, D.K. Milton, Characterization of UVC light sensitivity of vaccinia virus, *Appl Environ Microbiol* 73 (2007) 5760–5766. <https://doi.org/10.1128/AEM.00110-07>.
- [108] J.J. McDevitt, S.N. Rudnick, L.J. Radonovich, Aerosol susceptibility of influenza virus to UV-C light, *Appl Environ Microbiol* 78 (2012) 1666–1669. <https://doi.org/10.1128/AEM.06960-11>.

- [109] C.C. Tseng, C.S. Li, Inactivation of virus-containing aerosols by ultraviolet germicidal irradiation, *Aerosol Science and Technology* 39 (2005) 1136–1142. <https://doi.org/10.1080/02786820500428575>.
- [110] H.A. E, T.R. J, *Aerobiology: Experimental Considerations, Observations, and Future Tools*, *Appl Environ Microbiol* 83 (2017) e00809-17. <https://doi.org/10.1128/AEM.00809-17>.
- [111] T.W. Kethley, K. Branch, Ultraviolet lamps for room air disinfection, *Arch Environ Health* 25 (1972) 205–214. <https://doi.org/10.1080/00039896.1972.10666162>.
- [112] L. Zhong, H. Luo, Improving an In-duct System for Bioaerosol Hazard Mitigation: Evaluating the Role of Particle Size and Relative Humidity in Ultraviolet Germicidal Irradiation Efficiency, Under Review (n.d.).
- [113] C.C. Tseng, C.S. Li, Inactivation of virus-containing aerosols by ultraviolet germicidal irradiation, *Aerosol Science and Technology* 39 (2005) 1136–1142. <https://doi.org/10.1080/02786820500428575>.
- [114] C.M. Walker, G. Ko, Effect of ultraviolet germicidal irradiation on viral aerosols, *Environ Sci Technol* 41 (2007) 5460–5465. <https://doi.org/10.1021/es070056u>.
- [115] W.J. Snelling, A. Afkhami, H.L. Turkington, C. Carlisle, S.L. Cosby, J.W.J. Hamilton, N.G. Ternan, P.S.M. Dunlop, Efficacy of single pass UVC air treatment for the inactivation of coronavirus, MS2 coliphage and *Staphylococcus aureus* bioaerosols, *J Aerosol Sci* 164 (2022). <https://doi.org/10.1016/j.jaerosci.2022.106003>.

- [116] T.H. Kuehn, *Viral Aerosol Survivability, Transmission, and Sampling in an Environmental Chamber*, 2014.
- [117] M.M. Jensen, *Inactivation of Airborne Viruses by Ultraviolet Irradiation*, 1964.  
<https://journals.asm.org/journal/am>.
- [118] N. Ruetalo, S. Berger, J. Niessner, M. Schindler, Inactivation of aerosolized SARS-CoV-2 by 254 nm UV-C irradiation, *Indoor Air* 32 (2022).  
<https://doi.org/10.1111/ina.13115>.
- [119] Y. Liu, Z. Ning, Y. Chen, M. Guo, Y. Liu, N.K. Gali, L. Sun, Y. Duan, J. Cai, D. Westerdahl, X. Liu, K. Xu, K. fai Ho, H. Kan, Q. Fu, K. Lan, Aerodynamic analysis of SARS-CoV-2 in two Wuhan hospitals, *Nature* 582 (2020) 557–560.  
<https://doi.org/10.1038/s41586-020-2271-3>.
- [120] P.Y. Chia, K.K. Coleman, Y.K. Tan, S.W.X. Ong, M. Gum, S.K. Lau, X.F. Lim, A.S. Lim, S. Sutjipto, P.H. Lee, T.T. Son, B.E. Young, D.K. Milton, G.C. Gray, S. Schuster, T. Barkham, P.P. De, S. Vasoo, M. Chan, B.S.P. Ang, B.H. Tan, Y.S. Leo, O.T. Ng, M.S.Y. Wong, K. Marimuthu, D.C. Lye, P.L. Lim, C.C. Lee, L.M. Ling, L. Lee, T.H. Lee, C.S. Wong, S. Sadarangani, R.J. Lin, D.H.L. Ng, M. Sadasiv, T.W. Yeo, C.Y. Choy, G.S.E. Tan, F. Dimatatac, I.F. Santos, C.J. Go, Y.K. Chan, J.Y. Tay, J.Y.L. Tan, N. Pandit, B.C.H. Ho, S. Mendis, Y.Y.C. Chen, M.Y. Abdad, D. Moses, Detection of air and surface contamination by SARS-CoV-2 in hospital rooms of infected patients, *Nat Commun* 11 (2020). <https://doi.org/10.1038/s41467-020-16670-2>.

- [121] R.A. Stern, A. Al-Hemoud, B. Alahmad, P. Koutrakis, Levels and particle size distribution of airborne SARS-CoV-2 at a healthcare facility in Kuwait, *Science of the Total Environment* 782 (2021). <https://doi.org/10.1016/j.scitotenv.2021.146799>.
- [122] American Society of Heating Refrigerating and Air-Conditioning Engineers, American National Standards Institute, 185.1: Method of Testing UV-C Lights for Use in Air-Handling Units or Air Ducts to Inactivate Airborne, *ASHRAE Standards and Guidelines 2020* (2020).
- [123] J. Wu, H. Luo, L. Zhong, Development of a multi-functional HVAC facility for the evaluation of air cleaning technologies and ventilation performance, 2022.
- [124] Method of Testing General Ventilation Air-Cleaning Devices for Removal Efficiency by Particle Size from IHS, (2017). [www.ashrae.org](http://www.ashrae.org).
- [125] S.W. Kim, M.A. Ramakrishnan, P.C. Raynor, S.M. Goyal, Effects of humidity and other factors on the generation and sampling of a coronavirus aerosol, *Aerobiologia (Bologna)* 23 (2007) 239–248. <https://doi.org/10.1007/s10453-007-9068-9>.
- [126] J. Wu, J. Chen, J.S. Olfert, L. Zhong, Filter evaluation and selection for heating, ventilation, and air conditioning systems during and beyond the COVID-19 pandemic, *Indoor Air* 32 (2022). <https://doi.org/10.1111/ina.13099>.
- [127] Method of Testing UV-C Lights for Use in Air-Handling Units or Air Ducts to Inactivate Airborne Microorganisms, 2020. [www.ashrae.org/technology](http://www.ashrae.org/technology).
- [128] Z. Zuo, T.H. Kuehn, H. Verma, S. Kumar, S.M. Goyal, J. Appert, P.C. Raynor, S. Ge, D.Y.H. Pui, Association of airborne virus infectivity and survivability with its

- carrier particle size, *Aerosol Science and Technology* 47 (2013) 373–382.  
<https://doi.org/10.1080/02786826.2012.754841>.
- [129] M.E. Martínez Retamar, C. Passalía, R.J. Brandi, M.D. Labas, Dose estimation methodology for the UV inactivation of bioaerosols in a Continuous-Flow reactor, *Aerosol Science and Technology* 53 (2019) 8–20.  
<https://doi.org/10.1080/02786826.2018.1533914>.
- [130] Water quality-Detection and enumeration of bacteriophages-Part 1: Enumeration of F-specific RNA bacteriophages Qualité de l'eau-Détection et dénombrement des bactériophages-Partie 1: Dénombrement des bactériophages ARN F spécifiques, 1995.
- [131] kevinstewart, Six-Stage and Two-Stage Viable Andersen Cascade Impactor - User Manual, 2007. [www.thermo.com/WEEERoHS](http://www.thermo.com/WEEERoHS).
- [132] J.M. Macher, Positive-Hole Correction of Multiple-Jet Impactors for Collecting Viable Microorganisms, *Am Ind Hyg Assoc J* 50 (1989) 561–568.  
<https://doi.org/10.1080/15298668991375164>.
- [133] C.J. Hogan, E.M. Kettleson, M.H. Lee, B. Ramaswami, L.T. Angenent, P. Biswas, Sampling methodologies and dosage assessment techniques for submicrometre and ultrafine virus aerosol particles, *J Appl Microbiol* 99 (2005) 1422–1434.  
<https://doi.org/10.1111/j.1365-2672.2005.02720.x>.
- [134] H.C. Men, M.L. Mecartney, J.C. ~ E M M I N ~ E R, *Microscop Minimizing Transmission Electron Microscopy Beam Damage during the Study of Surface Reactions on Sodium Chloride*, 1998.

- [135] H. Zhang, A.C.K. Lai, Evaluation of Single-Pass Disinfection Performance of Far-UVC Light on Airborne Microorganisms in Duct Flows, *Environ Sci Technol* 56 (2022) 17849–17857. <https://doi.org/10.1021/acs.est.2c04861>.
- [136] C.M. Walker, G. Ko, Effect of ultraviolet germicidal irradiation on viral aerosols, *Environ Sci Technol* 41 (2007) 5460–5465. <https://doi.org/10.1021/es070056u>.
- [137] V.T. Morgan, The Overall Convective Heat Transfer from Smooth Circular Cylinders, *Adv Heat Transf* (1975). [https://doi.org/10.1016/S0065-2717\(08\)70075-3](https://doi.org/10.1016/S0065-2717(08)70075-3).
- [138] S.W. Churchill, M. Bernstein, A correlating equation for forced convection from gases and liquids to a circular cylinder in crossflow, *J Heat Transfer* (1977). <https://doi.org/10.1115/1.3450685>.
- [139] J. Taborek, Heat transfer of a cylinder in crossflow, *Int J Heat Fluid Flow* (1986). [https://doi.org/10.1016/0142-727x\(86\)90066-4](https://doi.org/10.1016/0142-727x(86)90066-4).
- [140] M.F. Modest, Radiative Exchange Between Partially Specular Gray Surfaces, *Radiative Heat Transfer* (2013) 197–228. <https://doi.org/10.1016/b978-0-12-386944-9.50006-6>.
- [141] W.J. Kowalski, W.P. Bahnfleth, Design and optimization of UVGI air disinfection systems, *Architectural Engineering* (2001) 118.
- [142] F. Opitz, P. Treffinger, J. Wöllenstein, Modeling of Radiative Heat Transfer in an Electric Arc Furnace, *Metallurgical and Materials Transactions B: Process Metallurgy and Materials Processing Science* 48 (2017) 3301–3315. <https://doi.org/10.1007/s11663-017-1078-6>.

- [143] D.A. Andrienko, S.T. Surzhikovt, J.S. Shang, G.P. Huang, On view-factor approach for radiation transfer equation, 45th AIAA Plasmadynamics and Lasers Conference (2014). <https://doi.org/10.2514/6.2014-2488>.
- [144] H. Luo, L. Zhong, Numerical Analysis of Effects of Ventilation Conditions on an In-duct UVGI System for Infection Control, n.d.
- [145] A. Capetillo, C.J. Noakes, P.A. Sleight, Computational fluid dynamics analysis to assess performance variability of in-duct UV-C systems, *Sci Technol Built Environ* 21 (2015) 45–53. <https://doi.org/10.1080/10789669.2014.968512>.
- [146] H. Luo, C. Zhang, J. Zhu, Development of a numerical model for the hydrodynamics simulation of liquid-solid circulating fluidized beds, *Powder Technol* 348 (2019). <https://doi.org/10.1016/j.powtec.2019.03.018>.
- [147] F. Atci, Y.E. Cetin, M. Avci, O. Aydin, Evaluation of in-duct UV-C lamp array on air disinfection: A numerical analysis, *Sci Technol Built Environ* 27 (2020) 98–108. <https://doi.org/10.1080/23744731.2020.1776549>.
- [148] C.K. Ho, Radiation Dose Modeling in FLUENT ® Modeling Approach, *Security* (2009).
- [149] Y. Yang, H. Zhang, A.C. Lai, Lagrangian modeling of inactivation of airborne microorganisms by in-duct ultraviolet lamps, *Build Environ* 188 (2021) 107465. <https://doi.org/10.1016/j.buildenv.2020.107465>.
- [150] D.-K. Kim, D.-H. Kang, UVC LED Irradiation Effectively Inactivates Aerosolized Viruses, Bacteria, and Fungi in a Chamber-Type Air Disinfection System, (2018). <https://doi.org/10.1128/AEM>.

- [151] L.R. Koller, Bactericidal effects of ultraviolet radiation produced by low pressure mercury vapor lamps, *J Appl Phys* 10 (1939) 624–630. <https://doi.org/10.1063/1.1707353>.
- [152] H.C. Rentschler, R. Nagy, BACTERICIDAL ACTION OF ULTRAVIOLET RADIATION ON AIR-BORNE ORGANISMS, n.d.
- [153] S.J. Webb, C.C. Tai, DIFFERENTIAL, LETHAL AND MUTAGENIC ACTION OF 254nm AND 320-400nm RADIATION ON SEMI-DRIED BACTERIA, Pergamon Press, n.d.
- [154] C.Y. Lin, C.S. Li, Control effectiveness of ultraviolet germicidal irradiation on bioaerosols, *Aerosol Science and Technology* 36 (2002) 474–478. <https://doi.org/10.1080/027868202753571296>.
- [155] M.E. Martínez Retamar, C. Passalía, R.J. Brandi, M.D. Labas, Dose estimation methodology for the UV inactivation of bioaerosols in a Continuous-Flow reactor, *Aerosol Science and Technology* 53 (2019) 8–20. <https://doi.org/10.1080/02786826.2018.1533914>.
- [156] H. Luo, L. Zhong, Ultraviolet germicidal irradiation ( UVGI ) for in-duct airborne bioaerosol disinfection : Review and analysis of design factors, *Build Environ* 197 (2021) 107852. <https://doi.org/10.1016/j.buildenv.2021.107852>.
- [157] H. Zhang, X. Jin, S.S. Nunayon, A.C.K. Lai, Disinfection by in-duct ultraviolet lamps under different environmental conditions in turbulent airflows, *Indoor Air* 30 (2020) 500–511. <https://doi.org/10.1111/ina.12642>.

- [158] C.A. Gilkeson, C. Noakes, Application of CFD simulation to predicting upper-room UVGI effectiveness, *Photochem Photobiol* 89 (2013) 799–810. <https://doi.org/10.1111/php.12013>.
- [159] W. Li, M. Li, J.R. Bolton, J. Qu, Z. Qiang, Impact of inner-wall reflection on UV reactor performance as evaluated by using computational fluid dynamics: The role of diffuse reflection, *Water Res* 109 (2017) 382–388. <https://doi.org/10.1016/j.watres.2016.11.068>.
- [160] M. Li, Z. Qiang, J.R. Bolton, W. Ben, Impact of reflection on the fluence rate distribution in a UV reactor with various inner walls as measured using a micro-fluorescent silica detector, *Water Res* 46 (2012) 3595–3602. <https://doi.org/10.1016/j.watres.2012.04.004>.
- [161] M.A. Kotov, A.N. Shemyakin, N.G. Solovyov, M.Y. Yakimov, Symmetrization and Amplification of Germicidal Radiation Flux Produced by a Mercury Amalgam UV Lamp in Cylindrical Cavity with Diffusely Reflective Walls, *Symmetry (Basel)* 14 (2022). <https://doi.org/10.3390/sym14010125>.
- [162] Klaran Crystal IS, Using UV Reflective Materials to Maximize Disinfection. Accessed: 19/05/20., (2016) 6.
- [163] J. Simonet, C. Gantzer, Inactivation of poliovirus 1 and F-specific RNA phages and degradation of their genomes by UV irradiation at 254 nanometers, *Appl Environ Microbiol* 72 (2006) 7671–7677. <https://doi.org/10.1128/AEM.01106-06>.
- [164] B. Calgua, A. Carratalà, L. Guerrero-Latorre, A. de Abreu Corrêa, T. Kohn, R. Sommer, R. Girones, UVC Inactivation of dsDNA and ssRNA Viruses in Water:

- UV Fluences and a qPCR-Based Approach to Evaluate Decay on Viral Infectivity, *Food Environ Virol* 6 (2014) 260–268. <https://doi.org/10.1007/s12560-014-9157-1>.
- [165] B.M. Pecson, L.V. Martin, T. Kohn, Quantitative PCR for determining the infectivity of bacteriophage MS2 upon inactivation by heat, UV-B radiation, and singlet oxygen: Advantages and limitations of an enzymatic treatment to reduce false-positive results, *Appl Environ Microbiol* 75 (2009) 5544–5554. <https://doi.org/10.1128/AEM.00425-09>.
- [166] S.E. Beck, R.A. Rodriguez, M.A. Hawkins, T.M. Hargy, T.C. Larason, K.G. Linden, Comparison of UV-induced inactivation and RNA damage in MS2 phage across the germicidal UV spectrum, *Appl Environ Microbiol* 82 (2016) 1468–1474. <https://doi.org/10.1128/AEM.02773-15>.
- [167] T. Sigstam, G. Gannon, M. Cascella, B.M. Pecson, K.R. Wigginton, T. Kohn, Subtle differences in virus composition affect disinfection kinetics and mechanisms, *Appl Environ Microbiol* 79 (2013) 3455–3467. <https://doi.org/10.1128/AEM.00663-13>.
- [168] L. Guerrero-Latorre, E. Gonzales-Gustavson, A. Hundesa, R. Sommer, G. Rosina, UV disinfection and flocculation-chlorination sachets to reduce hepatitis E virus in drinking water, *Int J Hyg Environ Health* 219 (2016) 405–411. <https://doi.org/10.1016/j.ijheh.2016.04.002>.
- [169] M.J. Mattle, T. Kohn, Inactivation and tailing during UV254 disinfection of viruses: Contributions of viral aggregation, light shielding within viral aggregates, and recombination, *Environ Sci Technol* 46 (2012) 10022–10030. <https://doi.org/10.1021/es302058v>.

- [170] J. Sangsanont, H. Katayama, F. Kurisu, H. Furumai, Capsid-Damaging Effects of UV Irradiation as Measured by Quantitative PCR Coupled with Ethidium Monoazide Treatment, *Food Environ Virol* 6 (2014) 269–275. <https://doi.org/10.1007/s12560-014-9162-4>.
- [171] T. Tanaka, O. Nogariya, N. Shionoiri, Y. Maeda, A. Arakaki, Integrated molecular analysis of the inactivation of a non-enveloped virus, feline calicivirus, by UV-C radiation, *J Biosci Bioeng* 126 (2018) 63–68. <https://doi.org/10.1016/j.jbiosc.2018.01.018>.
- [172] E.K. Loveday, K.S. Hain, I. Kochetkova, J.F. Hedges, A. Robison, D.T. Snyder, S.K. Brumfield, M.J. Young, M.A. Jutila, C.B. Chang, M.P. Taylor, Effect of inactivation methods on sars-cov-2 virion protein and structure, *Viruses* 13 (2021). <https://doi.org/10.3390/v13040562>.
- [173] C.W. Lo, R. Matsuura, K. Iimura, S. Wada, A. Shinjo, Y. Benno, M. Nakagawa, M. Takei, Y. Aida, UVC disinfects SARS-CoV-2 by induction of viral genome damage without apparent effects on viral morphology and proteins, *Sci Rep* 11 (2021). <https://doi.org/10.1038/s41598-021-93231-7>.
- [174] M.A. Schuit, T.C. Larason, M.L. Krause, B.M. Green, B.P. Holland, S.P. Wood, S. Grantham, Y. Zong, C.J. Zarobila, D.L. Freeburger, D.M. Miller, J.K. Bohannon, S.A. Ratnesar-Shumate, E.R. Blatchley, X. Li, P.A. Dabisch, C.C. Miller, SARS-CoV-2 inactivation by ultraviolet radiation and visible light is dependent on wavelength and sample matrix, *J Photochem Photobiol B* 233 (2022). <https://doi.org/10.1016/j.jphotobiol.2022.112503>.

- [175] P. Tian, D. Yang, C. Quigley, M. Chou, X. Jiang, Inactivation of the tulane virus, a novel surrogate for the human norovirus, *J Food Prot* 76 (2013) 712–718. <https://doi.org/10.4315/0362-028X.JFP-12-361>.
- [176] D.I. Walker, L.J. Cross, T.A. Stapleton, C.L. Jenkins, D.N. Lees, J.A. Lowther, Assessment of the Applicability of Capsid-Integrity Assays for Detecting Infectious Norovirus Inactivated by Heat or UV Irradiation, *Food Environ Virol* 11 (2019) 229–237. <https://doi.org/10.1007/s12560-019-09390-4>.
- [177] E. Araud, M. Fuzawa, J.L. Shisler, J. Li, T.H. Nguyen, UV Inactivation of Rotavirus and Tulane Virus Targets Different Components of the Virions, (2020). <https://doi.org/10.1128/AEM>.
- [178] D. Wang, P. Tian, Inactivation conditions for human norovirus measured by an in situ capture-qRT-PCR method, *Int J Food Microbiol* 172 (2014) 76–82. <https://doi.org/10.1016/j.ijfoodmicro.2013.11.027>.
- [179] K.A. Stacey, B.S. Strauss, U. Light, K.C. Smith, RADIATION RESEARCH SUPPLEMENT 6, 54-79 (1966) Sessions II and II: Chemical Nature of Induced Structural Defects in DNA Physical and Chemical Changes Induced in Nucleic Acids by, n.d. <https://about.jstor.org/terms>.
- [180] M.M. Becker, Z. Wang, Origin of Ultraviolet Damage in DNA, *J. Mol. Biol* 210 (1989) 429–438.
- [181] P. Arguelles, Estimating UV-C Sterilization Dosage for COVID-19 Pandemic Mitigation Efforts, (2020). <https://doi.org/10.13140/RG.2.2.12837.65761>.

- [182] J.M. Coffin, Structure, Replication, and Recombination of Retrovirus Genomes: Some Unifying Hypotheses, *J. Gen. Virol.* 42 (1979) 1–26. <https://doi.org/10.1099/0022-1317-42-1-1>.
- [183] C.B. Beggs, E.J. Avital, Upper-room ultraviolet air disinfection might help to reduce COVID-19 transmission in buildings: A feasibility study, *PeerJ* (2020). <https://doi.org/10.7717/peerj.10196>.
- [184] B.M. Pecson, L.V. Martin, T. Kohn, Quantitative PCR for determining the infectivity of bacteriophage MS2 upon inactivation by heat, UV-B radiation, and singlet oxygen: Advantages and limitations of an enzymatic treatment to reduce false-positive results, *Appl Environ Microbiol* 75 (2009) 5544–5554. <https://doi.org/10.1128/AEM.00425-09>.
- [185] RStudio Team, RStudio: integrated development environment for R. RStudio, Inc., Boston, MA 14 (2022).
- [186] M. Li, J. Li, Y. Yang, W. Liu, Z. Liang, G. Ding, X. Chen, Q. Song, C. Xue, B. Sun, Investigation of mouse hepatitis virus strain A59 inactivation under both ambient and cold environments reveals the mechanisms of infectivity reduction following UVC exposure, *J Environ Chem Eng* 10 (2022). <https://doi.org/10.1016/j.jece.2022.107206>.
- [187] B.K. Mayer, Y. Yang, D.W. Gerrity, M. Abbaszadegan, The Impact of Capsid Proteins on Virus Removal and Inactivation during Water Treatment Processes, *Microbiol Insights* 8s2 (2015) MBI.S31441. <https://doi.org/10.4137/mbi.s31441>.

- [188] L.M. Kundu, U. Linne, M. Marahiel, T. Carell, RNA is more UV resistant than DNA: The formation of UV-induced DNA lesions is strongly sequence and conformation dependent, *Chemistry - A European Journal* 10 (2004) 5697–5705. <https://doi.org/10.1002/chem.200305731>.
- [189] Y. Kozai, Y. Sugino, Ultraviolet Inactivation of Avian Sarcoma Viruses: Biological and Biochemical Analysis' MASATOSHI OWADA, SEIJI IHARA, KUMAO TOYOSHIMA, 1976.
- [190] Y.K. Law, R.A. Forties, X. Liu, M.G. Poirier, B. Kohler, Sequence-dependent thymine dimer formation and photoreversal rates in double-stranded DNA, *Photochemical and Photobiological Sciences* 12 (2013) 1431–1439. <https://doi.org/10.1039/c3pp50078k>.
- [191] B. Ma, P.M. Gundy, C.P. Gerba, M.D. Sobsey, K.G. Linden, UV Inactivation of SARS-CoV-2 across the UVC Spectrum: KrCl\* Excimer, Mercury-Vapor, and Light-Emitting-Diode (LED) Sources, *Appl Environ Microbiol* 87 (2021). <https://doi.org/10.1128/AEM.01532-21>.
- [192] S.J. Boegel, M. Gabriel, M. Sasges, B. Petri, M.R. D'Agostino, A. Zhang, J.C. Ang, M.S. Miller, S.M. Meunier, M.G. Aucoin, Robust Evaluation of Ultraviolet-C Sensitivity for SARS-CoV-2 and Surrogate Coronaviruses, *Microbiol Spectr* 9 (2021). <https://doi.org/10.1128/spectrum.00537-21>.
- [193] M. Saknimit, I. Inatsuki, Y. Sugiyama, K.-I. Yagami, Virucidal Efficacy of Physico-chemical Treatments Against Coronaviruses and Parvoviruses of Laboratory Animals, 1988.

- [194] Y. Liu, Y. Cai, X. Zhang, Induction of Caspase-Dependent Apoptosis in Cultured Rat Oligodendrocytes by Murine Coronavirus Is Mediated during Cell Entry and Does Not Require Virus Replication, *J Virol* 77 (2003) 11952–11963. <https://doi.org/10.1128/jvi.77.22.11952-11963.2003>.
- [195] N. Hirano, S. Hind, K. Fujiwara, Physico-Chemical Properties of Mouse Hepatitis Virus (MHV-2) Grown on DBT Cell Culture, 1978.
- [196] E.K. Loveday, K.S. Hain, I. Kochetkova, J.F. Hedges, A. Robison, D.T. Snyder, S.K. Brumfield, M.J. Young, M.A. Jutila, C.B. Chang, M.P. Taylor, Effect of inactivation methods on sars-cov-2 virion protein and structure, *Viruses* 13 (2021). <https://doi.org/10.3390/v13040562>.
- [197] C.W. Lo, R. Matsuura, K. Iimura, S. Wada, A. Shinjo, Y. Benno, M. Nakagawa, M. Takei, Y. Aida, UVC disinfects SARS-CoV-2 by induction of viral genome damage without apparent effects on viral morphology and proteins, *Sci Rep* 11 (2021). <https://doi.org/10.1038/s41598-021-93231-7>.
- [198] M.A. Schuit, T.C. Larason, M.L. Krause, B.M. Green, B.P. Holland, S.P. Wood, S. Grantham, Y. Zong, C.J. Zarobila, D.L. Freeburger, D.M. Miller, J.K. Bohannon, S.A. Ratnesar-Shumate, E.R. Blatchley, X. Li, P.A. Dabisch, C.C. Miller, SARS-CoV-2 inactivation by ultraviolet radiation and visible light is dependent on wavelength and sample matrix, *J Photochem Photobiol B* 233 (2022). <https://doi.org/10.1016/j.jphotobiol.2022.112503>.
- [199] M. Biasin, A. Bianco, G. Pareschi, A. Cavalleri, C. Cavatorta, C. Fenizia, P. Galli, L. Lessio, M. Lualdi, E. Tombetti, A. Ambrosi, E.M.A. Redaelli, I. Saulle, D.

- Trabattoni, A. Zanutta, M. Clerici, UV-C irradiation is highly effective in inactivating SARS-CoV-2 replication, *Sci Rep* 11 (2021). <https://doi.org/10.1038/s41598-021-85425-w>.
- [200] R. Sesti-Costa, C. von Z. Negrão, J.F. Shimizu, A. Nagai, R.S.N. Tavares, D. Adamoski, W. Costa, M.A. Fontoura, T.J. da Silva, A. de Barros, A. Girasole, M. de Carvalho, V. de C. Teixeira, A.L.B. Ambrosio, F. Granja, J.L. Proença-Módena, R.E. Marques, S.M.G. Dias, UV 254 nm is more efficient than UV 222 nm in inactivating SARS-CoV-2 present in human saliva, *Photodiagnosis Photodyn Ther* 39 (2022). <https://doi.org/10.1016/j.pdpdt.2022.103015>.
- [201] J. Hobson-Peters, A.A. Amarilla, L. Rustanti, D.C. Marks, E. Roulis, A.A. Khromykh, N. Modhiran, D. Watterson, S. Reichenberg, F. Tolksdorf, C. Sumian, A. Seltsam, U. Gravemann, H.M. Faddy, Inactivation of SARS-CoV-2 infectivity in platelet concentrates or plasma following treatment with ultraviolet C light or with methylene blue combined with visible light, *Transfusion (Paris)* 63 (2023) 288–293. <https://doi.org/10.1111/trf.17238>.
- [202] E.I. Patterson, T. Prince, E.R. Anderson, A. Casas-Sanchez, S.L. Smith, C. Cansado-Utrilla, T. Solomon, M.J. Griffiths, Á. Acosta-Serrano, L. Turtle, G.L. Hughes, Methods of Inactivation of SARS-CoV-2 for Downstream Biological Assays, *Journal of Infectious Diseases* 222 (2020) 1462–1467. <https://doi.org/10.1093/infdis/jiaa507>.
- [203] N. Storm, L.G.A. McKay, S.N. Downs, R.I. Johnson, D. Birru, M. de Samber, W. Willaert, G. Cennini, A. Griffiths, Rapid and complete inactivation of SARS-CoV-

- 2 by ultraviolet-C irradiation, *Sci Rep* 10 (2020). <https://doi.org/10.1038/s41598-020-79600-8>.
- [204] B. Ma, P.M. Gundy, C.P. Gerba, M.D. Sobsey, K.G. Linden, UV Inactivation of SARS-CoV-2 across the UVC Spectrum: KrCl\* Excimer, Mercury-Vapor, and Light-Emitting-Diode (LED) Sources, *Appl Environ Microbiol* 87 (2021). <https://doi.org/10.1128/AEM.01532-21>.
- [205] S. Freeman, K. Kibler, Z. Lipsky, S. Jin, G.K. German, K. Ye, Systematic evaluating and modeling of SARS-CoV-2 UVC disinfection, *Sci Rep* 12 (2022). <https://doi.org/10.1038/s41598-022-09930-2>.
- [206] L.X. Li, R.H. Nissly, A. Swaminathan, I.M. Bird, N.R. Boyle, M.S. Nair, D.I. Greenawalt, A. Gontu, V.S. Cavener, T. Sornberger, J.D. Freihaut, S. V. Kuchipudi, W.P. Bahnfleth, Inactivation of HCoV-NL63 and SARS-CoV-2 in aqueous solution by 254 nm UV-C, *J Photochem Photobiol B* 245 (2023) 112755. <https://doi.org/10.1016/j.jphotobiol.2023.112755>.
- [207] J. Simonet, C. Gantzer, Inactivation of poliovirus 1 and F-specific RNA phages and degradation of their genomes by UV irradiation at 254 nanometers, *Appl Environ Microbiol* 72 (2006) 7671–7677. <https://doi.org/10.1128/AEM.01106-06>.
- [208] S.P. Sherchan, S.A. Snyder, C.P. Gerba, I.L. Pepper, Inactivation of MS2 coliphage by UV and hydrogen peroxide: Comparison by cultural and molecular methodologies, *J Environ Sci Health A Tox Hazard Subst Environ Eng* 49 (2014) 397–403. <https://doi.org/10.1080/10934529.2014.854607>.

- [209] B. Calgua, A. Carratalà, L. Guerrero-Latorre, A. de Abreu Corrêa, T. Kohn, R. Sommer, R. Girones, UVC Inactivation of dsDNA and ssRNA Viruses in Water: UV Fluences and a qPCR-Based Approach to Evaluate Decay on Viral Infectivity, *Food Environ Virol* 6 (2014) 260–268. <https://doi.org/10.1007/s12560-014-9157-1>.
- [210] S.E. Beck, R.A. Rodriguez, M.A. Hawkins, T.M. Hargy, T.C. Larason, K.G. Linden, Comparison of UV-induced inactivation and RNA damage in MS2 phage across the germicidal UV spectrum, *Appl Environ Microbiol* 82 (2016) 1468–1474. <https://doi.org/10.1128/AEM.02773-15>.
- [211] Y. Wang, E. Araud, J.L. Shisler, T.H. Nguyen, B. Yuan, Influence of algal organic matter on MS2 bacteriophage inactivation by ultraviolet irradiation at 220 nm and 254 nm, *Chemosphere* 214 (2019) 195–202. <https://doi.org/10.1016/j.chemosphere.2018.09.065>.
- [212] T. Sigstam, G. Gannon, M. Cascella, B.M. Pectson, K.R. Wigginton, T. Kohn, Subtle differences in virus composition affect disinfection kinetics and mechanisms, *Appl Environ Microbiol* 79 (2013) 3455–3467. <https://doi.org/10.1128/AEM.00663-13>.
- [213] M.J. Mattle, T. Kohn, Inactivation and tailing during UV254 disinfection of viruses: Contributions of viral aggregation, light shielding within viral aggregates, and recombination, *Environ Sci Technol* 46 (2012) 10022–10030. <https://doi.org/10.1021/es302058v>.
- [214] G.W. Park, K.G. Linden, M.D. Sobsey, Inactivation of murine norovirus, feline calicivirus and echovirus 12 as surrogates for human norovirus (NoV) and coliphage (F+) MS2 by ultraviolet light (254 nm) and the effect of cell association on UV

- inactivation, *Lett Appl Microbiol* 52 (2011) 162–167.  
<https://doi.org/10.1111/j.1472-765X.2010.02982.x>.
- [215] S.C. Weng, N. Dunkin, K.J. Schwab, J. McQuarrie, K. Bell, J.G. Jacangelo, Infectivity reduction efficacy of UV irradiation and peracetic acid-UV combined treatment on MS2 bacteriophage and murine norovirus in secondary wastewater effluent, *J Environ Manage* 221 (2018) 1–9.  
<https://doi.org/10.1016/j.jenvman.2018.04.064>.
- [216] J.E. Lee, K.D. Zoh, G.P. Ko, Inactivation and UV disinfection of murine norovirus with TiO<sub>2</sub> under various environmental conditions, *Appl Environ Microbiol* 74 (2008) 2111–2117. <https://doi.org/10.1128/AEM.02442-07>.
- [217] J.A. Thurston-Enriquez, C.N. Haas, J. Jacangelo, K. Riley, C.P. Gerba, Inactivation of feline calicivirus and adenovirus type 40 by UV radiation, *Appl Environ Microbiol* 69 (2003) 577–582. <https://doi.org/10.1128/AEM.69.1.577-582.2003>.
- [218] Q.S. Meng, C.P. Gerba, COMPARATIVE INACTIVATION OF ENTERIC ADENOVIRUSES, POLIOVIRUS AND COLIPHAGES BY ULTRAVIOLET IRRADIATION, 1996.
- [219] Gwy-Am Shin, Karl G. Linden, Mark D. Sobesy, Low pressure ultraviolet inactivation of pathogenic enteric viruses and bacteriophages, [Http://Jees.Nrc.Ca](http://Jees.Nrc.Ca) (2005).
- [220] S.S. Thompson, J.L. Jackson, M. Suva-Castillo, W.A. Yanko, Z. El Jack, J. Kuo, C.-L. Chen, F.P. Williams, D.P. Schnurr, Detection of Infectious Human Adenoviruses

- in Tertiary-Treated and Ultraviolet-Disinfected Wastewater, *Water Environment Research* 75 (2003) 163–170. <https://doi.org/10.2175/106143003x140944>.
- [221] D.A. Battigelli, M.D. Sobsey, D.C. Lobe, *THE INACTIVATION OF HEPATITIS A VIRUS AND OTHER MODEL VIRUSES BY UV IRRADIATION*, 1993.
- [222] K. Furuse, I. Watanabe, Effects of ultraviolet light (UV) irradiation on RNA phage in H<sub>2</sub>O and in D<sub>2</sub>O, *Virology* 46 (1971) 171–172. [https://doi.org/10.1016/0042-6822\(71\)90018-3](https://doi.org/10.1016/0042-6822(71)90018-3).
- [223] J.A. Tree, M.R. Adams, D.N. Lees, Virus inactivation during disinfection of wastewater by chlorination and UV irradiation and the efficacy of F+ bacteriophage as a ‘viral indicator,’ *Water Science and Technology* 35 (1997) 227–232. [https://doi.org/https://doi.org/10.1016/S0273-1223\(97\)00263-1](https://doi.org/https://doi.org/10.1016/S0273-1223(97)00263-1).
- [224] R. Sommer, W. Pribil, S. Appelt, P. Gehringer, H. Eschweiler, H. Leth, A. Cabaj, T. Haider, *INACTIVATION OF BACTERIOPHAGES IN WATER BY MEANS OF NON-IONIZING (UV-253.7 nm) AND IONIZING (GAMMA) RADIATION: A COMPARATIVE APPROACH*, 2001.
- [225] R. Sommer, T. Haider, A. Cabaj, W. Pribil, M. Lhotsky, Time dose reciprocity in UV disinfection of water, *Water Science and Technology* 38 (1998) 145–150. [https://doi.org/https://doi.org/10.1016/S0273-1223\(98\)00816-6](https://doi.org/https://doi.org/10.1016/S0273-1223(98)00816-6).
- [226] H. Mamane-Gravetz, K.G. Linden, A. Cabaj, R. Sommer, Spectral sensitivity of *Bacillus subtilis* spores and MS2 coliphage for validation testing of ultraviolet reactors for water disinfection, *Environ Sci Technol* 39 (2005) 7845–7852. <https://doi.org/10.1021/es048446t>.

- [227] M.R. Templeton, R.C. Andrews, R. Hofmann, Impact of iron particles in groundwater on the UV inactivation of bacteriophages MS2 and T4, *J Appl Microbiol* 101 (2006) 732–741. <https://doi.org/10.1111/j.1365-2672.2006.02980.x>.
- [228] G. Ko, T.L. Cromeans, M.D. Sobsey, UV inactivation of adenovirus type 41 measured by cell culture mRNA RT-PCR, *Water Res* 39 (2005) 3643–3649. <https://doi.org/10.1016/j.watres.2005.06.013>.
- [229] A. Wiedenmann, U. Straub, C.-H. Wang, B. Flehmig, D. Schoenen, DISINFECTION OF HEPATITIS A VIRUS AND MS-2 COLIPHAGE IN WATER BY ULTRAVIOLET IRRADIATION: COMPARISON OF UV-SUSCEPTIBILITY, 1993. <http://iwaponline.com/wst/article-pdf/27/3-4/335/26866/335.pdf>.
- [230] L.F. Batch, C.R. Schulz, K.G. Linden, Evaluating water quality effects on UV disinfection of MS2 coliphage, *J Am Water Works Assoc* 96 (2004) 75–87. <https://doi.org/10.1002/j.1551-8833.2004.tb10651.x>.
- [231] A.M. De Roda Husman, P. Bijkerk, W. Lodder, H. Van Den Berg, W. Pribil, A. Cabaj, P. Gehringer, R. Sommer, E. Duizer, Calicivirus inactivation by nonionizing (253.7-nanometer-wavelength [UV]) and ionizing (gamma) radiation, *Appl Environ Microbiol* 70 (2004) 5089–5093. <https://doi.org/10.1128/AEM.70.9.5089-5093.2004>.
- [232] M.A. Butkus, M.P. Labare, J.A. Starke, K. Moon, M. Talbot, Use of aqueous silver to enhance inactivation of coliphage MS-2 by UV disinfection, *Appl Environ*

- Microbiol 70 (2004) 2848–2853. <https://doi.org/10.1128/AEM.70.5.2848-2853.2004>.
- [233] J.A. Oppenheimer, J.G. Jacangelo, J.-M. Laine, J.E. Hoagland, Testing the Equivalency of Ultraviolet Light and Chlorine for Disinfection of Wastewater to Reclamation Standards, n.d. <https://www.jstor.org/stable/25044837>.
- [234] S. Nuanualsuwan, T. Mariam, S. Himathongkham, D.O. Cliver, Ultraviolet Inactivation of Feline Calicivirus, Human Enteric Viruses and Coliphages, Photochem Photobiol 76 (2002) 406–410. [https://doi.org/10.1562/0031-8655\(2002\)0760406uiofch2.0.co2](https://doi.org/10.1562/0031-8655(2002)0760406uiofch2.0.co2).
- [235] A.M. Rauth, THE PHYSICAL STATE OF VIRAL NUCLEIC ACID AND THE SENSITIVITY OF VIRUSES TO ULTRAVIOLET LIGHT, n.d.
- [236] T.J. Nieuwstad, A.H. Havelaar, The Kinetics of Batch Ultraviolet Inactivation of Bacteriophage MS2 and Microbiological Calibration of an Ultraviolet Pilot Plant, Journal of Environmental Science and Health. Part A: Environmental Science and Engineering and Toxicology 29 (1994) 1993–2007. <https://doi.org/10.1080/10934529409376160>.
- [237] V. Lazarova, P. Savoye, Technical and sanitary aspects of wastewater disinfection by UV irradiation for landscape irrigation, 2004. <http://iwaponline.com/wst/article-pdf/50/2/203/421475/203.pdf>.
- [238] R.A. Rodriguez, S. Bounty, S. Beck, C. Chan, C. McGuire, K.G. Linden, Photoreactivation of bacteriophages after UV disinfection: Role of genome structure

and impacts of UV source, *Water Res* 55 (2014) 143–149.  
<https://doi.org/10.1016/j.watres.2014.01.065>.

- [239] W.J. Lodder, H.H.J.L. Van Den Berg, S.A. Rutjes, M. Bouwknecht, J.F. Schijven, A.M. De Roda Husman, Reduction of bacteriophage MS2 by filtration and irradiation determined by culture and quantitative real-time RT-PCR, *J Water Health* 11 (2013) 256–266. <https://doi.org/10.2166/wh.2013.204>.
- [240] K.S. Fallon, T.M. Hargy, E.D. Mackey, H.B. Wright, J.L. Clancy, J.L. Clancy, Development and characterization of nonpathogenic surrogates for UV reactor validation, 2007.
- [241] N. Augsburger, A.T. Rachmadi, N. Zaouri, Y. Lee, P.Y. Hong, Recent Update on UV Disinfection to Fulfill the Disinfection Credit Value for Enteric Viruses in Water, *Environ Sci Technol* 55 (2021) 16283–16298.  
<https://doi.org/10.1021/acs.est.1c03092>.
- [242] C.P. Gerba, D.M. Gramos, N. Nwachuku, Comparative inactivation of enteroviruses and adenovirus 2 by UV light, *Appl Environ Microbiol* 68 (2002) 5167–5169.  
<https://doi.org/10.1128/AEM.68.10.5167-5169.2002>.
- [243] H. Woo, S.E. Beck, L.A. Boczek, K.M. Carlson, N.E. Brinkman, K.G. Linden, O.R. Lawal, S.L. Hayes, H. Ryu, Efficacy of inactivation of human enteroviruses by dual-wavelength germicidal ultraviolet (UV-C) light emitting diodes (LEDs), *Water (Switzerland)* 11 (2019). <https://doi.org/10.3390/w11061131>.
- [244] W.F. Hill, F.E. Hamblet, W.H. Benton, E.W. Akin, Ultraviolet Devitalization of Eight Selected Enteric Viruses in Estuarine Water<sup>1</sup>, 1970.

- [245] S. Torii, M.H. Corre, F. Miura, M. Itamochi, K. Haga, K. Katayama, H. Katayama, T. Kohn, Genotype-dependent kinetics of enterovirus inactivation by free chlorine and ultraviolet (UV) irradiation, *Water Res* 220 (2022). <https://doi.org/10.1016/j.watres.2022.118712>.
- [246] A.H. Havelaar, Virus, Bacteriophages and Water purification, *Veterinary Quarterly* 9 (1987) 356–360. <https://doi.org/10.1080/01652176.1987.9694125>.
- [247] S. Torii, F. Miura, M. Itamochi, K. Haga, K. Katayama, H. Katayama, Impact of the heterogeneity in free chlorine, uv254, and ozone susceptibilities among coxsackievirus b5 on the prediction of the overall inactivation efficiency, *Environ Sci Technol* 55 (2021) 3156–3164. <https://doi.org/10.1021/acs.est.0c07796>.
- [248] B.V. Bravo, UV LIGHT INACTIVATION OF ADENOVIRUS, COXSACKIEVIRUS AND MURINE NOROVIRUS CORE View metadata, citation and similar papers at core.ac.uk provided by Illinois Digital Environment for Access to Learning and Scholarship Repository, n.d.
- [249] B.K. Mayer, H. Ryu, D. Gerrity, M. Abbaszadegan, Development and validation of an integrated cell culture-qRT-PCR assay for simultaneous quantification of coxsackieviruses, echoviruses, and polioviruses in disinfection studies, *Water Science and Technology* 61 (2010) 375–387. <https://doi.org/10.2166/wst.2010.818>.
- [250] J. Wang, A. Mauser, S.F. Chao, K. Remington, R. Treckmann, K. Kaiser, D. Pifat, J.A. Hotta, Virus inactivation and protein recovery in a novel ultraviolet-C reactor, *Vox Sang* 86 (2004) 230–238. <https://doi.org/10.1111/j.0042-9007.2004.00485.x>.

- [251] H.S. von Brodorotti, H. Mahnel, [Comparative studies on susceptibility of viruses to ultraviolet rays], *Zentralbl Veterinarmed B* 29 (1982) 129–36.
- [252] Z. Zavadová, H. Libíková, Comparison of the sensitivity to ultraviolet irradiation of reovirus 3 and some viruses of the Kemerovo group., *Acta Virol* 19 (1975) 88–90.
- [253] E.I. Budowsky, S.E. Bresl~n, E.A.F. W3, N. V Zi~el~z~ova, *Archives of Virology Principles of Selective Inactivation of Viral Genome I. UV-Indueed Inactivation of Influenza Virus*, 1981.
- [254] I. Tamm' And, D.J. Fluke', THE EFFECT OF MONOCHROMATIC ULTRAVIOLET RADIATION ON THE INFECTIVITY AND HEMAGGLUTINATING ABILITY OF THE INFLUENZA VIRUS TYPE A STRAIN PR-8', n.d. <https://journals.asm.org/journal/jb>.
- [255] V. Vignali, T. Hoff, J.J. de Vries-Idema, A.L.W. Huckriede, J.M. van Dijn, P. van Rijn, An Efficient UV-C Disinfection Approach and Biological Assessment Strategy for Microphones, *Applied Sciences (Switzerland)* 12 (2022). <https://doi.org/10.3390/app12147239>.
- [256] M. Kojima, K. Mawatari, T. Emoto, R. Nishisaka-Nonaka, T.K.N. Bui, T. Shimohata, T. Uebanso, M. Akutagawa, Y. Kinouchi, T. Wada, M. Okamoto, H. Ito, K. Tojo, T. Daidoji, T. Nakaya, A. Takahashi, Irradiation by a combination of different peak-wavelength ultraviolet-light emitting diodes enhances the inactivation of influenza A viruses, *Microorganisms* 8 (2020) 1–15. <https://doi.org/10.3390/microorganisms8071014>.

- [257] K. Narita, K. Asano, K. Naito, H. Ohashi, M. Sasaki, Y. Morimoto, T. Igarashi, A. Nakane, Ultraviolet C light with wavelength of 222 nm inactivates a wide spectrum of microbial pathogens, *Journal of Hospital Infection* 105 (2020) 459–467. <https://doi.org/10.1016/j.jhin.2020.03.030>.
- [258] G. Abraham', The Effect of Ultraviolet Radiation on the Primary Transcription of Influenza Virus Messenger RNAs, 1979.
- [259] L.J.N. Ross, P. Wildy, K.R. Cameron, Formation of small plaques by herpes viruses irradiated with ultraviolet light, *Virology* 45 (1971) 808–812. [https://doi.org/10.1016/0042-6822\(71\)90201-7](https://doi.org/10.1016/0042-6822(71)90201-7).
- [260] A. Hollaender, J.W. Oliphant, THE INACTIVATING EFFECT OF MONOCHROMATIC ULTRAVIOLET RADIATION ON INFLUENZA VIRUS and 2937A in the inactivation of influenza virus A and compare it with the inactivation spectrum of Escherichia coli and of a number of other viruses and virus-like agents. EXPERIMENTAL TECHNIQUE FOR PREPARATION AND TESTING OF VIRUS MATERIAL, n.d.
- [261] G.J. Jakab, M.E. Knight, DECREASED INFLUENZA VIRUS PATHOGENESIS BY INFECTION WITH GERMICIDAL UV-IRRADIATED AIRBORNE VIRUS, 1982.
- [262] S.P. Sherchan, S.A. Snyder, C.P. Gerba, I.L. Pepper, Inactivation of MS2 coliphage by UV and hydrogen peroxide: Comparison by cultural and molecular methodologies, *J Environ Sci Health A Tox Hazard Subst Environ Eng* 49 (2014) 397–403. <https://doi.org/10.1080/10934529.2014.854607>.

- [263] Y. Wang, E. Araud, J.L. Shisler, T.H. Nguyen, B. Yuan, Influence of algal organic matter on MS2 bacteriophage inactivation by ultraviolet irradiation at 220 nm and 254 nm, *Chemosphere* 214 (2019) 195–202. <https://doi.org/10.1016/j.chemosphere.2018.09.065>.
- [264] by B. Sara Elizabeth Beck S, WAVELENGTH-SPECIFIC EFFECTS OF ULTRAVIOLET LIGHT ON MICROORGANISMS AND VIRUSES FOR IMPROVING WATER DISINFECTION, 2003.
- [265] D. Schmelling, ULTRAVIOLET DISINFECTION GUIDANCE MANUAL FOR THE FINAL LONG TERM 2 ENHANCED SURFACE WATER TREATMENT RULE, 2006. <http://www.epa.gov/safewater/disinfection/lt2/compliance.html>.
- [266] P. Loughran, G. Jenner, R. Haverland, Resource Consent Application to Discharge Treated Wastewater to the CMA from the Porirua Wastewater, 2020.
- [267] Y. Aoyagi, M. Takeuchi, K. Yoshida, M. Kurouchi, N. Yasui, N. Kamiko, T. Araki, Y. Nanishi, Inactivation of Bacterial Viruses in Water Using Deep Ultraviolet Semiconductor Light-Emitting Diode, *Journal of Environmental Engineering* 137 (2011) 1215–1218. [https://doi.org/10.1061/\(asce\)ee.1943-7870.0000442](https://doi.org/10.1061/(asce)ee.1943-7870.0000442).
- [268] W.A.M. Hijnen, E.F. Beerendonk, G.J. Medema, Inactivation credit of UV radiation for viruses, bacteria and protozoan (oo)cysts in water: A review, *Water Res* 40 (2006) 3–22. <https://doi.org/10.1016/j.watres.2005.10.030>.
- [269] S. Rattanakul, K. Oguma, H. Sakai, S. Takizawa, Inactivation of Viruses by Combination Processes of UV and Chlorine, 2014.

- [270] R.M. Jenny, O.D. Simmons, M. Shatalov, J.J. Ducoste, Modeling a continuous flow ultraviolet Light Emitting Diode reactor using computational fluid dynamics, *Chem Eng Sci* 116 (2014) 524–535. <https://doi.org/10.1016/j.ces.2014.05.020>.
- [271] S. Rattanakul, K. Oguma, Inactivation kinetics and efficiencies of UV-LEDs against *Pseudomonas aeruginosa*, *Legionella pneumophila*, and surrogate microorganisms, *Water Res* 130 (2018) 31–37. <https://doi.org/10.1016/j.watres.2017.11.047>.
- [272] J.C.H. Chang, S.F. Ossoff, D.C. Lobe, M.H. Dorfman, C.M. Dumais, R.G. Qualls, J.D. Johnson, *UV Inactivation of Pathogenic and Indicator Microorganisms*, 1985.
- [273] G.D. Harris, V. Dean Adams, D.L. Sorensen, M.S. Curtis, *ULTRAVIOLET INACTIVATION OF SELECTED BACTERIA AND VIRUSES WITH PHOTOREACTIVATION OF THE BACTERIA*, 1987.
- [274] A. Maier, D. Tougianidou, A. Wiedenmann, K. Botzenhart, Detection of poliovirus by cell culture and by PCR after UV disinfection, *Water Science and Technology* 31 (1995) 141–145. [https://doi.org/https://doi.org/10.1016/0273-1223\(95\)00255-L](https://doi.org/https://doi.org/10.1016/0273-1223(95)00255-L).
- [275] T. Helentjaris, E. Ehrenfeld, *Inhibition of Host Cell Protein Synthesis by UV-Inactivated Poliovirus*, 1977.
- [276] J.M. Bishop, N. Quintrell, G. Koch, Poliovirus double-stranded RNA: Inactivation by ultraviolet light, *J Mol Biol* 24 (1967) 125–128. [https://doi.org/https://doi.org/10.1016/0022-2836\(67\)90096-4](https://doi.org/https://doi.org/10.1016/0022-2836(67)90096-4).
- [277] R. Dulbecco, M. Vogt, *BIOLOGICAL PROPERTIES OF POLIOMYELITIS VIRUSES AS STUDIED BY THE PLAQUE TECHNIQUE*, *Ann N Y Acad Sci* 61 (1955) 790–800. <https://doi.org/10.1111/j.1749-6632.1955.tb42535.x>.

- [278] Specific Cross-linking of Capsid Proteins to Virus RNA by Ultraviolet Irradiation of Poliovirus, 1982.
- [279] S. Nuanualsuwan, D.O. Cliver, Infectivity of RNA from inactivated poliovirus, *Appl Environ Microbiol* 69 (2003) 1629–1632. <https://doi.org/10.1128/AEM.69.3.1629-1632.2003>.
- [280] J.A. Tree, M.R. Adams, D.N. Lees, Disinfection of feline calicivirus (a surrogate for Norovirus) in wastewaters, *J Appl Microbiol* 98 (2005) 155–162. <https://doi.org/10.1111/j.1365-2672.2004.02442.x>.
- [281] M.R. Karim, G.S. Fout, C.H. Johnson, K.M. White, S.U. Parshionikar, Propidium monoazide reverse transcriptase PCR and RT-qPCR for detecting infectious enterovirus and norovirus, *J Virol Methods* 219 (2015) 51–61. <https://doi.org/10.1016/j.jviromet.2015.02.020>.
- [282] S. Young, J. Torrey, V. Bachmann, T. Kohn, Relationship Between Inactivation and Genome Damage of Human Enteroviruses Upon Treatment by UV254, Free Chlorine, and Ozone, *Food Environ Virol* 12 (2020) 20–27. <https://doi.org/10.1007/s12560-019-09411-2>.
- [283] Q. Zhong, A. Carratalà, R. Ossola, V. Bachmann, T. Kohn, Cross-resistance of UV- or chlorine dioxide-resistant echovirus 11 to other disinfectants, *Front Microbiol* 8 (2017). <https://doi.org/10.3389/fmicb.2017.01928>.
- [284] C.-H. Wang, S.-Y. Tschen-F, B. Flehmig, Antigenicity of hepatitis ultra-violet inactivation A virus after, 1995.

- [285] R Di Stefano, G Burgio, P Ammatuna, A Sinatra, A Chiarini, Thermal and ultraviolet inactivation of plaque purified measles virus clones, *G Batteriol Virol Immunol* 69 (1976) 3–11.
- [286] S. Xu, D. Wang, D. Yang, H. Liu, P. Tian, Alternative methods to determine infectivity of Tulane virus: A surrogate for human norovirus, *Food Microbiol* 48 (2015) 22–27. <https://doi.org/10.1016/j.fm.2014.12.004>.
- [287] Enteric Viruses in Drinking Water Document for Public Consultation Prepared by the Federal-Provincial-Territorial Committee on Drinking Water Consultation period ends, 2017.
- [288] K. Dan~r, A. Mayr, *Archives of Virology In vitro Studies on Borna Virus II. Properties of the Virus*, 1979.
- [289] Y. Kozai, Y. Sugino, *Ultraviolet Inactivation of Avian Sarcoma Viruses: Biological and Biochemical Analysis*’ MASATOSHI OWADA, SEIJI IHARA, KUMAO TOYOSHIMA, 1976.
- [290] K. Bister, H.E. Varmus, E. Stavnezer, E. Hunter, P.K. Vogt6, *Biological and Biochemical Studies on the Inactivation of Avian Oncoviruses by Ultraviolet Irradiation1*, 1977.
- [291] *Ultraviolet Inactivation of Moloney Leukaemia Virus: Relative Target Size Required for Virus Replication and Rescue of “Defective” Murine Sarcoma Virus*, n.d.

- [292] G. Kelloff, S.A. Aaronson, R. V. Gilden, Inactivation of murine sarcoma and leukemia viruses by ultra-violet irradiation, *Virology* 42 (1970) 1133–1135. [https://doi.org/10.1016/0042-6822\(70\)90361-2](https://doi.org/10.1016/0042-6822(70)90361-2).
- [293] H. Yoshikura, Ultraviolet inactivation of murine leukemia and sarcoma viruses, *Int J Cancer* 7 (1971) 131–140. <https://doi.org/10.1002/ijc.2910070115>.
- [294] Mechanisms of Early and Late Polykaryocytosis Induced by the Bovine Leukaemia Virus, 1981.
- [295] A. Shimizu, N. Shimizu, A. Tanaka, A. Jinno-Oue, B.B. Roy, M. Shinagawa, O. Ishikawa, H. Hoshino, Human T-cell leukaemia virus type I is highly sensitive to UV-C light, *Journal of General Virology* 85 (2004) 2397–2406. <https://doi.org/10.1099/vir.0.19578-0>.
- [296] H. Yoshikura, Thermostability of Human Immunodeficiency Virus (HIV-1) in a Liquid Matrix Is Far Higher than That of an Ecotropic Murine Leukemia Virus, *Japanese Journal of Cancer Research* 80 (1989) 1–5. <https://doi.org/10.1111/j.1349-7006.1989.tb02235.x>.
- [297] H. Schöbel, G. Diem, J. Kiechl, D. Chisté, G. Bertacchi, A. Mayr, D. Wilflingseder, C. Lass-Flörl, W. Posch, Antimicrobial efficacy and inactivation kinetics of a novel LED-based UV-irradiation technology, *Journal of Hospital Infection* 135 (2023) 11–17. <https://doi.org/10.1016/j.jhin.2022.12.023>.
- [298] H.S. von Brodorotti, H. Mahnel, [Comparative studies on susceptibility of viruses to ultraviolet rays], *Zentralbl Veterinarmed B* 29 (1982) 129–136. <http://europepmc.org/abstract/MED/6283768>.

- [299] A. Smirnov, S. Kapitulez, N. Kaverin, Effects of UV-irradiation upon Venezuelan equine encephalomyelitis virus, 1992.
- [300] N.P. Dubinin, G.D. Zasukhina, V.A. Nesmashnova, G.N. Lvova, Spontaneous and Induced Mutagenesis in Western Equine Encephalomyelitis Virus in Chick Embryo Cells with Different Repair Activity (excision repair system/RNA-containing virus/mammalian cell culture), 1975. <https://www.pnas.org>.
- [301] J. White, K. Matlin, A. Helenius, Cell Fusion by Semliki Forest, Influenza, and Vesicular Stomatitis Viruses MATERIALS AND METHODS Viruses and Cells, n.d.
- [302] M. Weiss, M.C. Horzinek, Resistance of Berne virus to physical and chemical treatment, *Vet Microbiol* 11 (1986) 41–49. [https://doi.org/10.1016/0378-1135\(86\)90005-2](https://doi.org/10.1016/0378-1135(86)90005-2).
- [303] P.H.S. Bay, M.E. Reichmann, UV Inactivation of the Biological Activity of Defective Interfering Particles Generated by Vesicular Stomatitis Virus, 1979.
- [304] N.R. Kallenbach, P.A. Cornelius, D. Negus, D. Montgomerie, S. Englander, Inactivation of Viruses by Ultraviolet Light<sup>1</sup>, in: n.d.: pp. 70–82. <https://doi.org/10.1159/000416558>.
- [305] F.G. Terpstra, A.B. Van't Wout, H. Schuitemaker, F.A.C. Van Engelenburg, D.W.C. Dekkers, R. Verhaar, D. De Korte, A.J. Verhoeven, Potential and limitation of UVC irradiation for the inactivation of pathogens in platelet concentrates, *Transfusion (Paris)* 48 (2008) 304–313. <https://doi.org/10.1111/j.1537-2995.2007.01524.x>.

- [306] Ann Kristin Øye, Espen Rimstad, Inactivation of infectious salmon anaemia virus, viral haemorrhagic septicaemia virus and infectious pancreatic necrosis virus in water using UVC irradiation, *DISEASES OF AQUATIC ORGANISMS Dis Aquat Org* 48 (2001) 1–5.
- [307] H. Liltved, C. Vogelsang, I. Modahl, B.H. Dannevig, High resistance of fish pathogenic viruses to UV irradiation and ozonated seawater, *Aquac Eng* 34 (2006) 72–82. <https://doi.org/10.1016/j.aquaeng.2005.05.002>.
- [308] W. Levinson<sup>3</sup>, H. Rubin, *Radiation Studies of Avian Tumor Viruses and of Newcastle Disease Virus*<sup>\*\*</sup>, 1966.
- [309] H. Rub<sup>&</sup>, H.M. Temin<sup>~</sup>, *A Radiological Study of Cell-Virus Interaction in the Rous Sarcoma*<sup>'</sup>, 1959.
- [310] B. Ma, Y.S. Linden, P.M. Gundy, C.P. Gerba, M.D. Sobsey, K.G. Linden, Inactivation of coronaviruses and phage Phi6 from irradiation across UVC wavelengths, *Environ Sci Technol Lett* 8 (2021) 425–430. <https://doi.org/10.1021/acs.estlett.1c00178>.
- [311] B. Ma, P.M. Gundy, C.P. Gerba, M.D. Sobsey, K.G. Linden, UV Inactivation of SARS-CoV-2 across the UVC Spectrum: KrCl<sup>\*</sup> Excimer, Mercury-Vapor, and Light-Emitting-Diode (LED) Sources, *Appl Environ Microbiol* 87 (2021). <https://doi.org/10.1128/AEM.01532-21>.
- [312] J. Gibson, B.P. Poon, J. Lam, A. Sultana, N. Christie-Holmes, S. Mubareka, S.D. Gray-Owen, R. Farnood, Exploring the Differences in the Response of SARS-CoV-

2 Delta and Omicron to Ultraviolet Radiation, ACS ES&T Engineering (2023).  
<https://doi.org/10.1021/acsestengg.3c00019>.

- [313] J. Han, L. Ruan, Stability of SARS Coronavirus in Human Specimens and Environment and Its Sensitivity to Heating and UV Irradiation Root response and regulation mechanism of tea tree tolerance to soil potassium deficiency (41601329) View project National Science and Technology Major Project View project, 2003. <https://www.researchgate.net/publication/8995908>.
- [314] M. Eickmann, U. Gravemann, W. Handke, F. Tolksdorf, S. Reichenberg, T.H. Müller, A. Seltsam, Inactivation of three emerging viruses – severe acute respiratory syndrome coronavirus, Crimean–Congo haemorrhagic fever virus and Nipah virus – in platelet concentrates by ultraviolet C light and in plasma by methylene blue plus visible light, *Vox Sang* 115 (2020) 146–151. <https://doi.org/10.1111/vox.12888>.
- [315] J.L. Sagripanti, C.D. Lytle, Estimated Inactivation of Coronaviruses by Solar Radiation With Special Reference to COVID-19, *Photochem Photobiol* 96 (2020) 731–737. <https://doi.org/10.1111/php.13293>.
- [316] L.M. Kasman, L.D. Porter, *Bacteriophages*, StatPearls Publishing, 2023. <https://www.ncbi.nlm.nih.gov/books/NBK493185/> (accessed August 14, 2023).
- [317] S.A. Sattar, J. Tetro Bsc, S. Bidawid Msc, J. Farber, D. Syed, A. Sattar, Foodborne spread of hepatitis A: Recent studies on virus survival, transfer and inactivation, n.d.
- [318] P.C. De Groen, Hepatitis E, 2004. <https://www.cdc.gov/hepatitis/hev/hevfaq.htm> (accessed August 14, 2023).

- [319] C.E. Wobus, L.B. Thackray, H.W. Virgin, Murine Norovirus: a Model System To Study Norovirus Biology and Pathogenesis, *J Virol* 80 (2006) 5104–5112. <https://doi.org/10.1128/jvi.02346-05>.
- [320] S.L. Boatright-Horowitz, Avian Bornaviral Ganglioneuritis: Current Debates and Unanswered Questions, *Vet Med Int* 2020 (2020). <https://doi.org/10.1155/2020/6563723>.
- [321] A.M. Dastjerdi, D.R. Snodgrass, J.C. Bridger, Characterisation of the bovine enteric calici-like virus, Newbury agent 1, *FEMS Microbiol Lett* 192 (2000) 125–131. [www.fems-microbiology.org](http://www.fems-microbiology.org).
- [322] R. Hofmann-Lehmann, M.J. Hosie, K. Hartmann, H. Egberink, U. Truyen, S. Tasker, S. Belák, C. Boucraut-Baralon, T. Frymus, A. Lloret, F. Marsilio, M.G. Pennisi, D.D. Addie, H. Lutz, E. Thiry, A.D. Radford, K. Möstl, Calicivirus Infection in Cats, *Viruses* 14 (2022). <https://doi.org/10.3390/v14050937>.
- [323] M. Mochizuki, M. Hashimoto, F. Roerink, Y. Tohya, Y. Matsuura, N. Sasaki, Molecular and seroepidemiological evidence of canine calicivirus infections in Japan, *J Clin Microbiol* 40 (2002) 2629–2631. <https://doi.org/10.1128/JCM.40.7.2629-2631.2002>.
- [324] M.W. Cloyd, Human Retroviruses, University of Texas Medical Branch at Galveston, 1996. <https://www.ncbi.nlm.nih.gov/books/NBK7934/> (accessed August 15, 2023).
- [325] S. Payne, Family Togaviridae, in: *Viruses*, Elsevier, 2017: pp. 141–148. <https://doi.org/10.1016/b978-0-12-803109-4.00016-7>.

- [326] P.J. Walker, R.G. Dietzgen, D.A. Joubert, K.R. Blasdell, Rhabdovirus accessory genes, *Virus Res* 162 (2011) 110–125. <https://doi.org/10.1016/j.virusres.2011.09.004>.
- [327] B H Dannevig, S Mjaaland and E Rimstad, *Infectious Salmon Anemia Virus*, 2008.
- [328] P.J. Koettters, L. Hassanieh, S.A. Stohlman, T. Gallagher, M.M.C. Lai, Mouse Hepatitis Virus Strain JHM Infects a Human Hepatocellular Carcinoma Cell Line, 1999. <http://www.idealibrary.com>.
- [329] A.N. Vlasova, A. Diaz, D. Damtie, L. Xiu, T.H. Toh, J.S.Y. Lee, L.J. Saif, G.C. Gray, Novel Canine Coronavirus Isolated from a Hospitalized Patient With Pneumonia in East Malaysia, *Clinical Infectious Diseases* 74 (2022) 446–454. <https://doi.org/10.1093/cid/ciab456>.
- [330] C. Peng, L. Chen, M. Tang, A database for deliquescence and efflorescence relative humidities of compounds with atmospheric relevance, *Fundamental Research* 2 (2022) 578–587. <https://doi.org/10.1016/j.fmre.2021.11.021>.
- [331] T.D. Campbell, R. Febrian, J.T. McCarthy, H.E. Kleinschmidt, J.G. Forsythe, P.J. Bracher, Prebiotic condensation through wet–dry cycling regulated by deliquescence, *Nat Commun* 10 (2019). <https://doi.org/10.1038/s41467-019-11834-1>.
- [332] Q.N. Zhang, L.J. Zhao, S.H. Chen, X. Guo, Y.M. Luan, Y.H. Zhang, Hygroscopic property of inorganic salts in atmospheric aerosols measured with physisorption analyzer, *Atmos Environ* 247 (2021). <https://doi.org/10.1016/j.atmosenv.2020.118171>.

- [333] E. Huynh, A. Olinger, D. Woolley, R.K. Kohli, J.M. Choczynski, J.F. Davies, K. Lin, L.C. Marr, R.D. Davis, R.D.D. Performed, Evidence for a semisolid phase state of aerosols and droplets relevant to the airborne and surface survival of pathogens ENVIRONMENTAL SCIENCES, (n.d.). <https://doi.org/10.1073/pnas.2109750119/-/DCSupplemental>.
- [334] X. Li, D. Gupta, H.J. Eom, H.K. Kim, C.U. Ro, Deliquescence and efflorescence behavior of individual NaCl and KCl mixture aerosol particles, *Atmos Environ* 82 (2014) 36–43. <https://doi.org/10.1016/j.atmosenv.2013.10.011>.
- [335] Z. Chaudhry, S.A. Ratnesar-Shumate, T.J. Buckley, J.M. Kalter, J.U. Gilberry, J.P. Eshbaugh, E.C. Corson, J.L. Santarpia, C.C. Carter, Understanding water uptake in bioaerosols using laboratory measurements, field tests, and modeling, in: *Chemical, Biological, Radiological, Nuclear, and Explosives (CBRNE) Sensing XIV*, SPIE, 2013: p. 871017. <https://doi.org/10.1117/12.2016151>.
- [336] B.U. Lee, S.H. Kim, S.S. Kim, Hygroscopic growth of *E. coli* and *B. subtilis* bioaerosols, 2002. [www.elsevier.com/locate/jaerosci](http://www.elsevier.com/locate/jaerosci).
- [337] T.H. Kuehn, *Viral Aerosol Survivability, Transmission, and Sampling in an Environmental Chamber*, 2014.
- [338] E.J. Dubovi Amn, T.G. Akers, *Airborne Stability of Tailless Bacterial Viruses S-13 and MS-2*, 1970.
- [339] K. Lin, L.C. Marr, Humidity-Dependent Decay of Viruses, but Not Bacteria, in Aerosols and Droplets Follows Disinfection Kinetics, *Environ Sci Technol* 54 (2020) 1024–1032. <https://doi.org/10.1021/acs.est.9b04959>.

- [340] J.E. Benbough, Some Factors Affecting the Survival of Airborne Viruses, *J. Gen. Virol* 10 (1971) 209–220.
- [341] W. Yang, L.C. Marr, Mechanisms by which ambient humidity may affect viruses in aerosols, *Appl Environ Microbiol* 78 (2012) 6781–6788. <https://doi.org/10.1128/AEM.01658-12>.
- [342] C.R. Bryan, A.W. Knight, R.M. Katona, A.C. Sanchez, E.J. Schindelholz, R.F. Schaller, Physical and chemical properties of sea salt deliquescent brines as a function of temperature and relative humidity, *Science of the Total Environment* 824 (2022). <https://doi.org/10.1016/j.scitotenv.2022.154462>.
- [343] M. Pan, L. Carol, J.A. Lednicky, A. Eiguren-Fernandez, S. Hering, Z.H. Fan, C.Y. Wu, Determination of the distribution of infectious viruses in aerosol particles using water-based condensational growth technology and a bacteriophage MS2 model, *Aerosol Science and Technology* 53 (2019) 583–593. <https://doi.org/10.1080/02786826.2019.1581917>.
- [344] H.J. Walls, D.S. Ensor, L.A. Harvey, J.H. Kim, R.T. Chartier, S. V. Hering, S.R. Spielman, G.S. Lewis, Generation and sampling of nanoscale infectious viral aerosols, *Aerosol Science and Technology* 50 (2016) 802–811. <https://doi.org/10.1080/02786826.2016.1191617>.
- [345] M.H. Woo, Y.M. Hsu, C.Y. Wu, B. Heimbuch, J. Wander, Method for contamination of filtering facepiece respirators by deposition of MS2 viral aerosols, *J Aerosol Sci* 41 (2010) 944–952. <https://doi.org/10.1016/j.jaerosci.2010.07.003>.

- [346] F.A. Handler, Modeling ultraviolet dose-response of Bacillus spore clusters in air, *Aerosol Science and Technology* 50 (2016) 148–159. <https://doi.org/10.1080/02786826.2015.1137556>.
- [347] K. Muinonen, D. Stankevich, Y.G. Shkuratov, S. Kaasalainen, J. Piironen, Shadowing effect in clusters of opaque spherical particles, 2001. [www.elsevier.com/locate/jqsrt](http://www.elsevier.com/locate/jqsrt).
- [348] M. Otero Fernandez, R.J. Thomas, H. Oswin, A.E. Haddrell, J.P. Reid, Transformative Approach To Investigate the Microphysical Factors Influencing Airborne Transmission of Pathogens, 2020. <https://doi.org/10.1016/j.jqsrt.2020.100001>.
- [349] A.P. Ault, T.L. Guasco, O.S. Ryder, J. Baltrusaitis, L.A. Cuadra-Rodriguez, D.B. Collins, M.J. Ruppel, T.H. Bertram, K.A. Prather, V.H. Grassian, Inside versus outside: Ion redistribution in nitric acid reacted sea spray aerosol particles as determined by single particle analysis, *J Am Chem Soc* 135 (2013) 14528–14531. <https://doi.org/10.1021/ja407117x>.
- [350] D.P. Clark, N.J. Pazdernik, M.R. McGehee, Chapter 24 - Viruses, Viroids, and Prions, in: D.P. Clark, N.J. Pazdernik, M.R. McGehee (Eds.), *Molecular Biology (Third Edition)*, Academic Cell, 2019: pp. 749–792. <https://doi.org/10.1016/B978-0-12-813288-3.00024-0>.
- [351] D. Schmelling, ULTRAVIOLET DISINFECTION GUIDANCE MANUAL FOR THE FINAL LONG TERM 2 ENHANCED SURFACE WATER TREATMENT RULE, 2006. <http://www.epa.gov/safewater/disinfection/lt2/compliance.html>.

- [352] J.W. Tang, The effect of environmental parameters on the survival of airborne infectious agents, *J R Soc Interface* 6 (2009).  
<https://doi.org/10.1098/rsif.2009.0227.focus>.
- [353] M.F. Modest, View Factors, *Radiative Heat Transfer* (2013) 129–159.  
<https://doi.org/10.1016/b978-0-12-386944-9.50004-2>.
- [354] J. Ignjatović, T. Šušteršič, A. Bodić, S. Cvijić, J. Đuriš, A. Rossi, V. Dobričić, S. Ibrić, N. Filipović, Comparative assessment of in vitro and in silico methods for aerodynamic characterization of powders for inhalation, *Pharmaceutics* 13 (2021).  
<https://doi.org/10.3390/pharmaceutics13111831>.
- [355] M.J. Oldham, R.F. Phalen, T. Heistracher, Computational fluid dynamic predictions and experimental results for particle deposition in an airway model, in: *Aerosol Science and Technology*, 2000: pp. 61–71.  
<https://doi.org/10.1080/027868200303939>.
- [356] W.H. Finlay, 2 - Particle size distributions, in: W.H. Finlay (Ed.), *The Mechanics of Inhaled Pharmaceutical Aerosols*, Academic Press, London, 2001: pp. 3–15.  
<https://doi.org/https://doi.org/10.1016/B978-012256971-5/50003-1>.
- [357] E. Pfrommer, C. Dreier, G. Gabriel, T. Dallenga, R. Reimer, K. Schepanski, R. Scherließ, U.E. Schaible, T. Gutschmann, Enhanced tenacity of mycobacterial aerosols from necrotic neutrophils, *Sci Rep* 10 (2020).  
<https://doi.org/10.1038/s41598-020-65781-9>.
- [358] D.A. Kuzmanovic, I. Elashvili, C. Wick, C. O’Connell, S. Krueger, Bacteriophage MS2: Molecular weight and spatial distribution of the protein and RNA components

by small-angle neutron scattering and virus counting, *Structure* 11 (2003) 1339–1348. <https://doi.org/10.1016/j.str.2003.09.021>.

[359] S.K. Ray, N.K. Mohalik, A.M. Khan, D. Mishra, N.K. Varma, J.K. Pandey, P.K. Singh, CFD modeling to study the effect of particle size on dispersion in 20l explosion chamber: An overview, *Int J Min Sci Technol* 30 (2020) 321–327. <https://doi.org/10.1016/j.ijmst.2020.04.005>.

[360] G.H. Wan, C.L. Wu, Y.F. Chen, S.H. Huang, Y.L. Wang, C.W. Chen, Particle size concentration distribution and influences on exhaled breath particles in mechanically ventilated patients, *PLoS One* 9 (2014). <https://doi.org/10.1371/journal.pone.0087088>.

[361] J. Littleton, G. Cohen, Memorandum of Understanding ASHRAE and IUVA, n.d.

[362] D. Chen, R. Hofmann, Y. Lawryshyn, E. Mackey, RED Bias in Performance Evaluation of In-duct UVGI Air Disinfection Systems, 2023. <https://ugd.blue-ocean-robotics.com/>.

## Appendix A: View factor model equations

### Direct emissive irradiance from a cylinder

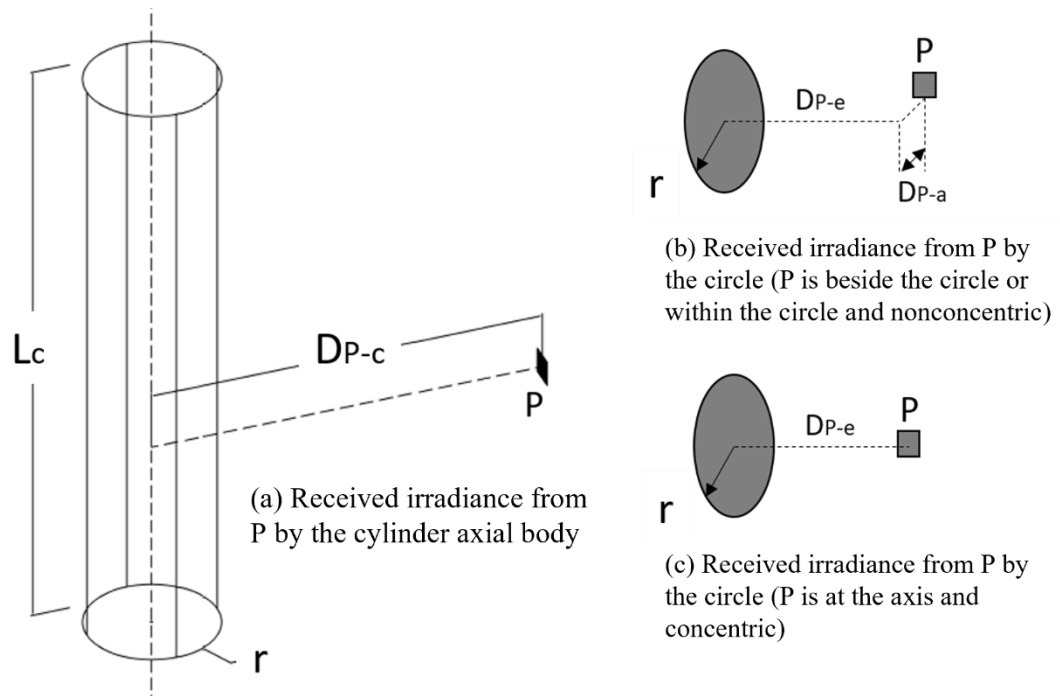


**Figure A1: cylinder view factor classifications**

The view factor's calculation with respect to the cylinders have been reported in literature and readily to use. The equations for the above mentioned four classifications for the cylinder axial body and cylinder circle (beside the circle, within the circle and at the axis) are given as [61,141,353]:

$$F_{P-cylinder}(L_c, D_{P-c}) = \frac{L_c}{\pi D_{P-c}} \left[ \frac{r}{L_c} \tan^{-1} \frac{L_c}{r \sqrt{\left(\frac{D_{P-c}}{r}\right)^2 - 1}} + \frac{a - 2 \frac{D_{P-c}}{r}}{\sqrt{ab}} \tan^{-1} \frac{a \left(\frac{D_{P-c}}{r} - 1\right)}{b \left(\frac{D_{P-c}}{r} + 1\right)} - \tan^{-1} \sqrt{\frac{\frac{D_{P-c}}{r} - 1}{\frac{D_{P-c}}{r} + 1}} \right] \quad (A1)$$

$$\text{where } a = \left(1 + \frac{D_{P-c}}{r}\right)^2 + \left(\frac{L_c}{r}\right)^2 \text{ and } b = \left(1 - \frac{D_{P-c}}{r}\right)^2 + \left(\frac{L_c}{r}\right)^2$$

$$F_{P-circle}(D_{P-a}, D_{P-e}) = \frac{D_{P-e}}{2D_{P-a}} \left[ \frac{1 + \left(\frac{D_{P-e}}{D_{P-a}}\right)^2 + \left(\frac{r}{D_{P-a}}\right)^2}{\sqrt{\left[1 + \left(\frac{D_{P-e}}{D_{P-a}}\right)^2 + \left(\frac{r}{D_{P-a}}\right)^2\right]^2 - 4\left(\frac{r}{D_{P-a}}\right)^2}} - 1 \right] \quad (A2)$$

$$F_{P-noncentric}(D_{P-a}, D_{P-e}) = \frac{1}{2} \left[ 1 - \frac{1 + \left(\frac{D_{P-e}}{D_{P-a}}\right)^2 - \left(\frac{r}{D_{P-a}}\right)^2}{\sqrt{\left[1 + \left(\frac{D_{P-e}}{D_{P-a}}\right)^2 + \left(\frac{r}{D_{P-a}}\right)^2\right]^2 - 4\left(\frac{r}{D_{P-a}}\right)^2}} \right] \quad (A3)$$

$$\text{if } P \text{ and the circle is concentric: } F_{P-concentric}(D_{P-e}) = \frac{1}{\left(\frac{D_{P-e}}{r}\right)^2 + 1}$$

Where  $L_c$  is the length of the cylinder,  $r$  is the radius of the cylinder,  $D_{P-c}$  is the normal distance between the viewpoint  $P$  (differential surface) and the cylinder axis,  $D_{P-a}$  is the normal distance between the viewpoint and the cylinder's axis,  $D_{P-e}$  is the normal distance between the viewpoint and cylinder's circle. Implementing the Eqs. (A1)-(A3) into the view factor model equations in Table 1, the spatial irradiance distribution can be computed.

**Diffuse reflection irradiance**

The diffusive reflection was considered as the secondary diffusely emitting irradiance from a wall element to the spatial point differential surface. In literature, the analytical solution of the view factor for the differential area to a parallel finite element of which its perpendicular to the element corner is given as [61,141]:

$$F_{P-we} \left( \frac{c}{e}, \frac{d}{e} \right) = \frac{1}{2\pi} \left\{ \frac{c/e}{\sqrt{1+(c/e)^2}} \tan^{-1} \frac{d/e}{\sqrt{1+(c/e)^2}} + \frac{d/e}{\sqrt{1+(d/e)^2}} \tan^{-1} \frac{c/e}{\sqrt{1+(d/e)^2}} \right\} \quad (A4)$$

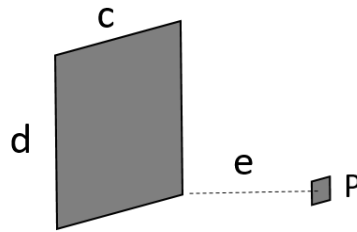


**Figure A2: View factor of the differential area parallel to a finite wall element and perpendicular to the element corner**

Thus, for any two differential elements that may not perpendicularly coincide at the element corner, the view factor can be obtained by algebraic operation of the areas perpendicularly coincide at the element corner. Taking left wall as an example (see Figure A3), since the backward diffuse reflection was not taken into consideration, thus, only the contributions from the wall cells that  $y_w < y$  ( $P'$  (projection of viewpoint at the left wall) is at the right side of wall element center  $O$ ) shall be considered. In this case, four scenarios are identified and have the view factors written as:

$$\begin{aligned}
(a) F_{we}^d &= F_{P-we} \left( \frac{\Delta y / 2 + |y - y_w|}{e}, \frac{|z - z_w| + \Delta z / 2}{e} \right) + F_{P-we} \left( \frac{|y - y_w| + \Delta y / 2}{e}, \frac{|z - z_w| + \Delta z / 2}{e} \right) \\
&+ F_{P-we} \left( \frac{|y - y_w| + \Delta y / 2}{e}, \frac{\Delta z / 2 - |z - z_w|}{e} \right) + F_{P-we} \left( \frac{\Delta y / 2 - |y - y_w|}{e}, \frac{\Delta z / 2 - |z - z_w|}{e} \right)
\end{aligned} \tag{A5}$$

$$\begin{aligned}
(b) F_{we}^d &= F_{P-we} \left( \frac{\Delta y / 2 + |y - y_w|}{e}, \frac{|z - z_w| + \Delta z / 2}{e} \right) - F_{P-we} \left( \frac{|y - y_w| + \Delta y / 2}{e}, \frac{|z - z_w| - \Delta z / 2}{e} \right) \\
&- F_{P-we} \left( \frac{|y - y_w| - \Delta y / 2}{e}, \frac{\Delta z}{e} \right)
\end{aligned} \tag{A6}$$

$$\begin{aligned}
(c) F_{we}^d &= F_{P-we} \left( \frac{\Delta y / 2 + |y - y_w|}{e}, \frac{|z - z_w| + \Delta z / 2}{e} \right) + F_{P-we} \left( \frac{|y - y_w| + \Delta y / 2}{e}, \frac{\Delta z / 2 - |z - z_w|}{e} \right) \\
&- F_{P-we} \left( \frac{|y - y_w| - \Delta y / 2}{e}, \frac{\Delta z}{e} \right)
\end{aligned} \tag{A7}$$

$$\begin{aligned}
(d) F_{we}^d &= F_{P-we} \left( \frac{\Delta y / 2 + |y - y_w|}{e}, \frac{|z - z_w| + \Delta z / 2}{e} \right) + F_{P-we} \left( \frac{\Delta y / 2 - |y - y_w|}{e}, \frac{|z - z_w| + \Delta z / 2}{e} \right) \\
&- F_{P-we} \left( \frac{\Delta y}{e}, \frac{|z - z_w| + \Delta z / 2}{e} \right)
\end{aligned} \tag{A8}$$

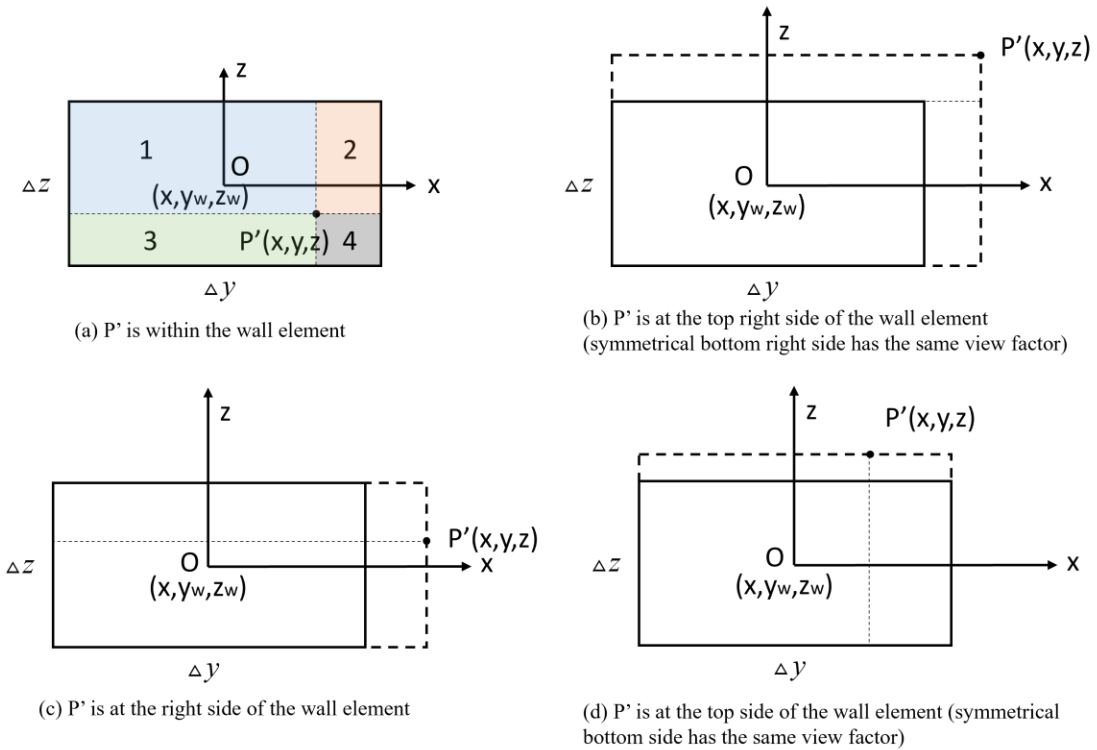


**Figure A3: Schematic of the view factor algebraic operation for the left wall element**

**that**  $y_w < y$

It should be noted the coordinate system is based on the configuration of the left wall of the ventilation duct. For the upper- or bottom-walls, z is replaced by x.

Table A1 Schematic diagram and model equations of the viewpoint P receiving the radiation from the twin-tube UV lamp

**Scenarios**

**View factor model equations<sup>1</sup>**

**One-lamp case: direct emissive irradiance**

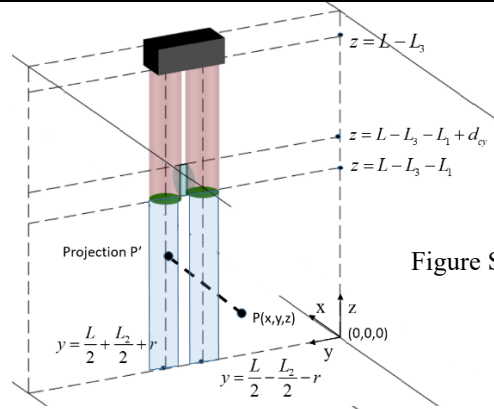


Figure S6(a)

P is vertically below cylinder #1 or #2's. The irradiance from the two cylinders (classification ) and two circles (classification ) is considered.

$$z < L - L_1 - L_3 \text{ \& } (x - r)^2 + \left[ y - \left( \frac{L}{2} - \frac{L_2}{2} - r \right) \right]^2 < r^2 :$$

$$F_{P-tube} = F_{P-cy2}(|L - z - L_3|, D_{P-c2}) - F_{P-cy2}(|L - z - L_1 - L_3|, D_{P-c2}) + F_{P-cy3} \left( \left| \frac{L}{2} - y \right| + \frac{L_2}{2}, D_{P-c3} \right) - F_{P-cy3} \left( \left| \frac{L}{2} - y \right| - \frac{L_2}{2}, D_{P-c3} \right) + F_{P-nonconcentric1}(D_{P-a1}, D_{P-e1}) + F_{P-circle2}(D_{P-a2}, D_{P-e2}) \quad (S14a)$$

$$\text{where } D_{P-c1} = \sqrt{x^2 + (L/2 - L_2/2 - r - y)^2}; D_{P-c2} = \sqrt{x^2 + (L/2 + L_2/2 + r - y)^2}; D_{P-c3} = \sqrt{x^2 + (z - (L - L_3 - L_1 + r))^2} \quad (S14b)$$

II

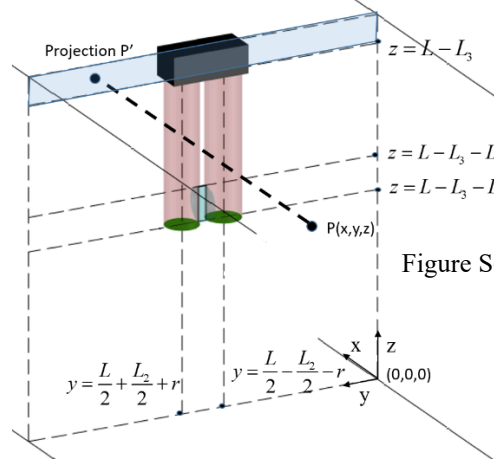


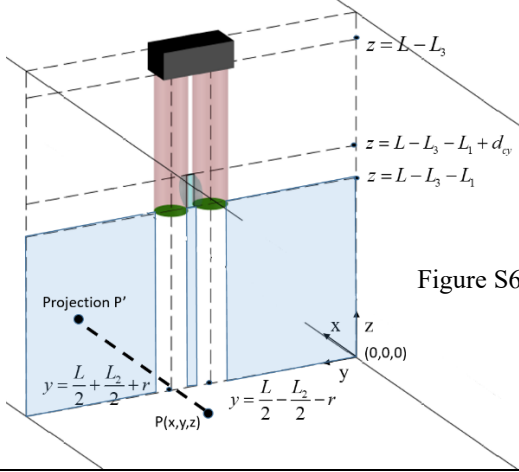
Figure S6(b)

P is above the top of the UV lamp. Only the emissive irradiance from three cylinders classification ) is considered.

$$\frac{L}{2} - \frac{L_2}{2} - r < y < \frac{L}{2} : F_{P-tube} = F_{P-cy1}(|z - (L - L_3 - L_1)|, D_{P-c1}) - F_{P-cy1}(|z - (L - L_3)|, D_{P-c1}) + F_{P-cy2}(|z - (L - L_3 - L_1)|, D_{P-c2}) - F_{P-cy2}(|z - (L - L_3)|, D_{P-c2}) + F_{P-cy3} \left( \left| \frac{L_2}{2} - \left( \frac{L}{2} - y \right) \right|, D_{P-c3} \right) + F_{P-cy3} \left( \left| \frac{L_2}{2} + \left( \frac{L}{2} - y \right) \right|, D_{P-c3} \right) \quad (S15a)$$

$$y < \frac{L}{2} - \frac{L_2}{2} - r : F_{P-tube} = F_{P-cy1}(|z - (L - L_3 - L_1)|, D_{P-c1}) - F_{P-cy1}(|z - (L - L_3)|, D_{P-c1}) + F_{P-cy2}(|z - (L - L_3 - L_1)|, D_{P-c2}) - F_{P-cy2}(|z - (L - L_3)|, D_{P-c2}) + F_{P-cy3} \left( \left| \left( y - \frac{L}{2} \right) + \frac{L_2}{2} \right|, D_{P-c3} \right) - F_{P-cy3} \left( \left| \left( y - \frac{L}{2} \right) - \frac{L_2}{2} \right|, D_{P-c3} \right) \quad (S15b)$$

$$\text{where } D_{P-c1} = \sqrt{x^2 + (L/2 - L_2/2 - r - y)^2}; D_{P-c2} = \sqrt{x^2 + (L/2 + L_2/2 + r - y)^2}; D_{P-c3} = \sqrt{x^2 + (z - (L - L_3 - L_1 + r))^2} \quad (S15c)$$



P is below the bottom of the UV lamp and vertically beside cylinders #1 and #2. The irradiance from two cylinders (classification) is considered.

Figure S6(c)

$$\frac{L}{2} - \frac{L_2}{2} - r < y < \frac{L}{2} \text{ \& } (x-r)^2 + \left[ y - \left( \frac{L}{2} - \frac{L_2}{2} - r \right) \right]^2 > r^2 :$$

$$F_{P-nube} = F_{P-cy1}(|L-z-L_3|, D_{P-c1}) - F_{P-cy1}(|L-z-L_1-L_3|, D_{P-c1}) + F_{P-cy2}(|L-z-L_3|, D_{P-c2}) - F_{P-cy2}(|L-z-L_1-L_3|, D_{P-c2}) \\ + F_{P-cy3} \left| y - \left( -\frac{L_2}{2} + \frac{L}{2} \right) \right|, D_{P-c3} + F_{P-cy3} \left| \left( \frac{L_2}{2} + \left( \frac{L}{2} - y \right) \right) \right|, D_{P-c3} + F_{P-circle1}(D_{P-a1}, D_{P-e1}) + F_{P-circle2}(D_{P-a2}, D_{P-e2}) \quad (S16a)$$

$$y < \frac{L}{2} - \frac{L_2}{2} - r \text{ \& } (x-r)^2 + \left[ y - \left( \frac{L}{2} - \frac{L_2}{2} - r \right) \right]^2 > r^2 :$$

$$F_{P-nube} = F_{P-cy1}(|L-z-L_3|, D_{P-c1}) - F_{P-cy1}(|L-z-L_1-L_3|, D_{P-c1}) + F_{P-cy2}(|L-z-L_3|, D_{P-c2}) - F_{P-cy2}(|L-z-L_1-L_3|, D_{P-c2}) \\ + F_{P-cy3} \left| \left( \frac{L}{2} - y \right) + \frac{L_2}{2} \right|, D_{P-c3} - F_{P-cy3} \left| \left( \frac{L}{2} - y \right) - \frac{L_2}{2} \right|, D_{P-c3} + F_{P-circle1}(D_{P-a1}, D_{P-e1}) + F_{P-circle2}(D_{P-a2}, D_{P-e2}) \quad (S16b)$$

$$\text{where } D_{P-a1} = \sqrt{x^2 + (L/2 - L_2/2 - r - y)^2}; D_{P-e1} = |L - z - L_1 - L_3|; D_{P-a2} = \sqrt{x^2 + (L/2 + L_2/2 + r - y)^2}; D_{P-e2} = |L - z - L_1 - L_3| \quad (S16c)$$

Note: II: If  $x=0; y = \frac{L}{2} - \frac{L_2}{2} - r$  or  $y = \frac{L}{2} + \frac{L_2}{2} + r$ ,  $F_{P-nonconcentric}$  is replaced with  $F_{P-concentric}$ .

### One lamp per row (two rows) case: Direct emissive irradiance

$$|x| < L_{10} - r$$

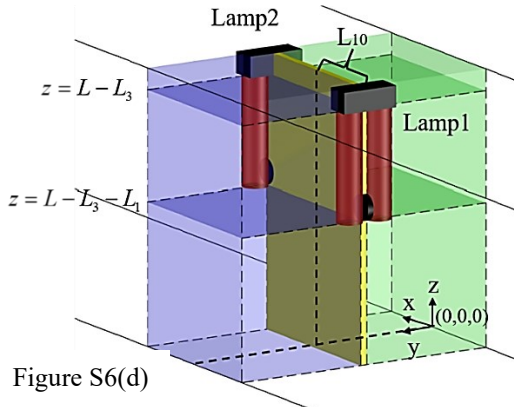


Figure S6(d)

$L_{10}$  is the distance between the center of lamp1 and the mid of lamp2 along the x-axis

Summation of the full direct emissive irradiance from the two UV lamps.

Note: for the region between the two cylinders of the UV lamp1 or lamp2, only receive the direct emissive from the two cylinders without the contributions from lamp2 or lamp1 due to the narrowed gap (significant shadowing effects).

$|x| > L_{10} - r$  : Fraction of z block by the cylinder #3 (the viewpoint P is vertically within the cylinder #3 or above the cylinder #3).

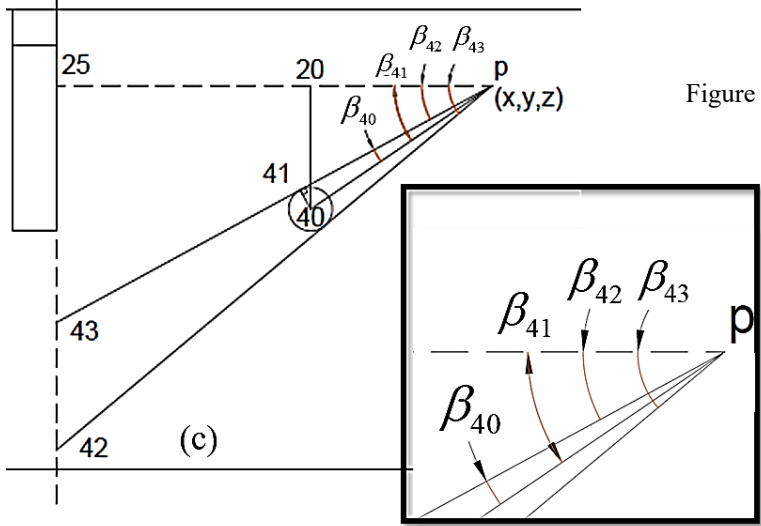
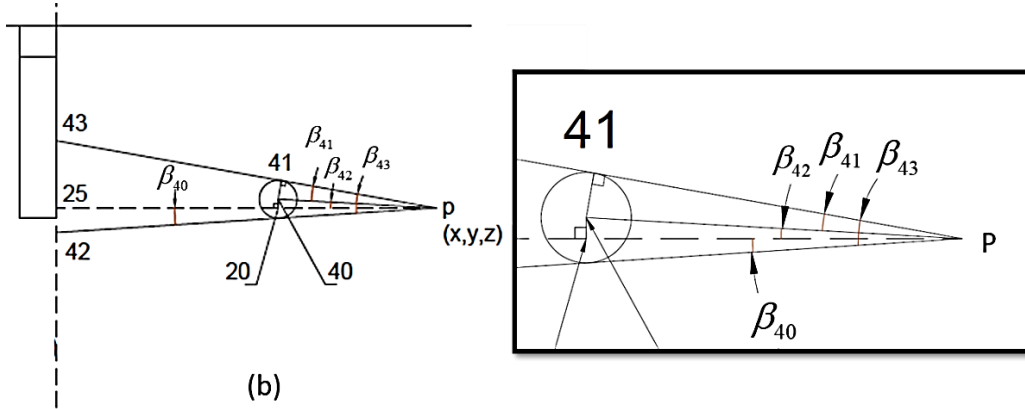


Figure S6(e)

$$(b) : z_{42} = z - (x_{25} - x) \tan \left( \arcsin \left( \frac{r_{cylinder}}{\sqrt{(x_{40} - x)^2 + (z_{40} - z)^2}} \right) - \arctan \left( \frac{z_{40} - z}{x_{20} - x} \right) \right)$$

$$z_{43} = z + (x_{25} - x) \tan \left( \arcsin \left( \frac{r_{cylinder}}{\sqrt{(x_{40} - x)^2 + (z_{40} - z)^2}} \right) + \arctan \left( \frac{z_{40} - z}{x_{20} - x} \right) \right)$$

$$(c) : z_{42} = z - (x_{25} - x) \tan \left( \arctan \left( \frac{z_{40} - z}{x_{20} - x} \right) + \arcsin \left( \frac{r_{cylinder}}{\sqrt{(x_{40} - x)^2 + (z_{40} - z)^2}} \right) \right)$$

$$z_{43} = z - (x_{25} - x) \tan \left( \arctan \left( \frac{z_{40} - z}{x_{20} - x} \right) - \arcsin \left( \frac{r_{cylinder}}{\sqrt{(x_{40} - x)^2 + (z_{40} - z)^2}} \right) \right)$$

$$z_{42} > z_{31}$$

$$l_{z\_cy3\_block} = 0 \quad (S17)$$

$$z_{30} < z_{42} < z_{31}; z_{43} > z_{31}$$

$$l_{z\_cy3\_block} = L_{31\_42} \quad (S18)$$

$$z_{42} < z_{30}; z_{43} > z_{31} \quad (S19)$$

$$l_{z\_cy3\_block} = L_{cylinder}$$

$$z_{30} < z_{42} < z_{31}; z_{30} < z_{43} < z_{31}$$

$$l_{z\_cy3\_block} = L_{43\_42} \quad (S20)$$

$$z_{42} < z_{30}; z_{30} < z_{43} < z_{31}$$

$$l_{z\_cy3\_block} = L_{43\_30} \quad (S21)$$

$$z_{42} < z_{30}; z_{43} < z_{30}$$

$$l_{z\_cy3\_block} = 0 \quad (S22)$$

$|x| > L_{10} - r$  : Fraction of y block by the cylinder #1 and #2 (the viewpoint P is at the range of lamp #1 right cylinder or in between two cylinders of lamp #1 or within the range of lamp #1 left cylinder or on the left side of lamp #1 left cylinder).

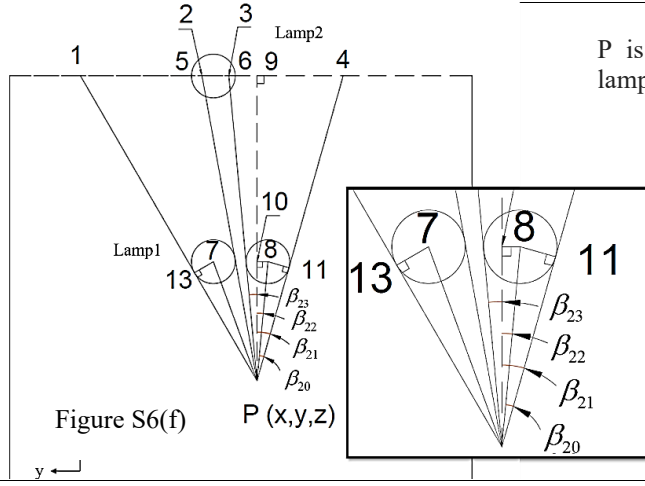


Figure S6(f)

P is at the range of lamp #1 right cylinder

$$= \arcsin \left( \frac{r_{cylinder}}{\sqrt{(x_8 - x)^2 + (y_8 - y)^2}} \right);$$

$$\beta_{22} = \arctan \left( \frac{abs(y_8 - y)}{abs(x_8 - x)} \right);$$

$$\beta_{21} = \beta_{20} + \beta_{22}; \beta_{23} = \beta_{20} - \beta_{22}$$

$$y_1 = y + (x_{lamp2} - x) \tan \beta_4 \quad y_4 < y_6; y_3 > y_5 : l_{y\_block} = d_{cylinder}$$

$$y_2 = y + (x_{lamp2} - x) \tan \beta_2 \quad y_4 < y_6; y_6 < y_3 < y_5; y_2 > y_5 :$$

$$y_3 = y + (x_{lamp2} - x) \tan \beta_{23} \quad l_{y\_block} = L_{3\_6}$$

$$y_4 = y - (x_{lamp2} - x) \tan \beta_{24} \quad y_4 < y_6; y_3 < y_6; y_2 > y_5 :$$

$$l_{y\_block} = 0$$

$$y_4 < y_6; y_3 < y_6; y_6 < y_2 < y_5 :$$

$$l_{y\_block} = L_{2\_5}$$

(S23)

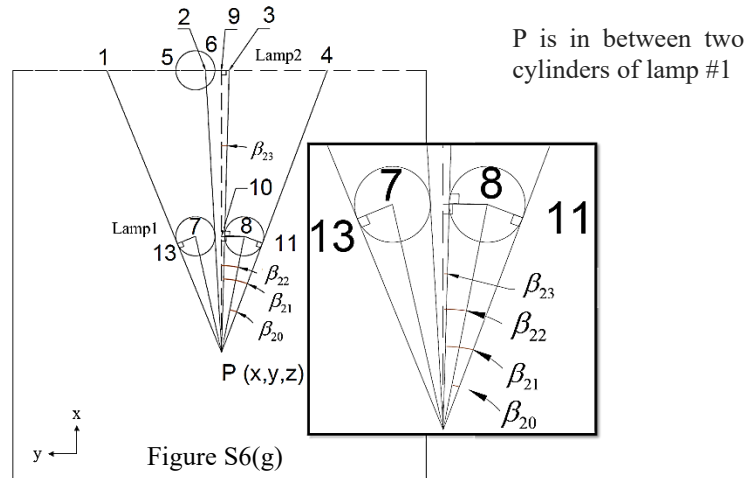


Figure S6(g)

P is in between two cylinders of lamp #1

$$\beta_{20} = \arcsin \left( \frac{r_{cylinder}}{\sqrt{(x_8 - x)^2 + (y_8 - y)^2}} \right)$$

$$\beta_{22} = \arctan \left( \frac{abs(y_8 - y)}{abs(x_8 - x)} \right);$$

$$\beta_{21} = \beta_{20} + \beta_{22}; \beta_{23} = \beta_{22} - \beta_{20}$$

$$y_1 = y + (x_{lamp2} - x) \tan \beta_4 \quad y_4 < y_6; y_3 < y_6; y_2 > y_5 :$$

$$y_2 = y + (x_{lamp2} - x) \tan \beta_2 \quad l_{y\_block} = 0$$

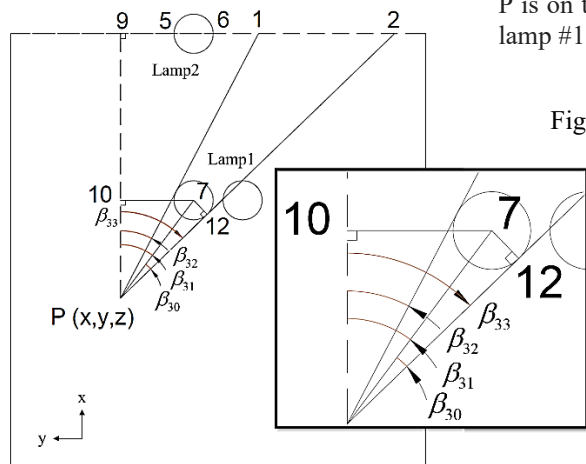
$$y_3 = y - (x_{lamp2} - x) \tan \beta_{23} \quad y_4 < y_6; y_3 < y_6; y_6 < y_2 < y_5 :$$

$$y_4 = y - (x_{lamp2} - x) \tan \beta_{24} \quad l_{y\_block} = L_{2\_5}$$

(S24)

P is within the range of lamp #1 left cylinder

$$l_{y\_block} = d_{cylinder} \quad (S25)$$



P is on the left side of lamp #1 left cylinder

Figure S6(h)

$$\beta_{30} = \arcsin \left( \frac{r_{cylinder}}{\sqrt{(x_7 - x)^2 + (y_7 - y)^2}} \right) \begin{cases} y_1 = y - (x_{lamp2} - x) \tan \beta_{32} & y_6 < y_1 < y_5; y_2 < y_6 : \\ y_2 = y - (x_{lamp2} - x) \tan \beta_{33} & l_{y\_block} = L_{1\_6} \end{cases}$$

$$\beta_{31} = \arctan \left( \frac{abs(y_7 - y)}{abs(x_7 - x)} \right); \quad y_1 < y_6; y_2 < y_6 : l_{y\_block} = 0 \quad (S26)$$

$$\beta_{32} = \beta_{31} - \beta_{30}; \quad \beta_{33} = \beta_{30} + \beta_{31}$$

## Appendix B: UDF code for UV irradiance model (example for the “projection area” method calculation)

We attached the example UDF code for calculating the shadowing effect from the lamp 1 on the left illuminating column of lamp 2 using the “projection area” method (shadowing effect see Figure B1).

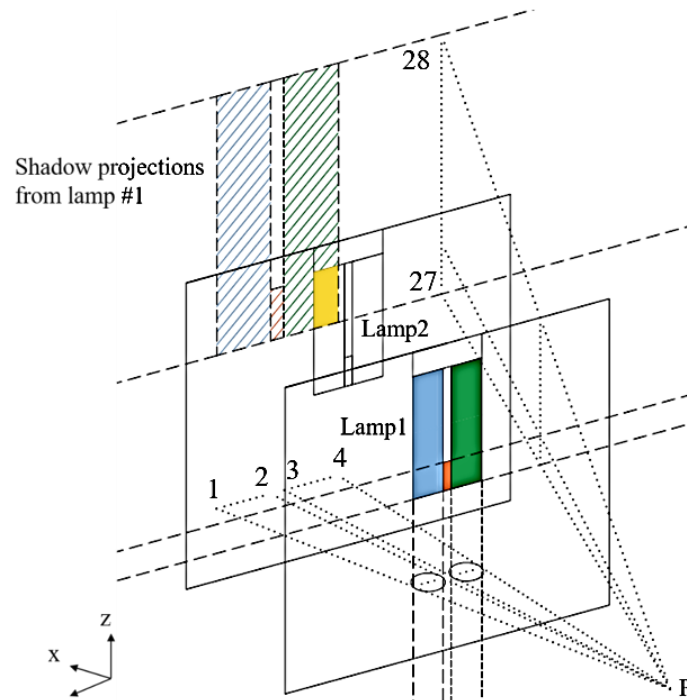


Figure B1 Schematic illustration of the shadowing effects between Lamp1 and Lamp2 placed in two rows

```

DEFINE_ON_DEMAND(direct_irradiance_lamp2_column1)
{
  Domain* d; /* declare domain pointer since it is not passed as an argument to the DEFINE macro */
  Thread* t;
  cell_t c;
  real x[ND_ND];
  real y[ND_ND];
  d = Get_Domain(1); /* Get the domain using ANSYS FLUENT utility */

  /* Loop over all cell threads in the domain */
  thread_loop_c(t, d)
  {
    /* Loop over all cells */
    begin_c_loop(c, t)
    {
      C_CENTROID(x, c, t); /*get the coordinates information for each cell at the thread t*/
      C_CENTROID(y, c, t);

      if (x[0] < 0.60466)
      {
        x[0] = fabs(x[0] - 0.68686); /*x coordinate with respect to the lamp2, convert for view factor
calculation*/
        x[1] = fabs(x[1] - 0.0003971332); /*y coordinate with respect to lamp center*/
        y[1] = fabs(y[1] - 0.0003971332);
        con1 = pow(x[0] - r, 2) + pow(L / 2 - L2 / 2 - r - x[1], 2);
        con2 = pow(x[0] - r, 2) + pow(L / 2 + L2 / 2 + r - x[1], 2);
        con3 = L - L3;
        con4 = L - L3 - L1;
        con5 = L - L3 - L1 + dia;

        llamp2col = 0;
        llamp2cir1 = 0;
        Fpc1 = Fpc2 = Fpc3 = Fpc4 = Fpc5 = Fpc6 = Fpc7 = Fpc8 = Fpc9 = Fpc10 = Fpc11 = Fpc12 =
Fpc131 = Fpc132 = Fpc14 = Fpc15 = Fpc16 = Fpc171 = Fpc172 = Fpc18 = Fpc19 = Fpc20 = Fpc211 =
Fpc212 = Fpc22 = Fpc23 = Fpc241 = Fpc242 = Fpc25 = Fpc26 = Fpc271 = Fpc272 = 0;
        Fpc1t = Fpc2t = Fpc3t = 0;

        zshadowlengthco3 = 0;
        lshadowlamp2col = 0;
        lfraction = 0;
        shadowfraction = 0;
        shadowareaco3 = 0;
        yshadowlengthco3 = 0;
        y31 = 0;
        y30 = 0;
        y1 = 0;
        y2 = 0;
        y3 = 0;
        y4 = 0;

        /*calculating the shadowing area*/
        xlamp1center = 0.61066;
        ylamp1colleft = L / 2 + L2 / 2 + dia;
        ylamp1colright = L / 2 + L2 / 2;
        ylamp1colcenter = L / 2 + L2 / 2 + r;
        ylamp1col2left = L / 2 - L2 / 2;

```

```

ylamp1co2right = L / 2 - L2 / 2 - dia;
ylamp1co2center = L / 2 - L2 / 2 - r;
zlampcenter = L - L3 - L1 + r;

xlamp2center = 0.68686;
ylamp2colleft = L / 2 + L2 / 2 + dia;
ylamp2colright = L / 2 + L2 / 2;
ylamp2colcenter = L / 2 + L2 / 2 + r;
ylamp2co2left = L / 2 - L2 / 2;
ylamp2co2right = L / 2 - L2 / 2 - dia;
ylamp2co2center = L / 2 - L2 / 2 - r;

ylamp1co3left = L / 2 + L2 / 2;
xlamp1co3bot = 0.61066 - r;
ylamp1co3right = L / 2 - L2 / 2;
xlamp1co3top = 0.61066 + r;

if (y[2] > con4 && y[2] < con3) /* z is above the lamp column and below the lampwall, only the
cylinders*/
{
/*calculate the direct irradiance from lamp2 column 1 without shadow effect*/
lenpc21 = fabs(L - L3 - x[2]);
lenpc22 = fabs(L1 - (L - L3 - x[2]));
Dpc2 = pow(x[0] * x[0] + pow(x[1] - (L / 2 - L2 / 2 - r), 2), 0.5);
a21 = pow(1 + Dpc2 / r, 2) + pow(lenpc21 / r, 2);
b21 = pow(1 - Dpc2 / r, 2) + pow(lenpc21 / r, 2);
a22 = pow(1 + Dpc2 / r, 2) + pow(lenpc22 / r, 2);
b22 = pow(1 - Dpc2 / r, 2) + pow(lenpc22 / r, 2);

Fpc2 = lenpc21 * (r * atan(lenpc21 / (r * pow(fabs(pow(Dpc2 / r, 2) - 1), 0.5))) / lenpc21 + (a21
- 2 * Dpc2 / r) * atan(pow(a21 * fabs(Dpc2 / r - 1) / (a21 * (Dpc2 / r + 1)), 0.5)) / pow(a21 * b21, 0.5) -
atan(pow(fabs(Dpc2 / r - 1) / (Dpc2 / r + 1), 0.5))) / (3.1415926 * Dpc2)
+ lenpc22 * (r * atan(lenpc22 / (r * pow(fabs(pow(Dpc2 / r, 2) - 1), 0.5))) / lenpc22 + (a22 -
2 * Dpc2 / r) * atan(pow(a22 * fabs(Dpc2 / r - 1) / (a22 * (Dpc2 / r + 1)), 0.5)) / pow(a22 * b22, 0.5) -
atan(pow(fabs(Dpc2 / r - 1) / (Dpc2 / r + 1), 0.5))) / (3.1415926 * Dpc2);
Ilamp2co1 = Icy1 * exp(-abs * Dpc2) * Fpc2 / Acy2;

/*calculate the shadow length by column 3 along z direction*/
if (y[2] < con5)
{
l20_21 = r;
lp_20 = pow(pow(y[0] - xlamp1center, 2) + pow(y[2] - zlampcenter, 2), 0.5);
l20_25 = fabs(y[2] - zlampcenter);
lp_25 = fabs(y[0] - xlamp1center);
lp_24 = fabs(y[0] - xlamp2center);
l22_24 = lp_24 * tan(fabs(atan(l20_25 / lp_25) + asin(l20_21 / lp_20)));
l23_24 = lp_24 * tan(fabs(atan(l20_25 / lp_25) - asin(l20_21 / lp_20)));
z22 = fabs(y[2] + l22_24);
z23 = fabs(y[2] - l23_24);

if (z22 > L - L3)
{
zshadowlengthco3 = L1;
}
else if (z22 < L - L3)
{

```

```

        zshadowlengthco3 = L1 - (L - L3 - z22);
    }
}
else if (y[2] > con5)
{
    l20_21 = r;
    lp_20 = pow(pow(y[0] - xlamp1center, 2) + pow(y[2] - zlampcenter, 2), 0.5);
    l20_25 = fabs(y[2] - zlampcenter);
    lp_25 = fabs(y[0] - xlamp1center);
    lp_24 = fabs(y[0] - xlamp2center);
    l22_24 = lp_24 * tan(fabs(atan(l20_25 / lp_25) - asin(l20_21 / lp_20)));
    l23_24 = lp_24 * tan(fabs(atan(l20_25 / lp_25) + asin(l20_21 / lp_20)));
    z22 = fabs(y[2] - l22_24);
    z23 = fabs(y[2] - l23_24);

    if (z22 < L - L3 - L1)
    {
        zshadowlengthco3 = 0;
    }
    if (z22 > L - L3 - L1)
    {
        zshadowlengthco3 = L1 - (L - L3 - z22);
    }
}

/*calculate the lshadowlamp2co1*/
if (y[1] < ylamp1co2right) /*p is at the right side of the lamp1's right column*/
{
    /*calculate the projecting point from P to lamp2 at y direction*/
    l8_11 = r;
    lp_8 = pow(pow(y[0] - xlamp1center, 2) + pow(y[1] - ylamp1co2center, 2), 0.5);
    l8_10 = fabs(y[1] - ylamp1co2center);
    lp_10 = fabs(y[0] - xlamp1center);
    lp_9 = fabs(y[0] - xlamp2center);

    alpha2 = fabs(atan(l8_10 / lp_10) - asin(l8_11 / lp_8));
    l4_9 = lp_9 * tan(alpha2);
    alpha3 = fabs(atan(l8_10 / lp_10) + asin(l8_11 / lp_8));
    l3_9 = lp_9 * tan(alpha3);

    l7_13 = r;
    lp_7 = pow(pow(y[0] - xlamp1center, 2) + pow(y[1] - ylamp1co1center, 2), 0.5);
    l7_10 = fabs(y[1] - ylamp1co1center);

    alpha6 = fabs(atan(l7_10 / lp_10) - asin(l7_13 / lp_7));
    l2_9 = lp_9 * tan(alpha6);
    alpha7 = fabs(atan(l7_10 / lp_10) + asin(l7_13 / lp_7));
    l1_9 = lp_9 * tan(alpha7);

    y1 = fabs(y[1] + l1_9);
    y2 = fabs(y[1] + l2_9);
    y3 = fabs(y[1] + l3_9);
    y4 = fabs(y[1] + l4_9);

    /*calculate the shadow effect by column 3 along y direction*/
    l36_33 = fabs(y[1] - ylamp1co3left);

```

```

lp_33 = fabs(y[0] - xlamp1co3bot);
lp_32 = fabs(y[0] - xlamp2center);
l35_34 = fabs(y[1] - ylamp1co3right);
lp_34 = fabs(y[0] - xlamp1co3top);

l30_32 = l36_33 * lp_32 / lp_33;
l31_32 = l35_34 * lp_32 / lp_34;
y30 = fabs(y[1] + l30_32);
y31 = fabs(y[1] + l31_32);

if (y31 > ylamp2co1left)
{
    yshadowlengthco3 = 0;
    shadowareaco3 = yshadowlengthco3 * zshadowlengthco3;
    shadowfraction = shadowareaco3 / 0.000612;
}
else if (y31 < ylamp2co1left && y31 > ylamp2co1right && y30 > ylamp2co1left)
{
    yshadowlengthco3 = fabs(y31 - ylamp2co1left);
    shadowareaco3 = yshadowlengthco3 * zshadowlengthco3;
    shadowfraction = shadowareaco3 / 0.000612;
}
else if (y31 < ylamp2co1right && y30 > ylamp2co1left)
{
    yshadowlengthco3 = 0.012;
    shadowareaco3 = yshadowlengthco3 * zshadowlengthco3;
    shadowfraction = shadowareaco3 / 0.000612;
}

/*calculate the combined shadow effect by column 1 and column 3*/
if (y4 > ylamp2co1left) /*scenario #1, can see the whole lamp2 left column*/
{
    Ifraction = 1;
    Ishadowlamp2co1 = llamp2co1 * (Ifraction - Ifraction * shadowfraction);
}
else if (y4 < ylamp2co1left && y4 > ylamp2co1right && y3 > ylamp2co1left) /*scenario
#2, can see partial of lamp2 left column*/
{
    l5_4 = fabs(y4 - ylamp2co1left);
    Ifraction = 1 - l5_4 / 0.012;
    Ishadowlamp2co1 = llamp2co1 * (Ifraction - Ifraction * shadowfraction);
}
else if (y4 < ylamp2co1right && y3 > ylamp2co1left) /*scenario #3, whole lamp2 left
column is blocked by lamp1 right column*/
{
    Ishadowlamp2co1 = 0;
}
else if (y4 < ylamp2co1right && y3 < ylamp2co1left && y3 > ylamp2co1right) /*scenario
#4, can see partial of lamp2 left column*/
{
    l6_3 = fabs(y3 - ylamp2co1right);
    Ifraction = 1 - l6_3 / 0.012;
    Ishadowlamp2co1 = llamp2co1 * (Ifraction - Ifraction * shadowfraction);
}
else if (y2 < ylamp2co1left && y2 > ylamp2co1right) /*scenario #5, can see partial of
lamp2 left column through lamp 1 left column*/

```

```

    {
        l5_2 = fabs(y2 - ylamp2co1left);
        Ifraction = 1 - l5_2 / 0.012;
        lshadowlamp2co1 = llamp2co1 * (Ifraction - Ifraction * shadowfraction);
    }
}
else if (y[1] > ylamp1co2right && y[1] < ylamp1co2left) /*p is within the range of the
lamp1's right column*/
{
    /*calculate the projecting point from P to lamp2 at y direction*/
    l8_11 = r;
    lp_8 = pow(pow(y[0] - xlamp1center, 2) + pow(y[1] - ylamp1co2center, 2), 0.5);
    l8_10 = fabs(y[1] - ylamp1co2center);
    lp_10 = fabs(y[0] - xlamp1center);
    lp_9 = fabs(y[0] - xlamp2center);

    if (y[1] > ylamp1co2center)
    {
        alpha2 = fabs(atan(l8_10 / lp_10) + asin(l8_11 / lp_8));
        l4_9 = lp_9 * tan(alpha2);
        alpha3 = fabs(atan(l8_10 / lp_10) - asin(l8_11 / lp_8));
        l3_9 = lp_9 * tan(alpha3);
    }
    else if (y[1] < ylamp1co2center)
    {
        alpha2 = fabs(atan(l8_10 / lp_10) - asin(l8_11 / lp_8));
        l4_9 = lp_9 * tan(alpha2);
        alpha3 = fabs(atan(l8_10 / lp_10) + asin(l8_11 / lp_8));
        l3_9 = lp_9 * tan(alpha3);
    }
    else if (y[1] == ylamp1co2center)
    {
        alpha2 = asin(l8_11 / lp_8);
        l4_9 = lp_9 * tan(alpha2);
        l3_9 = l4_9;
    }
}

l7_13 = r;
lp_7 = pow(pow(y[0] - xlamp1center, 2) + pow(y[1] - ylamp1co1center, 2), 0.5);
l7_10 = fabs(y[1] - ylamp1co1center);

alpha6 = atan(l7_10 / lp_10) - asin(l7_13 / lp_7);
l2_9 = lp_9 * tan(alpha6);
alpha7 = atan(l7_10 / lp_10) + asin(l7_13 / lp_7);
l1_9 = lp_9 * tan(alpha7);

y1 = fabs(y[1] + l1_9);
y2 = fabs(y[1] + l2_9);
y3 = fabs(y[1] + l3_9);
y4 = fabs(y[1] - l4_9);

/*calculate the shadow effect by column 3 along y direction*/
l36_33 = fabs(y[1] - ylamp1co3left);
lp_33 = fabs(y[0] - xlamp1co3bot);
lp_32 = fabs(y[0] - xlamp2center);
l35_34 = fabs(y[1] - ylamp1co3right);

```

```

lp_34 = fabs(y[0] - xlamp1co3top);

l30_32 = l36_33 * lp_32 / lp_33;
l31_32 = l35_34 * lp_32 / lp_34;
y30 = fabs(y[1] + l30_32);
y31 = fabs(y[1] + l31_32);

if (y31 > ylamp2co1left)
{
    yshadowlengthco3 = 0;
    shadowareaco3 = yshadowlengthco3 * zshadowlengthco3;
    shadowfraction = shadowareaco3 / (0.012 * L1);
}
else if (y31 < ylamp2co1left && y31 > ylamp2co1right && y30 > ylamp2co1left)
{
    yshadowlengthco3 = fabs(y31 - ylamp2co1left);
    shadowareaco3 = yshadowlengthco3 * zshadowlengthco3;
    shadowfraction = shadowareaco3 / (0.012 * L1);
}
else if (y31 < ylamp2co1right && y30 > ylamp2co1left)
{
    yshadowlengthco3 = 0.012;
    shadowareaco3 = yshadowlengthco3 * zshadowlengthco3;
    shadowfraction = shadowareaco3 / (0.012 * L1);
}

/*calculate the combined shadow effect by column 1 and column 3*/
if (y3 > ylamp2co1right && y3 < ylamp2co1left) /*scenario #1, can see the part of
lamp2 left column*/
{
    l6_3 = fabs(y3 - ylamp2co1right);
    Ifraction = 1 - l6_3 / 0.012;
    Ishadowlamp2co1 = llamp2co1 * (Ifraction - Ifraction * shadowfraction);
}
else if (y3 > ylamp2co1left && y4 < ylamp2co1right) /*scenario #2, whole lamp2 left
column is blocked*/
{
    Ishadowlamp2co1 = 0;
}
else if (y2 < ylamp2co1left && y2 > ylamp2co1right) /*scenario #3, can see the part of
lamp2 left column*/
{
    l5_2 = fabs(y2 - ylamp2co1left);
    Ifraction = 1 - l5_2 / 0.012;
    Ishadowlamp2co1 = llamp2co1 * (Ifraction - Ifraction * shadowfraction);
}
else if (y1 > ylamp2co1left && y2 < ylamp2co1right) /*scenario #4, whole lamp2 left
column is blocked*/
{
    Ishadowlamp2co1 = 0;
}
else if (y2 > ylamp2co1left && y3 < ylamp2co1right) /*scenario #5, whole lamp2 left
column can be seen*/
{
    Ifraction = 1;
    Ishadowlamp2co1 = Ishadowlamp2co1 * (Ifraction - Ifraction * shadowfraction);
}

```

```

    }
  }
  else if (y[1] > ylamp1co2left && y[1] < ylamp1co1right)      /*p is in between the lamp1's
two columns*/
  {
    /*calculate the projecting point from P to lamp2 at y direction*/
    l7_13 = r;
    lp_10 = fabs(y[0] - xlamp1center);
    lp_9 = fabs(y[0] - xlamp2center);
    lp_7 = pow(pow(y[0] - xlamp1center, 2) + pow(y[1] - ylamp1co1center, 2), 0.5);
    l7_10 = fabs(y[1] - ylamp1co1center);
    alpha6 = fabs(atan(l7_10 / lp_10) - asin(l7_13 / lp_7));
    l2_9 = lp_9 * tan(alpha6);

    y2 = fabs(2 * y[1] + l2_9);      /*temporaily*/

    /*calculate the shadow effect by column 3 along y direction*/
    l36_33 = fabs(y[1] - ylamp1co3left);
    lp_33 = fabs(y[0] - xlamp1co3bot);
    lp_32 = fabs(y[0] - xlamp2center);
    l37_33 = fabs(y[1] - ylamp1co3right);
    l30_32 = l36_33 * lp_32 / lp_33;
    l31_32 = l37_33 * lp_32 / lp_33;

    y30 = fabs(y[1] + l30_32);
    y31 = fabs(y[1] - l31_32);

    if (y30 > ylamp2co1left)
    {
      yshadowlengthco3 = 0.012;
      shadowareaco3 = yshadowlengthco3 * zshadowlengthco3;
      shadowfraction = shadowareaco3 / (0.012 * L1);
    }
    else if (y30 < ylamp2co1left && y30 > ylamp2co1right)
    {
      yshadowlengthco3 = fabs(y30 - ylamp2co1left);
      shadowareaco3 = yshadowlengthco3 * zshadowlengthco3;
      shadowfraction = shadowareaco3 / (0.012 * L1);
    }
  }

  /*calculate the combined shadow effect by column 1 and column 3*/
  if (y2 > ylamp2co1left)      /*scenario #1, can see the whole lamp2 left column*/
  {
    Ifraction = 1;
    Ishadowlamp2co1 = llamp2co1 * (Ifraction - Ifraction * shadowfraction);
  }
  else if (y2 < ylamp2co1left && y2 > ylamp2co1right) /*scenario #2, can see partial lamp2
left column*/
  {
    l5_2 = fabs(y2 - ylamp2co1left);
    Ifraction = 1 - l5_2 / 0.012;
    Ishadowlamp2co1 = llamp2co1 * Ifraction;
  }
  }
  else if (y[1] > ylamp1co1right && y[1] < ylamp1co1left)      /*p is within the range of the
lamp1's left column*/

```

```

{
  Ishadowlamp2co1 = 0;
}
else if (y[1] > ylamp1co1left) /*p is at the left side of the lamp1's left column*/
{
  /*calculate the projecting point from P to lamp2 at y direction*/
  l7_13 = r;
  lp_10 = fabs(y[0] - xlamp1center);
  lp_9 = fabs(y[0] - xlamp2center);
  lp_7 = pow(pow(y[0] - xlamp1center, 2) + pow(y[1] - ylamp1co1center, 2), 0.5);
  l7_10 = fabs(y[1] - ylamp1co1center);
  alpha7 = fabs(atan(l7_10 / lp_10) - asin(l7_13 / lp_7));
  l1_9 = lp_9 * tan(alpha7);

  y1 = (y[1] - l1_9);

  /*calculate the shadow effect by column 3 along y direction*/
  l38_34 = fabs(y[1] - ylamp1co3left);
  lp_34 = fabs(y[0] - xlamp1co3top);
  l37_33 = fabs(y[1] - ylamp1co3right);
  lp_33 = fabs(y[0] - xlamp1co3bot);
  lp_32 = fabs(y[0] - xlamp2center);

  l30_32 = l38_34 * lp_32 / lp_34;
  l31_32 = l37_33 * lp_32 / lp_33;
  y30 = fabs(y[1] - l30_32);
  y31 = fabs(y[1] - l31_32);

  shadowfraction = 0;

  /*calculate the combined shadow effect by column 1 and column 3*/
  if (y1 > ylamp2co1right) /*scenario #1, can see part of the lamp2 left column*/
  {
    l5_1 = fabs(y1 - ylamp2co1left);
    Ifraction = l5_1 / 0.012;
    Ishadowlamp2co1 = Ilamp2co1 * (Ifraction - Ifraction * shadowfraction);
  }
  else if (y1 < ylamp2co1right) /*scenario #2, can the whole lamp2 left column*/
  {
    Ifraction = 1;
    Ishadowlamp2co1 = Ilamp2co1 * (Ifraction - Ifraction * shadowfraction);
  }
}
}
if (y[2] < con4) /* z is below the lamp column, cylinders + circles */
{
  /*calculate the direct irradiance from lamp2 column 1 without shadow effect*/
  lenpc141 = fabs(L - L3 - x[2]);
  lenpc142 = fabs(L - L3 - L1 - x[2]);
  Dpc14 = pow(x[0] * x[0] + pow(L / 2 - L2 / 2 - r - x[1], 2), 0.5);
  a141 = pow(1 + Dpc14 / r, 2) + pow(lenpc141 / r, 2);
  b141 = pow(1 - Dpc14 / r, 2) + pow(lenpc141 / r, 2);
  a142 = pow(1 + Dpc14 / r, 2) + pow(lenpc142 / r, 2);
  b142 = pow(1 - Dpc14 / r, 2) + pow(lenpc142 / r, 2);
}

```

```

Fpc14 = lenpc141 * (r * atan(lenpc141 / (r * pow(fabs(pow(Dpc14 / r, 2) - 1), 0.5))) / lenpc141
+ (a141 - 2 * Dpc14 / r) * atan(pow(a141 * fabs(Dpc14 / r - 1) / (a141 * (Dpc14 / r + 1)), 0.5)) / pow(a141 *
b141, 0.5) - atan(pow(fabs(Dpc14 / r - 1) / (Dpc14 / r + 1), 0.5))) / (3.1415926 * Dpc14)
- lenpc142 * (r * atan(lenpc142 / (r * pow(fabs(pow(Dpc14 / r, 2) - 1), 0.5))) / lenpc142 +
(a142 - 2 * Dpc14 / r) * atan(pow(a142 * fabs(Dpc14 / r - 1) / (a142 * (Dpc14 / r + 1)), 0.5)) / pow(a142 *
b142, 0.5) - atan(pow(fabs(Dpc14 / r - 1) / (Dpc14 / r + 1), 0.5))) / (3.1415926 * Dpc14);
Ilamp2co1 = Icy1 * exp(-abs * Dpc14) * Fpc14 / Acy1;

Dpa3 = pow(x[0] * x[0] + pow(L / 2 - L2 / 2 - r - x[1], 2), 0.5);
Dpe3 = fabs(L - x[2] - L1 - L3);
Fpc171 = Dpe3 * ((1 + pow(Dpe3 / Dpa3, 2) + pow(r / Dpa3, 2)) / pow(pow(1 + pow(Dpe3 /
Dpa3, 2) + pow(r / Dpa3, 2), 2) - 4 * pow(r / Dpa3, 2), 0.5) - 1) / (2 * Dpa3);
Ilamp2cir1 = Icir1 * exp(-abs * pow(Dpe3 * Dpe3 + Dpa3 * Dpa3, 0.5)) * Fpc171 / Acir1;

/*calculate the shadow length by column 3 along z direction*/
l20_21 = r;
lp_20 = pow(pow(y[0] - xlamp1center, 2) + pow(y[2] - zlampcenter, 2), 0.5);
l20_25 = fabs(y[2] - zlampcenter);
lp_25 = fabs(y[0] - xlamp1center);
lp_24 = fabs(y[0] - xlamp2center);
l22_24 = lp_24 * tan(fabs(atan(l20_25 / lp_25) + asin(l20_21 / lp_20)));
l23_24 = lp_24 * tan(fabs(atan(l20_25 / lp_25) - asin(l20_21 / lp_20)));

z22 = fabs(y[2] + l22_24);
z23 = fabs(y[2] + l23_24);

if (z23 > L - L3)
{
zshadowlengthco3 = 0; /*shadow fraction by column 3*/
zlightfractionco1 = 1; /*light fraction (not blocked) by column 1*/
}
if (z23 < L - L3 && z22 < L - L3)
{
zshadowlengthco3 = z22 - z23;
zlightfractionco1 = (z23 - (L - L3 - L1)) / L1;
}
if (z23 < L - L3 && z22 > L - L3)
{
zshadowlengthco3 = L - L3 - z23;
zlightfractionco1 = (z23 - (L - L3 - L1)) / L1;
}

/*calculate the Ishadowlamp2co1*/
if (y[1] < ylamp1co2right) /*p is at the right side of the lamp1's right column*/
{
/*calculate the projecting point from P to lamp2 at y direction*/
l8_11 = r;
lp_8 = pow(pow(y[0] - xlamp1center, 2) + pow(y[1] - ylamp1co2center, 2), 0.5);
l8_10 = fabs(y[1] - ylamp1co2center);
lp_10 = fabs(y[0] - xlamp1center);
lp_9 = fabs(y[0] - xlamp2center);

alpha2 = fabs(atan(l8_10 / lp_10) - asin(l8_11 / lp_8));
l4_9 = lp_9 * tan(alpha2);
alpha3 = fabs(atan(l8_10 / lp_10) + asin(l8_11 / lp_8));
l3_9 = lp_9 * tan(alpha3);

```

```

l7_13 = r;
lp_7 = pow(pow(y[0] - xlamp1center, 2) + pow(y[1] - ylamp1co1center, 2), 0.5);
l7_10 = fabs(y[1] - ylamp1co1center);

alpha6 = fabs(atan(l7_10 / lp_10) - asin(l7_13 / lp_7));
l2_9 = lp_9 * tan(alpha6);
alpha7 = fabs(atan(l7_10 / lp_10) + asin(l7_13 / lp_7));
l1_9 = lp_9 * tan(alpha7);

y1 = fabs(y[1] + l1_9);
y2 = fabs(y[1] + l2_9);
y3 = fabs(y[1] + l3_9);
y4 = fabs(y[1] + l4_9);

/*calculate the shadow effect by column 3 along y direction*/
l36_33 = fabs(y[1] - ylamp1co3left);
lp_33 = fabs(y[0] - xlamp1co3bot);
lp_32 = fabs(y[0] - xlamp2center);
l35_34 = fabs(y[1] - ylamp1co3right);
lp_34 = fabs(y[0] - xlamp1co3top);

l30_32 = l36_33 * lp_32 / lp_33;
l31_32 = l35_34 * lp_32 / lp_34;
y30 = fabs(y[1] + l30_32);
y31 = fabs(y[1] + l31_32);

if (y31 > ylamp2co1left)
{
    yshadowlengthco3 = 0;
    shadowareaco3 = yshadowlengthco3 * zshadowlengthco3;
    shadowfraction = shadowareaco3 / (0.012 * L1);          /*shadow fraction
due to co3 along y and z direction*/
}
else if (y31 < ylamp2co1left && y31 > ylamp2co1right && y30 > ylamp2co1left)
{
    yshadowlengthco3 = fabs(y31 - ylamp2co1left);
    shadowareaco3 = yshadowlengthco3 * zshadowlengthco3;
    shadowfraction = shadowareaco3 / (0.012 * L1);
}
else if (y31 < ylamp2co1right && y30 > ylamp2co1left)
{
    yshadowlengthco3 = 0.012;
    shadowareaco3 = yshadowlengthco3 * zshadowlengthco3;
    shadowfraction = shadowareaco3 / (0.012 * L1);
}

/*calculate the combined shadow effect by column 1 and column 3*/
if (y4 > ylamp2co1left)          /*scenario #1, can see the whole lamp2 left column*/
{
    shadowfractionco1 = 0 * (1 - zlightfractionco1);          /*shadowfraction due to co1
along y and z direction*/
    Ifraction = 1 - shadowfractionco1;
    Ishadowlamp2co1 = Ilamp2co1 * (Ifraction - Ifraction * shadowfraction) + Ilamp2cir1;
}

```

```

else if (y4 < ylamp2co1left && y4 > ylamp2co1right && y3 > ylamp2co1left) /*scenario
#2, can see partial of lamp2 left column*/
{
    l5_4 = fabs(y4 - ylamp2co1left);
    shadowfractionco1 = (l5_4 / 0.012) * (1 - zlightfractionco1);
    Ifraction = 1 - shadowfractionco1;
    Ishadowlamp2co1 = Ilamp2co1 * (Ifraction - Ifraction * shadowfraction) + Ilamp2cir1;
}
else if (y4 < ylamp2co1right && y3 > ylamp2co1left) /*scenario #3, lamp2 left column
is partial blocked by lamp1 right column*/
{
    Ishadowlamp2co1 = Ilamp2co1 * zlightfractionco1 + Ilamp2cir1;
}
else if (y4 < ylamp2co1right && y3 < ylamp2co1left && y3 > ylamp2co1right) /*scenario
#4, can see partial of lamp2 left column*/
{
    l6_3 = fabs(y3 - ylamp2co1right);
    shadowfractionco1 = (l6_3 / 0.012) * (1 - zlightfractionco1);
    Ifraction = 1 - shadowfractionco1;
    Ishadowlamp2co1 = Ilamp2co1 * (Ifraction - Ifraction * shadowfraction) + Ilamp2cir1;
}
else if (y2 < ylamp2co1left && y2 > ylamp2co1right) /*scenario #5, can see partial of
lamp2 left column through lamp 1 left column*/
{
    l5_2 = fabs(y2 - ylamp2co1left);
    shadowfractionco1 = (l5_2 / 0.012) * (1 - zlightfractionco1);
    Ifraction = 1 - shadowfractionco1;
    Ishadowlamp2co1 = Ilamp2co1 * (Ifraction - Ifraction * shadowfraction) + Ilamp2cir1;
}
}
else if (y[1] > ylamp1co2right && y[1] < ylamp1co2left) /*p is within the range of the
lamp1's right column*/
{
    /*calculate the projecting point from P to lamp2 at y direction*/
    l8_11 = r;
    lp_8 = pow(pow(y[0] - xlamp1center, 2) + pow(y[1] - ylamp1co2center, 2), 0.5);
    l8_10 = fabs(y[1] - ylamp1co2center);
    lp_10 = fabs(y[0] - xlamp1center);
    lp_9 = fabs(y[0] - xlamp2center);

    if (y[1] > ylamp1co2center)
    {
        alpha2 = fabs(atan(l8_10 / lp_10) + asin(l8_11 / lp_8));
        l4_9 = lp_9 * tan(alpha2);
        alpha3 = fabs(atan(l8_10 / lp_10) - asin(l8_11 / lp_8));
        l3_9 = lp_9 * tan(alpha3);
    }
    else if (y[1] < ylamp1co2center)
    {
        alpha2 = fabs(atan(l8_10 / lp_10) - asin(l8_11 / lp_8));
        l4_9 = lp_9 * tan(alpha2);
        alpha3 = fabs(atan(l8_10 / lp_10) + asin(l8_11 / lp_8));
        l3_9 = lp_9 * tan(alpha3);
    }
    else if (y[1] == ylamp1co2center)
    {

```

```

    alpha2 = asin(l8_11 / lp_8);
    l4_9 = lp_9 * tan(alpha2);
    l3_9 = l4_9;
}

l7_13 = r;
lp_7 = pow(pow(y[0] - xlamp1center, 2) + pow(y[1] - ylamp1co1center, 2), 0.5);
l7_10 = fabs(y[1] - ylamp1co1center);

alpha6 = atan(l7_10 / lp_10) - asin(l7_13 / lp_7);
l2_9 = lp_9 * tan(alpha6);
alpha7 = atan(l7_10 / lp_10) + asin(l7_13 / lp_7);
l1_9 = lp_9 * tan(alpha7);

y1 = fabs(y[1] + l1_9);
y2 = fabs(y[1] + l2_9);
y3 = fabs(y[1] + l3_9);
y4 = fabs(y[1] - l4_9);

/*calculate the shadow effect by column 3 along y direction*/
l36_33 = fabs(y[1] - ylamp1co3left);
lp_33 = fabs(y[0] - xlamp1co3bot);
lp_32 = fabs(y[0] - xlamp2center);
l35_34 = fabs(y[1] - ylamp1co3right);
lp_34 = fabs(y[0] - xlamp1co3top);

l30_32 = l36_33 * lp_32 / lp_33;
l31_32 = l35_34 * lp_32 / lp_34;
y30 = fabs(y[1] + l30_32);
y31 = fabs(y[1] + l31_32);

if (y31 > ylamp2co1left)
{
    yshadowlengthco3 = 0;
    shadowareaco3 = yshadowlengthco3 * zshadowlengthco3;
    shadowfraction = shadowareaco3 / (0.012 * L1);
}
else if (y31 < ylamp2co1left && y31 > ylamp2co1right && y30 > ylamp2co1left)
{
    yshadowlengthco3 = fabs(y31 - ylamp2co1left);
    shadowareaco3 = yshadowlengthco3 * zshadowlengthco3;
    shadowfraction = shadowareaco3 / (0.012 * L1);
}
else if (y31 < ylamp2co1right && y30 > ylamp2co1left)
{
    yshadowlengthco3 = 0.012;
    shadowareaco3 = yshadowlengthco3 * zshadowlengthco3;
    shadowfraction = shadowareaco3 / (0.012 * L1);
}

/*calculate the combined shadow effect by column 1 and column 3*/
if (y3 > ylamp2co1right && y3 < ylamp2co1left) /*scenario #1, can see the part of
lamp2 left column*/
{
    l6_3 = fabs(y3 - ylamp2co1right);
    shadowfractionco1 = (l6_3 / 0.012) * (1 - zlightfractionco1);
}

```

```

        Ifraction = 1 - shadowfractionco1;
        Ishadowlamp2co1 = Ilamp2co1 * (Ifraction - Ifraction * shadowfraction) + Ilamp2cir1;
    }
    else if (y3 > ylamp2co1left && y4 < ylamp2co1right) /*scenario #4, whole lamp2 left
column is blocked at y direction, but may not at z direction*/
    {
        Ishadowlamp2co1 = Ilamp2co1 * zlightfractionco1 + Ilamp2cir1;
    }
    else if (y2 < ylamp2co1left && y2 > ylamp2co1right) /*scenario #3, can see the part of
lamp2 left column*/
    {
        l5_2 = fabs(y2 - ylamp2co1left);
        shadowfractionco1 = (l5_2 / 0.012) * (1 - zlightfractionco1);
        Ifraction = 1 - shadowfractionco1;
        Ishadowlamp2co1 = Ilamp2co1 * (Ifraction - Ifraction * shadowfraction) + Ilamp2cir1;
    }
    else if (y1 > ylamp2co1left && y2 < ylamp2co1right) /*scenario #4, whole lamp2 left
column is blocked at y direction, but may not at z direction*/
    {
        Ishadowlamp2co1 = Ilamp2co1 * zlightfractionco1 + Ilamp2cir1;
    }
    else if (y2 > ylamp2co1left && y3 < ylamp2co1right) /*scenario #5, whole lamp2 left
column can be seen*/
    {
        shadowfractionco1 = 0 * (1 - zlightfractionco1);
        Ifraction = 1 - shadowfractionco1;
        Ishadowlamp2co1 = Ilamp2co1 * (Ifraction - Ifraction * shadowfraction) + Ilamp2cir1;
    }
}
else if (y[1] > ylamp1co2left && y[1] < ylamp1co1right) /*p is in between the lamp1's
two columns*/
{
    /*calculate the projecting point from P to lamp2 at y direction*/
    l7_13 = r;
    lp_10 = fabs(y[0] - xlamp1center);
    lp_9 = fabs(y[0] - xlamp2center);
    lp_7 = pow(pow(y[0] - xlamp1center, 2) + pow(y[1] - ylamp1co1center, 2), 0.5);
    l7_10 = fabs(y[1] - ylamp1co1center);
    alpha6 = fabs(atan(l7_10 / lp_10) - asin(l7_13 / lp_7));
    l2_9 = lp_9 * tan(alpha6);

    y2 = fabs(2 * y[1] + l2_9); /*temporarily*/

    /*calculate the shadow effect by column 3 along y direction*/
    l36_33 = fabs(y[1] - ylamp1co3left);
    lp_33 = fabs(y[0] - xlamp1co3bot);
    lp_32 = fabs(y[0] - xlamp2center);
    l37_33 = fabs(y[1] - ylamp1co3right);
    l30_32 = l36_33 * lp_32 / lp_33;
    l31_32 = l37_33 * lp_32 / lp_33;

    y30 = fabs(y[1] - l30_32);
    y32 = fabs(y[1] + l31_32);

    if (y30 > ylamp2co1left)
    {

```

```

        yshadowlengthco3 = 0.012;
        shadowareaco3 = yshadowlengthco3 * zshadowlengthco3;
        shadowfraction = shadowareaco3 / (0.012 * L1);
    }
else if (y30 < ylamp2co1left && y30 > ylamp2co1right)
{
    yshadowlengthco3 = fabs(y30 - ylamp2co1left);
    shadowareaco3 = yshadowlengthco3 * zshadowlengthco3;
    shadowfraction = shadowareaco3 / (0.012 * L1);
}

/*calculate the combined shadow effect by column 1 and column 3*/
if (y2 > ylamp2co1left) /*scenario #1, can see the whole lamp2 left column*/
{
    shadowfractionco1 = 0 * (1 - zlightfractionco1);
    Ifraction = 1 - shadowfractionco1;
    Ishadowlamp2co1 = Ilamp2co1 * (Ifraction - Ifraction * shadowfraction) + Ilamp2cir1;
}
else if (y2 < ylamp2co1left && y2 > ylamp2co1right) /*scenario #2, can see partial lamp2
left column*/
{
    l5_2 = fabs(y2 - ylamp2co1left);
    shadowfractionco1 = (l5_2 / 0.012) * (1 - zlightfractionco1);
    Ifraction = 1 - shadowfractionco1;
    Ishadowlamp2co1 = Ilamp2co1 * (Ifraction - Ifraction * shadowfraction) + Ilamp2cir1;
}
}
else if (y[1] > ylamp1co1right && y[1] < ylamp1co1left) /*p is within the range of the
lamp1's left column*/
{
    Ishadowlamp2co1 = Ilamp2co1 * zlightfractionco1 + Ilamp2cir1;
}
else if (y[1] > ylamp1co1left) /*p is at the left side of the lamp1's left column*/
{
    /*calculate the projecting point from P to lamp2 at y direction*/
    l7_13 = r;
    lp_10 = fabs(y[0] - xlamp1center);
    lp_9 = fabs(y[0] - xlamp2center);
    lp_7 = pow(pow(y[0] - xlamp1center, 2) + pow(y[1] - ylamp1co1center, 2), 0.5);
    l7_10 = fabs(y[1] - ylamp1co1center);
    alpha7 = fabs(atan(l7_10 / lp_10) - asin(l7_13 / lp_7));
    l1_9 = lp_9 * tan(alpha7);

    y1 = (y[1] - l1_9);

    /*calculate the shadow effect by column 3 along y direction*/
    l38_34 = fabs(y[1] - ylamp1co3left);
    lp_34 = fabs(y[0] - xlamp1co3top);
    l37_33 = fabs(y[1] - ylamp1co3right);
    lp_33 = fabs(y[0] - xlamp1co3bot);
    lp_32 = fabs(y[0] - xlamp2center);

    l30_32 = l38_34 * lp_32 / lp_34;
    l31_32 = l37_33 * lp_32 / lp_33;
    y30 = fabs(y[1] - l30_32);
    y31 = fabs(y[1] - l31_32);

```

```

shadowfraction = 0;

/*calculate the combined shadow effect by column 1 and column 3*/
if (y1 > ylamp2co1right) /*scenario #1, can see part of the lamp2 left column*/
{
    l5_1 = fabs(y1 - ylamp2co1left);
    shadowfractionco1 = (1 - l5_1 / 0.012) * (1 - zlightfractionco1);
    Ifraction = 1 - shadowfractionco1;
    Ishadowlamp2co1 = Ilamp2co1 * (Ifraction - Ifraction * shadowfraction) + Ilamp2cir1;
}
else if (y1 < ylamp2co1right) /*scenario #2, can the whole lamp2 left column*/
{
    shadowfractionco1 = 0 * (1 - zlightfractionco1);
    Ifraction = 1 - shadowfractionco1;
    Ishadowlamp2co1 = Ilamp2co1 * (Ifraction - Ifraction * shadowfraction) + Ilamp2cir1;
}
}
}
}
else
{
    Ishadowlamp2co1 = 0;
}
C_UDMI(c, t, 2) = Ishadowlamp2co1;
C_UDMI(c, t, 40) = Ilamp2co1;
C_UDMI(c, t, 41) = Ifraction;
C_UDMI(c, t, 42) = y1;
C_UDMI(c, t, 43) = l1_9;
}
end_c_loop(c, t)
}
}
}

```

## Appendix C: UDF codes for UV dose calculation

```
#include "udf.h"
#include "dpm.h"
#include "sg_disco.h" /* to access the UV intensity values at the cell */
#define C_DO(c,t)C_STORAGE_R_XV(c,t,SV_DO_IRRAD,0)
#define fdout "doseout.txt"
#define ftrack "trackfilters.txt"
#define flime "restime.txt"
#define fileuv "output.dpm"
FILE *pdout;
FILE *ptrack;
FILE *ptime;
FILE *fuv;
static real uv_intensity;
static real x0, y00, z0;
/* Macro for integrating the UV intensity over time along a particle trajectory */
DEFINE_DPM_SCALAR_UPDATE(uv_dosage, cell, thread, initialize, p)
{
  cphase_state_t *c = &(p->cphase);
  if (initialize)
  {
    {
      p->user[0] = 0.;
      uv_intensity = C_UDMI(cell, thread, 18);
      x0=p->state.pos[0];
      y00=p->state.pos[1];
      z0=p->state.pos[2];
    }
  }
  else
  {
    /* UV intensity integrated over time using Trapezoidal rule */
    p->user[0] += P_DT(p) * .5 * (uv_intensity + C_UDMI(cell, thread, 18));
    uv_intensity = C_UDMI(cell, thread, 18);
  }
}
/* Macro for writing the UV dosage, residence time and the ID for low dosed */
/* particles at reactor outlet. */
DEFINE_DPM_OUTPUT(uv_output, header, fp, p, thread, plane)
{
  char name[100];

  if (header)
  {
    {
      fuv = fopen(fileuv,"w");
      if (NNULLP(thread))
      {
        fprintf(fuv,"%s %d\n",THREAD_HEAD(thread)->dpm_summary.sort_file_name,14);
      }
    }
  }
  else
  {
    fprintf(fuv,"%s %d\n",plane->sort_file_name,14);
    fprintf(fuv,"%10s %10s %10s %10s %10s %10s %10s %10s"

```

```

"%10s %10s %10s %10s %10s %10s %10s %10s %s)\n",
"X0","Y0","Z0",
"X","Y","Z","U","V","W","diameter","T","mass-flow",
"time","UV-Dosage","name");
fclose(fuv);
}
else
{
fuv = fopen(fileuv,"a");
sprintf(name,"%s:%d",p->injection->name,p->part_id);
fprintf(fuv,
"((%10.6g %10.6g %10.6g %10.6g %10.6g %10.6g "
"%10.6g %10.6g %10.6g %10.6g %10.6g %10.6g %10.6g %10.6g) %s)\n",
x0,y0,z0,
p->state.pos[0], p->state.pos[1], p->state.pos[2],
p->state.V[0], p->state.V[1], p->state.V[2],
p->state.diam, p->state.temp, p->flow_rate, p->state.time,
p->user[0], name);
fclose(fuv);
}
}
}

```

## Appendix D: Average accumulated UV dose at the UVGI reactor outlet

In this thesis, the effect of particle size on the UVGI inactivation efficiency was investigated based on the experimental data from the Andersen impactors, which classify particles by aerodynamic diameter. The DPM equation (Eq. (38)) requires the input of particle geometric diameter [354,355]. Thus, the aerodynamic diameter of each stage shall be converted to geometric diameter in CFD simulations using the following correlation (assuming spherical particles and Cunningham correction ratio close to 1) [356]:

$$d_a = \sqrt{\rho_p} d_v \quad (\text{D1})$$

where  $d_a$ ,  $d_v$ , and  $\rho_p$  are the particle aerodynamic diameter ( $\mu\text{m}$ ), particle geometric diameter ( $\mu\text{m}$ ), and specific particle density, respectively. The components of a PBS bioaerosol include NaCl salt (a major component in PBS), MS2 cell, and water, which have densities of around  $2.16 \text{ g/cm}^3$  [357],  $1.41 \text{ g/cm}^3$  [358], and  $1 \text{ g/cm}^3$ . Assuming the average density of the above components represents the density of corresponding bioaerosols ( $1.52 \text{ g/cm}^3$  for MS2 bioaerosols), we obtain the corresponding cut-off geometric diameter for different impactor stages:  $0.53 \mu\text{m}$  (MS2) for stage 6;  $0.89 \mu\text{m}$  (MS2) for stage 5;  $1.70 \mu\text{m}$  (MS2) for stage 4;  $2.68 \mu\text{m}$  (MS2) for stage 3; and  $3.81 \mu\text{m}$  (MS2) for stage 2.

However, the exact concentrations of each component remain unknown, resulting in an unclear overall density of the MS2 bioaerosols and potential uncertainties in geometric diameter using this method. This may lead to incorrect particle trajectory simulations and inadequate UV dose estimations. To address this issue, we conducted preliminary CFD

simulations with geometric particle diameters varying from 0.1  $\mu\text{m}$ , 1  $\mu\text{m}$ , 5  $\mu\text{m}$ , and 10  $\mu\text{m}$  to identify whether particle size variations affect the accumulated UV doses at the duct outlet. The results, tabulated below, demonstrate that the particle size variations on the submicrometer scale have negligible influence ( $< 5.1\%$ ) on the accumulated UV dose, likely due to the significantly small particle settling velocity (0.003 m/s for a 10  $\mu\text{m}$  water droplet) compared to the supply air velocity (0.5 – 1.35 m/s). These simulation results agree with previous research in the literature, which reported that varying particle size from 1  $\mu\text{m}$  to 10  $\mu\text{m}$  has an insignificant effect on the drag force and velocity vector path of a dust-air flow[359]; and the particle concentration distributions in a room under different ventilation modes resemble each other to the extent that differences can only be detected in the small-size regions (0.25 – 0.5  $\mu\text{m}$ ) out of the 0.25 – 3.5  $\mu\text{m}$  detection region [360]. Thus, the geometric diameter of 1  $\mu\text{m}$  was selected as the representative size for calculating the accumulated UV dose for bioaerosols in this study. The calculated doses were 15.37  $\text{J}/\text{m}^2$ , 9.21  $\text{J}/\text{m}^2$ , and 6.07  $\text{J}/\text{m}^2$  for supply air velocities of 0.5 m/s, 0.9 m/s, and 1.35 m/s, respectively.

Table D1 CFD simulation predictions of the average accumulative UV dose at UVGI reactor outlet across different particle sizes

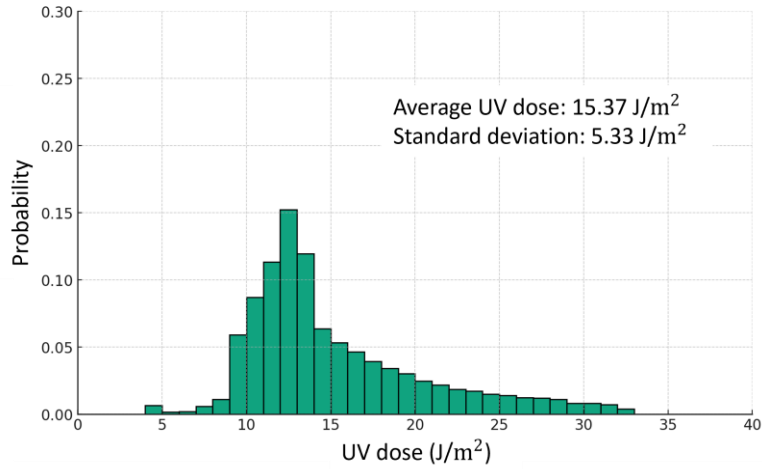
Velocity	UV doses ( $\text{J}/\text{m}^2$ )				Maximum difference
	0.1 $\mu\text{m}$	1 $\mu\text{m}$	5 $\mu\text{m}$	10 $\mu\text{m}$	
0.5 m/s	15.45	15.37	15.16	14.71	5.03%
0.9 m/s	9.25	9.21	9.13	8.95	3.35%
1.35 m/s	6.18	6.07	5.98	5.88	5.10%

In addition, the average accumulated UV dose was used to determine the UV rate constant in this study. It is important to note that UV dose distributions, in relation to particle counts

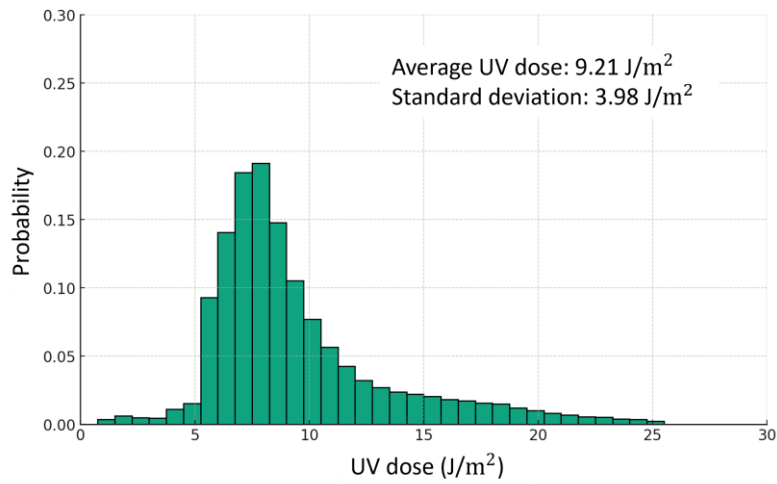
within the in-duct UVGI system, are non-uniform (Figure D1), a result of the uneven UV irradiance field and bioaerosol particle transport. This variability suggests that the derived UV rate constant might not be universally applicable across different UVGI systems if the UV dose distributions (and their standard deviations) vary, even under identical average UV doses, considering the overdosed UV irradiance on one particle will not transfer to and average with other underexposed particles.

In the water disinfection applications, this potential issue is addressed by employing the reduction equivalent dose (RED) to characterize the provided effective UV doses across different UV reactors, which is obtained from the biosimetry test in the liquid filled petri dishes [265]. However, this approach has not been implemented in airborne applications, largely because creating a uniform UV dose distribution within an airborne UVGI reactor is challenging. Additionally, the complex sizes and distributions of bioaerosols complicate the accurate determination of UV dose. Consequently, neither studies nor protocols have established a standardized method for determining RED in airborne UVGI applications. This gap in methodology is highlighted as a research goal in the 2021 memorandum of understanding between ASHRAE and IUVA [361].

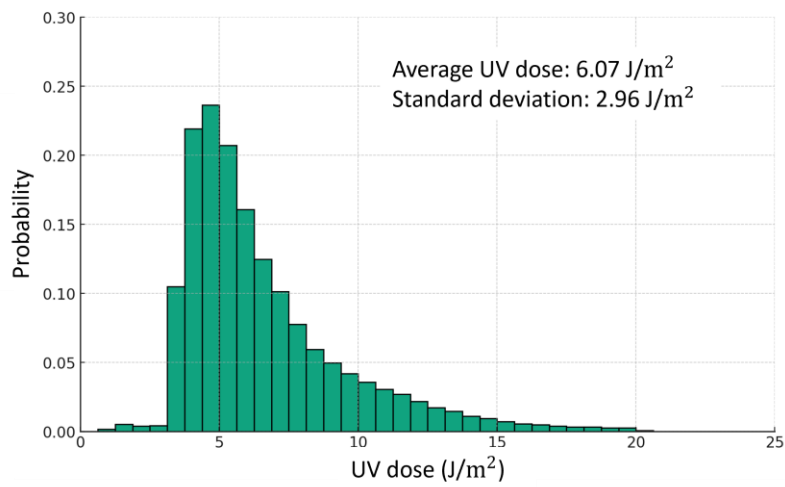
Nevertheless, it should be noted that UV dose distributions are generally narrower in in-duct UVGI systems compared to water UV disinfection systems, due to higher turbulence and a more uniform irradiance distribution within the UVGI reactor [362]. Therefore, in the context of airborne UVGI research, the average UV dose is predominantly used. This study also adopts the average UV dose methodology to align with and be comparable to existing research data in the literature.



(a) 0.5m/s



(b) 0.9 m/s



(c) 1.35m/s

Figure D1 UV dose distributions at the end of the duct under different air velocities

## Appendix E: ANOVA results and multiple comparisons

Table E1 ANOVA results and multiple comparisons for the UV rate constants across different impactor stages at 25% RH.

ANOVA results											
Table Analyzed	Data 3										
Data sets analyzed	A-E										
ANOVA summary											
F	45.59										
P value	<0.0001										
P value summary	****										
Significant diff. among means (P <	Yes										
R squared	0.8428										
Brown-Forsythe test											
F (DFn, DFd)											
P value											
P value summary											
Are SDs significantly different (P < 0.05)?											
ANOVA table											
	SS	DF	MS	F (DFn, DFP value)							
Treatment (between columns)	0.01198	4	0.002994	F (4, 34) = P<0.0001							
Residual (within columns)	0.002233	34	6.57E-05								
Total	0.01421	38									
Ordinary one-way ANOVA											
Number of families	1										
Number of comparisons per family	10										
Alpha	0.05										
Tukey's multiple comparisons test	Mean 1	Mean 2	Mean Diff.	SE of diff.	n1	n2	q	DF	95.00% CI of diff.	Adjusted P	
stage 2 vs. stage 3	0.07237	0.07474	-0.00237	0.004194	8	7	0.7991	34	-0.01445 to 0.009708	0.9792	
stage 2 vs. stage 4	0.07237	0.06685	0.00552	0.004052	8	8	1.927	34	-0.006148 to 0.01719	0.6551	
stage 2 vs. stage 5	0.07237	0.1074	-0.03503	0.004052	8	8	12.23	34	-0.04670 to -0.02336	<0.0001	
stage 2 vs. stage 6	0.07237	0.1054	-0.03303	0.004052	8	8	11.53	34	-0.04470 to -0.02136	<0.0001	
stage 3 vs. stage 4	0.07474	0.06685	0.00789	0.004194	7	8	2.66	34	-0.004188 to 0.01997	0.3465	
stage 3 vs. stage 5	0.07474	0.1074	-0.03266	0.004194	7	8	11.01	34	-0.04474 to -0.02058	<0.0001	
stage 3 vs. stage 6	0.07474	0.1054	-0.03066	0.004194	7	8	10.34	34	-0.04274 to -0.01858	<0.0001	
stage 4 vs. stage 5	0.06685	0.1074	-0.04055	0.004052	8	8	14.15	34	-0.05222 to -0.02888	<0.0001	
stage 4 vs. stage 6	0.06685	0.1054	-0.03855	0.004052	8	8	13.45	34	-0.05022 to -0.02688	<0.0001	
stage 5 vs. stage 6	0.1074	0.1054	0.002	0.004052	8	8	0.698	34	-0.009668 to 0.01367	0.9874	

Table E2 ANOVA results and multiple comparisons for the UV rate constants across different impactor stages at 40% RH.

ANOVA results										
Table Analyzed	Data 3									
Data sets analyzed	A-E									
ANOVA summary										
F	86.06									
P value	<0.0001									
P value summary	****									
Significant diff. among means (P < )	Yes									
R squared	0.8936									
Brown-Forsythe test										
F (DFn, DFd)										
P value										
P value summary										
Are SDs significantly different (P < 0.05)?										
ANOVA table										
	SS	DF	MS	F (DFn, DF)	P value					
Treatment (between columns)	0.0494	4	0.01235	F (4, 41) =	P<0.0001					
Residual (within columns)	0.005884	41	0.000144							
Total	0.05529	45								
Ordinary one-way ANOVA										
Number of families	1									
Number of comparisons per family	10									
Alpha	0.05									
Tukey's multiple comparisons test										
	Mean 1	Mean 2	Mean Diff.	SE of diff.	n1	n2	q	DF	95.00% CI of diff.	Adjusted P
stage 2 vs. stage 3	0.1175	0.112	0.0055	0.005504	9	10	1.413	41	-0.01020 to 0.02120	0.8542
stage 2 vs. stage 4	0.1175	0.1091	0.0084	0.005647	9	9	2.104	41	-0.007711 to 0.02451	0.5763
stage 2 vs. stage 5	0.1175	0.1857	-0.0682	0.005647	9	9	17.08	41	-0.08431 to -0.05209	<0.0001
stage 2 vs. stage 6	0.1175	0.1728	-0.0553	0.005647	9	9	13.85	41	-0.07141 to -0.03919	<0.0001
stage 3 vs. stage 4	0.112	0.1091	0.0029	0.005504	10	9	0.7451	41	-0.01280 to 0.01860	0.9841
stage 3 vs. stage 5	0.112	0.1857	-0.0737	0.005504	10	9	18.94	41	-0.08940 to -0.05800	<0.0001
stage 3 vs. stage 6	0.112	0.1728	-0.0608	0.005504	10	9	15.62	41	-0.07650 to -0.04510	<0.0001
stage 4 vs. stage 5	0.1091	0.1857	-0.0766	0.005647	9	9	19.18	41	-0.09271 to -0.06049	<0.0001
stage 4 vs. stage 6	0.1091	0.1728	-0.0637	0.005647	9	9	15.95	41	-0.07981 to -0.04759	<0.0001
stage 5 vs. stage 6	0.1857	0.1728	0.0129	0.005647	9	9	3.23	41	-0.003211 to 0.02901	0.1707

Table E3 ANOVA results and multiple comparisons for the UV rate constants across different impactor stages at 60% RH.

ANOVA results										
Table Analyzed	Data 3									
Data sets analyzed	A-E									
ANOVA summary										
F	70.05									
P value	<0.0001									
P value summary	****									
Significant diff. among means (P <	Yes									
R squared	0.8564									
Brown-Forsythe test										
F (DFn, DFd)										
P value										
P value summary										
Are SDs significantly different (P < 0.05)?										
ANOVA table										
	SS	DF	MS	F (DFn, DFP value						
Treatment (between columns)	0.01764	4	0.004409	F (4, 47) = P<0.0001						
Residual (within columns)	0.002958	47	6.29E-05							
Total	0.0206	51								
Ordinary one-way ANOVA										
Number of families	1									
Number of comparisons per family	10									
Alpha	0.05									
Tukey's multiple comparisons test	Mean 1	Mean 2	Mean Diff.	SE of diff.	n1	n2	q	DF	95.00% CI of diff.	Adjusted P
stage 2 vs. stage 3	0.09535	0.1055	-0.01015	0.003645	9	10	3.938	47	-0.02049 to 0.0001896	0.0566
stage 2 vs. stage 4	0.09535	0.09064	0.00471	0.003645	9	10	1.827	47	-0.005630 to 0.01505	0.6973
stage 2 vs. stage 5	0.09535	0.1368	-0.04145	0.003498	9	12	16.76	47	-0.05137 to -0.03153	<0.0001
stage 2 vs. stage 6	0.09535	0.128	-0.03265	0.003566	9	11	12.95	47	-0.04276 to -0.02254	<0.0001
stage 3 vs. stage 4	0.1055	0.09064	0.01486	0.003548	10	10	5.923	47	0.004796 to 0.02492	0.0011
stage 3 vs. stage 5	0.1055	0.1368	-0.0313	0.003397	10	12	13.03	47	-0.04094 to -0.02166	<0.0001
stage 3 vs. stage 6	0.1055	0.128	-0.0225	0.003466	10	11	9.179	47	-0.03233 to -0.01267	<0.0001
stage 4 vs. stage 5	0.09064	0.1368	-0.04616	0.003397	10	12	19.22	47	-0.05580 to -0.03652	<0.0001
stage 4 vs. stage 6	0.09064	0.128	-0.03736	0.003466	10	11	15.24	47	-0.04719 to -0.02753	<0.0001
stage 5 vs. stage 6	0.1368	0.128	0.0088	0.003312	12	11	3.758	47	-0.0005935 to 0.01819	0.0762

Table E4 ANOVA results and multiple comparisons for the UV rate constants across different RH for stage 2.

ANOVA results										
Table Analyzed	s2									
Data sets analyzed	A-C									
ANOVA summary										
F	192.7									
P value	<0.0001									
P value summary	****									
Significant diff. among means (P < )	Yes									
R squared	0.9437									
Brown-Forsythe test										
F (DFn, DFd)										
P value										
P value summary										
Are SDs significantly different (P < 0.05)?										
ANOVA table										
	SS	DF	MS	F (DFn, DF)	P value					
Treatment (between columns)	0.008631	2	0.004315	F (2, 23) =	P<0.0001					
Residual (within columns)	0.000515	23	2.24E-05							
Total	0.009146	25								
Ordinary one-way ANOVA										
Number of families	1									
Number of comparisons per family	3									
Alpha	0.05									
Tukey's multiple comparisons test										
	Mean 1	Mean 2	Mean Diff.	SE of diff.	n1	n2	q	DF	95.00% CI of diff.	Adjusted P
25%RH vs. 40%RH	0.07237	0.1175	-0.04513	0.002299	8	9	27.76	23	-0.05089 to -0.03937	<0.0001
25%RH vs. 60%RH	0.07237	0.09535	-0.02298	0.002299	8	9	14.13	23	-0.02874 to -0.01722	<0.0001
40%RH vs. 60%RH	0.1175	0.09535	0.02215	0.002231	9	9	14.04	23	0.01656 to 0.02774	<0.0001

Table E5 ANOVA results and multiple comparisons for the UV rate constants across different RH for stage 3.

ANOVA results										
Table Analyzed	s3									
Data sets analyzed	A-C									
ANOVA summary										
F	56.5									
P value	<0.0001									
P value summary	****									
Significant diff. among means (P < )	Yes									
R squared	0.8248									
Brown-Forsythe test										
F (DFn, DFd)										
P value										
P value summary										
Are SDs significantly different (P < 0.05)?										
ANOVA table										
	SS	DF	MS	F (DFn, DF) P value						
Treatment (between columns)	0.006209	2	0.003104	F (2, 24) = P<0.0001						
Residual (within columns)	0.001319	24	5.49E-05							
Total	0.007527	26								
Ordinary one-way ANOVA										
Number of families	1									
Number of comparisons per family	3									
Alpha	0.05									
Tukey's multiple comparisons test										
	Mean 1	Mean 2	Mean Diff.	SE of diff.	n1	n2	q	DF	95.00% CI of diff.	Adjusted P
25%RH vs. 40%RH	0.07474	0.112	-0.03726	0.003653	7	10	14.43	24	-0.04638 to -0.02814	<0.0001
25%RH vs. 60%RH	0.07474	0.1055	-0.03076	0.003653	7	10	11.91	24	-0.03988 to -0.02164	<0.0001
40%RH vs. 60%RH	0.112	0.1055	0.0065	0.003315	10	10	2.773	24	-0.001778 to 0.01478	0.1438

Table E6 ANOVA results and multiple comparisons for the UV rate constants across different RH for stage 4.

ANOVA results										
Table Analyzed	s4									
Data sets analyzed	A-C									
ANOVA summary										
F	24.31									
P value	<0.0001									
P value summary	****									
Significant diff. among means (P < )	Yes									
R squared	0.6695									
Brown-Forsythe test										
F (DFn, DFd)										
P value										
P value summary										
Are SDs significantly different (P < 0.05)?										
ANOVA table										
	SS	DF	MS	F (DFn, DF) P value						
Treatment (between columns)	0.007573	2	0.003787	F (2, 24) = P<0.0001						
Residual (within columns)	0.003739	24	0.000156							
Total	0.01131	26								
Ordinary one-way ANOVA										
Number of families	1									
Number of comparisons per family	3									
Alpha	0.05									
Tukey's multiple comparisons test										
	Mean 1	Mean 2	Mean Diff.	SE of diff.	n1	n2	q	DF	95.00% CI of diff.	Adjusted P
25%RH vs. 40%RH	0.06685	0.1091	-0.04225	0.006065	8	9	9.852	24	-0.05740 to -0.02710	<0.0001
25%RH vs. 60%RH	0.06685	0.09064	-0.02379	0.00592	8	10	5.683	24	-0.03857 to -0.009005	0.0014
40%RH vs. 60%RH	0.1091	0.09064	0.01846	0.005735	9	10	4.552	24	0.004139 to 0.03278	0.0099

Table E7 ANOVA results and multiple comparisons for the UV rate constants across different RH for stage 5.

ANOVA results											
Table Analyzed	s5										
Data sets analyzed	A-C										
ANOVA summary											
F	108										
P value	<0.0001										
P value summary	****										
Significant diff. among means (P < )	Yes										
R squared	0.8925										
Brown-Forsythe test											
F (DFn, DFd)											
P value											
P value summary											
Are SDs significantly different (P < 0.05)?											
ANOVA table											
	SS	DF	MS	F (DFn, Df)	P value						
Treatment (between columns)	0.02699	2	0.01349	F (2, 26) =	P<0.0001						
Residual (within columns)	0.00325	26	0.000125								
Total	0.03024	28									
Ordinary one-way ANOVA											
Number of families	1										
Number of comparisons per family	3										
Alpha	0.05										
Tukey's multiple comparisons test											
	Mean 1	Mean 2	Mean Diff.	SE of diff.	n1	n2	q	DF	95.00% CI of diff.	Adjusted P	
25%RH vs. 40%RH	0.1074	0.1857	-0.0783	0.005433	8	9	20.38	26	-0.09180 to -0.06480	<0.0001	
25%RH vs. 60%RH	0.1074	0.1368	-0.0294	0.005103	8	12	8.148	26	-0.04208 to -0.01672	<0.0001	
40%RH vs. 60%RH	0.1857	0.1368	0.0489	0.00493	9	12	14.03	26	0.03665 to 0.06115	<0.0001	

Table E8 ANOVA results and multiple comparisons for the UV rate constants across different RH for stage 6.

ANOVA results										
Table Analyzed	s6									
Data sets analyzed	A-C									
ANOVA summary										
F	113.1									
P value	<0.0001									
P value summary	****									
Significant diff. among means (P < 0.05)	Yes									
R squared	0.9005									
Brown-Forsythe test										
F (DFn, DFd)										
P value										
P value summary										
Are SDs significantly different (P < 0.05)?										
ANOVA table										
	SS	DF	MS	F (DFn, DFd)	P value					
Treatment (between columns)	0.02038	2	0.01019	F (2, 25) =	P<0.0001					
Residual (within columns)	0.002253	25	9.01E-05							
Total	0.02264	27								
Ordinary one-way ANOVA										
Number of families	1									
Number of comparisons per family	3									
Alpha	0.05									
Tukey's multiple comparisons test										
	Mean 1	Mean 2	Mean Diff.	SE of diff.	n1	n2	q	DF	95.00% CI of diff.	Adjusted P
25%RH vs. 40%RH	0.1054	0.1728	-0.0674	0.004613	8	9	20.66	25	-0.07889 to -0.05591	<0.0001
25%RH vs. 60%RH	0.1054	0.128	-0.0226	0.004411	8	11	7.245	25	-0.03359 to -0.01161	<0.0001
40%RH vs. 60%RH	0.1728	0.128	0.0448	0.004267	9	11	14.85	25	0.03417 to 0.05543	<0.0001

Table E9 ANOVA results and multiple comparisons for the UV rate constants across different RH for overall particle size.

ANOVA results										
Table Analyzed	overall									
Data sets analyzed	A-C									
ANOVA summary										
F	106.1									
P value	<0.0001									
P value summary	****									
Significant diff. among means (P < 0.05)	Yes									
R squared	0.9099									
Brown-Forsythe test										
F (DFn, DFd)										
P value										
P value summary										
Are SDs significantly different (P < 0.05)?										
ANOVA table										
	SS	DF	MS	F (DFn, DFd)	P value					
Treatment (between columns)	0.021	2	0.0105	F (2, 21) =	P<0.0001					
Residual (within columns)	0.002079	21	9.9E-05							
Total	0.02308	23								
Ordinary one-way ANOVA										
Number of families	1									
Number of comparisons per family	3									
Alpha	0.05									
Tukey's multiple comparisons test										
	Mean 1	Mean 2	Mean Diff.	SE of diff.	n1	n2	q	DF	95.00% CI of diff.	Adjusted P
25%RH vs. 40%RH	0.1055	0.1761	-0.0706	0.004974	8	8	20.07	21	-0.08314 to -0.05806	<0.0001
25%RH vs. 60%RH	0.1055	0.1267	-0.0212	0.004974	8	8	6.027	21	-0.03374 to -0.008662	0.001
40%RH vs. 60%RH	0.1761	0.1267	0.0494	0.004974	8	8	14.04	21	0.03686 to 0.06194	<0.0001

# Appendix F: Rstudio code for extracting genome composition information

```
# 00 - UV inactivation virus sequence attributes
# 2023.05.12
# HAO LUO
# LIBRARIES-----
library(stringr)
# SET WORKING DIRECTORY-----
# Set the working directory.
setwd("G:/My Drive/UALBERTA/8th - genomic model/model calculation/all ssrna")
# DATA INPUT-----
files = c(
  "3_GA.txt","3_ms2.txt","5_hev.txt","8_ms2.txt","11_poliovirus.txt","coxsackievirus_B6.txt","echovirus_ty
  pe_12.txt","feline_calicivirus.txt","polivorius.txt"
)
# DATA MANIPULATION-----
# Number of different sequences to assess.
num_files = length(files)
# Sequence information to extract from text files.
seq_vars = c("Length", "FINAL_TT_TOTAL", "FINAL_TC_TOTAL","FINAL_CT_TOTAL",
  "FINAL_CC_TOTAL", "FINAL_YR_TOTAL"
)

# Define empty matrix seq_data to fill in with sequence information.
seq_extract = matrix(NA, nrow = num_files, ncol = length(seq_vars))
# Define row names
rownames(seq_extract) = str_remove(files, ".txt")
# Define column names
colnames(seq_extract) = seq_vars
# Loop through each file and count and record sequence information in each file.
for (i in 1:num_files) {

  # Read in each file, separated by line.
  eachfile = scan(files[i], character(0), sep = "\n")
  # Count sequence information.
  length = as.numeric( nchar( eachfile[2] ))
  num_TT_total = as.numeric ( str_count ( eachfile[2],"TT" ))
  num_TTT_total = as.numeric ( str_count ( eachfile[2],"TTT" ))
  num_TTTT_total = as.numeric ( str_count ( eachfile[2],"TTTT" ))
  num_TTTTT_total = as.numeric ( str_count ( eachfile[2],"TTTTT" ))
  num_TTTTTT_total = as.numeric ( str_count ( eachfile[2],"TTTTTT" ))
  num_TTTTTTT_total = as.numeric ( str_count ( eachfile[2],"TTTTTTT" ))
  FINAL_TT_TOTAL=num_TT_total+num_TTT_total+num_TTTTT_total-
  num_TTTTTT_total+num_TTTTTTT_total
  num_CT_total = as.numeric ( str_count ( eachfile[2],"CT" ))
  num_TC_total = as.numeric ( str_count ( eachfile[2],"TC" ))
  FINAL_TC_TOTAL=num_CT_total
  FINAL_CT_TOTAL=num_TC_total
  num_CC_total = as.numeric ( str_count ( eachfile[2],"CC" ))
  num_CCC_total = as.numeric ( str_count ( eachfile[2],"CCC" ))
  num_CCCC_total = as.numeric ( str_count ( eachfile[2],"CCCC" ))
```

```

num_CCCCC_total = as.numeric ( str_count ( eachfile[2],"CCCCC" ))
num_CCCCCC_total = as.numeric ( str_count ( eachfile[2],"CCCCCC" ))
num_CCCCCC_total = as.numeric ( str_count ( eachfile[2],"CCCCCC" ))
FINAL_CC_TOTAL=num_CC_total+num_CCC_total+num_CCCCC_total-
num_CCCCCC_total+num_CCCCCC_total
num_TTA_total = as.numeric ( str_count ( eachfile[2],"TTA" ))
num_TTG_total = as.numeric ( str_count ( eachfile[2],"TTG" ))
num_TCA_total = as.numeric ( str_count ( eachfile[2],"TCA" ))
num_TCG_total = as.numeric ( str_count ( eachfile[2],"TCG" ))
num_CTA_total = as.numeric ( str_count ( eachfile[2],"CTA" ))
num_CTG_total = as.numeric ( str_count ( eachfile[2],"CTG" ))
num_CCA_total = as.numeric ( str_count ( eachfile[2],"CCA" ))
num_CCG_total = as.numeric ( str_count ( eachfile[2],"CCG" ))

FINAL_YR_TOTAL=num_TTA_total+num_TTG_total+num_TCA_total+num_TCG_total+num_CTA_to
tal+num_CTG_total+num_CCA_total+num_CCG_total

# Records sequence information for virus i in seq_info matrix.
seq_extract[i,]= c(length, FINAL_TT_TOTAL,FINAL_CT_TOTAL, FINAL_CT_TOTAL,
FINAL_CC_TOTAL, FINAL_YR_TOTAL
)
}

# DATA OUTPUT-----
# Outputs data as an R file.
save(seq_extract, file = 'virus-seq-attributes.RData')

```

## Appendix G: Statistical analysis of the UV rate constant model

Table G1 Results of the multiple regression analysis of the UV rate constant model for genome damage

Model forms	Statistics			
	Parameters	Values	P value	R <sup>2</sup>
Summation in number: $k = a \times UU_{number} + b \times length + c \times GC_{number} + d$	a	$-4.2144 \times 10^{-4}$	$1.6692 \times 10^{-4}$	0.9396
	b	$1.3316 \times 10^{-4}$	$7.2147 \times 10^{-6}$	
	c	$-1.8074 \times 10^{-4}$	$1.0296 \times 10^{-4}$	
	d	0.0100	$1.4792 \times 10^{-6}$	
Summation in ratio: $k = a \times length + b \times GC_{ratio} + c$	a	$1.7362 \times 10^{-5}$	$3.4719 \times 10^{-25}$	0.9259
	b	-0.0855	0.02632	
	c	0.0523	0.00753	
Summation with exponents in number: $k = a \times (UU_{number}^b)$	a	0.0026	$2.9663 \times 10^{-7}$	0.9204
	b	0.6046	$3.0812 \times 10^{-29}$	
Summation with exponents in ratio: $k = a \times (length^b) + c$	a	$7.3029 \times 10^{-5}$	0.2028	0.9225
	b	0.8494	$4.5352 \times 10^{-14}$	
	c	0.0053	0.1191	
Multiplication with exponents in number: $k = a \times (CU_{number}^b \times YR_{number}^c)$	a	$8.6568 \times 10^{-4}$	$1.3198 \times 10^{-5}$	0.9274
	b	-0.6248	0.00644	
	c	1.2822	$2.400 \times 10^{-8}$	
Multiplication with exponents in ratio: $k = YR_{ratio}^a \times length^b$	a	3.995	$4.3585 \times 10^{-30}$	0.8802
	b	0.7013	$3.0838 \times 10^{-24}$	

Table G2 Results of the principal components regression analysis of the UV rate constant model for genome damage

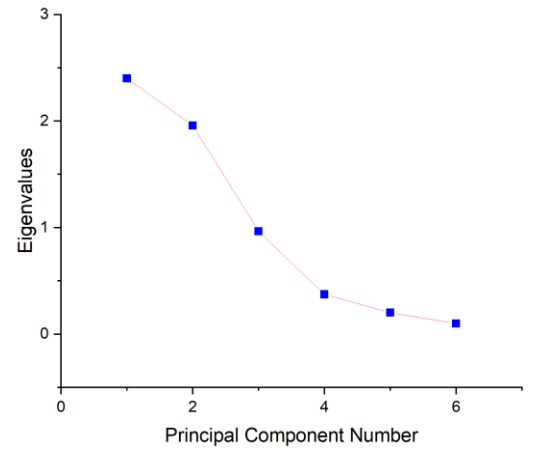
Principal components regression in number			
Parameters	Coefficients of PC1	Coefficients of PC2	Plots
UU	0.37539	-0.56552	
UC	0.37938	0.14743	
CU	0.37908	0.19628	
CC	0.3717	0.70658	
YR	0.37982	-0.25483	
Length	0.37979	-0.23563	
GC	0.3805	0.01472	

Linear regression ( $R^2=0.9056$ ):  
 $k = 0.0140 \times PC1_{number} + 0.0293$

Principal components regression in ratio			
Parameters	Coefficients of PC1	Coefficients of PC2	Plots
UU	-0.40849	0.45229	
UC	0.4203	0.48299	
CU	0.41719	0.47595	
CC	0.41025	-0.19421	
YR	-0.02365	0.49779	

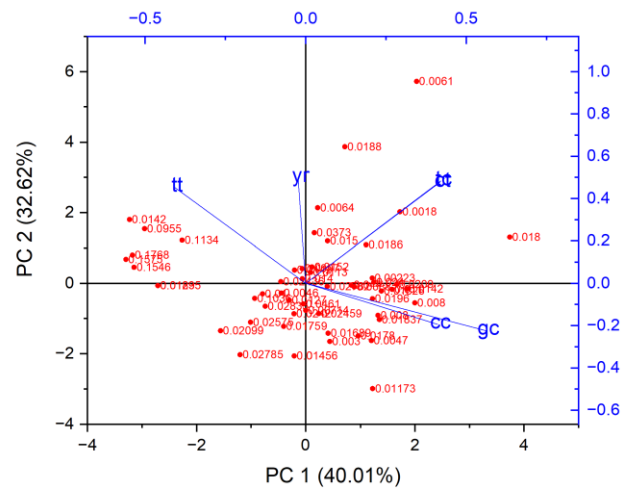
---

GC	0.55998	-0.22387
----	---------	----------

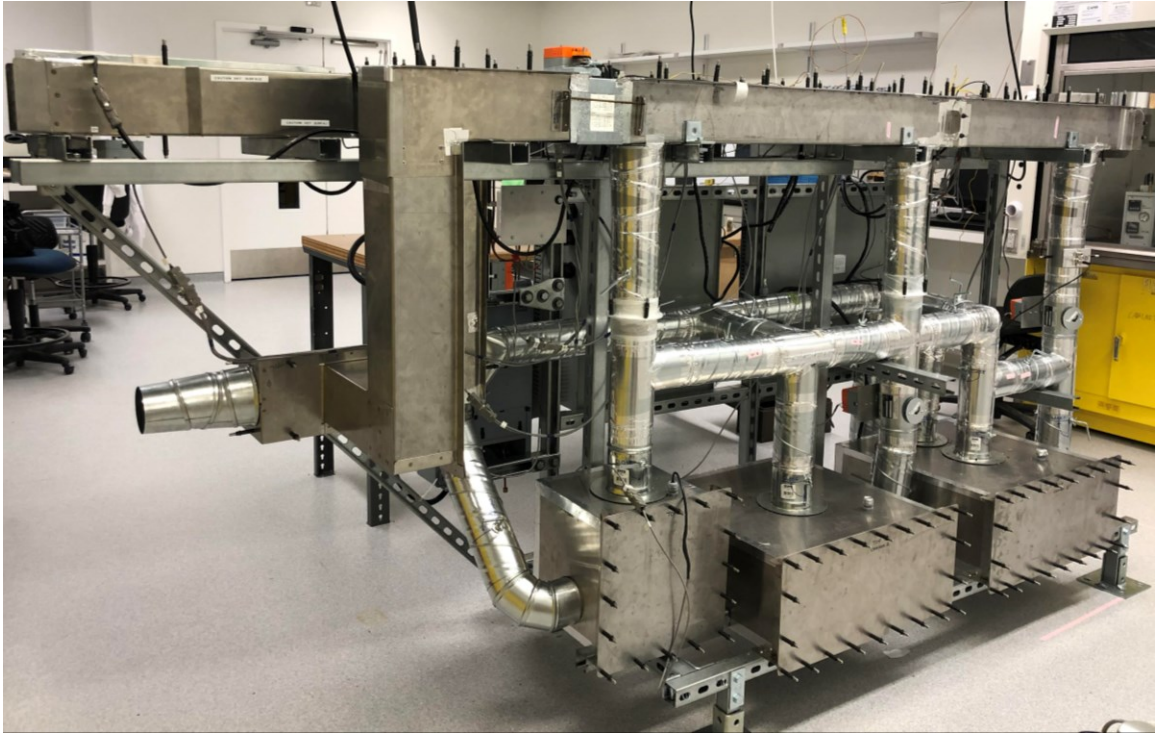


Linear regression ( $R^2=0.9235$ ):

$$k = -0.0021PC1_{ratio} + 1.7773 \times 10^{-5} length + 0.0104$$



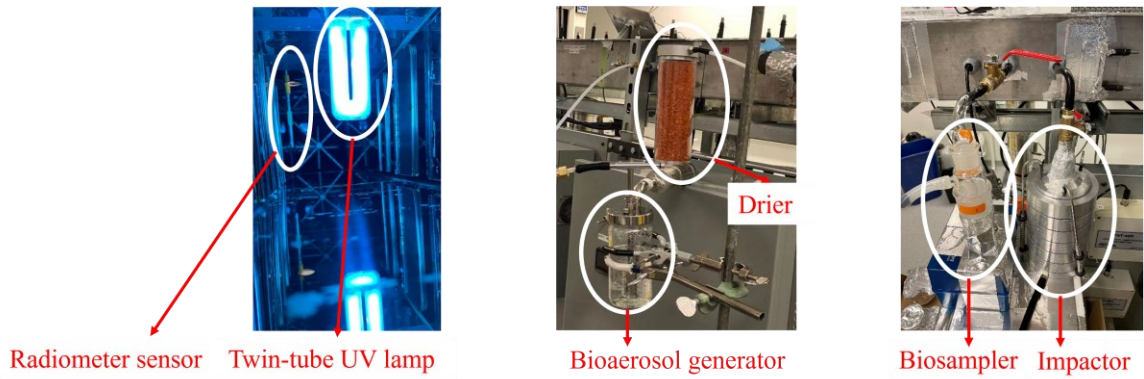
## Appendix H: The pilot HVAC setup and in-duct UVGI system



(a)



(b)



(c)

Figure H1 (a) – (b) A pilot-scale HVAC setup and an in-duct UVGI reactor, and (c) setup for UV irradiance measurement, bioaerosol generation and samplings

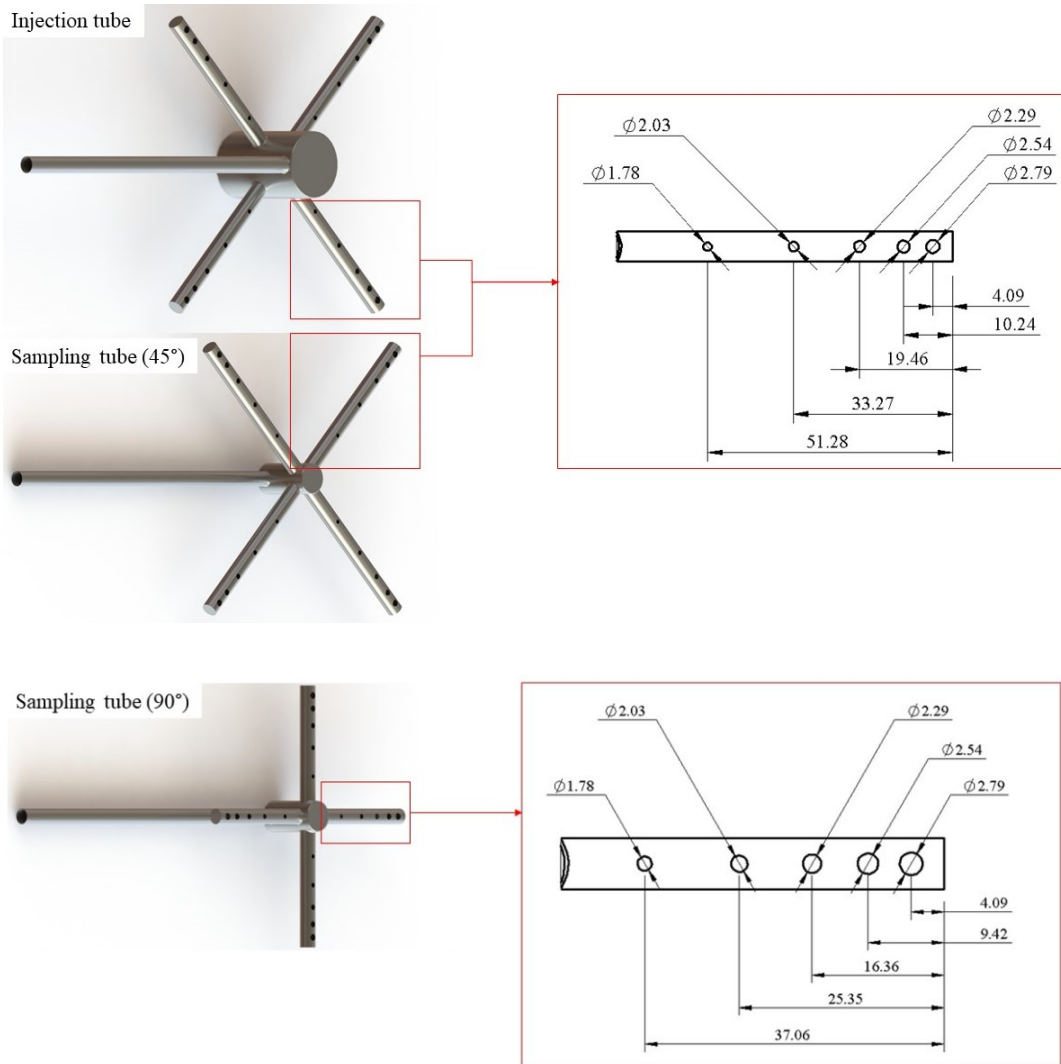


Figure H2 Design of cross-shaped tubes (units: cm) [123]